Photon beam asymmetries for the $p(\vec{\gamma},K^+)\Lambda$ and $p(\vec{\gamma},K^+)\Sigma^0$ reactions at SPring-8/LEPS

Mizuki Sumihama

Department of physics
Osaka University

February, 2003

Abstract

We have constructed the LEPS facility for quark nuclear-physics studies at BL33LEP of SPring-8 in 2000. The LEPS facility provides linear-polarized photons produced by the backward-Compton scattering (BCS) process between laser photons and 8-GeV electrons. The first experiment has been carried out by using the linear-polarized photon beam and the liquid hydrogen target from December 2000 to June 2001. By measuring the recoil electron energy, the BCS photons are tagged with a resolution of 15 MeV (RMS). The energy of the tagged photons ranges from 1.5 GeV to 2.4 GeV. The magnetic spectrometer is optimized to study the ϕ-meson photoproduction at forward angles. Detailed descriptions on the SPring-8/LEPS facility and the LEPS spectrometer are given in this thesis.

There are a large number of nucleon resonances predicted in the quark models which are not observed in the reactions associated with π mesons. These resonances are called 'missing resonances'. It is essential to fully understand the excited states to gain deeper insight into the structure of baryons. The K^+ photoproduction involving strangeness is known to play a decisive role to give information on missing resonances. Especially, the precise measurements of the photon beam asymmetries for the K^+ photoproductions were awaited for a long time. This thesis reports the results of the photon beam asymmetries for the $p(\vec{\gamma},K^+)\Lambda(1116)$ and $p(\vec{\gamma},K^+)\Sigma^0(1193)$ reactions obtained in the energy range 1.5 GeV $\leq E_\gamma \leq$ 2.4 GeV and the angular range $0.6 \leq \cos\Theta_{cm} \leq 1$. The photon beam asymmetries for these reactions were measured for the first time in this energy range. The signs of the photon beam asymmetries for both the reactions were found to be positive in the measured kinematical region. The experimental data will provide precious information on the existence of new excited states of the nucleon. It is found that the present models cannot reproduce our data, perfectly. The present photon beam asymmetry data stimulate the further development of the theoretical models. The present data will extend our knowledge of the K^+ photoproduction mechanism including the effect of nucleon resonances.

Contents

Chapter 1

Introduction

1.1 Excitation spectrum of nucleon

In 1960s, one realized that the hundreds of hadrons, which had been identified experimentally, did not represent the fundamental constituents of matter. In fact, hadrons were found to have an internal structure, and could be classified on the basis of a restricted set of new particles at more basic level. These new particles are "quarks" and "gluons". Soon after the concept of quarks and gluons was established, a new description of the strong interaction in terms of quark and gluon degree-of-freedom was developed. The fundamental equations for the description of the dynamics of quarks and gluons have been summarized in Quantum Chromo Dynamics (QCD). However, the QCD is only solved in the perturbative region at extremely high energies. To describe the actual quark and gluon world in hadrons, the effective theories working in the non-perturbative region have to be developed. This is the current subject in hadron physics in 2000s.

In view of the standing points mentioned above, experimental information on hadron structures is still poor. To gain deeper insight into the structure of baryons, it is essential to fully understand its excited states. The excited spectrum of the nucleon reflects its underlying structure and contains a signature stemming from the sub-constituents at more fundamental level.

Information on the nucleon resonances, N^* and Δ^*, can be obtained by a variety of experiments. A general principle is to transfer an amount of energy to the nucleon by means of a hadronic or electromagnetic probe. Due to this energy-momentum transfer, the nucleonic system is left into one of its excited states which eventually decays into a set of stable particles. Historically, a substantial amount of information on the excited states of the nucleon has been accumulated by studies of the πN and N(γ,π) reactions. However, it has been realized that intermediate resonances are limited in the pionic reactions. This problem is addressed by recent calculations with constituent quark models [1, 2]. Considerably larger number of nucleon resonances are predicted by theoretical calculations than ones observed in the pionic reactions. These nucleon resonances are called 'missing resonances'. Quark model studies suggest a part of these missing resonances may couple to strange channels, such as KΛ and KΣ channels [2]. It is believed that the production of a strange quark pair $s\bar{s}$, in addition to the presence of up and down quarks, can provide precious information to understand the hadron spectrum. Therefore, the K^+ photoproduction can be good means to search for the missing

nucleon resonances.

1.2 Missing resonance D_{13}

The reactions involving a strangeness are a promising field to give information on new excited states of the nucleon. One of these reactions is the kaon photoproduction denoted as p(γ,K)Y with Y = Λ, Σ. The electromagnetic probe has a great advantage to study the nucleon structure because the electromagnetic coupling to a nucleon is better understood than its hadronic counterpart.

In 1998, the experimental results of the kaon photoproduction were reported by the ELSA/ SAPHIR collaboration at Bonn [3, 4]. An indication for observing a missing resonance was found in the total cross section data for the p(γ,K^+)Λ reaction measured by the SAPHIR collaboration [3] as shown in Fig. 1.1. The total cross section data shows a bump structure

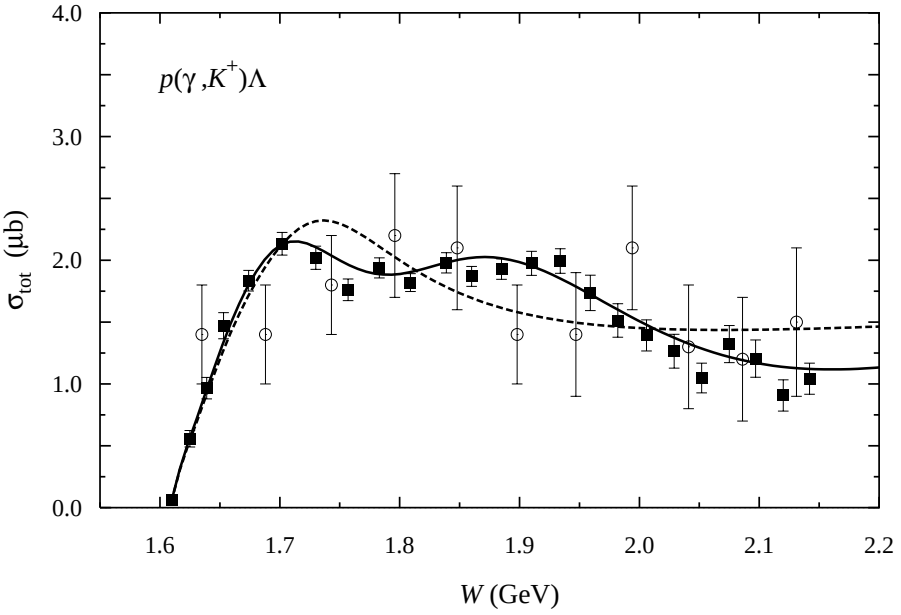

Figure 1.1: Total cross section for the p(γ,K^+)Λ reaction. The solid squares are the data measured by the ELSA/SAPHIR collaboration [3]. The open circles are old data obtained by the bubble chamber experiment at DESY [5]. The dashed line is the result of the theoretical calculation without the D_{13}(1960) resonance, and the solid line is the theoretical calculation with the D_{13}(1960) [6].

around W = 1.9 GeV in the total c.m. energy (E_γ = 1.5 GeV in the photon beam energy). This structure was predicted to come from the missing nucleon resonance D_{13}(1960) by Mart and Bennhold [6]. The D_{13}(1960) resonance is predicted to strongly couple to the KΛ channel by a quark model [2]. Fig. 1.1 shows that the SAPHIR data of the total cross section was

well reproduced by assuming the missing nucleon resonance $D_{13}(1960)$ using the effective-Lagrangian approach. However, only cross section data was used for this study. It is difficult and dangerous to conclude the existence of the missing resonance $D_{13}(1960)$. In fact, there still remains a continued controversy in the theoretical description of the cross sections [7, 8], because there are ambiguities of meson-hadron couplings and form factors at hadronic vertices together with the ambiguity in the nucleon resonance amplitudes. Therefore, additional observables are necessary to examine the theoretical models.

1.3 Theoretical models of the kaon photoproduction

The dominant Feynman diagrams of the kaon photoproduction process in an isobar model are shown in Fig. 1.2. The kaon photoproduction is described by the diagrams at the tree

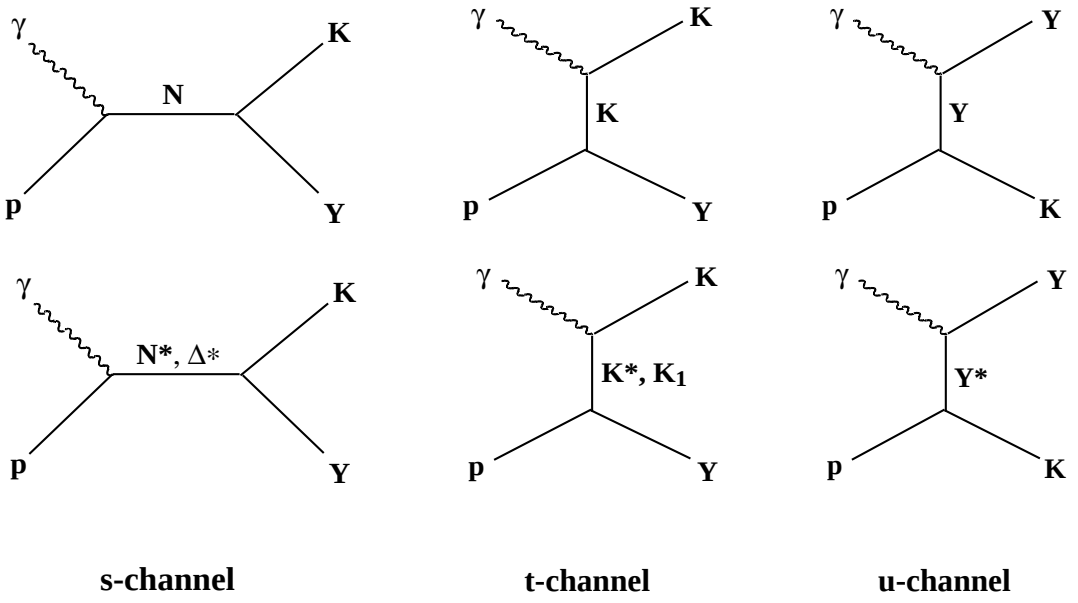

Figure 1.2: Diagrams contributing to the kaon photoproduction at the tree level. The upper row corresponds to the Born terms and the lower row corresponds to the terms of the exchange of resonances. In the s-channel, proton and resonances are exchanged. The exchanged mesons in the t-channel are K, K^* and K_1. The hyperon as Λ, Σ, and hyperon resonances are exchanged in the u-channel.

level. In the s-channel, proton and resonances (N^*, Δ^*) are exchanged. The exchanged mesons in the t-channel are K, K^* and K_1. The hyperons (Λ, Σ^0 and Σ^+) and hyperon resonances are exchanged in the u-channel. The upper row in Fig. 1.2 corresponds to the Born terms and the lower row corresponds to the terms of resonances.

Intermediate particles in the reaction dynamics are treated as effective fields with their own characteristics like mass, photo-coupling amplitudes and decay widths. The coupling

constants for the individual resonances are not determined theoretically. They are treated as free parameters and are extracted by performing a global fit of the model calculations to the available data. Then, these values obtained by the fitting procedure are compared to quark model predictions. Assuming the SU(3) symmetry, the coupling constants $g_{K\Lambda p}$ and $g_{K\Sigma p}$ are fixed by the well-known $g_{\pi NN}$ coupling.

The SU(3) symmetry is broken due to the mass difference between the strange and the up/down quarks. Assuming that the SU(3) symmetry is broken at a 20% level, the following ranges for $g_{K\Lambda p}$ and $g_{K\Sigma^0 p}$ are permissible at present [9, 10]:

$$-4.5 \leq g_{K\Lambda p}/\sqrt{4\pi} \leq -3.0, \tag{1.1a}$$

$$0.9 \leq g_{K\Sigma^0 p}/\sqrt{4\pi} \leq 1.3. \tag{1.1b}$$

The hadronic form factors are introduced to take into account the finite extension of the particles at the hadronic vertices. There are two choices of the functional form of the hadronic form factors. The one is suggested by Haberzettl F_H [11, 12] and the other is suggested by Davidson and Workman F_{DW} [13]. The introduction of the hadronic form factor leads to the introduction of a free parameter, the cutoff mass Λ.

Mart and Bennhold [6] use a tree level isobar model to study the $p(\gamma,K^+)\Lambda$ reaction. They include three nucleon resonances, $S_{11}(1650)$, $P_{11}(1710)$ and $P_{13}(1720)$ in the s-channel which were found to be dominant in the $p(\gamma,K^+)\Lambda$ reaction. In the t-channel, K^* and K_1 are included in their model. They introduce the hadronic form factor at hadronic vertices suggested by Haberzettl F_H [11, 12]. By using this model, they reproduce the SAPHIR data of the total cross section including a missing resonance $D_{13}(1960)$ as shown in Fig. 1.1. The $D_{13}(1960)$ resonance is predicted to have a significant $K\Lambda$ decay width [2]. They also predict

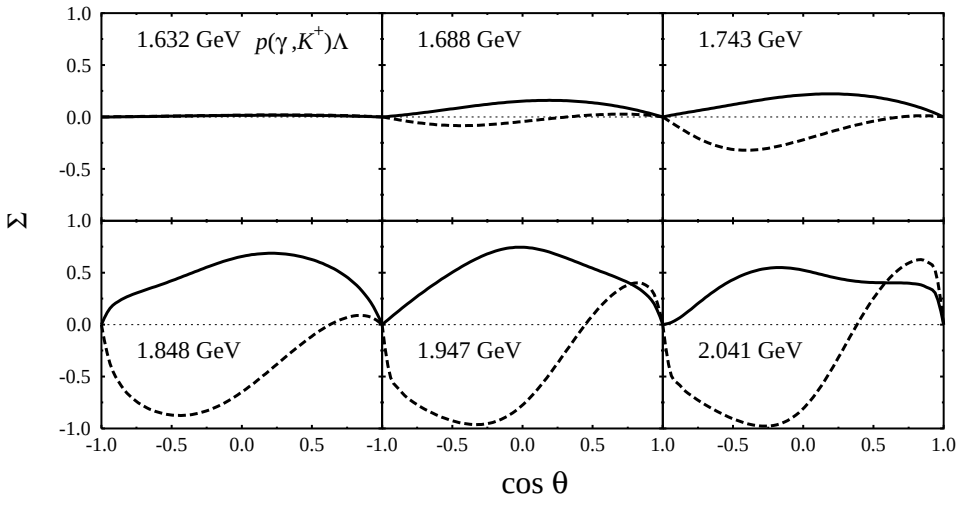

Figure 1.3: The angular distribution of the photon beam asymmetry for the $p(\gamma,K^+)\Lambda$ reaction. The dashed line is the theoretical calculation without the $D_{13}(1960)$ resonance and the solid line is the theoretical calculation with the $D_{13}(1960)$ [6].

the spin observables and the differential cross section. Fig. 1.3 shows the angular ($\cos\theta_{cm}$) distributions of the photon beam asymmetry obtained by their model calculations. The total c.m. energy W is displayed in the figure. The solid line is obtained by including the resonance $D_{13}(1960)$ and the dashed line shows their model calculation without the $D_{13}(1960)$. The large effects are found in the photon beam asymmetry. The new resonance leads to a sign change. Therefore, they suggest that measurements of the photon beam asymmetry are suited to check the validity of model calculations.

Janssen *et al.* calculated the photon beam asymmetry of the K^+ photoproduction in a tree level isobar model [7, 14]. They showed that the model calculations are sensitive to various ambiguities. Fig. 1.4 and Fig. 1.5 show the angular distribution of the photon beam asymmetry for the $p(\gamma,K^+)\Lambda$ and the $p(\gamma,K^+)\Sigma^0$ reaction calculated with some different models by Janssen *et al.*.

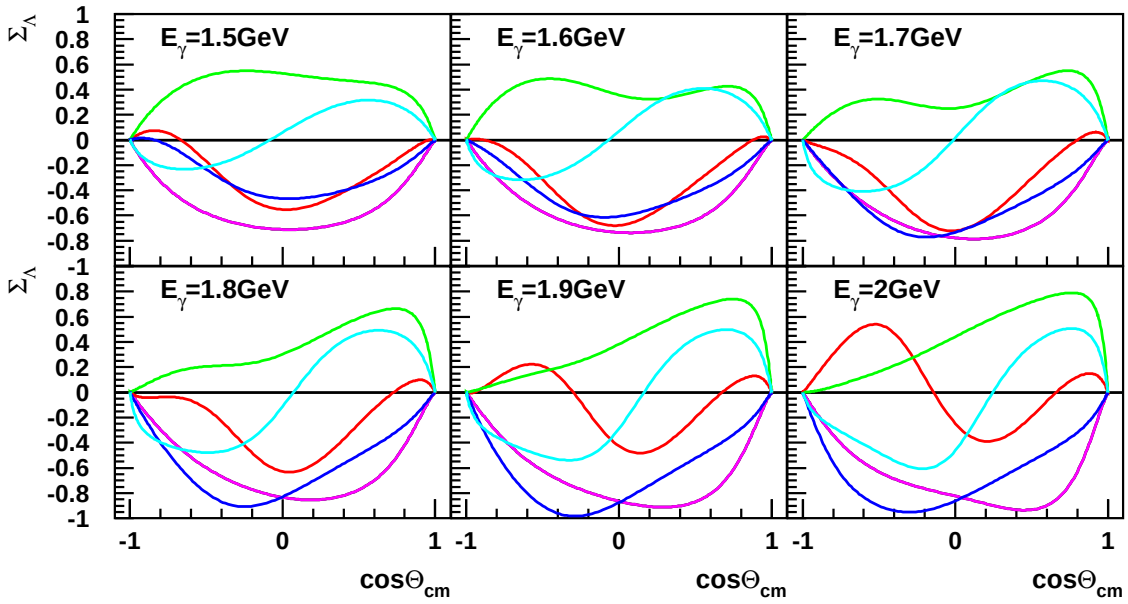

Figure 1.4: The angular distribution of the photon beam asymmetry of the $p(\gamma,K^+)\Lambda$ reaction [7, 14]. The pink and green lines are the results of the model A with the hadronic form factor F_{DW} and F_H. The red and blue lines are the results of the model B with the hadronic form factor F_{DW} and F_H. The light blue lines are the results of the model C with the hadronic form factor F_{DW}. The photon energy E_γ is displayed in the figures.

In the model A, they use a small cutoff mass ($\Lambda \geq 0.4$ GeV). The hyperon resonances $\Lambda^*(1800)$ and $\Lambda^*(1810)$ in the u-channel are included in the model B. They use the coupling constants of Eq. 1.1 not to restrict the SU(3) symmetry in the model C. The hadronic form factors F_{DW} and F_H are used in their models. They include the missing resonance D_{13} in addition to three dominant nucleon resonances, $S_{11}(1650)$, $P_{11}(1710)$ and $P_{13}(1720)$ in all the models. Including the D_{13} resonance reduces the χ^2 values obtained by the fitting procedure

of the results of the models to the experimental data of the cross section measured by the SAPHIR collaboration.

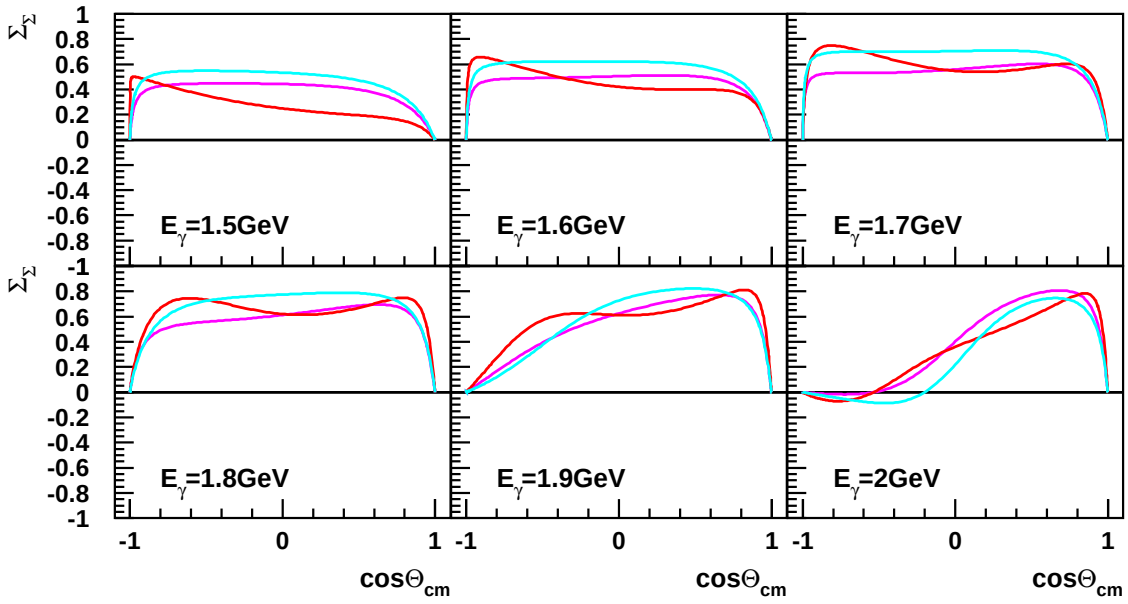

Figure 1.5: The angular distribution of the photon beam asymmetry of the p(γ,K$^+$)Σ^0 reaction [7, 14]. The pink, red and light blue lines are the results of the model A, B and C with the hadronic form factor F_{DW}. The photon energy E_γ is displayed in the figures.

The photon beam asymmetry is quite sensitive to the model differences. Even if the models can reproduce the cross section data, they show quite different values of the photon beam asymmetry in the the p(γ,K$^+$)Λ reaction.

1.4 Meson exchange in t-channel

The contribution of the t-channel meson exchange is expected to become large above the resonance region ($E_\gamma > 2.0$ GeV). Exchanged mesons in the kaon photoproduction are K, K* and K_1 (Fig. 1.2). The kaon photoproduction at the photon energy of 5, 8, 11 and 16 GeV has been measured in SLAC in 1970s [15, 16]. Fig. 1.6 shows the differential cross section for the p(γ,K$^+$)Λ and p(γ,K$^+$)Σ^0 reactions obtained at the photon energies, 5, 8, 11 and 16 GeV in SLAC. The differential cross section data for the reaction p(γ,K$^+$)Λ shows that the contribution of the K-exchange process is significant at very forward angles (-t < 0.25 GeV^2) while the contribution is not significant for the p(γ,K$^+$)Σ^0 reaction. This experimental result comes from the fact that the coupling constant $g_{K\Sigma N}$ associated with the p(γ,K$^+$)Σ^0 reaction is weaker than $g_{K\Lambda N}$ [17]. The best experiment to investigate the meson exchange process is to measure the differential cross sections for the two reactions, p(γ,K$^+$)Λ and p(γ,K$^+$)Σ^0, at forward angles,

precisely. Since the LEPS spectrometer covers extremely forward angles, the experimental data can be best suited to discuss the reaction mechanism of kaon photoproductions leading the Λ and Σ hyperons with good accuracy and statistics.

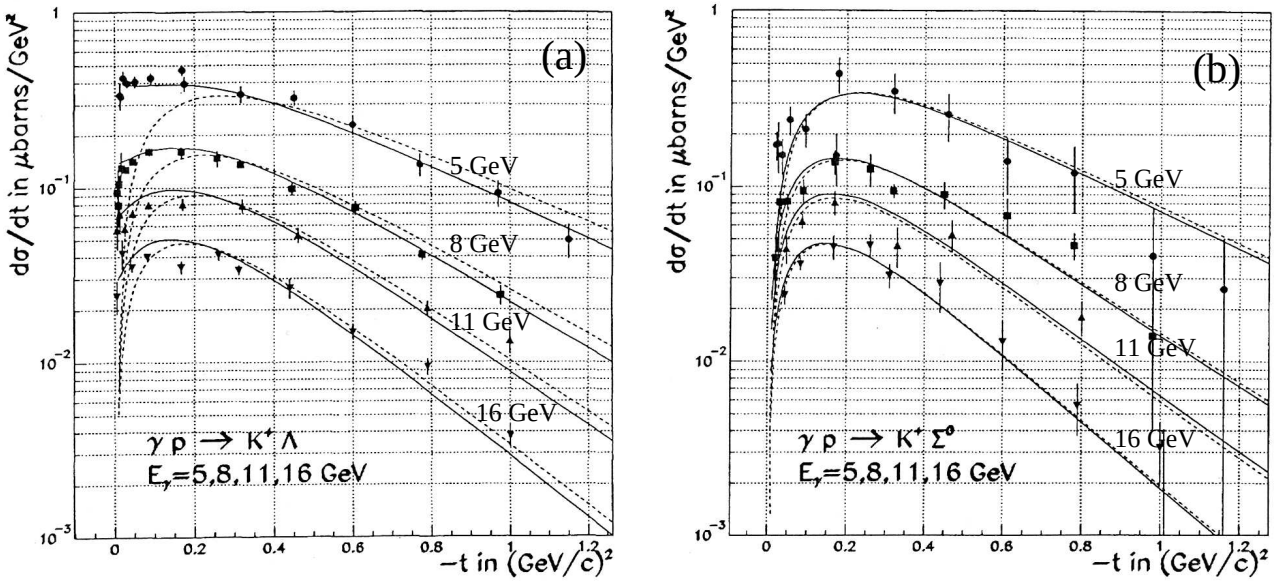

Figure 1.6: Differential cross sections for (a) the p(γ,K$^+$)Λ and (b) the p(γ,K$^+$)Σ^0 reactions at the photon energies, 5, 8, 11 and 16 GeV. The plots are the experimental results in SLAC [15]. The solid line denotes the results by the K + K*-exchanged model and the dashed line denotes the results by the K*-exchanged model [17].

Furthermore, the possibility of measuring the photon beam asymmetry with the polarized photon beam by backward-Compton scattering is unique. The photon beam asymmetry provides precious information on the contribution of the t-channel meson exchange. The dominance of the unnatural parity exchange (K, K_1) leads to the photon beam asymmetry equal to -1 while the natural parity exchange (K*) leads to the photon beam asymmetry equal to $+1$ [18, 19]. Fig. 1.7 shows the photon beam asymmetries for the p(γ,K$^+$)Λ and p(γ,K$^+$)Σ^0 reactions measured at the photon energy of 16 GeV in SLAC [16]. At forward angles, the photon beam asymmetry for the p(γ,K$^+$)Λ reaction drops and indicates that the contribution of the K-exchange process is dominant in the K$^+\Lambda$ production at forward angles. We measured the photon beam asymmetries at forward angles up to 2.4 GeV in the photon energy. Our data provides information on the meson-exchanges in the t-channel.

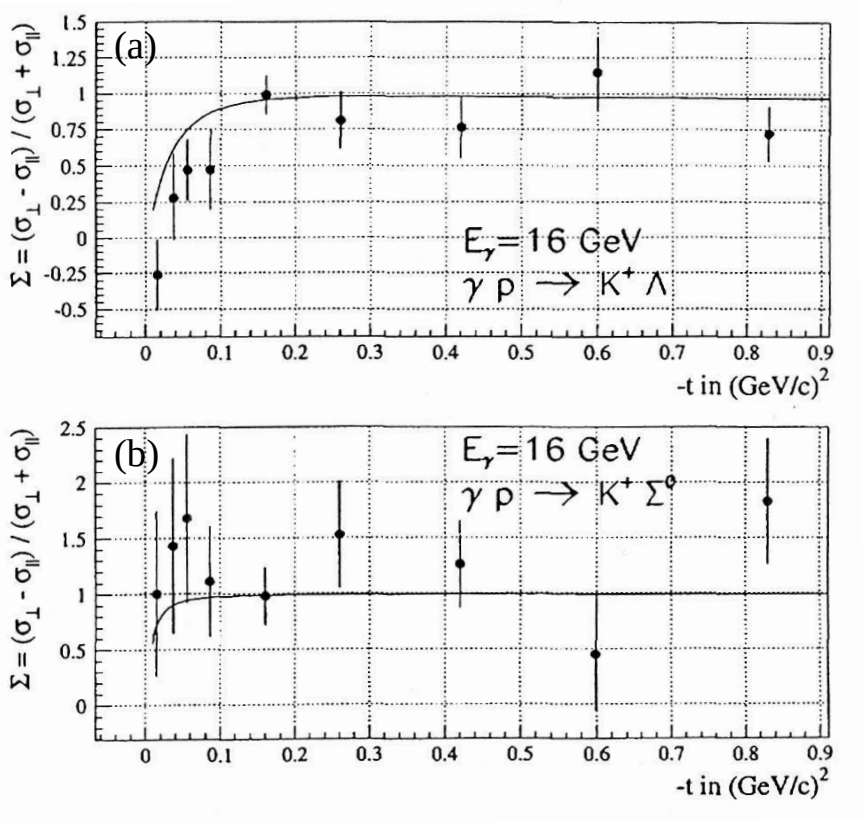

Figure 1.7: Photon beam asymmetries for the $p(\gamma,K^+)\Lambda$ (a) and $p(\gamma,K^+)\Sigma^0$ (b) reactions at the photon energy of 16 GeV. The plots are the experimental results in SLAC [16]. The solid line denotes the results by the K + K*-exchanged model [17].

In this thesis, I report the first experimental results concerning the $p(\gamma,K^+)\Lambda$ and $p(\gamma,K^+)\Sigma^0$ reactions measured at SPring-8/LEPS facility. In order to achieve the present experiment, we constructed a new magnetic spectrometer and the detection systems in 2000. The experimental setup has been reviewed. Details of the measurements, analyses, and the experimental results of the photon beam asymmetry are described in this thesis.

Chapter 2

Experiment

The photon beam asymmetries of the $p(\gamma,K^+)\Lambda$ and $p(\gamma,K^+)\Sigma^0$ reactions have been measured at the SPring-8/LEPS facility. The SPring-8/LEPS facility provides a linear-polarized photon beam with a high intensity and a large degree of polarization. The linear-polarized photons are produced by the backward-Compton-scattering process of laser photons from circulating 8-GeV electrons in the storage ring. Since the energy of the electron beam in SPring-8 is 8 GeV, the photon beam with a few GeV energy can be produced.

The LEPS magnetic spectrometer has been used to detect kaons in the $p(\gamma,K^+)\Lambda$ and $p(\gamma,K^+)\Sigma^0$ reactions. The K^+ events are identified by measuring measure momenta and time-of-flights. The SPring-8/LEPS facility and the LEPS spectrometer are described in detail in this chapter.

2.1 SPring-8 facility

The SPring-8 (Super-Photon ring-8 GeV) [20] is a third-generation synchrotron-radiation (SR) facility which has been completed in 1997. Third-generation facilities are optimized to get a high-brightness SOR light-source by using insertion devices, mainly undulators. There are three third-generation SR facilities with $E_e > 5$ GeV, in the world. They are ESRF (Grenoble), APS (Argonne) and SPring-8 (Japan). SPring-8 is the largest and brightest. The energy of circulating electrons in SPring-8 is 8 GeV.

The accelerator complex of SPring-8 is composed of an injector linac, a booster synchrotron, and a low-emittance and high-brightness storage ring. Fig. 2.1 shows the schematic view of the accelerator complex. Electrons are generated at an electron gun and are accelerated to an energy of 1 GeV in the injector linac with a length of 140 m. A 1 GeV electron beam is transported to the booster synchrotron with a 396 m circumference, and are accelerated up to 8 GeV. The 8-GeV electron beam is injected from the synchrotron into the storage ring with a 1436 m circumference and stored.

The 8-GeV electrons circulate in the storage ring with a frequency of 0.2088 MHz. The time interval of the successive bunches for electrons is 1.966 nsec. There are about 2440 bunches on the circle in the storage ring. Electrons are filled in some bunches with various filling patterns. The maximum current of the 8 GeV electron beam is 100 mA. The typical lifetime of the storage beam is 50 hour in the actual operation mode. The electron beam has a small

emittance of $\varepsilon = 6$ nm·rad [1] with the average beam widths of $\sigma_x = 75$ μm and $\sigma_y = 25$ μm in the horizontal and vertical directions.

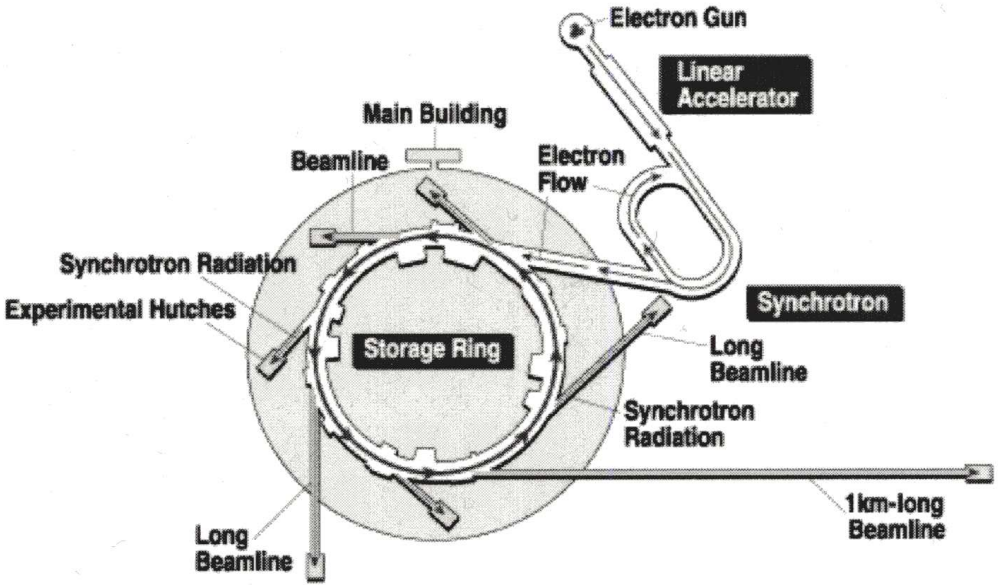

Figure 2.1: Schematic view of the accelerator complex of SPring-8.

The stored electron beam is used to generate synchrotron radiation photons at bending magnets, undulators and wigglers. The radiation photons are provided to various beam lines with the experimental hutches in the experimental hall. The photons with a high-brightness and low emittance are commonly used mainly for researches in material and life sciences. There are 62 beam lines and 37 lines are used. One of the beam lines called BL33LEP is used by the LEPS group. In the LEPS beam line, the high energy photon beam produced by the backward-Compton-scattering process is used in the experiments for photo-nuclear and nucleon reactions instead of radiation photons.

2.2 LEPS facility

RCNP (Research Center for Nuclear Physics) in Osaka University, JASRI (Japan Synchrotron Radiation Institute) and JAERI (Japan Atomic Energy Research Institute) have cooperated to establish the LEPS beam line for quark nuclear-physics studies at SPring-8. At the Laser-Electron-Photon facility at SPring-8 (LEPS), a multi-GeV photon beam is produced by the backward-Compton-scattering (BCS) process of laser photons from the circulating 8-GeV electrons [22, 23, 24, 25, 26].

The schematic view of the LEPS beam line is shown in Fig. 2.2. The beam line consists of three parts; (a) Laser-electron collision part in the storage (SR) ring, (b) Laser hutch for laser injection, and (c) Experimental hutch where a spectrometer is placed. The BCS process

[1] The emittance is different for the x and y-direction [20]

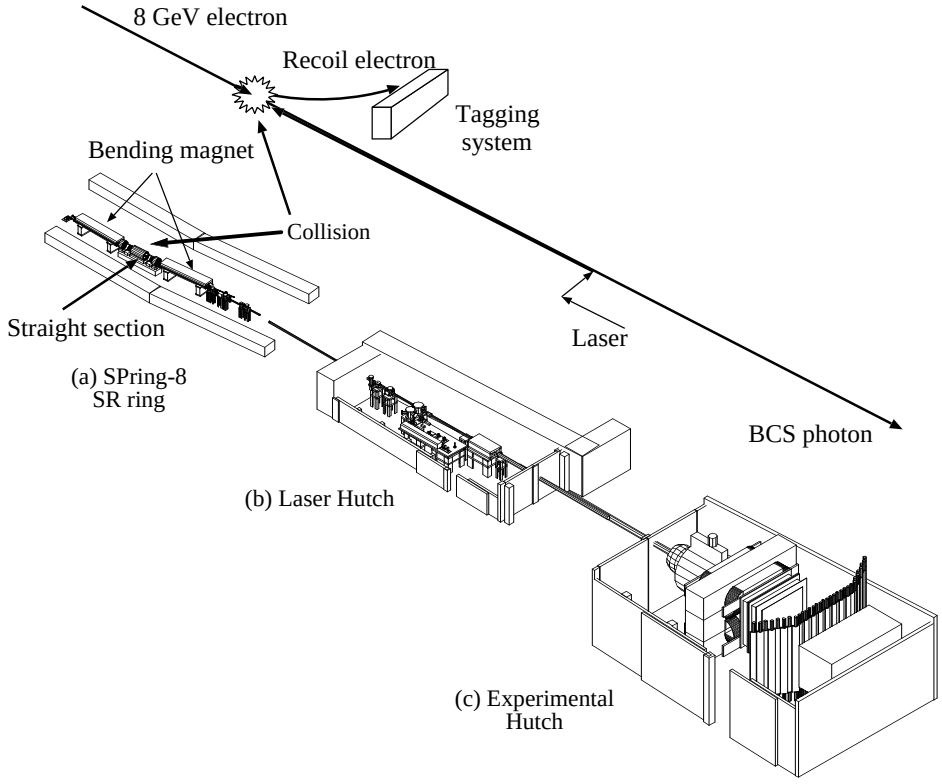

Figure 2.2: Schematic view of the LEPS facility at SPring-8. The facility consists of three parts;(a) Laser-electron collision part in the storage (SR) ring, (b) Laser hutch for a laser injection, and (c) Experimental hutch. A schematic explanation of the collision between an electron and a laser photon in backward-Compton scattering is inserted in the figure.

is illustrated in the figure. Laser photons which are optimized in the laser hutch are injected to the storage ring. We have a 7.8 m long straight section between two bending magnets in the storage ring as shown in Fig. 2.2. In this straight section, the BCS process takes place if a laser photon collides with a 8-GeV electron. Photons produced by the BCS process are provided to the experimental hutch and irradiate a target. The recoil electrons are detected by a tagging system placed at the exit of the bending magnet to measure the photon beam energy. A series of experiments by using the BCS photon beam started in 2000. The BCS process and devices to produce a linear-polarized photon beam are described in this section.

2.2.1 Backward Compton scattering

The general properties of the backward-Compton-scattering process in the laboratory system are described in this section. Fig. 2.3 shows the kinematical values of the backward-Compton-scattering process. If a laser photon with an energy k_1 strikes an electron with a high energy E_e with a relative angle $\theta_1 \simeq 180^\circ$, it is scattered with a scattering angle of θ_2. If

$E_e \gg k_1$, the scattered photon is directed strongly in the backward direction due to the Lorentz boost. The scattered photon (BCS photon) gains an enormous energy from the electron by

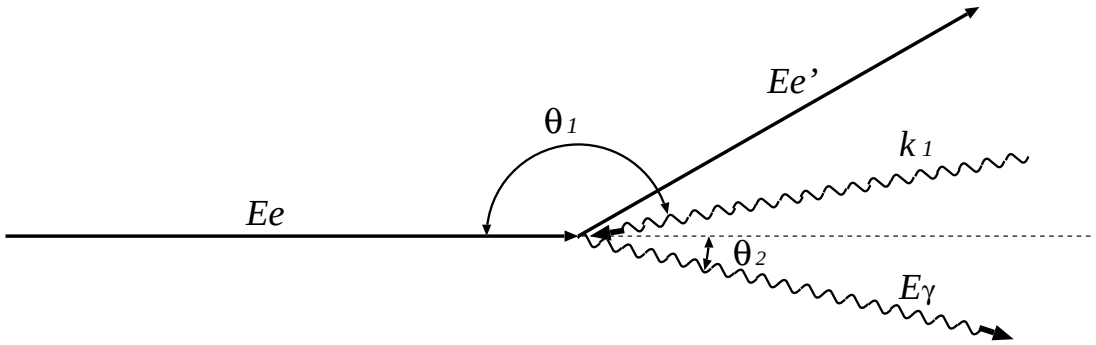

Figure 2.3: Kinematical variables of the backward-Compton-scattering process in the laboratory frame.

the Fitzgerald-Lorentz effect in the recoil process. The energy of a BCS photon E_γ is denoted as

$$E_\gamma = k_1 \frac{1-\beta cos\theta_1}{1-\beta cos\theta_2 + \frac{k_1(1-cos\theta)}{E_e}} \tag{2.1}$$

where β is an incident electron velocity in unit of the speed of light and $\theta = \theta_2 - \theta_1$. Assuming $\gamma = E_e/m_e \gg 1$, $\beta \simeq 1$, $\theta_1 \simeq 180^\circ$ and $\theta_2 \ll 1$, Eq. (2.1) can be rewritten as

$$E_\gamma = \frac{4E_e^2 k_1}{m_e^2 + 4E_e k_1 + \theta_2^2 \gamma^2 m_e^2}, \tag{2.2}$$

where m_e is the electron mass of 0.511 MeV and $\gamma \sim 16,000$ at $E_e = 8$GeV. The maximum energy of a BCS photon (Compton edge) is obtained at $\theta_2 = 0^\circ$:

$$E_\gamma^{max} = \frac{4E_e^2 k_1}{m_e^2 + 4E_e k_1}. \tag{2.3}$$

The maximum energy E_γ^{max} is shown in Fig. 2.4 as a function of incident electron energy E_e. Three lines in Fig. 2.4 represent the available photon energies with different wave lengths of laser photons. In the present experiment, a 351-nm Ar laser was used. Since the energy of circulating electrons at SPring-8 is 8 GeV, the maximum energy of the BCS photon beam is 2.4 GeV with a laser of a 351-nm wavelength. Fig. 2.5 shows the energy of the BCS photon beam as a function of scattering angles θ_2. BCS photons with an energy larger than 1 GeV are scattered inside a narrow cone (< 0.1 mrad). The size of the BCS photon beam is less than 1 cm at the target position, 70 m from the collision point assuming that the electron beam has no divergence nor energy spread.

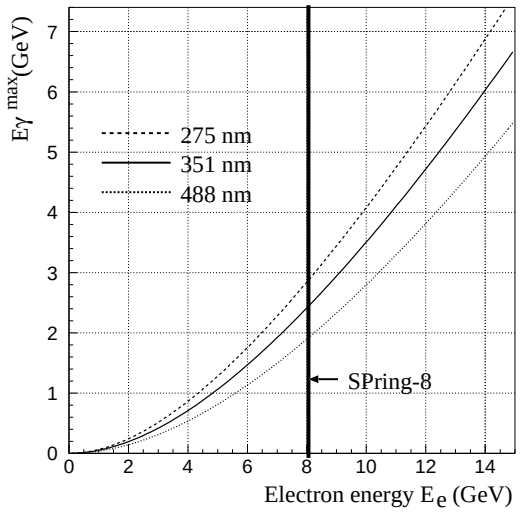

Figure 2.4: Maximum energies of BCS photons as a function of energy of the incident electron for laser photons with 275, 351 and 488 nm wavelengths, respectively.

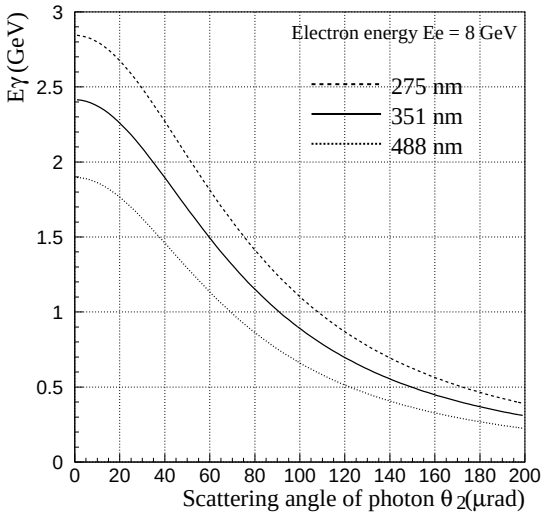

Figure 2.5: Energies of BCS photons as a function of scattering angles for laser photons with 275, 351 and 488 nm wavelengths.

The differential cross section of the BCS process is written as a function of the BCS photon energy [21]:

$$\frac{d\sigma}{dE_\gamma} = \frac{2\pi r_e^2 a}{E_\gamma^{max}}(\chi + 1 + cos^2\alpha) \tag{2.4a}$$

$$a = \frac{m_e^2}{m_e^2 + 4E_e k_1} \tag{2.4b}$$

$$\chi = \frac{\rho^2(1-a)^2}{1-\rho(1-a)} \tag{2.4c}$$

$$cos\alpha = \frac{1-\rho(1+a)}{1-\rho(1-a)} \tag{2.4d}$$

$$\rho = \frac{E_\gamma}{E_\gamma^{max}} \tag{2.4e}$$

where $\gamma_e = 2.818$ fm is the classical electron radius. Fig. 2.6 shows the differential cross sections for the BCS process between 8 GeV incident electrons and laser photons with three wave lengths of 275 nm, 351 nm and 488 nm. Photons with the sub-GeV energy can be efficiently obtained by the BCS process.

The linear (circular) polarized BCS photons can be made by using linear (circular) polarized laser photons. When a laser photon is polarized, the polarization is transferred to a BCS photon. The degree of polarization (P_γ) of a BCS photon is proportional to that of a laser

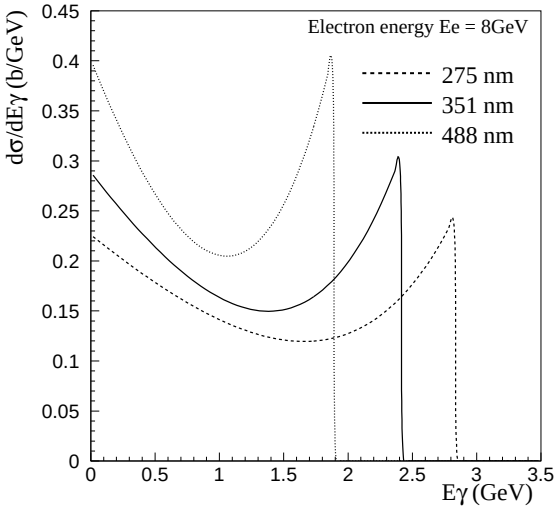

Figure 2.6: Differential cross sections of the BCS process with the 8 GeV incident electron beam for laser photons of three different wavelengths, 275, 351 and 488 nm.

photon (P_{laser}) [21]. The linear polarization is given by

$$P_\gamma = P_{laser}\frac{(1-cos\alpha)^2}{2(\chi+1+cos^2\alpha)}. \quad (2.5)$$

The circular polarization is given by

$$P_\gamma = P_{laser}\frac{(2+\chi)cos\alpha}{(\chi+1+cos^2\alpha)}. \quad (2.6)$$

Fig. 2.7 shows the linear and circular polarizations of a BCS photon as a function of E_γ by using the 8 GeV incident electron beam when the polarization of a laser photon is 100%. Three lines represent the polarization for laser photons with 275, 351 and 488 nm wavelengths. The degree of polarization is maximum at the Compton edge ($\theta_2 = 0°$). The spin-flip amplitude for highly relativistic electrons vanishes, and scattered photons almost retain the initial laser polarization at the Compton edge. In the case of the linear polarization, the maximum polarization is obtained as $P_\gamma = P_{laser}\frac{2a}{1+a^2}$ from Eq. (2.5). The linear polarization is about 94% at the maximum energy when the incident electron with $E_e = 8$ GeV and a 351-nm laser with 100% polarization are used. In the case of the circular polarization, photons scatter with an opposite helicity and retain the total degree of the polarization at the maximum energy, $P_\gamma = -P_{laser}$. The circular polarization is 100% at the maximum energy if a laser photon is 100% polarized.

In the present experiment, a linear-polarized photon beam was produced by an Ar laser with a 351 nm wavelength. The energy spectrum and the beam profile of the BCS photon beam were measured by a PWO ($PbWO_4$) crystal calorimeter which was placed in the laser hutch (at 42.8 m far from the center of the straight section) [27]. Fig. 2.8 shows the energy spectrum of the BCS photon beam, which demonstrates that high energy photons with E_γ^{max}=2.4 GeV

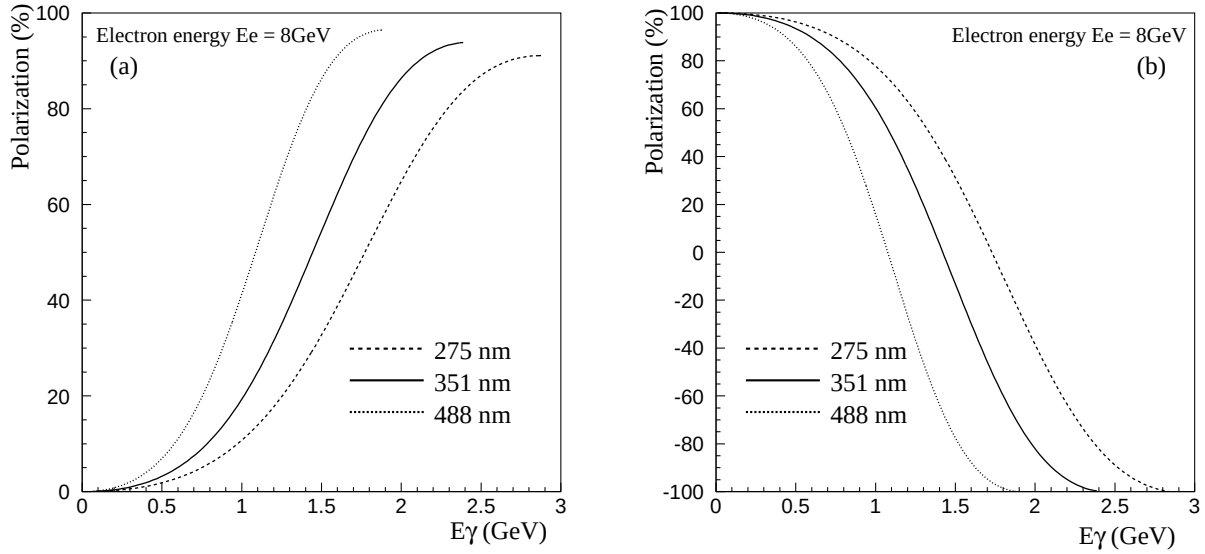

Figure 2.7: Polarization of the BCS photon as a function of E_γ by using the 8 GeV incident electron beam when the laser photon is 100% polarized. Three lines correspond to the polarizations obtained with laser photons with 275, 351 and 488 nm wavelengths. (a):Linear polarization and (b):Circular polarization.

are produced by the BCS process. The energy spectrum of the Bremsstrahlung beam created in the residual gas in the storage ring are also plotted in Fig. 2.8. The maximum energy of the Bremsstrahlung beam is 8 GeV corresponding to the electron beam energy. The distribution of the Bremsstrahlung beam extends at the low energy while the intensity of the BCS photon beam peaks at the maximum energy. The size of the BCS photon beam with $E_\gamma = 1.5$ GeV ~ 2.4 GeV was obtained to be $\sigma_x \sim 3.5$ mm and $\sigma_y \sim 2.0$ mm. The size difference between σ_x and σ_y is due to the emittance of the 8-GeV electron beam. The size of the 8 GeV electron beam at the center of the straight section is $\sigma_x = 0.4$ mm and $\sigma_y = 0.009$ mm.

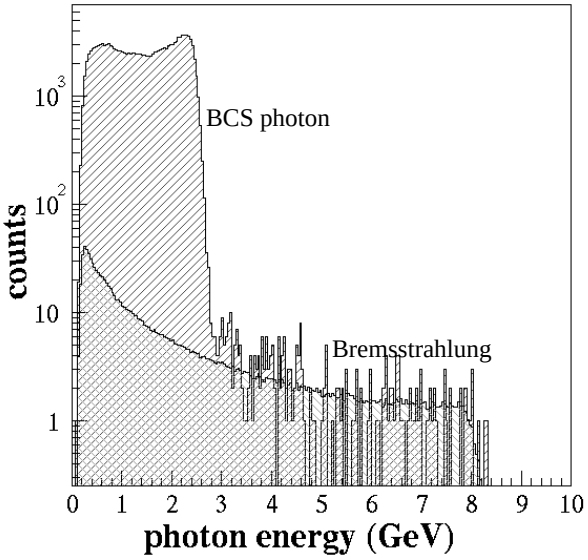

Figure 2.8: Energy spectrum of the BCS photon measured by a PWO crystal calorimeter [27]. The wavelength of laser photons is 351 nm.

2.2.2 Laser operating system

Fig. 2.9 shows the laser-operating system placed in the laser hutch (see Fig. 2.2). The operating system consists of an Ar laser, a half-wave-length plate ($\lambda/2$ plate), a beam expander, four mirrors and a polarization monitor. The direction, shape, and polarization of laser photons are controlled by this system to achieve a high intensity and a high polarization of the BCS photon beam. The Ar laser passes through the $\lambda/2$ plate to change its polarization direction. The shape of the laser beam is tuned by the beam expander. The direction and position of the laser beam are tuned by the third and forth mirrors. The laser beam is transferred to the beam line by the first and second mirrors. The polarization monitor is placed at the upstream of the collision part in the storage ring to measure laser photons which do not react with the 8-GeV electrons. Specifications of the elements used in the laser system are listed in Table 2.9.

Ar laser

In the present experiment, a ultra-violet (UV) multi-line of an Ar laser was used to get laser photons with a wavelength ranged from 333.6 nm to 363.8 nm. Fig. 2.10 shows the wavelength spectrum of the Ar laser measured by a monochromator. There are sharp peaks at 351.1 nm and 363.8 nm. All the laser photons with the wavelength from 333.6 nm to 363.8 nm were used as the incident laser photons. The typical power of the Ar laser is 5 W.

Half wavelength plate

The polarization of laser photons is controlled by a half-wave-length ($\lambda/2$) plate which changes the direction of polarization, from a vertically-polarized photons to a horizontally-polarized

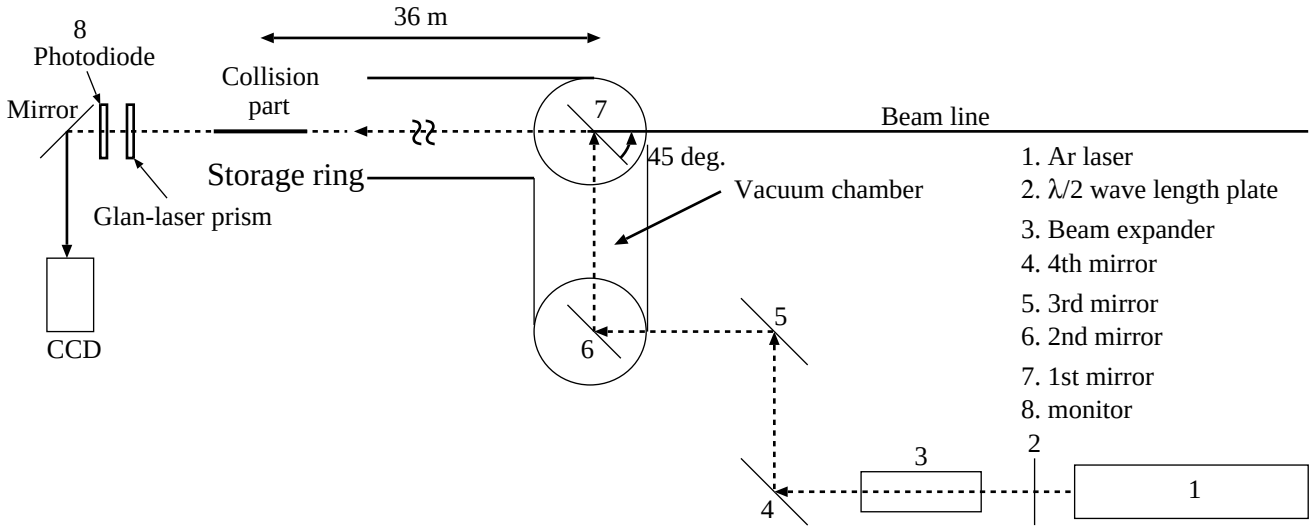

Figure 2.9: Schematic view of the laser operation system.

Table 2.1: Specifications of elements used in the LEPS laser system.

	Manufacture name (company)	Material	Size (mm)
Ar laser	Coherent Innova Sabre (Coherent)	-	-
$\lambda/2$ plate	for 351 nm (SURUGA)	Quartz	17×17×2t
Beam expander	(SURUGA)		
4th mirror	optical mirror (OPTO·LINE)	Quartz	ϕ80 × 12t
3rd mirror	optical mirror (OPTO·LINE)	Quartz	ϕ80 × 12t
2nd mirror	optical mirror (FUJITOKU)	Si (Aluminum)	ϕ100 × 19t
1st mirror	optical mirror (FUJITOKU)	Si (Aluminum)	ϕ100 × 6t
Glan-laser prism	PGL8310 (OptMax)	α-BBO	ϕ10 × 26t
Photo diode	S1406-05(HAMAMATSU)	-	-

photons. The $\lambda/2$ plate is placed just after the Ar laser. Since the Ar laser is vertically polarized, it is not necessary to change the polarization direction to produce a vertically-polarized photons. When a horizontally-polarized photon beam is made, the optic axis of the $\lambda/2$ plate is placed at 45° to change the polarization direction of the Ar laser from vertical to horizontal.

Expander

The laser photon beam travels a distance of about 36 m before it collides with a 8-GeV circulating electron. The laser photon beam is required to have a beam waist at the collision part in order to achieve a maximum luminosity. The laser beam is expanded and focused by using a beam expander which is located behind the $\lambda/2$ plate.

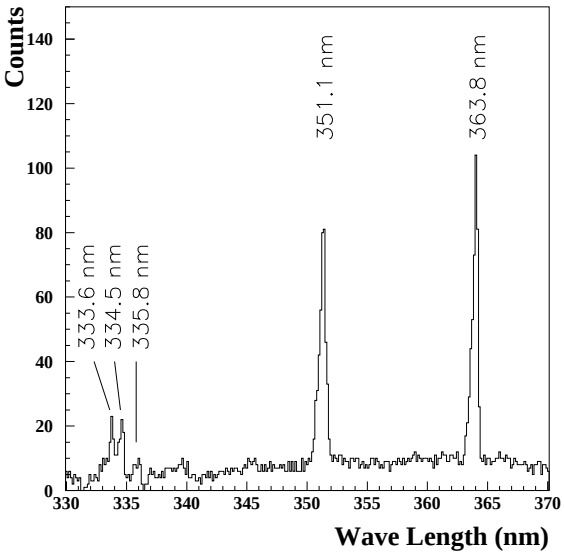

Figure 2.10: Wavelength spectrum of the Ar laser with a UV-multi-line measured by a monochromator.

Mirrors

Four mirrors are used in the laser operating system. The third and forth mirrors are used to control the direction and position of the laser beam. These mirrors are rotated by a motor with 17 μrad/1 pulse and 10 μrad/1 pulse in the horizontal and vertical direction. The laser beam is transported from the laser operating system to the beam line by the second mirror, and is injected into the storage ring by the first mirror on the beam line.

The reflectivity of a mirror is different for the horizontally and vertically polarized beam. The reflectivity for the vertical polarization is higher than that for the horizontal polarization by about 40% in the actual operation. Therefore, the intensity of the vertically polarized photon beam is higher than that of the horizontally polarized photon beam.

Monitor

The polarization of the laser photons is measured by using laser photons which pass through the collision part. A Glan-laser prism is used as a polarimeter to measure the polarization. The Glan-laser prism has a special axis. Only photons with the polarization parallel to this axis can pass through the prism. By rotating the prism and measuring the intensity of the laser beam after the prism, the intensity distribution of the laser beam is obtained as a function of the rotation angle ϕ. The intensity is measured by a photodiode (HAMAMATSU S1406-05). Fig. 2.11(a) and (b) show the intensity distribution measured by the photodiode for vertically and horizontally polarized laser photons. The data is fitted by a function of sinϕ. The polarization angle and degree are determined by this fitting. The laser beam is optimized to have the maximum polarization.

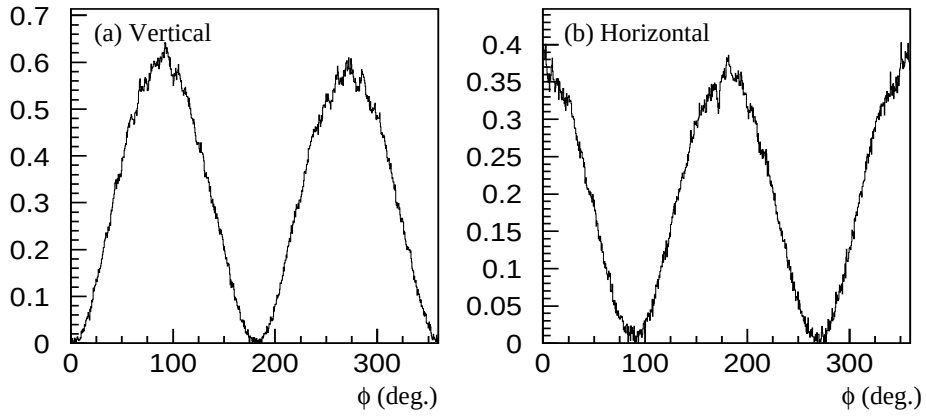

Figure 2.11: Intensity distribution of the laser beam measured by the photodiode for (a) vertically polarized laser photons and for (b) horizontally polarized laser photons. The distribution is fitted by a function of sinϕ. The line is the fitting function.

2.2.3 Tagging system (TAG)

The energy E_γ of the BCS photon beam is determined by the recoil electron energy $E_{e'}$ as

$$E_\gamma = E_e - E_{e'}. \tag{2.7}$$

The energy of the 8-GeV circuiting electron E_e was calculated on the basis of measured field distributions of magnets in the storage ring. The energy was determined as 7.975 $\pm$ 0.003 GeV [28]. The energy $E_{e'}$ is measured by a tagging system located in the storage ring. Since an electron scattered by the BCS process looses its energy, it is relatively strongly bent and deviates from the normal orbit in the 8-GeV ring when it passes through the bending magnet placed at the end of the straight section (see Fig. 2.2). The tagging system is installed at the exit of the bending magnet to detect the recoil electrons.

Fig. 2.12 shows the structure of the tagging system. The tagging system is placed at the outside of a beam vacuum pipe for the 8 GeV electron beam. The tagging system covers a region 4.5 - 6.5 GeV in the energy of recoil electrons. This energy region corresponds to the energy of the BCS photons 1.5 - 3.5 GeV. The lower limit of 1.5 GeV is due to the fact that the tagging system can't be positioned closer to the nominal orbit of the 8 GeV electrons. The tagging system consists of plastic scintillator (PL) hodoscopes and silicon strip detectors (SSD's) as shown in Fig. 2.12. There are two layers of the combination of the PL hodoscope and the SSD. Each PL hodoscope layer consists of 10 plastic scintillation counters. The size of the plastic scintillator is 10.0 mm high, 7.4 mm wide, and 3.0 mm thick. The plastic scintillators are stacked with an overlap of 1.0 mm as illustrated in Fig. 2.12. The PMT (HAMAMATSU R1635P) with a 3/8 inch diameter is coupled to the plastic scintillator through a light guide. The size of the SSD is 10.0 mm high, 51.2 mm wide, and 0.5 mm thick. The strip pitch is 0.1 mm. There are 512 strips in total.

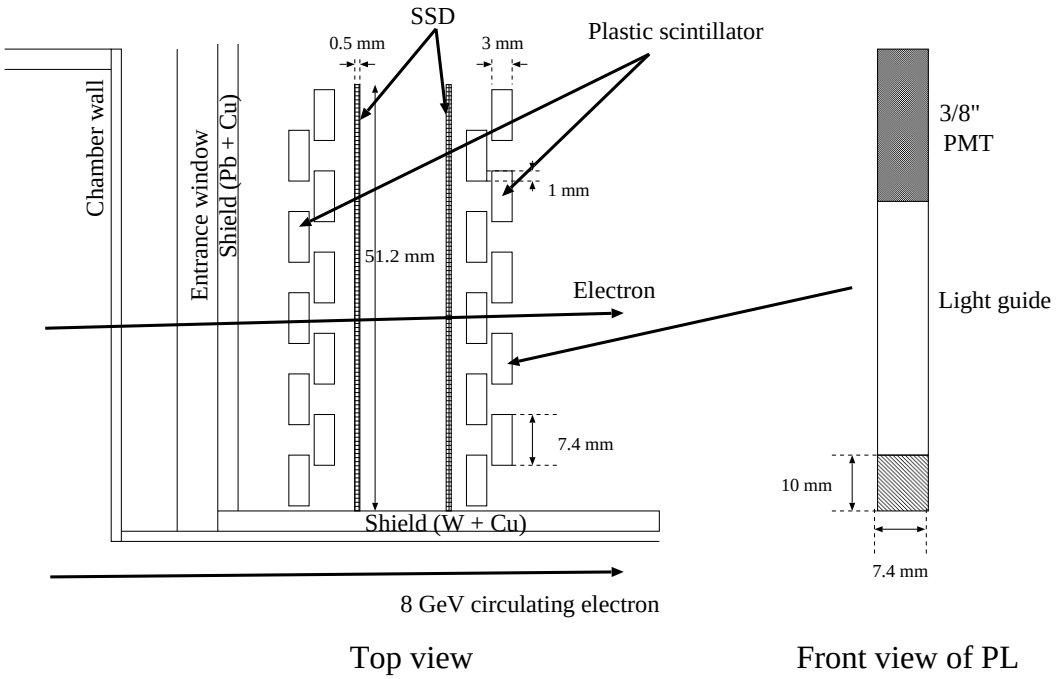

Figure 2.12: Tagging system.

The precise hit position of a recoil electron is measured by the SSD layers. The energy $E_{e'}$ is obtained by the hit positions. There are background events due to X-rays and electric showers. Therefore, it is difficult to identify a real track of a recoil electron by using only information from the SSD's. The plastic scintillator hodoscopes are used to define a real track of a recoil electron. After finding hits at both SSD layers, we search for the hits at the PL hodoscopes associated with the hits in the SSD's. If there are the associated hits, we obtain the energy $E_{e'}$ with the hit positions at the SSD's and then obtain the photon energy with Eq. (2.7). Fig. 2.13 shows the energy spectrum of BCS photons measured by the tagging system. The BCS photons above 2.4 GeV are generated by laser photons with a wavelength shorter than 351 nm as shown in Fig. 2.10. In Fig. 2.13, one sees three prominent dips at 1.74, 1.94 and 2.14 GeV which correspond to the overlap regions of four plastic scintillators covered from 1.5 GeV to 2.4 GeV. If a recoil electron passes through the overlap regions, the two scintillators are fired. Since these scintillators cover a space larger than that in the case of one hit, there are chances to find more than one hit in the SSD's. We select the events finding only one hit in the region covered by the fired scintillators to reduce background events. This selection make the events in the overlap regions reduce.

The energy resolution has been estimated by measuring electron-positron pair production by the BCS photons with the LEPS magnetic spectrometer [29]. The photon energy measured by the tagging system was compared with the energy reconstructed from the energies of an electron and a positron. The measured resolution of 15 MeV (RMS) is mainly determined by

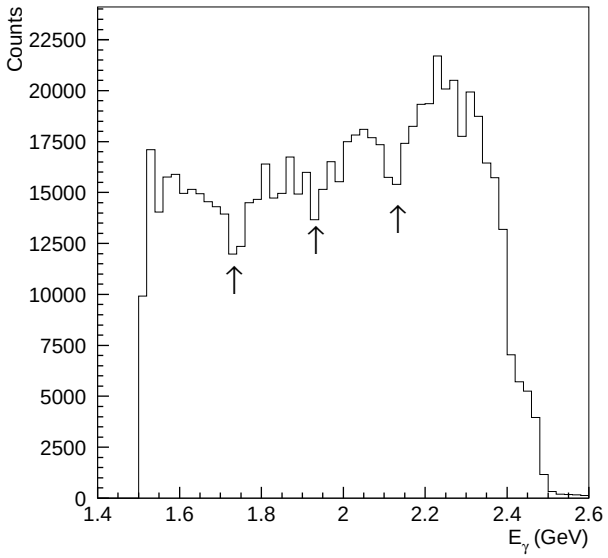

Figure 2.13: Energy spectrum of BCS photons measured with the tagging counter.

the energy and angular spreads of the 8-GeV circulating electron and uncertainty of a photon-electron interaction point. The 15 MeV resolution corresponds to about 0.5 mm in the tagging system. Since the position resolution of the SSD's in the tagging system is 100 μm/$\sqrt{12}$ = 28 μm (the strip pitch is 100 μm), it dose not become a limiting factor for the resolution.

2.2.4 Beam line setup

The BCS photon beam travels from the collision point to the experimental hutch through the laser hutch. Fig. 2.14 illustrates the setup of the beam line. There are some materials in the path of the photon beam. They are the first mirror, aluminum windows of the beam pipes and a X-ray absorber. When the photon beam hits these materials, some of photons convert to e^+e^- pairs. The materials and their conversion rate to e^+e^- pairs are summarized in Table 2.2. The first mirror is made of silicon with a thickness of 6 mm. Since the mirror is tilted by 45° to inject laser photons into the storage ring, the effective thickness is thus 6 $\times$ $\sqrt{2}$ mm. Aluminum plates with a thickness of 0.55 mm are used as windows of beam pipes, the exit of a beam pipe from the SR ring, and the enter and exit of a beam pipe which connects the laser hutch and experimental hutch. Three Al plates are used in total in the beam line. A lead absorber with a thickness of 1.5 mm is placed after the beam pipe from the SR ring to absorb X-rays. The detectors of a spectrometer are protected with this absorber from a radiation damage. The thickness of 1.5 mm is determined by the operation of the detectors and the radiation safety. The conversion rate of the photon beam is 42.5 % in total. The intensity of the photon beam is reduced by about 42.5 % before it arrives at a target in the experimental

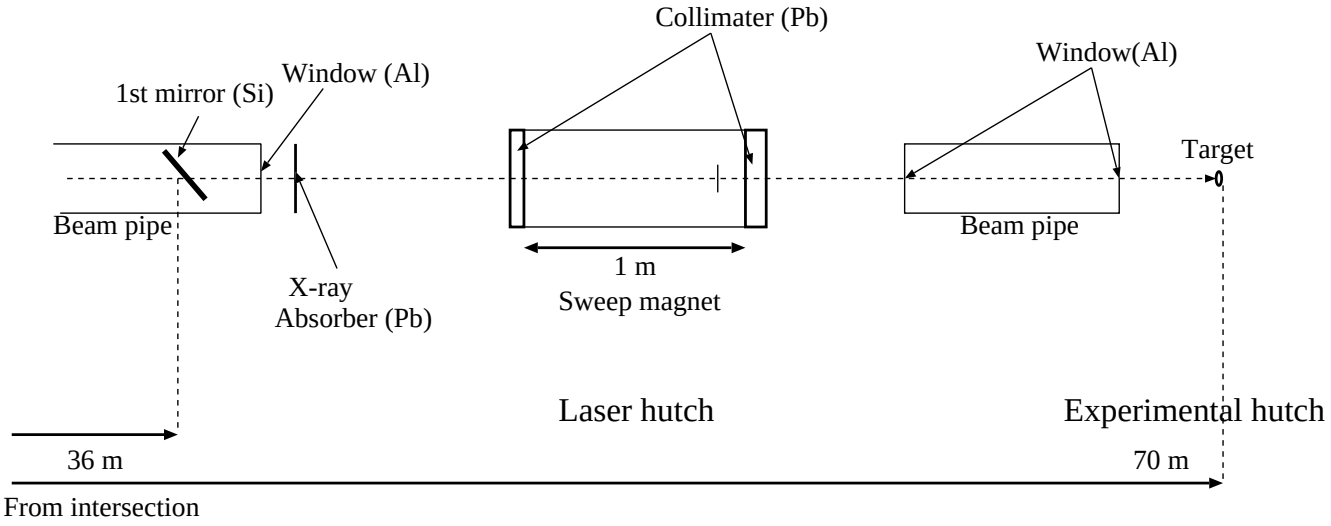

Figure 2.14: Schematic view of the LEPS beam line setup.

hutch. The transmission of the photons from the reaction point to the target was measured by the tagging counter and gamma counters. The measured transmission is 58%.

Table 2.2: Materials inserted in the beam line.

	Material	Radiation length (mm)	Thickness (mm)	Conversion rate (%)
First mirror	Si	93.6	$6\times\sqrt{2}$	11.0
Vacuum windows	Al	89.0	0.55×3	0.79×3
Absorber	Pb	5.6	1.5	29.1

The e^+e^- pairs created in the materials should be removed before a target. To remove the e^+e^- pairs, we use a sweep magnet located in the laser hutch. Fig. 2.15 shows the structure of the sweep magnet. The size of the iron yoke is 176 mm high, 560 mm wide, and 1000 mm long. Two permanent magnets are installed in the iron yoke. The size of each magnet is 35 mm high, 58 mm wide, and 1000 mm long. They are faced with a gap of 44 mm. The strength of the magnetic field is 0.6 T at the center. The e^+e^- pairs produced at the first mirror, the aluminum window, the X-ray absorber and the residual gas in the beam pipe are removed from the beam line by the sweep magnet. Lead collimaters are placed at the upstream and downstream positions of the sweep magnet. The thickness of the upstream (downstream) collimaters is 50 (150) mm. The upstream (downstream) collimaters have a hole with a diameter of 20 (25) mm. The e^+e^- pairs with a momentum below 2.1 GeV/c are blocked by the downstream collimater. The other e^+e^- pairs with a momentum above 2.1 GeV/c pass through the hole of

the downstream collimater.

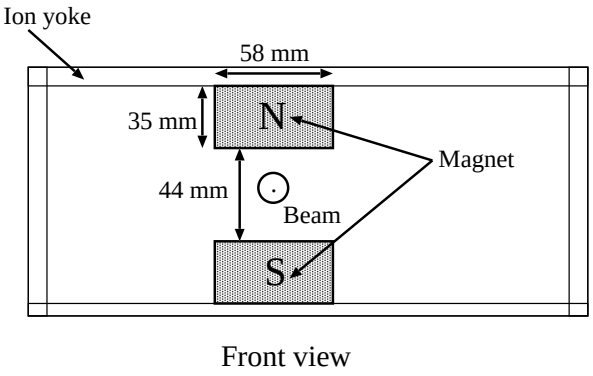

Figure 2.15: Structure of the sweep magnet.

2.3 LEPS spectrometer

The LEPS spectrometer is located in the experimental hutch to identify charged particles produced at the target. Fig. 2.16 shows the LEPS spectrometer. The incidence direction of the

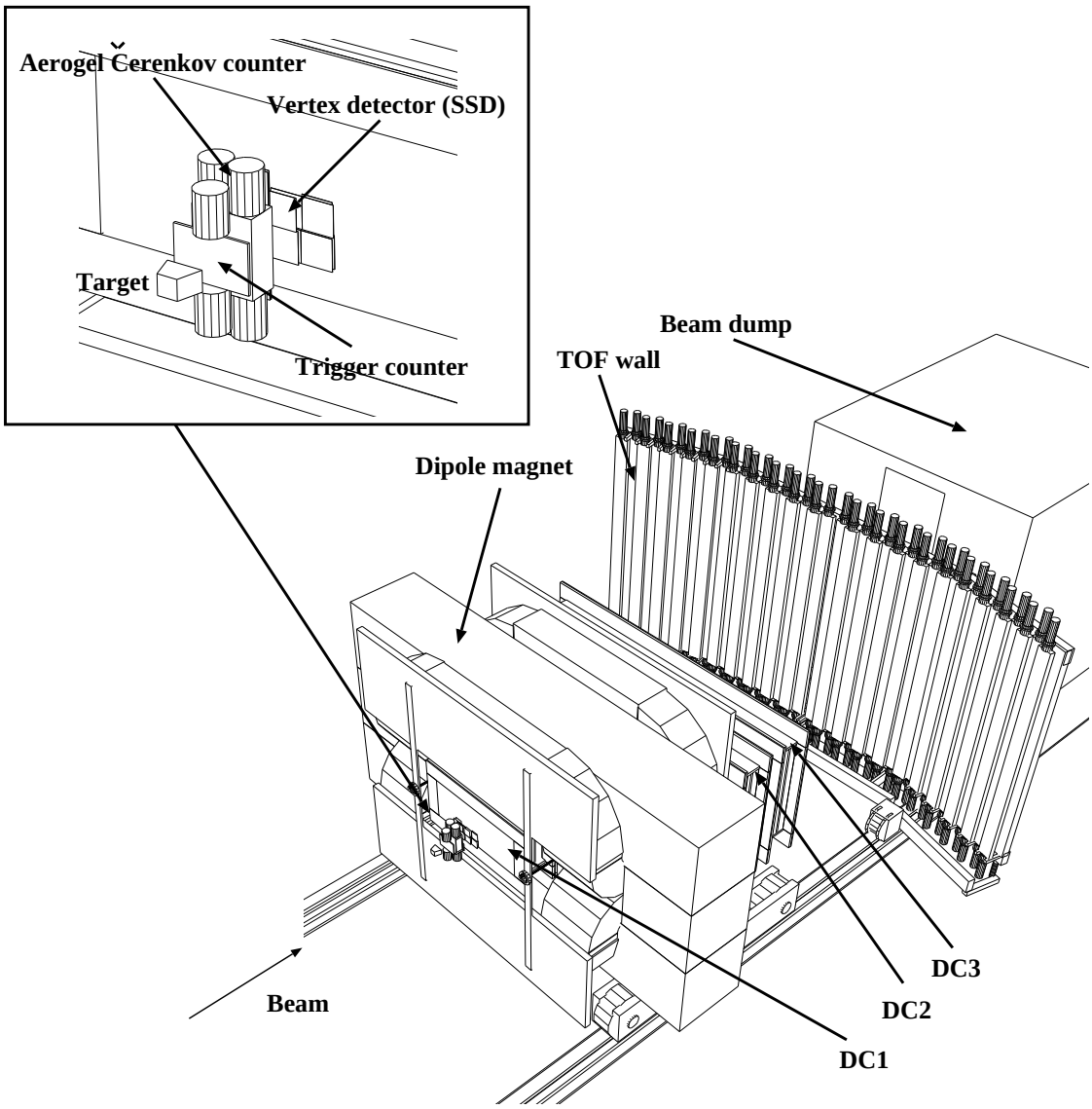

Figure 2.16: Overview of the LEPS spectrometer.

photon beam is displayed in the figure. The LEPS spectrometer consists of a upstream-veto counter, a trigger counter, a silica-aerogel Čerenkov counter, a vertex detector (silicon strip detectors), a dipole magnet, three drift chambers (DC1, DC2 and DC3), and a TOF wall. Charged particles produced at the target are defined by the trigger counter. The silica-aerogel Čerenkov counter is used to eliminate the e^+e^- background events. The vertex detector and three drift chambers are used as tracking devices with the dipole magnet to measure momenta

of charged particles. A time-of-flight is measured by using the TOF wall. A beam dump is placed behind the spectrometer for the purpose of a radiation shielding.

2.3.1 Upstream-veto counter

The photon beam partly converts to charged particles mainly by the e^+e^- pair production process in air, the residual gas or Al windows of the beam pipe. These charged particles should be eliminated before the target.

A upstream-veto counter was used to reject the event signals from such charged particles in the trigger level. Fig. 2.17 shows the upstream-veto counter. This counter is a plastic scintillator (BC-408) located at 4 m upstream from the target. The size is 200 mm high, 190 mm wide, and 5 mm thick. A 2-inch fine-mesh PMT (HAMAMATSU H7195) is coupled to the plastic scintillator through a light guide.

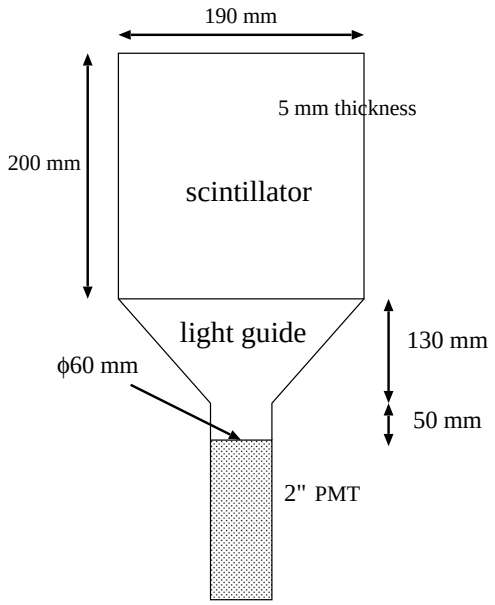

Figure 2.17: Upstream-veto counter.

2.3.2 LH_2 target

A liquid hydrogen (LH_2) target was used during the present experiment. The LH_2 target was located at 952 mm upstream of the center of the dipole magnet. Fig. 2.18 shows the liquid hydrogen target system which is in the vacuum chamber during the cooling [30]. The refrigerator uses the helium gas in the cooling process of the adiabatic expansion. Hydrogen gas is supplied through the SUS pile from the reservoir to the cell.

Liquid hydrogen is stored in a copper cell with a thickness of 8 mm. Fig. 2.19 shows the target cell. Copper was employed as a target cell material for good heat conductivity. The cell is a trapezoid shape and its length is 50 mm. The inner volume of the cell is 110 cm^3.

Alamid films with a thickness of 0.05 mm are used as the window films. The entrance of the beam is shaped as a circular window with a 35 mm diameter. The exit for produced particles is shaped as a square with the size of 40 mm high × 70 mm wide. When the cell is filled with the liquid hydrogen, the pressure is 1.05 atm and the temperature is 20.5 K. Due to over pressure, the entrance and exit films are bend out and the effective thickness becomes 56 mm. A large acceptance of $|\theta_x| < 35^\circ$ and $|\theta_y| < 22^\circ$ is achieved even when the reaction particles are ejected from the most upstream part of the cell.

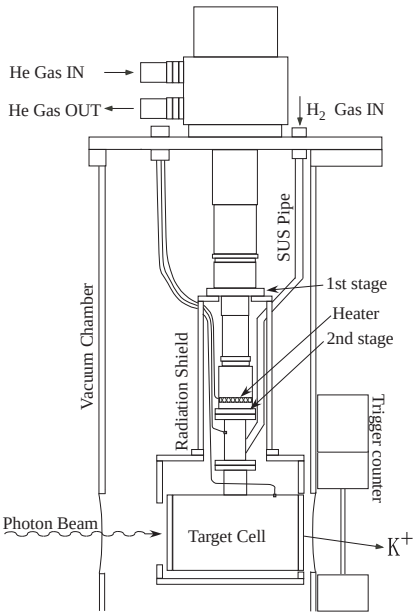

Figure 2.18: Target system. The target cell is installed in the vacuum chamber.

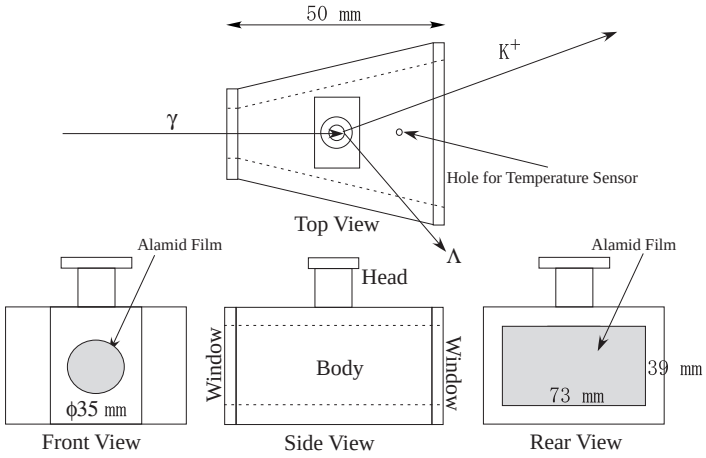

Figure 2.19: Target cell. A sample trajectory for the p(γ,K^+) reaction is illustrated.

2.3.3 Trigger counter (TRG)

A trigger counter (TRG) is a plastic scintillation counter located at the position of 10 cm downstream of the center of the target cell to identify the event signals from charged particles produced at the target. Fig. 2.20 shows the schematic drawing of the trigger counter. The size of the plastic scintillator (BC-408) is 94 mm high, 150 mm wide, and 5 mm thick. Two 2-inch-diameter fine-mesh PMT's (HAMAMATSU H6614-01) are coupled to the upper and lower sides of the plastic scintillator through light guides with a thickness of 15 mm. The trigger counter is used as a reference counter to measure the time-of-flight with the RF signals.

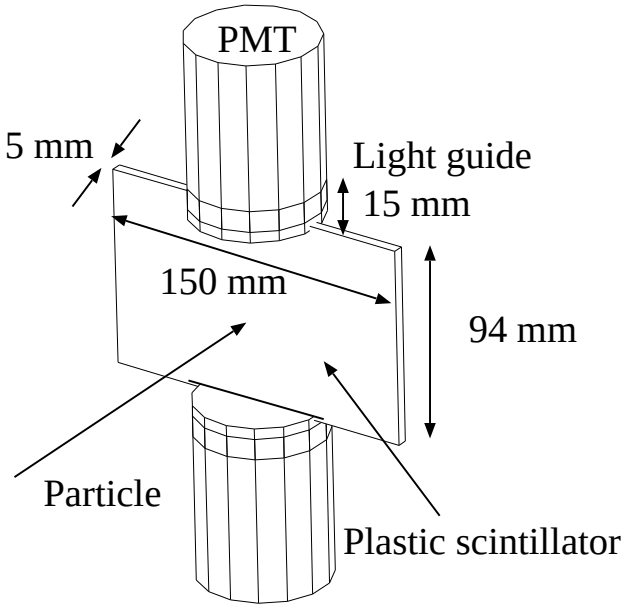

Figure 2.20: Trigger counter.

2.3.4 Silica-aerogel Čerenkov counter (AC)

Main background events are the e^+e^- pairs produced at the LH_2 target and at the TRG in a measurement of hadronic reactions. The cross section of the e^+e^- pair production in LH_2 is 21 mb which is two orders of magnitude larger than that of hadronic reactions of about 0.15 mb. The cross section of the e^+e^- pair production in a plastic scintillator is 380 mb while that of hadronic reactions is about 2.0 mb. The cross sections and conversion rates in the LH_2 target and the TRG are summarized in Table 2.3.

Table 2.3: Cross sections of the hadronic reaction and pair production, thickness, radiation lengths and conversion rates of the e^+e^- pair production for the hydrogen target and the trigger counter (TRG).

	Cross sections of hadronic (mb) / EM (mb)	Radiation length (cm)	Thickness (cm)	Conversion rate (%)
Target (LH_2)	0.15 / 21	866	5.0	0.74
TRG (CH)	2.0 / 380	42.4	0.5	1.51

When the beam intensity at the target is 5×10^5 photons/sec, the e^+e^- pairs are produced with the total rate of about 1×10^4/sec at the target and at the TRG. The rate of 1×10^4 cps is too high to be fully recorded by the data acquisition (DAQ) system. It is essentially

important to suppress the trigger rate associated with the e^+e^- events as much as possible. A silica-aerogel Čerenkov counter (AC) was used to reject the e^+e^- events at the trigger level. The index of refraction of the silica aerogel radiator used in the present experiment is 1.03.

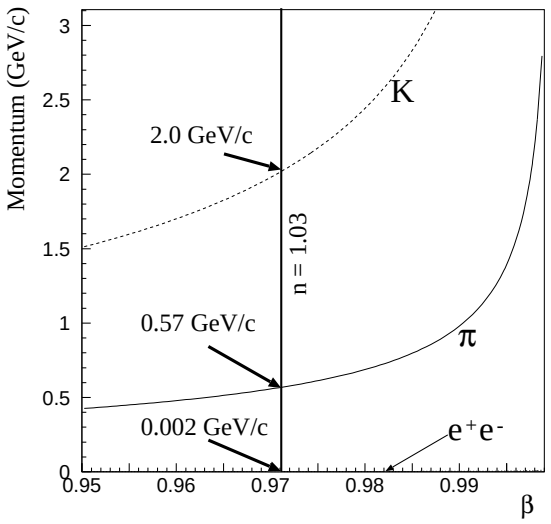

Figure 2.21: Relation between momentum and β for e^+e^-, π and K. A particle with $\beta > 1/\mathrm{n}$ emits Čerenkov lights. The line corresponding to an index of 1.03 is shown in the figure.

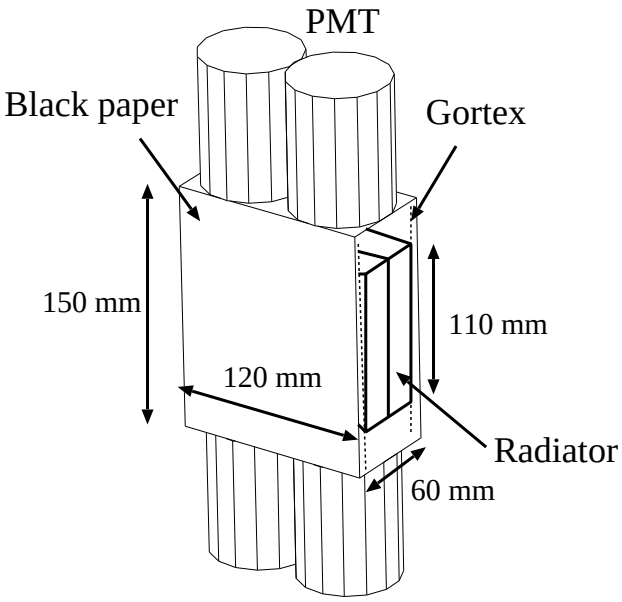

Figure 2.22: Silica aerogel Čerenkov counter (AC).

Fig. 2.21 shows the relation between momentum and velocity (β) of e^+e^-, pion and kaon. When a particle with a velocity $\beta > 1/\mathrm{n}$ passes through a transparent material with a refractive index n, Čerenkov lights are emitted. The Čerenkov thresholds for e^+e^-, pion and kaon are 0.002 GeV/c, 0.57 GeV/c and 2.0 GeV/c, respectably. Čerenkov lights are collected at the photocathode of a PMT. The signal is used as a veto signal in the trigger logic. Pion events with a high momentum are rejected by the AC veto signals. However, pions and kaons with momenta around the Čerenkov threshold are not rejected due to the small number of Čerenkov lights.

The AC is installed just behind the trigger counter to detect both an electron and a positron simultaneously. Because the e^+e^- pairs emerge with a small angle ($< 0.12°$), the e^+e^- pairs can be detected efficiently. The structure of the AC is shown in Fig. 2.22. The size of the counter box is 150 mm high, 120 mm wide, and 60 mm thick. The box is made of a black paper. The size of the silica aerogel radiator is 110 mm high $\times$ 110 mm wide, and 25 mm thick. The two sheets of radiators are inserted into the AC box as shown in Fig. 2.22. To collect Čerenkov lights emitted in the radiators, Gortex (white sheet) is used as a random reflector. The inside the AC box except for the photocathodes is covered with Gortex. The reflectivity

of Gortex is about 95% [31]. The collected lights are read by four 2-inch fine-mesh PMT's (Hamamatsu H6614-01) which are coupled to the upper and lower sides of the box.

To obtain a good efficiency, it is important to separate signal from noise and to reject e^+e^- pairs as good as possible. A CR high-pass filter was used to reduce the noise level with 60 Hz. Fig. 2.23 shows the circuit of the CR high-pass filter. The CR high-pass filter consists of a single capacitor (4700 pF) and resistor (100 kΩ). The CR filter was installed between a splitter and ADC module (FERA) as shown in Fig. 2.23. By inserting the filter between the splitter and the ADC module, noises of 60 Hz are greatly reduced in analog signals for both the ADC module and the discriminator. The pedestal peaks were quite sharp (within 3 channels in ADC). It was easy to decide the discriminated threshold.

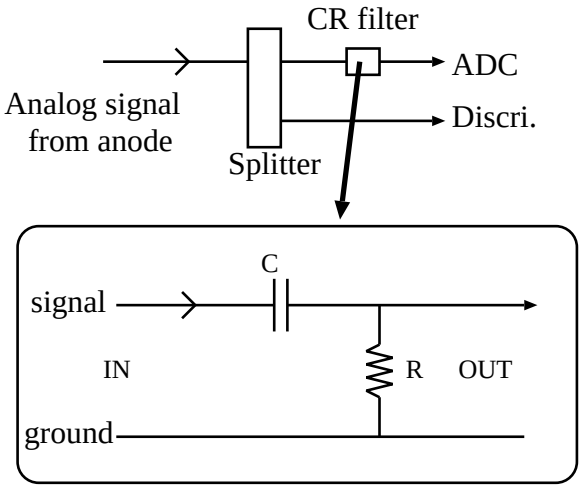

Figure 2.23: CR high-pass filter for the AC and the location in the circuit system.

Fig. 2.24 shows the ADC spectra obtained by the AC. The histograms by solid lines in Fig. 2.24 correspond to the signals by the e^+e^- events collected without gating the AC veto signal. The sharp peaks indicated by the dashed lines correspond to the events (pedestal peaks) collected with gating the AC veto signal. These events are mainly hadrons not to emit the Čerenkov lights in the AC. The pedestal peaks are so sharp to separate signals to noises. Fig. 2.25 shows the scatter plot of the velocity β vs. the momentum of particles detected by the LEPS spectrometer. Data shown in Fig. 2.25(a) were taken without gating the AC veto signal. Most of events are due to the e^+e^- creation as shown in Fig. 2.25(a). On the other hand, data in Fig. 2.25(b) were taken with gating the AC veto signal. One can see loci corresponding to pions, kaons and protons. The AC efficiency to detect the e^+e^- pairs is about 99.9 % corresponding to 7 photoelectrons. When the rate at the tagging system is about 600 kHz, the trigger rate without the AC veto signal reaches at about 12 kHz. This high rate is decreased to about 40 Hz by using the AC veto signal in the trigger logic. The trigger rate is sufficiently low for the DAQ system to handle with only a few % dead times.

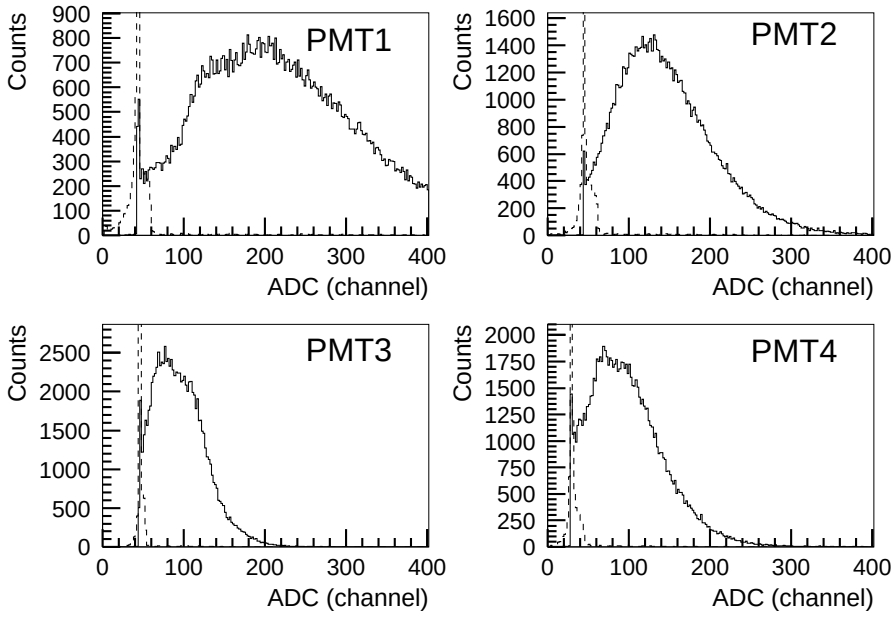

Figure 2.24: ADC spectra of PMT's used for the AC. The solid lines are for the e^+e^- events and the dashed lines are for the events by gating the AC veto signal.

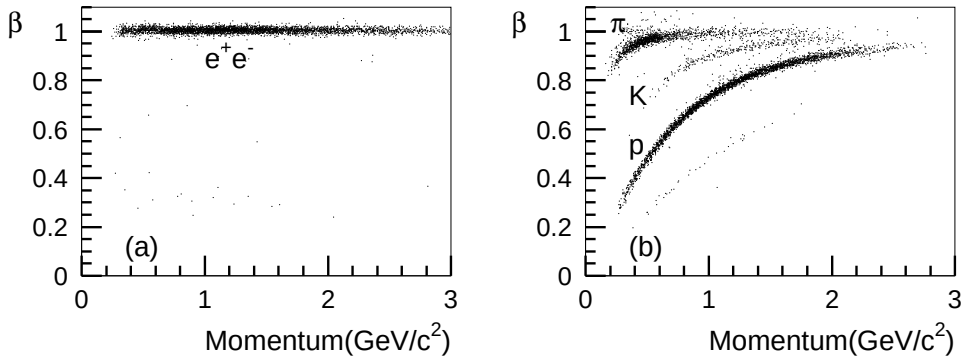

Figure 2.25: Scatter plots of the velocity β vs. the momentum of particles. (a) Scatter plots without the AC veto signal in the trigger logic. (b) Scatter plots with the AC veto signal.

2.3.5 e^+e^- Blocker

The e^+e^- pairs produced at the target and the TRG spread out mostly in the median plane by the magnetic field in the dipole magnet because they emerge with a small angle. Some of electrons or positrons with a low energy come out beyond the acceptance of the beam dump which is located behind the spectrometer, and hit directly thin walls of the experimental hutch. This causes a problem in terms of radiation safety. The e^+e^- blocker is used in the dipole magnet to block low energy particles. The schematic view of the e^+e^- blocker is shown in Fig. 2.26. The e^+e^- blocker with two lead bars is placed 20 cm downstream of the center

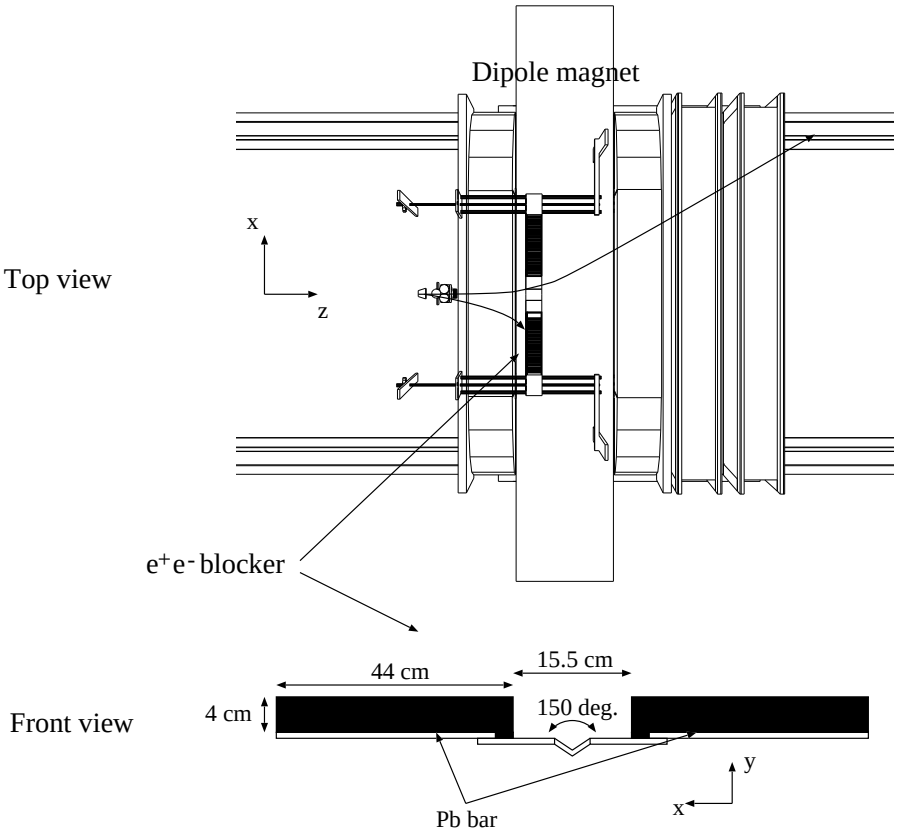

Figure 2.26: Drawing of the e^+e^- blocker.

of the dipole magnet. The blocker is allowed to move by 2 m. The size of each Pb bar is 4 cm high, 44 cm wide, and 10 cm thick. The gap distance between two Pb bars is 15.5 cm. The e^+e^-'s with above 1 GeV/c momentum can go through the gap. The gap distance can be changed by using the small pieces of the Pb blocks. The e^+e^- pair emerges mostly asymmetrically in energy. In most cases, one of pairs is blocked by the blocker, while the other survives and escapes through the 15.5 cm gap and is stopped by the beam dump. The Pb bars are supported by two thin channels with a 0.2 cm thickness. A V-shaped thin bar (SUS) with a thickness of 0.5 cm connects a thin channel with one another in the center. The V-shape structure opens at 150° and has 1.5 cm in depth to let the photon beam pass through (see

Fig. 2.26). The blocker is put down by the weight itself and the center in the y-direction is -7 mm.

2.3.6 Vertex detector (SVTX)

A vertex detector (SVTX) is used to determine a trajectory of a charged particle with drift chambers and determine a vertex point with a high precision by the track position close to the target. The SVTX is placed just after the AC. Fig. 2.27 shows the front view of the SVTX. The SVTX consists of two layers of silicon strip detectors (SSD's). One of layers is used to measure a x-position and the other is used to measure a y-position. The strip pitch is 0.12 mm and the thickness is 0.3 mm. The SVTX has a rhombic-shaped hole for the beam path which is 10 mm $\times$ 10 mm in size.

VLSI chips (VA) [32] are used as a readout circuit of the SSD's. Silicon strips and the VA chip are mounted on a printed circuit board called hybrid board. The hybrid board is connected to a repeater card which contains level converters for logic signals, buffer amplifier for analog output signals, and adjustable bias supplied for the VA chip. The VA ship is controlled by a VME board. Analog signals from the VA chip are sent to a flash ADC module through the repeater card. The analog signal from the silicon strip is read out only when the trigger signal is made. This readout system is used for the SSD's in the SVTX and the tagging system.

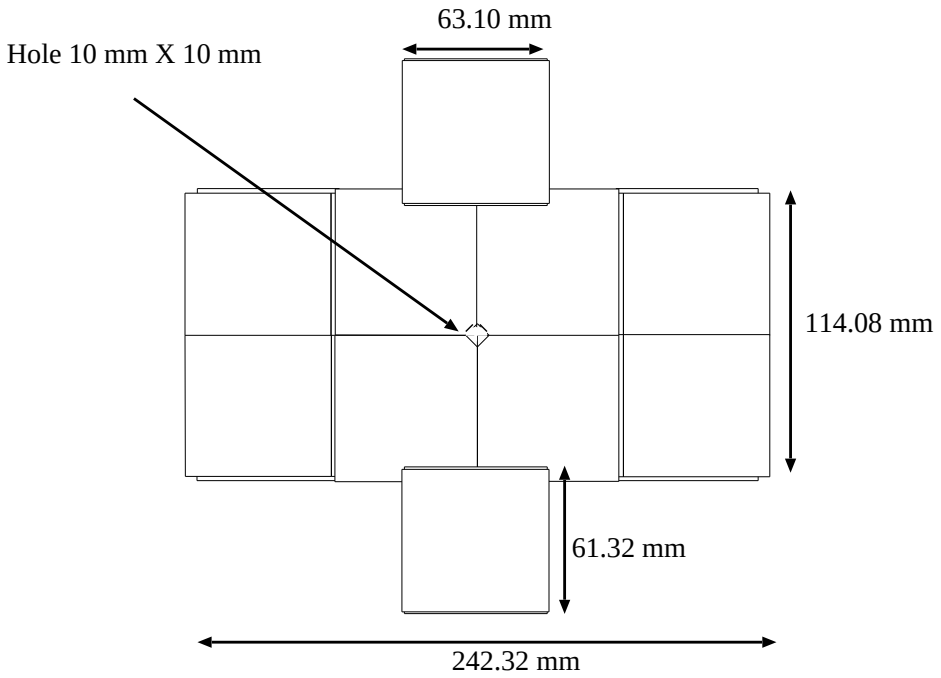

Figure 2.27: Front view of the SVTX.

2.3.7 Drift chambers

A tracking of a charged particle is performed by using hit information from the SVTX and three MWDC's (multi wire drift chambers). DC1 is located upstream of the dipole magnet. It has the active area of 600 mm × 300 mm. Fig. 2.28 shows a drawing of field, shield and sense wires in DC1. DC1 has 6 planes, x, x', u, u', v and x". The x" wires are made additionally because a charged particle begins to be spread out by the magnetic field in DC1. Sense wires of x-x' and u-u' are positioned with a 6 mm spacing and wires of x" and v are positioned with a 12 mm spacing. The field wires are arranged in a hexagonal shape. The shield wires are positioned along the windows to shape the electric field. The inclination angle of the u and v wires is 45° with respect to the horizontal plane. DC2 and DC3 are installed downstream of the dipole magnet and have the active area of 2000 mm × 800 mm. Both DC2 and DC3 have 5 planes, x, x', u, u' and v. The design of DC2 and DC3 is the same as DC1 as shown in Fig. 2.28, but there is no x" wires in DC2 and DC3. Sense wires of x-x' and u-u' are positioned with a 10 mm spacing, and the wires of v are positioned with a 20 mm spacing. The u and v direction are inclined by 30° with respect to the vertical plane. The material of the sense wires is gold-plated tungsten (Au-W) and the wire diameter is 25 and 30 μm for DC1 and DC2, DC3, respectively. The field and shield wires are made of Au-BeCu with a diameter of 100 μm. The windows are made of mylar with a thickness of 125 μm. The design parameters of the DC's are shown in Table 2.4.

The gas mixture used to operate the DC's is 70 % argon and 30 % isobutane. The position resolution of the DC's is approximately 200 μm. The efficiency is more than 98% and is typically 99%.

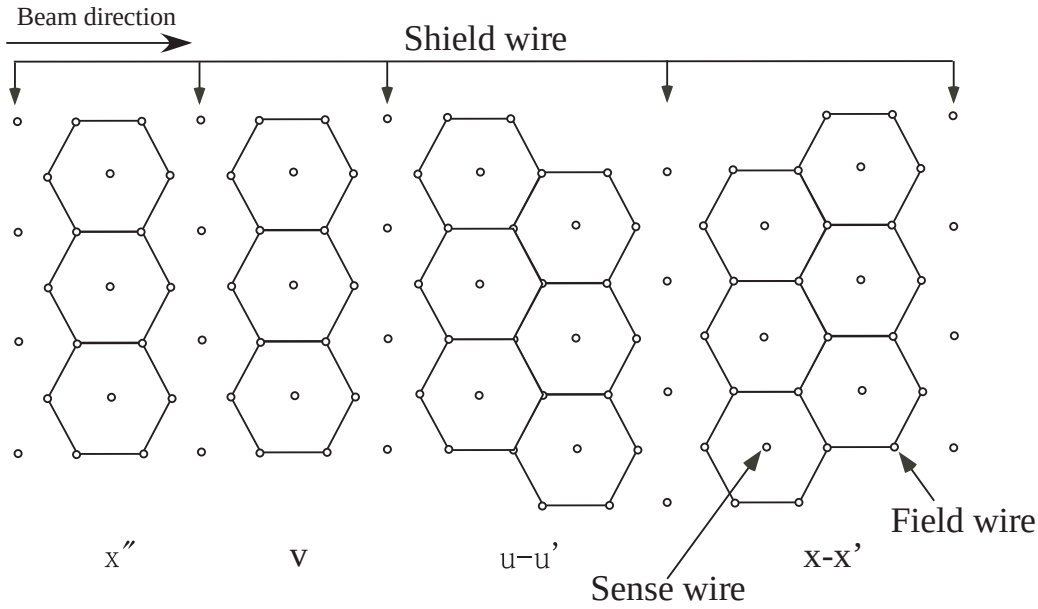

Figure 2.28: Drawing of field, shield and sense wires in the multi wire drift chamber, DC's.

Table 2.4: Design parameters of the MWDC's. The location of the center of each DC is along the z-axis. The location of z=0 is defined as the center of the dipole magnet.

	Coordinate	Orientation	Number of sense wire	Wire spacing (mm)	Active area x × y (mm^2)	Location z (cm)
DC1	x-x'	0°	48	6	600 × 300	-466.0
	u-u'	45°	48	6		
	v	135°	48	12		
	x"	0°	48	12		
DC2	x-x'	0°	104	10	2000 × 800	860.5
	u-u'	120°	78	10		
	v	60°	79	20		
DC3	x-x'	0°	104	10	2000 × 800	1260.5
	u-u'	120°	78	10		
	v	60°	79	20		

2.3.8 Dipole magnet

A dipole magnet is used as a momentum analyzer magnet to bend charged particles. The magnet is placed at the center of the spectrometer. The magnet has an aperture with 55 cm high and 135 cm wide. The length of the pole along the beam is 60 cm. Fig. 2.29 shows the

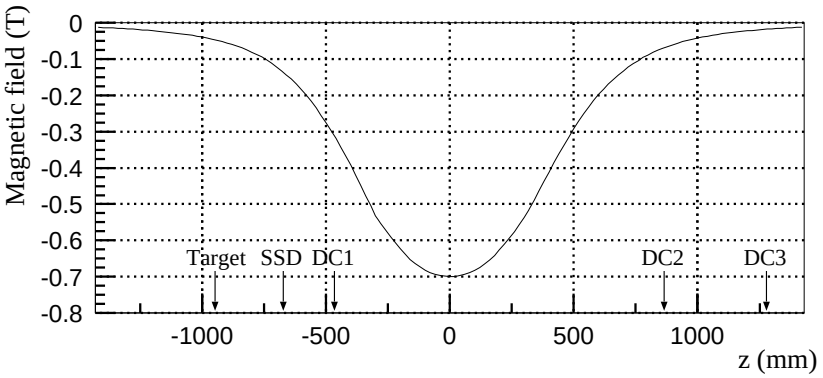

Figure 2.29: Distribution of the magnetic field B_y as a function of the z-position at x=0 and y=0. The position of z=0 corresponds to the center of the dipole magnet.

distribution of the magnetic field B_y along the y-direction as a function of the z-axis at x=0 and y=0. We used the TOSCA simulation program to obtain the distribution. The magnetic field was measured with a hole probe and the measured distribution was compared with the result obtained by the TOSCA simulation. They show a good agreement and then we used the distribution of the magnetic field obtained by TOSCA in the tracking. The direction of the magnetic field is from up to down. The strength of the magnetic field is 0.7 T (1.1 T) at the center when the current is set at 800 A (1510 A). The current was set at 800 A for the

present experiment.

2.3.9 TOF wall

Time-of-flights of charged particles are measured by a TOF wall. The TOF wall is placed downstream of the DC3 with a full angular coverage of the LEPS spectrometer. Fig. 2.30 shows

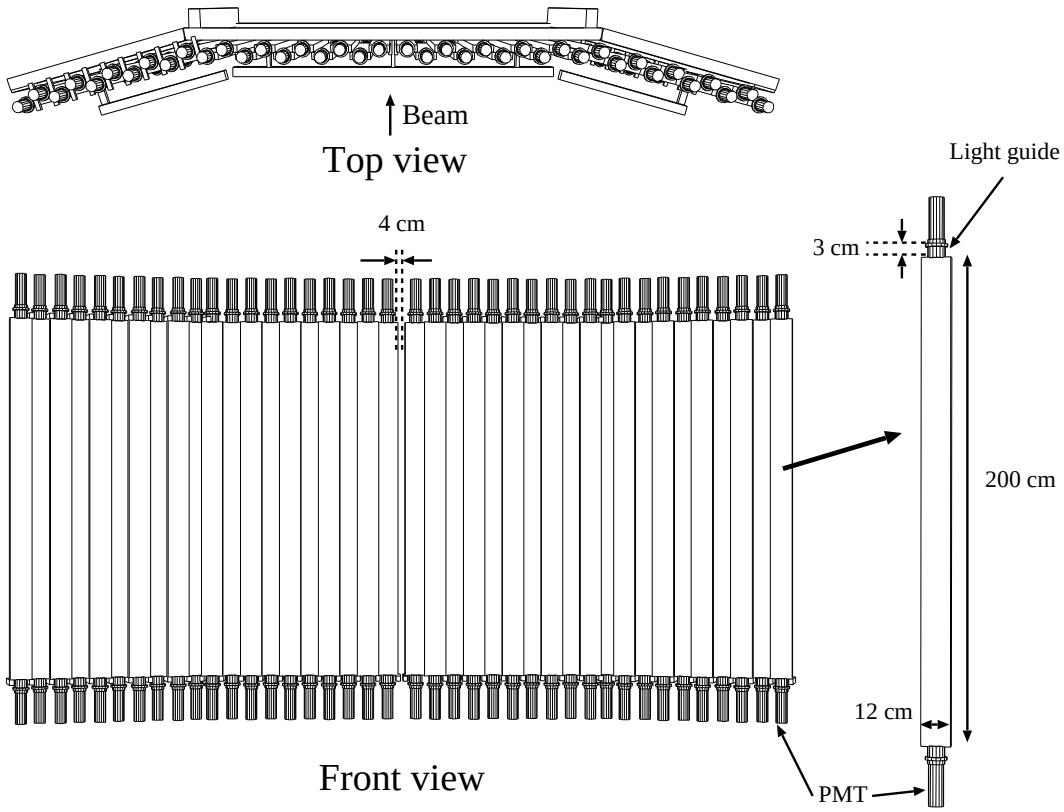

Figure 2.30: Drawing of the TOF wall.

a schematic view of the TOF wall and drawing of a TOF counter. The TOF wall consists of 40 plastic scintillator bars (BC-408). The size of a plastic scintillator bar (TOF counter) is 200 cm long, 12 cm wide, and 4 cm thick. Two 2-inch PMT's (Hamamatsu H7195) are attached to both sides through a light guide with a thickness of 3 cm. Each bar is overlapped with adjacent bars by 1 cm. Sideway bars are aligned in the planes tilted by $\pm$ 15 degrees as shown in the top view of Fig. 2.30. Ten bars are arranged in the right side and ten bars are placed in the left side. A 4-cm gap between the two TOF counters at the center allows for the photon beam to pass through. The TOF wall is movable on the rails between 1.5 and 4.5 m away from the center of the dipole magnet. In the present experiment, the z-position of the TOF wall was set at 3151.5 mm away from the center of the dipole magnet.

2.3.10 RF signal

The 508 MHz radio frequency (RF) system is used in the 8-GeV storage ring to recover the energy loss of circulating electrons due to synchrotron radiation. A time interval of the successive bunches of the RF to accelerate the electrons is 1.966 nsec. The RF signal is used to determine a start timing for the time-of-flight measurement. Fig. 2.31 shows a circuit diagram for the RF signals. The prescaler modules are 17K32 508-MHz 30 bit counters made by DIGITAL LABORATORY. The RF signals are prescaled with a factor 1/87. Three output logic signals are made. Two output signals are read by the FASTBUS TDC 1875S module and are used in the time-of-flight measurement. One output signal is delayed by 86 nsec relative to the other signal. The RF logic signal and the delayed signal are prepared to prevent the event loss due to the dead time of the trigger timing. The other signal from the prescaler with a factor 1/87 is read by the prescaler module with a prescal factor of 1/28. Three output signals are made. The two output signals are delayed by 1.8 μsec and 3.6 μsec relative to the other signal. These three signals are read by the FASTBUS TDC 1877A module. The data was used to study the accidental rate in the tagging system.

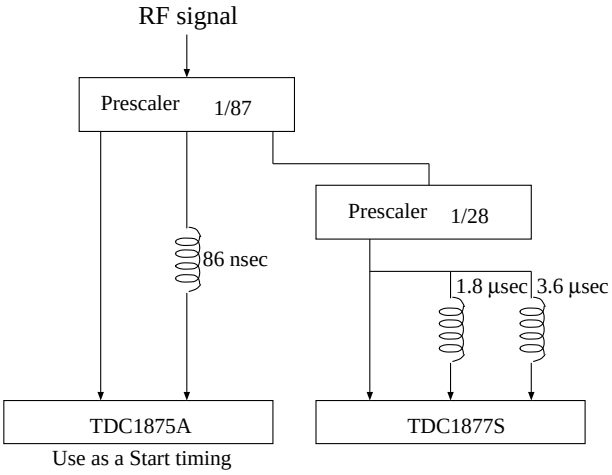

Figure 2.31: Circuit diagram for RF signals

2.4 Electronics and Triggers

We used four types of modules to collect ADC and TDC data from the detectors. LeCroy 4300B FERA (Fast Encoding & Readout ADC) modules are used in the CAMAC system to read analog signals from the hodoscopes in the tagging system, the upstream-veto counter, the TRG, the AC and the TOF counters. The gate width of FERA modules was set 150 nsec. Flash ADC modules are used in the VME system to read analog signals from the silicon strip detectors in the tagging system and the SVTX. LeCroy FASTBUS 1877S TDC modules are used in the FASTBUS system to read the discriminated signals from the hodoscopes in the tagging system and the drift timing from the DC1, DC2 and DC3. The FASTBUS 1877S TDC module provides

Table 2.5: Readout modules (digitizers) for detectors

Detector	ADC	TDC	used as trigger
TAG-PL	FERA	FASTBUS 1877S	TAG
TAG-SSD	Flash ADC	-	-
UPveto	FERA	FASTBUS 1875A	UPveto
TRG	FERA	FASTBUS 1875A	TRG
AC	FERA	FASTBUS 1875A	AC
SVTX	Flash ADC	-	-
DC's	-	FASTBUS 1877S	-
TOF	FERA	FASTBUS 1875A	TOF (M$\geq$1)
RF	-	FASTBUS 1875A/1877S	-

the time resolution of 0.5 nsec/channel and the 1 μsec dynamic range. LeCroy FASTBUS 1875A TDC modules are used in the FASTBUS system to read the discriminated signals from the upstream-veto counter, the TRG, the AC and the TOF counters, and RF signals. The FASTBUS 1875A TDC module provides the timing resolution of 0.025 nsec/channel with the 100 nsec dynamic range. The modules used for a signal readout are summarized in Table 2.5.

Fig. 2.32 shows a readout diagram for the TAG-PL, the upstream-veto counter, the TRG, the AC and TOF counters, and logic circuits for the trigger. The signals from the DC's and SSD's, and RF signals are not used in the trigger logic.

1. In the tagging system, OR signals from the PL hodoscopes corresponding to the photon energy 1.5 GeV to 2.4 GeV are made in each layer. Then the AND signal of them are used in the trigger logic.

2. A logic signal from the upstream-veto counter is used as a veto signal. The width of the veto signal was set 50 nsec.

3. A coincidence signal from both the PMT's of the TRG is used in the trigger logic. The coincidence signal supplies the common start and stop in the TDC modules. The width of the coincidence signal was set 25 nsec.

4. A OR signal by four PMT's of the AC is used to make a veto signal for a trigger logic. The width of the veto signal was set 50 nsec.

5. In the TOF system, a mean timing of the logic signals from the two PMT's of a TOF counter is made by a mean timer module (CAMAC C561). The signal from the mean timer module is read by the majority logic unit module 4532 (CAMAC). The signal of the multiplicity ≥ 1 was used in the trigger logic.

The hardware trigger signal was formed from the logic signals from the TAG-PL, the UPveto, the TRG, the AC and the TOF counters. The UPveto and AC signals are used as

veto signals. Fig. 2.33 shows a diagram of the trigger logic. We used two kinds of triggers defined as

$$\text{Hadron } trig. = TAG \cdot \overline{UPveto} \cdot TRG \cdot \overline{AC} \cdot TOF, \quad (2.8)$$

$$e^+e^- trig. = TAG \cdot \overline{UPveto} \cdot TRG \cdot TOF. \quad (2.9)$$

The one is a hadron trigger to detect hadronic events with the AC veto signal. The other is a e^+e^- trigger to detect e^+e^- events without the AC veto signal. Since the rate of the e^+e^- trigger is too high to take by the DAQ system, the e^+e^- trigger signals are prescaled to be about 20% of the rate of the hadron trigger. The trigger timing is determined by the timing of the TRG and make the ADC gate signal, and TDC common start and stop signals.

2.5 Data acquisition system (DAQ)

The DAQ system consists of digitizers, buffer sequencers, CPUs, and a data collection server. Fig. 2.34 shows a schematic view of the LEPS DAQ system. The COMPAC Alpha-Server 1200 was used as a data collection server. The Force 7V was used as a CPU of the local DAQ system. The data transfer speed of the network between the alpha server and the 7V is 3 MB/s. It is fast enough to collect the data with a 1 kHz event rate.

UNIX is chosen as the OS of these computers. Since UNIX is not a real-time OS, buffer sequencer modules are used in the local DAQ system to take care of the time-crucial processes. Data taken by a digitizer are transferred to a buffer sequencer in the event-by-event mode. The buffer sequencer module stores the data consisting of several events in its buffer memory. The buffer data is transferred to a CPU. By taking the event data from the buffer sequencer module as one package, the transaction rate of a CPU is reduced. Since the buffer sequencer modules treat the memory data in a double-buffer mode, the data are stored on another buffer during the data readout by a CPU. Therefore, the dead-time has been extremely small during the CPU readout.

There are three local DAQ systems shown in Fig. 2.35. The first one handles the pulse-height signals from the TAG-PL, the UPveto, the TRG, the AC and TOF counters. After analog signals are digitized by the FERA modules, the digitized data are collected with the universal I/O module (UIO) which is a VME module with an 8-MB memory [34] through the FERA divider. The UIO module is designed as a buffer sequencer which is used for data readout and buffering. The buffer data are transferred from the UIO to a VME CPU-board. The CPU sends the data to the data server.

The second system is prepared for the SSD's of the TAG and the SVTX. A Viking chip is placed near the SSD and read signals from 128 strips of the SSD. The 128 analog signals are sent to a flash ADC module (FADC) by the Viking chip. The analog signals from the Viking chip are digitized by the FADC and are stored in its memory. In the FADC module, pedestal and a base line are subtracted from the raw data, and then only the meaningful data are stored. The event data from several FADC modules are collected by the UIO module. The UIO stores the event data in its memory. A VME CPU board computer reads the buffer data and sends it to a data server.

The last system handles the timing signals from the TAG-PL, the UPveto, the TRG, the AC and TOF counters, and the drift time signals from the DC's. The digitized data are generated

by the FASTBUS TDC modules (1877S and 1875A). The Next-Generation FASTBUS (NGF) is used as a buffer sequencer module and a FASTBUS-VME interface. The NGF has a sequencer and memory to readout and store the data from the TDC modules. The NGF has a VME bus which has a CPU (a VME board computer) and a interrupt register. The CPU reads buffer data from the NGF memory and sends it to the data server when the buffer-change request comes to the interrupt register.

The typical dead time in the experiment was 3% under the condition with the trigger rate of 20 Hz.

2.6 Data summary

The experiment was carried out from the 13th December in 2000 to the 27th June in 2001. The total beam time for the experiment was about 100 days. We took data with the liquid hydrogen target and a linear-polarized photon beam. The data was taken with about 2×10^{12} photons at the target in total. About 48% of the data was collected with vertically polarized photons and 52% of the data was collected by horizontally polarized photons. The average polarization of the laser photon measured was 98.7% and 95.0% for the vertical and horizontal polarizations, respectively. The trigger rate of the tagging counter was typically 500 kcps (300 kcps) with the vertically (horizontally) polarized beam. Although hadronic events were of interest for the meson photoproduction, we also acquired data with the e^+e^- trigger to check the performance of the detectors. The trigger rate with the hadron trigger was about 20 Hz. The trigger rate with the e^+e^- trigger was about 4 Hz. We also took data with the empty target in order to estimate the background events for one day.

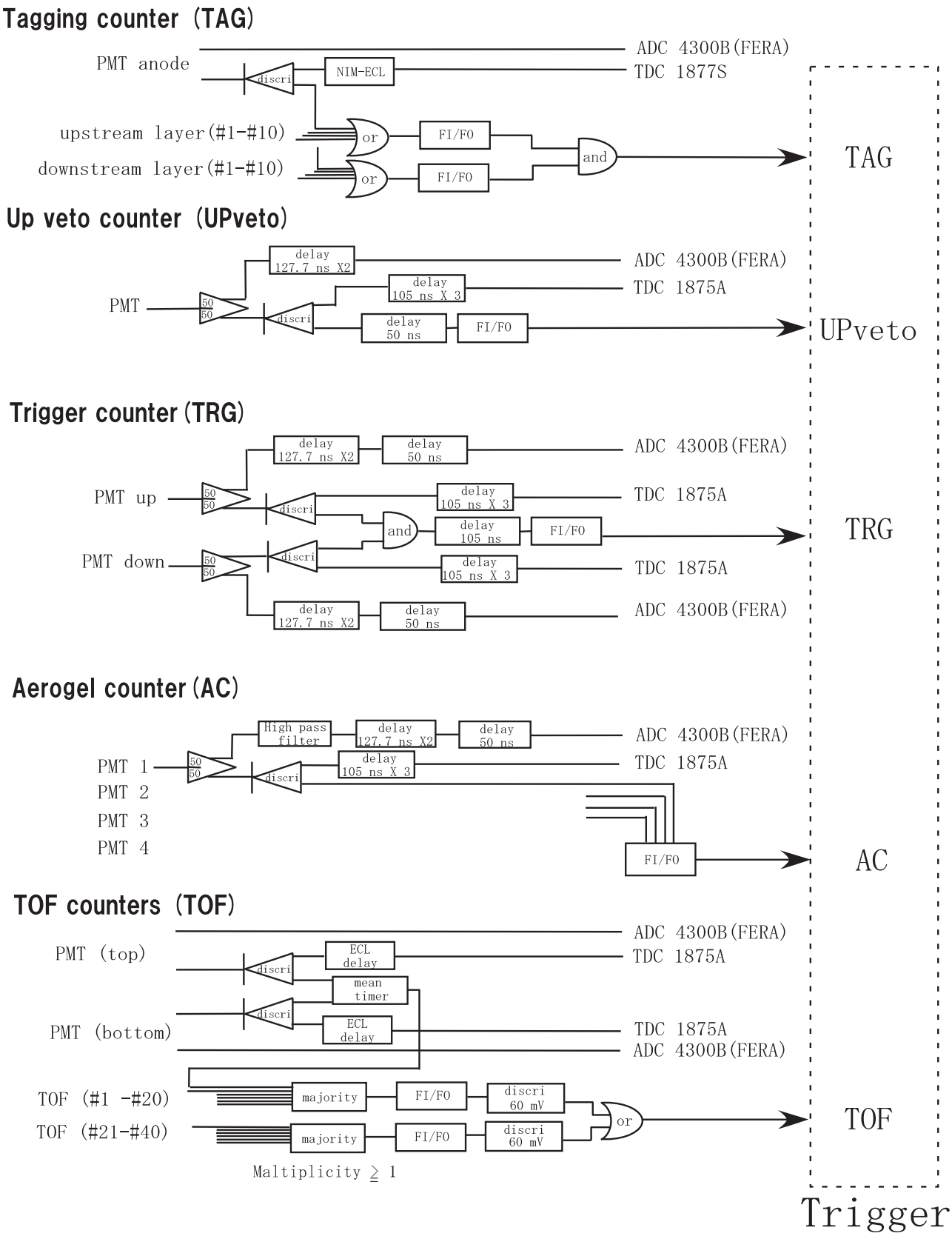

Figure 2.32: Diagram of the readout circuits for triggers.

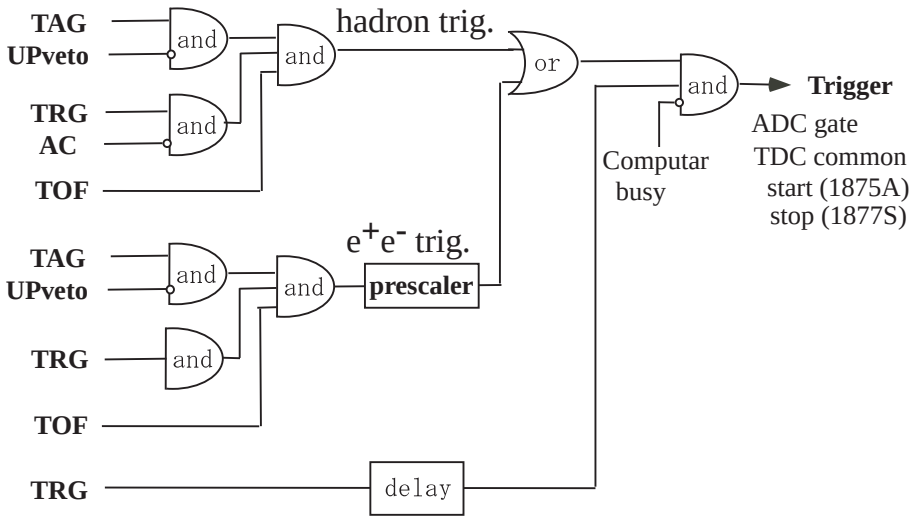

Figure 2.33: Diagram of the trigger logic for the hadron events.

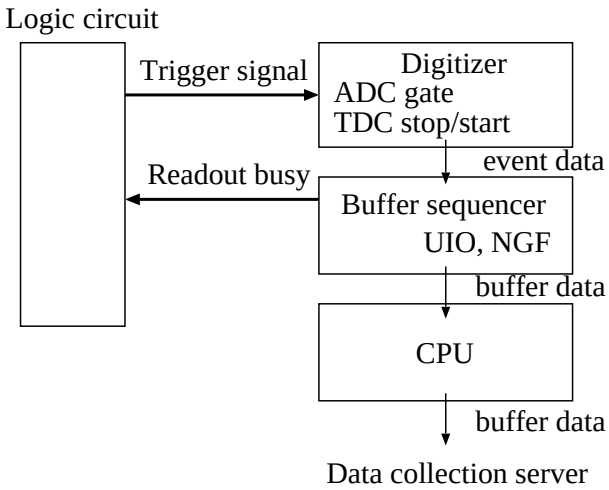

Figure 2.34: Schematic flow chart of the DAQ system.

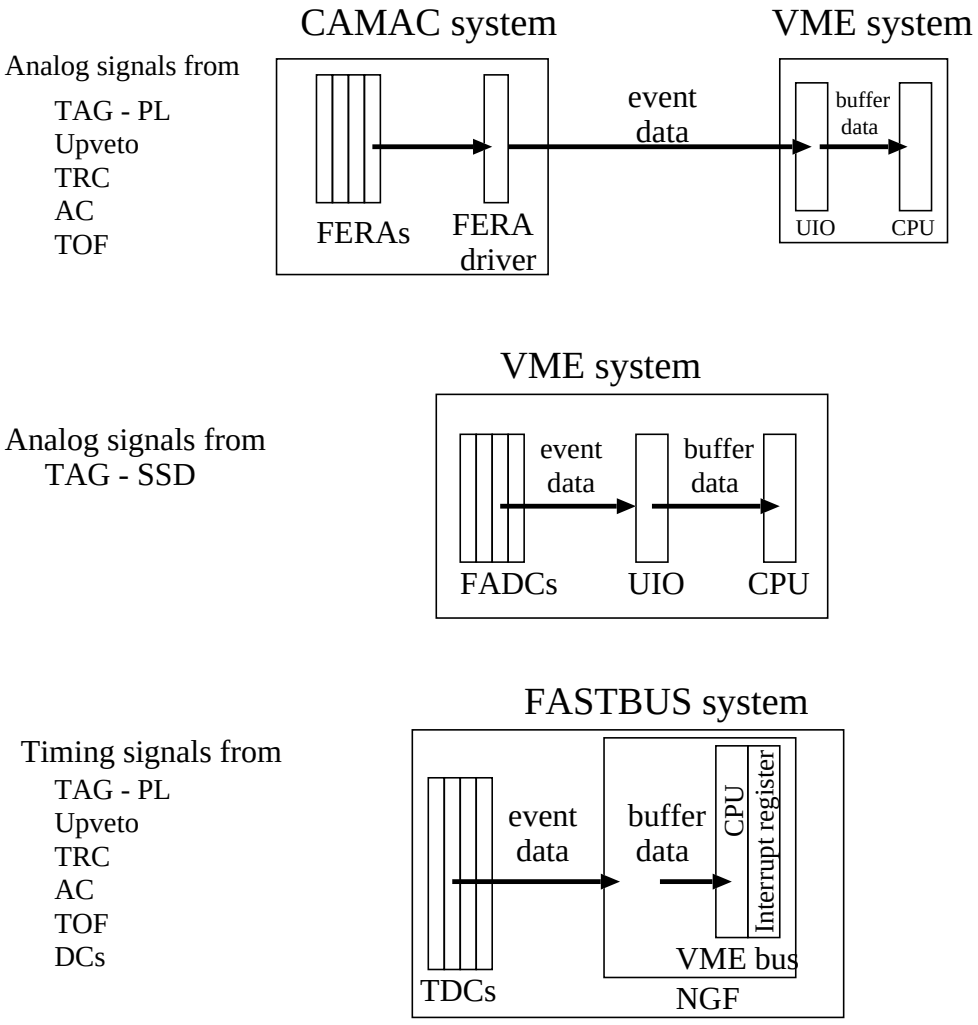

Figure 2.35: Data flow chart in the local DAQ systems.

Chapter 3

Data analysis

The LEPS program called LEPSana for the off-line analyses was developed by the LEPS collaboration. In LEPSana, the raw data which are digital outputs of ADC and TDC from the LEPS detectors, are analyzed and the ntuple data sets are made to use commonly for the various reaction analyses. The LEPSana code is composed of three main parts. The first part is "Tagging analysis" to calculate the energy of the photon beam. The tagging analysis was described in the section 2.2.3. The second part is "Tracking analysis" to perform the tracking and obtain momenta of charged particles. The last part is "TOF analysis" to calculate the time-of-flight of charged particles. The reconstruction of mass is performed after the Tracking and the TOF analyses are done. The physical quantities obtained by LEPSana are filled into ntuples. The Tracking and the TOF analyses, and the mass reconstruction are described in this chapter.

3.1 Measurement of momentum

The momentum reconstruction is performed by using information from the SVTX, DC1, DC2 and DC3/TOF wall. A trajectory of a charged particle is reconstructed by the hit information obtained by the detectors. There are tracks which can pass through the DC2 but go out from the sensitive area of the DC3. If there is no hit in the DC3, we used the hit information from the TOF wall instead of the DC3. If there are hits in the DC3, the TOF wall is not used for the tracking. The number of reconstructed tracks increase by about 7% of the addition of the DC2-TOF tracking. In the tracking analysis, we obtain the sign of the charge, the absolute momentum, the momentum vector, the path length from the target/trigger counter to the TOF wall, and the vertex points.

Before applying the track fitting, clustering is performed in each detector of the SVTX, DC1, DC2 and DC3. A cluster in the SVTX is made by a combination of a x-hit and y-hit in the x and y layer. The DC1 has three x-wires, two u-wires and one v-wire. A cluster is made by combining more than four wires in the DC1. At least, one hit in each plane of x, u and v planes is required. The DC2 has two x-wires, two u-wires and one v-wire. A cluster is made by combining more than three wires in the DC2. At least, one hit in each plane of x, u and v planes is required. The DC3 has also five wires and a cluster is made in the same way as the DC2.

After the clustering, the straight-line fitting in a 3-dimensional space is performed for all combinations of clusters in the upstream (the SVTX and DC1) and downstream (the DC2 and DC3/TOF) separately to determine the hit positions in the DC's from the wire address and the drift distance. Since the drift chambers measure only the drift distance, there is no information as to where the particle passed on a circle with a radius of the drift distance and also which side of the wire the particle passed (the left-right ambiguity). In order to solve this problem, the straight-line fitting is applied in the upstream and downstream separately. However, there is a possibility that the left-right ambiguity is not solved correctly for the low momentum particles because the straight line approximation is not applicable for the low momentum particles. If the left-right ambiguity is not solved, a chi-square of the fitting would be large. Therefore a hit for which the left-right ambiguity is not solved correctly should be removed. These hits are removed as outliers in the track fitting with the Kalman filter method.

After the straight-line fitting, the track candidates are found. The best 30 combinations of clusters in terms of χ^2 are selected in each stream of the upstream and downstream. All combinations of the upstream and downstream tracks are made and the consistency is checked by using the cross point. It is checked whether the upstream track and downstream track cross in the x-z plane in the center region and also whether there is not a big difference between the slope in the y-z plane for the upstream track and downstream track. After this consistency check, we perform the track fitting for all remaining track candidates. The positions x, y and directions dx/dz, dy/dz at the first plane in the SVTX are obtained from the results of the straight-line fitting. The momentum and charge of a particle are estimated by the bending radius at the cross point between a upstream and downstream track in a constant field approximation. These values are used as initial values for the track fitting with the Kalman filter method which is described in detail below.

3.2 Kalman filter

A trajectory of a charged particle is reconstructed by applying a fitting to hit positions at the detectors. The Kalman filter method was employed for the track fitting in the LEPSana program.

The Kalman filter [37, 38] is a technique to perform a least squares fit. The Kalman filter is a method of estimating the state of a dynamic system which is an evolving stochastic model of some time-varying phenomenon. A particle trajectory in a dynamic system is determined by the Kalman filter technique. The Kalman filter has some advantages,

1. Multiple scattering and energy loss are taken into account in a very efficient way.

2. A trajectory obtained by a fitting follows closely the real track of a particle which is scattered by multiple scattering.

3. There is no large matrix. The computing time grows in proportion to the number of measurement points n, which is efficient compared with the global fit method in proportion to n^3.

4. Outliers (background hits) can be easily removed.

5. The linear approximation of the track model needs not to be valid over the entire length of a track, but only between adjacent surfaces of a detector.

3.2.1 Principle of the Kalman filter technique

A trajectory is defined by a state vector on each detector surface (a plane). The components of a state vector are positions, directions and momentum which are used as track parameters. The track parameters are to be indicated in the equation (3.10). Three operations are performed in a dynamical system in the Kalman filter method as shown in Fig. 3.1. p_k is a state vector in the k plane. n is the number of the measurements (hits).

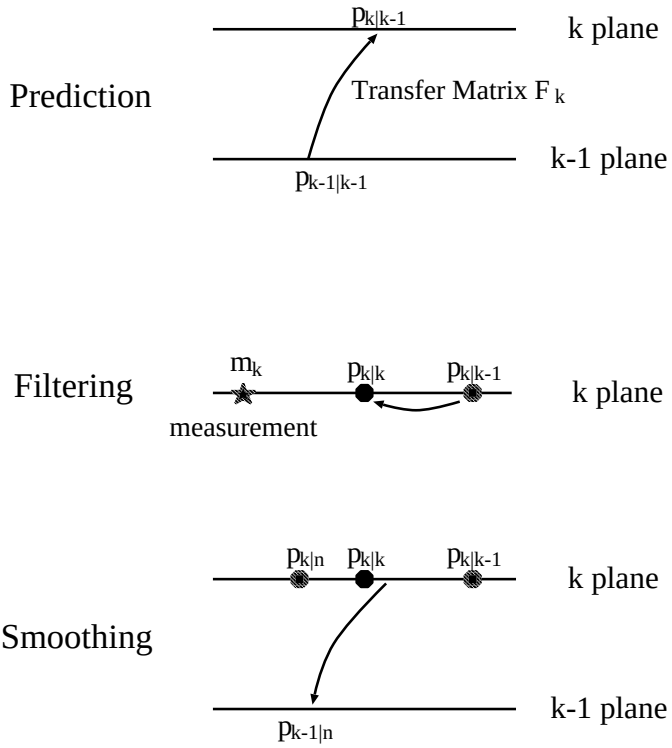

Figure 3.1: Operations of the Kalman filter technique.

1. Prediction : Determine a state vector $p_{k|k-1}$ - estimation of a state vector at the k plane taking into account all past measurements from the first plane to the k-1 plane.

2. Filtering : Determine a state vector $p_{k|k}$ - estimation of a state vector at the k plane taking into account the measurement m_k, in addition to all past measurements.

3. Smoothing : Determine a state vector $p_{k-1|n}$ - estimation of a state vector at a past plane taking into account all measurements from the first plane to the last plane.

The prediction and filter process are done from the first plane to the last plane. Then, the state vector at the last plane goes back to the first plane by the smoother process. These operations are performed to minimize the mean square estimation error. The formulas for these operations are as follows. A state vector on the k plane is denoted as p_k and a covariance matrix is denoted as C_k.

The predicted state vector ($p_{k|k-1}$) and the predicted covariance matrix ($C_{k|k-1}$) in the detector plane k are obtained as

$$p_{k|k-1} = F_k p_{k-1|k-1}, \tag{3.1a}$$
$$C_{k|k-1} = F_k C_{k-1|k-1} F_k^T + Q_k, \tag{3.1b}$$

by using the state vector $p_{k-1|k-1}$ and the covariance matrix $C_{k-1|k-1}$ at the $k-1$ plane (the previous plane). F_k is the transfer matrix which transfers the state vector in a dynamic system from the $k-1$ plane to the k plane. The predicted state vector $p_{k|k-1}$ contains information on measurements up to the $k-1$ plane. The predicted covariance matrix $C_{k|k-1}$ is a sum of two terms. The first term is the linear error propagation of the covariance matrix $C_{k-1|k-1}$. The second term Q_k is the covariance matrix of the process noise between the $k-1$ plane and the k plane. The process noise is an effect of materials on a trajectory, mainly multiple scattering and energy loss.

The filtered estimate ($p_{k|k}$, $C_{k|k}$) is written by a weighted mean of the prediction and a measurement m_k at the k plane as

$$p_{k|k} = C_{k|k}[C_{k|k-1}^{-1} p_{k|k-1} + H_k^T W_k m_k], \tag{3.2a}$$
$$C_{k|k} = [C_{k|k-1}^{-1} + H_k^T W_k H_k]^{-1}, \tag{3.2b}$$
$$W_k = V_k^{-1}, \tag{3.2c}$$

where V_k is a diagonal covariance matrix of a measurement error at the k plane and W_k is an inverse matrix of V_k. A state vector is updated by including information on a measurement at the current plane (m_k). The matrix H_k projects a state vector to a measurement as

$$m_k = H_k p_k. \tag{3.3}$$

The filtered residuals and chi-squares are obtained as

$$r_{k|k} = m_k - H_k p_{k|k}, \tag{3.4a}$$
$$R_{k|k} = C(r_{k|k}) = V_k - H_k C_{k|k} H_k^T, \tag{3.4b}$$
$$\chi^2_{k,f} = r_{k|k}^T R_{k|k}^{-1} r_{k|k}. \tag{3.4c}$$

The chi-square for a track is a sum of the individual chi-squares of all filter steps as

$$\chi^2_f = \sum_{k=1}^{n} \chi^2_{k,f}, \tag{3.5}$$

where n is the total number of filter steps (measurements). The filtered state vector at the last plane $p_{n|n}$ contains the full information obtained from all measurements when the filter has reached the last plane. A state vector at each plane with the full information can be obtained

by the smoothing procedure. The smoothing is operated step by step in the opposite direction of the filtering to pass back the full information. The smoothed state vector $p_{k|n}$ and covariance matrix $C_{k|n}$ are obtained as

$$\begin{aligned} p_{k|n} &= p_{k|k} + A_k(p_{k+1|n} - p_{k+1|k}), && \text{(3.6a)} \\ C_{k|n} &= C_{k|k} + A_k(C_{k+1|n} - C_{k+1|k})A_k^T, && \text{(3.6b)} \\ A_k &= C_{k|k}F_{k+1}^T C_{k+1|k}^{-1}. && \text{(3.6c)} \end{aligned}$$

The smoothed error is larger than the filtered one because the smoothed state vector has more information than the filtered state vector. The smoothed residuals and chi-squares are obtained as

$$\begin{aligned} r_{k|n} &= m_k - H_k p_{k|n}, && \text{(3.7a)} \\ R_{k|n} &= C(r_{k|n}) = V_k - H_k C_{k|n} H_k^T, && \text{(3.7b)} \\ \chi^2_{k,s} &= r^T_{k|n} R^{-1}_{k|n} r_{k|n}, && \text{(3.7c)} \end{aligned}$$

and the total chi-squares χ^2_s is calculated as

$$\chi^2_s = \sum_{k=1}^{n} \chi^2_{k,s}. \tag{3.8}$$

The filter/smoother operation is applied in order to find the optimal track parameters. The Kalman filter algorithm needs initial values of a state vector ($p_{1|1}$) and the covariance matrix ($C_{1|1}$) at the first detector plane. In general, however, the first observation is not the full state vector of position, direction and momentum. Therefore, in this case, the initial state vector and the initial covariance matrix are given arbitrary and large errors.

3.2.2 Goodness of fit

We test a goodness of a fit by using $\chi^2_{k,f}$ obtained by the filtering. Since the Kalman filter is mathematically equivalent to a least-squares estimator, the χ^2 contribution, $\chi^2_{k,f}$ follows the standard χ^2 distribution. The χ^2 probability is used to test a goodness of a fit and to eliminate backgrounds. The χ^2 probability with the number of degree of freedom *ndf* is defined as

$$prob(\chi^2, ndf) = \int_{\chi^2}^{\infty} f(\tilde{\chi}^2, ndf) d\tilde{\chi}^2. \tag{3.9}$$

The function $f(\chi^2, ndf)$ is the standard χ^2 distribution with the number of degree of freedom, *ndf*. Since an observation at each plane is one coordinate of position and the number of track parameters is five in general, the degree of freedom is the number of measurements minus five, $(n-5)$. The χ^2 probability should be uniformly distributed between 0 and 1. Most of backgrounds have a large chi-square along with a small χ^2 probability. Backgrounds are eliminated by using a critical cut-value of the χ^2 probability. Although good tracks with a large χ^2 are also rejected, the percentage is known as the critical cut-value. For example, 10 % of good tracks are thrown away together with backgrounds when the critical cut-value is 0.1. The quantity $1-\alpha$ (α is the critical cut-value) is called the 'confidence level'.

3.2.3 Application of the Kalman filter in LEPS off-line program

In this section, an application of the Kalman filter method and definitions of the functions in the LEPSana program are described.

Strategy of the fitting

The filter/smoother operation is applied a couple of times to find the optimal track parameters in the LEPSana program. In the filter/smoother operation, the state vector is transferred from the first plane to the last plane step by step by the filter process and then the state vector is passed back from the last plane to the first plane by the smoother process. When the state vector has reached the first plane, it is transferred to a next stage of the filter/smoother operation. This cycle is iterated until the filter chi-square $\chi^2_{k,f}$ is converged. The typical times of iterations are 3. The smoothed state vector at each plane is stored as the results of track parameters. The smoothed state vector is more precise than the filtered state vector because all information on measurements are included in the smoothed state vector.

This fitting procedure (the iteration cycle of filter/smoother operation) is applied twice. In the track fitting, we have to take into account the effect of multiple scattering of a particle in the LEPS spectrometer to get a correct chi-square value. However the particle identification is necessary to calculate a velocity of a particle, β, which gives a multiple scattering angle required in Eq. (3.18). Therefore, we perform the fitting procedure twice. In the first fitting, the filter/smoother operation is done assuming that a particle is a proton. When the proton target is used, the heaviest outgoing particle is a proton and multiple scattering of a proton gives a large error which doesn't give a strict limit to a deviation of parameters in a fitting. After the first fitting, the mass is calculated by using a momentum and a path length obtained in the first fitting and a measured TOF obtained by the TOF analysis. By using the calculated mass directly, β is calculated and used to give the multiple scattering angle in the second fitting. In the second fitting, since more realistic β is used to calculate the effect of multiple scattering, the correct chi-square value and the results of the track parameters are obtained.

After the fitting procedure is applied twice to include the multiple scattering effect, the χ^2 probability is checked to remove 'outliers'. There are background hits which have larger errors than expected. They are called outliers. Dominant causes of outliers are the creation of energetic electrons in gaseous detectors (δ-rays), a noise signal in a detector and hits from another particle's set of measurements (ghosts). Furthermore, we may make a mistake in the solving the left-right ambiguity in the drift chambers. These hits are removed as outliers. These outliers should be removed because they make chi-squares large even if the track is a good/real track. In the Kalman filter technique, it is easy to remove the measurement m_k by using the reduced residual. The smoothed chi-squares in Eq.(3.7) are used to search outliers because the smoothed estimate has the full information of measurements. After the fitting procedure is applied twice with the full measurements, if the χ^2 probability is less than the critical value, a measurement m_k with the largest $\chi^2_{k,s}$ is removed. We used 0.02 (the confidence level of 98%) as the critical cut-value because the distribution of the χ^2 probability was flat above this value before removing outliers. And again the fitting procedure is applied to the full measurements except for the measurement with the largest $\chi^2_{k,s}$. This procedure is continued until the χ^2 probability becomes greater than 0.02 or 7 outliers are found.

State vector

We use the following vector as the track parameters,

$$(x, y, t_x, t_y, \lambda) \tag{3.10}$$

where x and y are positions, t_x and t_y are slopes (directions) defined as $t_x = p_x/p_z, t_y = p_y/p_z$ with the momentum vector (p_x, p_y, p_z), and $\lambda = \mathrm{q}/p$ with charge q. A state vector is defined by these five track parameters as

$$p_k = (x, y, t_x, t_y, \lambda)^T. \tag{3.11}$$

A state vector is usually not observed directly. The quantities measured by a detector (m_k) are a function of a state vector p_k as Eq. (3.3). Since the SVTX has either x or y-coordinate at each plane and the DC's have one of x, u or v-coordinates at each plane, Eq. (3.3) is very simple as follows:

$$\begin{aligned}
\text{x-coordinate} : m_k &= x, && \text{(3.12a)}\\
\text{y-coordinate} : m_k &= y, && \text{(3.12b)}\\
\text{u-coordinate} : m_k &= x\cos\alpha - y\sin\alpha, && \text{(3.12c)}\\
\text{v-coordinate} : m_k &= x\cos\alpha + y\sin\alpha, && \text{(3.12d)}
\end{aligned}$$

where α is a stereo angle of DC wires. For example, in the case of the x-coordinate, the components of the matrix H_k are written as follows:

$$H_{xx} = 1, \tag{3.13}$$

and the other ones are 0. In the case of the u-coordinate, components of the matrix H_k are written as follows:

$$\begin{aligned}
H_{xx} &= cos\alpha, && \text{(3.14)}\\
H_{xy} &= -sin\alpha, && \text{(3.15)}
\end{aligned}$$

and the other ones are 0.

Transfer matrix

The transfer matrix F, which is a 5×5 matrix, is defined as

$$F = \begin{pmatrix}
\frac{dx'}{dx} & \frac{dx'}{dy} & \frac{dx'}{dt_x} & \frac{dx'}{dt_y} & \frac{dx'}{d\lambda} \\
\frac{dy'}{dx} & \frac{dy'}{dy} & \frac{dy'}{dt_x} & \frac{dy'}{dt_y} & \frac{dy'}{d\lambda} \\
\frac{dt'_x}{dx} & \frac{dt'_x}{dy} & \frac{dt'_x}{dt_x} & \frac{dt'_x}{dt_y} & \frac{dt'_x}{d\lambda} \\
\frac{dt'_y}{dx} & \frac{dt'_y}{dy} & \frac{dt'_y}{dt_x} & \frac{dt'_y}{dt_y} & \frac{dt'_y}{d\lambda} \\
\frac{d\lambda'}{dx} & \frac{d\lambda'}{dy} & \frac{d\lambda'}{dt_x} & \frac{d\lambda'}{dt_y} & \frac{d\lambda'}{d\lambda}
\end{pmatrix}. \tag{3.16}$$

The transfer matrix F transfers a state vector p to p'. The Runge-Kutta method [39] is used to calculate the transfer matrix F. In the Runge-Kutta method, we can calculate the required derivatives together with the track coordinates in the inhomogeneous magnetic field.

Covariance matrix of detector resolution and process noise

The covariance matrix V_k by detector resolutions is diagonal as follows:

$$V_k = \begin{pmatrix} \sigma_{xx}^2 & 0 & 0 & 0 & 0 \\ 0 & \sigma_{yy}^2 & 0 & 0 & 0 \\ 0 & 0 & \sigma_{t_x t_x}^2 & 0 & 0 \\ 0 & 0 & 0 & \sigma_{t_y t_y}^2 & 0 \\ 0 & 0 & 0 & 0 & \sigma_{\lambda\lambda}^2 \end{pmatrix}. \tag{3.17}$$

Since the observation at each plane in a detector is only one coordinate of positions, V_k also has one coordinate along with the measurements. For example, in the case of the x-coordinate, the components of the matrix V_k except for $V_{xx} = \sigma_{xx}$ are zero.

Multiple scattering is taken into account in the error matrix. Energy loss is not taken into account because it is negligible comparing with the multiple scattering effect in the LEPS spectrometer. The covariance matrix Q_k of the process noise [40] is calculated by a multiple scattering angle,

$$C_{MS} = \frac{13.6}{\beta cp} z\sqrt{l/X_0}[1 + 0.038ln(l/X_0)], \tag{3.18}$$

where z, p and l are the charge, the momentum and the path length in a material of a particle and X_0 is the radiation length. The main material in the LEPS spectrometer is gas (air and mixing gas of Argon and Isobutan in the drift chambers). The covariance matrix Q for the continuous and thick material such as gas in drift chambers is denoted as

$$Q = \begin{pmatrix} cov(t_x,t_x)\frac{l^2}{3} & cov(t_x,t_y)\frac{l^2}{3} & cov(t_x,t_x)\frac{l}{2} & cov(t_x,t_y)\frac{l}{2} & 0 \\ cov(t_x,t_y)\frac{l^2}{3} & cov(t_y,t_y)\frac{l^2}{3} & cov(t_x,t_y)\frac{l}{2} & cov(t_y,t_y)\frac{l}{2} & 0 \\ cov(t_x,t_x)\frac{l}{2} & cov(t_x,t_y)\frac{l}{2} & cov(t_x,t_x) & cov(t_x,t_y) & 0 \\ cov(t_x,t_y)\frac{l}{2} & cov(t_y,t_y)\frac{l}{2} & cov(t_x,t_y) & cov(t_y,t_y) & 0 \\ 0 & 0 & 0 & 0 & 0 \end{pmatrix} \tag{3.19a}$$

where

$$cov(t_x,t_x) = (1+t_x^2)(1+t_x^2+t_y^2)C_{MS}^2 \tag{3.19b}$$

$$cov(t_y,t_y) = (1+t_y^2)(1+t_x^2+t_y^2)C_{MS}^2 \tag{3.19c}$$

$$cov(t_x,t_y) = t_y t_x(1+t_x^2+t_y^2)C_{MS}^2 \tag{3.19d}$$

l : traversed length in the medium.

Initialization

The Kalman filter method needs initial values of a state vector and a covariance matrix. However the first measurement is only one coordinate of a position at the SVTX. Therefore the values obtained by the straight-line fitting are used as the initial values of a state vector. In the initial covariance matrix, an error of a position is set to 1 mm. The initial errors of the

momentum and the slope are determined to be 0.02 GeV/c to reduce the number of iterations of the filter/smoother cycle. The initial covariance matrix is written as

$$C_{1|1} = \begin{pmatrix} 1.0 & 0 & 0 & 0 & 0 \\ 0 & 1.0 & 0 & 0 & 0 \\ 0 & 0 & 0.02 & 0 & 0 \\ 0 & 0 & 0 & 0.02 & 0 \\ 0 & 0 & 0 & 0 & 0.02 \end{pmatrix} \quad (3.20)$$

unit: mm, GeV/c.

A fluctuation of a state vector at the first plane is large due to the arbitrary initial values. To make the fluctuation smaller, we assume a dummy plane in the program. The dummy plane, which is located at 5 mm upstream of the first plane of the SVTX, is used as the first plane in the Kalman filter algorithm. The dummy plane has the same coordinate as the first SVTX plane. The chi-square and state vector at the dummy plane are not used finally.

3.2.4 Performance

The performance of the Kalman filter code was evaluated by tracks generated in the g3leps which was a simulation code based on GEANT3.21 [36]. The resolutions of the tracking devices, the SVTX and the DC's, and time-of-flight were modeled with Gaussian distributions of the realistic values. The switch of multiple scattering was turned on to check whether the effect can be taken into account correctly in the program. In the real data, momenta of the K^+'s in the $p(\gamma,K^+)\Lambda$ and $p(\gamma,K^+)\Sigma^0$ reactions were ranged from 0.8 GeV/c to 2.2 GeV/c. The K^+'s were generated with the momentum distribution as shown in Fig. 3.2 and were analyzed in the

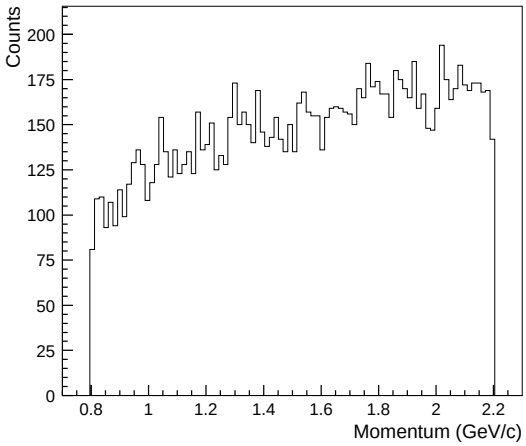

Figure 3.2: Momentum distribution of kaons generated in the MC simulation.

Kalman filter code. The chi-square distribution and the decay-in-flight events were checked.

Fig. 3.3(a) shows the distribution of the χ^2 probability ($prob(\chi^2)$) of the tracks reconstructed by the tracking analysis when the switch of the decay-in-flight is turned off in the GEANT

code. The χ^2 probability of the no-decay kaons should be more than the critical cut value 0.02 after the procedure to remove outliers. Most of the good tracks pass through the cut of $prob(\chi^2) > 0.02$ as as shown in Fig. 3.3(a). There is a few events (about 0.1%) with $prob(\chi^2) < 0.02$. These events still include outliers due to the wrong left-right ambiguity. The distribution slightly extends at the low $prob(\chi^2)$. These events have still a hit for which we have make a mistake in the solving the left-right ambiguity in the drift chambers.

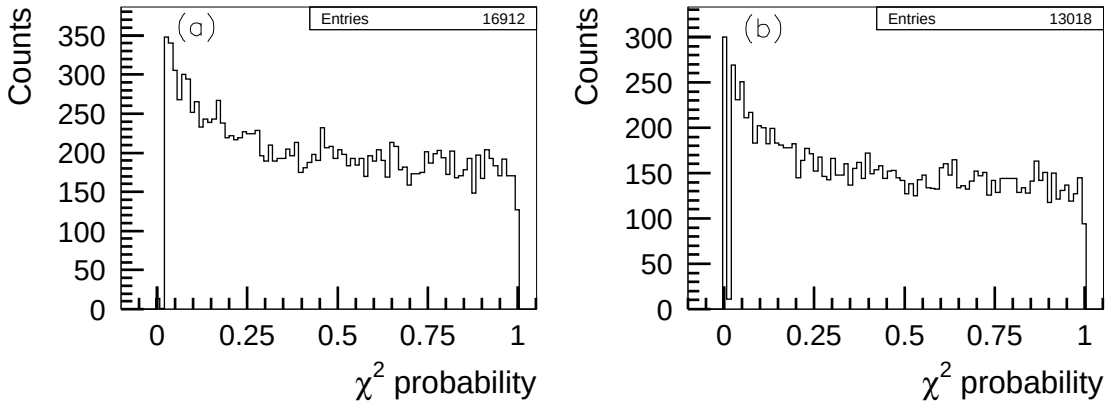

Figure 3.3: Results of the Kalman filter in the MC simulation. (a):χ^2 probability distribution when the switch of the decay-in-flight is off and (b):χ^2 probability distribution when the switch of the decay-in-flight is on.

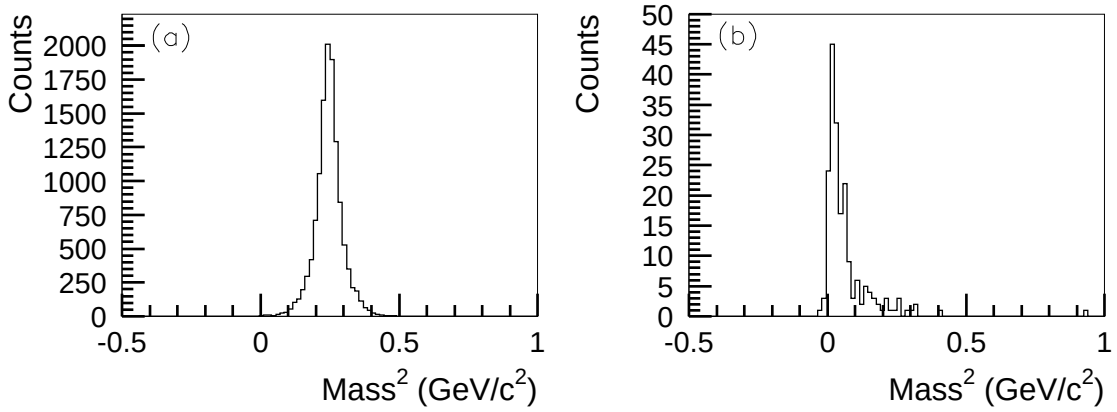

Figure 3.4: Results of the Kalman filter in the MC simulation. (a) and (b):Mass spectra of no decay-in-flight events and the decay-in-flight events.

Fig. 3.3(b) shows the distribution of the χ^2 probability when the switch of the decay-in-flight is turned on. The χ^2 probabilities for the events which do not decay until arriving at the SVTX are plotted. One can see the peak at $prob(\chi^2) = 0$ which corresponds to a large χ^2

(see Eq. 3.9). Such events are the decay-in-flight kaons. Fig. 3.4(a) and (b) show the spectra of the reconstructed mass-squared for the events with $prob(\chi^2) > 0.02$ and $prob(\chi^2) < 0.02$. The reconstructed mass-squared in Fig. 3.4(a) is consistent with the PDG value (Particle Data group) of the kaon mass-squared, 0.2437 GeV. On the other hand, the events in Fig. 3.4(b) are pions or muons from the decayed kaons. We choose the good events to select tracks with $prob(\chi^2) > 0.02$.

3.3 Measurement of time of flight

Particle identification is made by measuring a time of flight (TOF). A time of flight is given as

$$TOF = T_{stop} - T_{start}, \tag{3.21}$$

where T_{start} is the start time and T_{stop} is the stop time. The TOF counters were used to determine the stop time T_{stop}. Two methods were employed to determine the start time. In the first method (case I), the RF signals from the 8-GeV storage ring are used to give the start time. The time resolution is good due to the narrow width (12 ps) of the RF signal. In the second method (case II), the trigger counter (TRG) is used to give the start time. The time resolution is worse than that of the RF signal and depends on the pulse height of the TRG. Although the RF signal should be used, the electronics used for a record of the RF signal was out of order from the middle of the experiment. Therefore, we used the RF signal for about a half of data and used the TRG for the other half of data as flows:

$$TOF = T_{TOF} - T_{RF} \quad \text{in the case of I} \tag{3.22a}$$

$$TOF = T_{TOF} - T_{TRG} \quad \text{in the case of II,} \tag{3.22b}$$

where T_{TOF} is the stop time at the TOF wall, T_{RF} (T_{TRG}) is the start time determined by the RF signal (the TRG). When the RF signal (the TRG) is used, TOF is measured from the target (the TRG) to the TOF wall.

3.3.1 Calibration of the TOF counters

The stop time T_{TOF} is determined by averaging the TDC values from the top and bottom PMT's of a TOF counter after the pulse-height time-walk correction (slewing correction) is made. The timing of a discriminated signal (TDC) depends on a pulse height (ADC). The rising time of a output signal is earlier as a pulse height is larger. The time-walk correction and the overall timing (t_0) were obtained by using data of the e^+e^- pairs taken by the e^+e^- trigger. Since the e^+e^- pairs are ejected at forward angles, they spread out mostly in a median plane by the magnetic field in the dipole magnet as shown in Fig. 3.5. The arrival times of e^+'s or e^-'s which hit a certain TOF counter are almost the same. The flight length of the e^+e^-'s from the target to the TOF wall is about 4 m. The time-of-flights of the e^+e^-'s are ranged from 13.7 to 15.2 nsec. The e^+e^- data was taken by a Pb target with a thickness of 0.5 mm to make the contamination of the hadron events small. The Bremsstrahlung beam was used to obtain the high momentum e^+e^-'s which were needed to do the calibration in the two

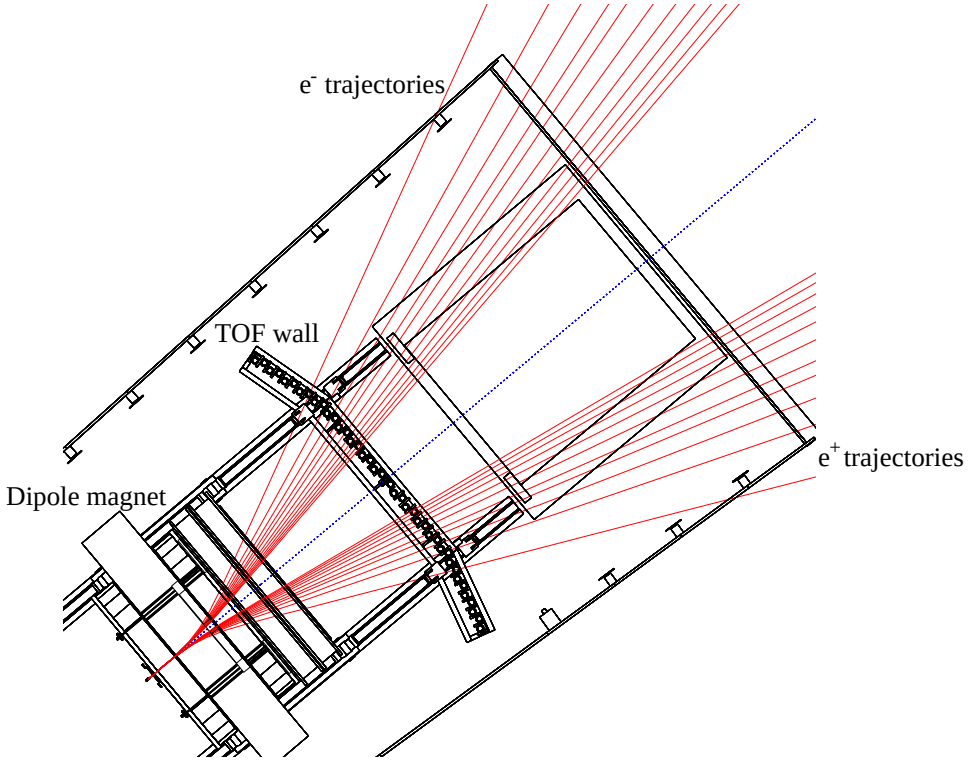

Figure 3.5: Electron and positron trajectories. The trajectories of e^+e^- pairs with the various photon energies are displayed in terms of their momentum from 0.5 to 1.5 GeV/c.

counters at the center of the TOF wall. The e^+e^-'s with above 4 GeV/c momentum can hit these two counters. In this measurement, the e^+e^- blocker was removed.

Fig. 3.6(a) shows the relation between the ADC values and the TDC values of a TOF counter for the e^+e^- data. The y-axis is the ADC values from the top PMT. The x-axis is the average TDC values given as

$$T_{no.corr.} = (\frac{TDC_t + TDC_b}{2}) \times 0.025, \tag{3.23}$$

where TDC_t (TDC_b) is the TDC value of the top (bottom) PMT. The factor of 0.025 is the time in one channel of the TDC module. One can see clearly the relation between the ADC and TDC values. The term for the time-walk correction is given by the ADC values from the top and bottom PMT's (ADC_t, ADC_b). The stop time T_{TOF} with the time-walk correction is determined as follows:

$$T_{TOF} = (\frac{TDC_t + TDC_b}{2} + \frac{A1}{\sqrt{ADC_t}} + \frac{A2}{\sqrt{ADC_b}} + B) \times 0.025, \tag{3.24}$$

where A1 and A2 are coefficients for the time-walk correction and B is the overall timing. These parameters were obtained for each TOF counter by a fitting of a function given by Eq. (3.24). In the present experiment, these parameters were A1, A2 ~ -1600. Fig. 3.6(b) shows

the relation between the ADC and the TDC after applying the time-walk correction. One can see that the relation is corrected.

The time resolution of each TOF counter was obtained for the e^+e^- events selected with the conditions of $|y| < 30$ mm and the ADC values $\sim$ MIP (the minimum ionaization peak). The time-of-flight was calculated by using the TOF wall and the RF signals as $T_{start} = T_{RF}$. The typical time resolution is 109 ps (σ) as shown in Fig. 3.7. Since the width of the RF signal is negligible compared with the resolution of a TOF counter, the time-of-flight resolution is limited only by the resolution of the TOF counters. The time resolutions of the TOF counters used in this experiment are shown in Table $A.1$ in Appendix A. The time resolution of the

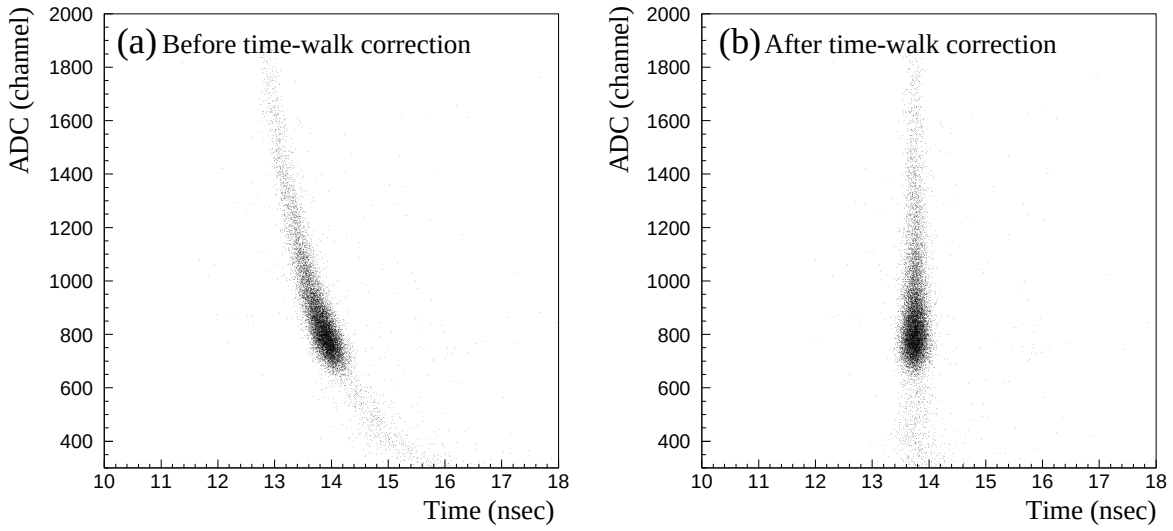

Figure 3.6: Relation between the pulse height (ADC channels) and the TDC values (nsec) of a TOF counter. (a) and (b): Scatter plots of the ADC vs. TDC before and after the time-walk correction.

TOF counter is position and pulse-height dependence. The time resolution is deteriorated by about 10% when a particle hit the sides of a TOF counter.

3.3.2 Correction of the 2 ns bunches of RF signals

The circulating electrons are bunched at every 1.966 nsec in the storage ring. The arrival time of a BCS photon at the target is synchronized with the RF signal. The RF signal has a 12 psec width associated with the width of the electron bucket. The 12 psec width can be ignored compared with the resolution of the TOF counters.

Fig. 3.8 shows the scatter plot of the ADC values of the TRG vs. the TDC values of the RF signals. Since the common start signals of the TDC modules are provided by the TRG, there is the relation between the TDC values of the RF signal and the ADC values of the TRG (the pulse-height time-walk correction). The 2 ns bunch structures are seen in Fig. 3.8.

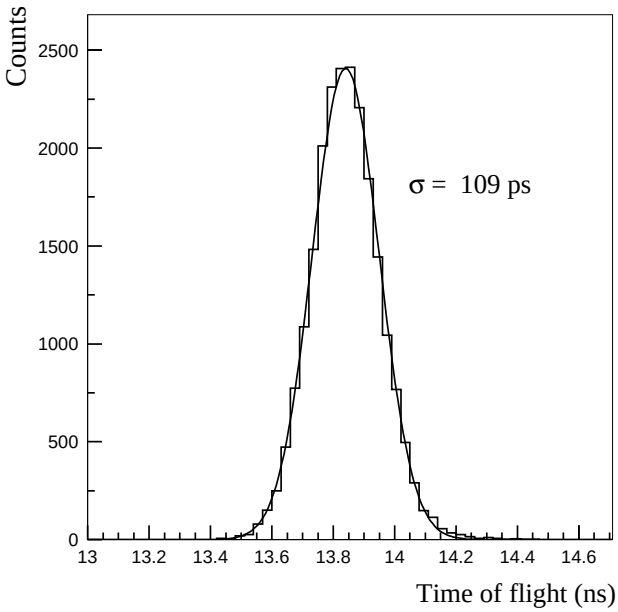

Figure 3.7: Time-of-flight of positrons which hit the # 18 TOF counter. The time resolution is 109 ps (σ).

After solving the 2 ns ambiguity, the timing of the RF signal (T_{RF}) is used as the start time to determine the time-of-flight.

How to solve 2 ns ambiguity

Fig. 3.9(a) and (b) show the TDC spectra of the RF signals before and after the time-walk correction of the TRG. The 2 nsec bunches are clearly seen after the correction in Fig. 3.9(b). The time-walk correction for the TRG is applied by using the TDC and ADC values of the TRG as follows:

$$\begin{aligned} T_{RF}^{corr} &= \\ TDC_{RF} &+ \frac{1}{2}(TDC_t + TDC_b + \frac{A1}{\sqrt{ADC_t}} + \frac{A2}{\sqrt{ADC_b}} + \frac{A3}{ADC_t} + \frac{A4}{ADC_b}) \end{aligned} \tag{3.25}$$

where ADC_t and ADC_b (TDC_t and TDC_b) is the ADC (TDC) values from the top and bottom PMT's of the TRG, and A1, A2, A3 and A4 are coefficients for the time-walk correction. These coefficients were obtained by a fitting to the TDC and ADC values in Fig. 3.8. In the present experiment, they were obtained to be A1 = −1912, A2 = −2057, A3 = 3534 and A4 = 6420. After the time-walk correction, each of peaks of the 2 nsec bunches of the RF signals in Fig. 3.9(b) is fitted by the Gaussian function. The 2 nsec ambiguity is solved by using these peak positions. There is a possibility that the 2 nsec ambiguity is not correctly solved for a part of the events in the boundary regions of the 2 nsec bunches. These events are about

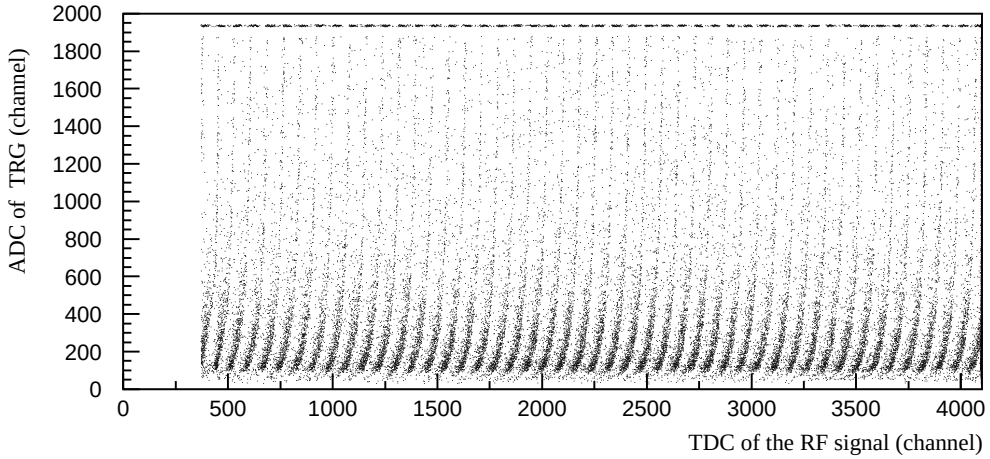

Figure 3.8: Scatter plot of the ADC of the TRG vs. the TDC of the RF signal.

1%. After solving the 2 nsec ambiguity, the TDC value of the RF signal (not including the time-walk correction of the TRG) is used as the start time T_{RF}.

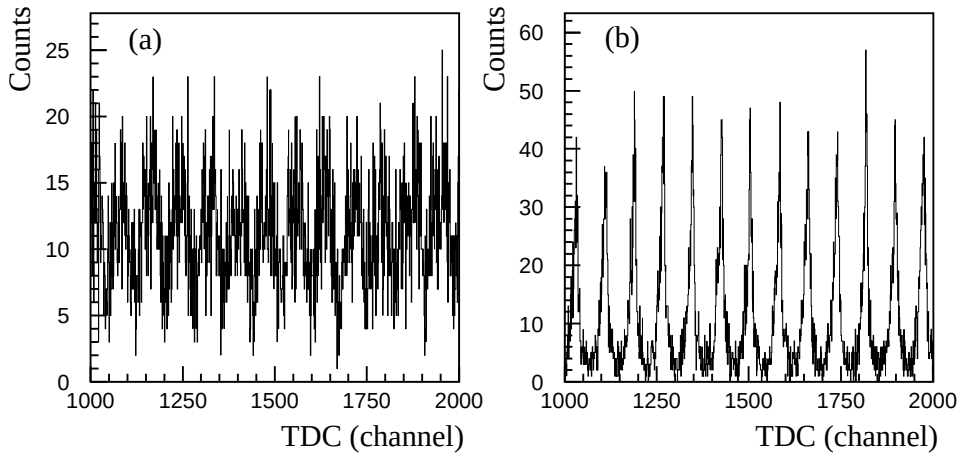

Figure 3.9: TDC spectra of the RF signal. (a) and (b): Before and after the time-walk correction. The peak width of each 2 nsec bunch is due to the time resolution of the TRG.

3.3.3 Calibration of the TRG

The TRG was used instead of the RF signals as the start time in the case II. The start times are determined by averaging the TDC values from the top and bottom PMT's of the

TRG after applying the time-walk correction. The start time T_{TRG} is given as

$$T_{TRG} = \frac{1}{2}(TDC_t + TDC_b + \frac{A1}{\sqrt{ADC_t}} + \frac{A2}{\sqrt{ADC_b}} + \frac{A3}{ADC_t} + \frac{A4}{ADC_b}) \quad (3.26)$$

where A1, A2, A3 and A4 are the same coefficients for the time-walk correction as Eq. (3.25). The time resolution of the TRG is typically 180 ps. The time resolution depends on the pulse height. Moreover, there is a problem due to a multi-hit in the TRG. When more than two particles hit the TRG, the time-walk correction can't be corrected because the relation between the energy deposit (ADC value) and the timing (TDC value) as Eq. (3.26) are not applicable. This multi-hits problem make the time resolution worse.

3.3.4 Effective velocities and attenuation lengths of the TOF counters

The effective attenuation length and effective velocity for photons (scintillation lights) in each TOF counter is obtained by using hadron events. These values are used to determine the hit position in the y-direction, and the energy deposition of charged particles at TOF counters. Information on the hit positions in the TOF counters is used to find the correct combination between a hit at a TOF counter and a track associated with the hit in the mass reconstruction. The analysis of the mass reconstruction is described in the next section.

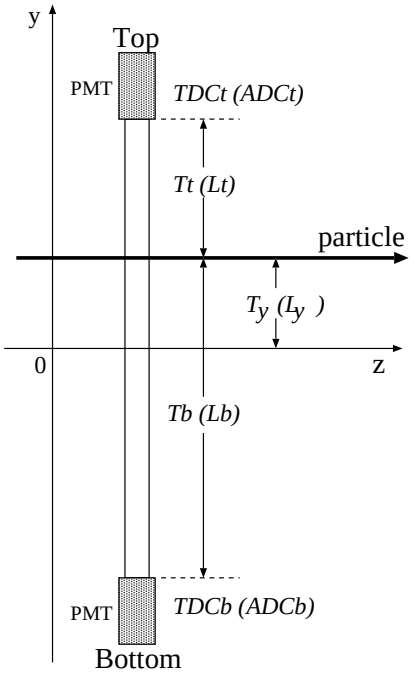

Tt : Time from a hit position to PMTt
Tb : Time from a hit position to PMTb
Ty : Time from y=0 to a hit position

$$Ty = \frac{Tb - Tt}{2}$$

Lt : Length from a hit position to PMTt
Lb : Length from a hit position to PMTb
Ly : Length from y=0 to a hit position

$$Ly = \frac{Lb - Lt}{2}$$

Figure 3.10: Schematic explanation for the method to calculate the effective velocities and attenuation lengths of the TOF counters.

Fig. 3.10 shows a scheme to calculate the effective velocities and attenuation lengths. T_y is the travel time of scintillation lights from the center of a counter (y=0) to the hit position of a charged particle. It is given by the time difference of the TDC values from the top and bottom PMT's as

$$T_y = (\frac{TDC_b - TDC_t}{2} + \frac{A1}{\sqrt{ADC_b}} - \frac{A2}{\sqrt{ADC_t}} + B) \times 0.025, \quad (3.27)$$

where A1 and A2 are the same coefficients as ones in Eq. (3.24) and B is an offset parameter. The time-walk correction is made in Eq. (3.27).

By using the effective velocity v_{eff} and T_y, the y-hit position y_{tdc} is given by

$$y_{tdc} = v_{eff} \cdot T_y. \quad (3.28)$$

The effective velocity v_{eff} was obtained by using the hit position y_{trk} determined by the tracking analysis. Fig. 3.11(a) shows the scatter plot of y_{trk} vs. T_y. The solid line is the result of a fitting by a linear function. In this fitting procedure, the effective velocity v_{eff} is determined as the slope. The effective velocity was obtained for each TOF counter. The typical value of the effective velocities is 14×10^9 cm/sec (about 47% of the speed of light). Fig. 3.11(b) shows the distribution of y_{trk} - y_{tdc}. The peak is fitted by the Gaussian function. The resolution is about 18 mm (σ).

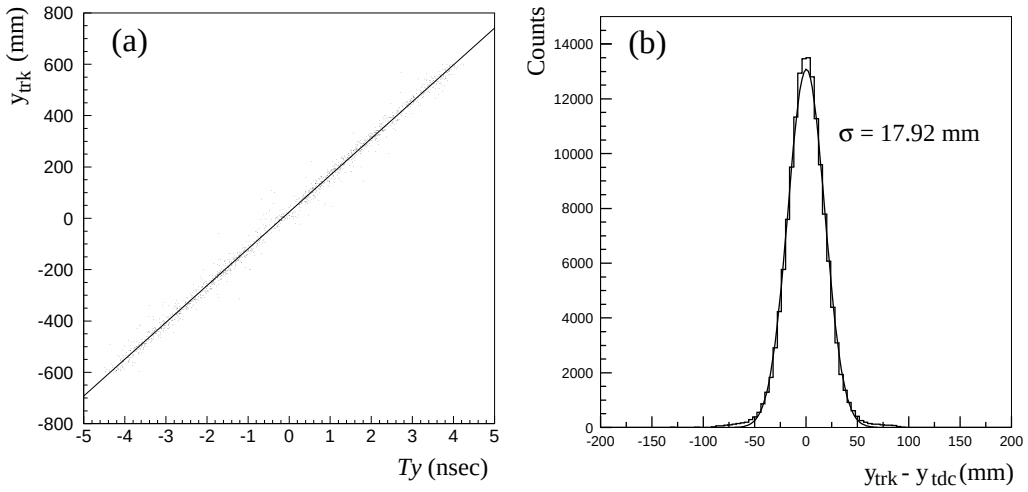

Figure 3.11: (a) Scatter plot of the y-position y_{trk} vs. the time difference T_y. The solid line is the result of a fitting by a linear function. (b) Distribution of y_{trk} - y_{tdc}. The solid line is the result of a fitting by the Gaussian function.

The ADC values from the top and bottom PMT's can be described with the effective attenuation length L_{att} as

$$ADC_t = A_t e^{-\frac{Lt}{L_{att}}} \quad (3.29a)$$

$$ADC_b = A_b e^{-\frac{Lb}{L_{att}}} \quad (3.29b)$$

where A_t and A_b are proportional to the energy deposition at the hit position. The y-hit position y_{adc} is written with these ADC values from the top and bottom PMT's as

$$\begin{aligned} y_{adc} &= L_y = \frac{L_b - L_t}{2} \\ &= \frac{L_{att}}{2} \cdot log(\frac{ADC_t}{ADC_b}) + B, \qquad (3.30a) \\ B &= \frac{L_{att}}{2} \cdot log(\frac{A_t}{A_b}), \qquad (3.30b) \end{aligned}$$

(see Fig. 3.10). Fig. 3.12(a) shows the scatter plot of y_{trk} vs. $\frac{1}{2}log(\frac{ADC_t}{ADC_b})$. The data points are fitted by the linear function. The solid line is the result of the fitting. In this fitting, the effective attenuation length L_{att} is determined as the slope. The typical value of the effective attenuation length is 150 cm. Fig. 3.12(b) shows the distribution of y_{trk} - y_{adc}. The peak is fitted by the Gaussian function. The resolution is about 44 mm (σ). The resolution of the y-position determined by the TDC values is much better than one determined by the ADC values. The time difference y_{tdc} obtained by the TDC values is used to find a correct combination of a track and a hit at a TOF counter.

The effective velocities, attenuation lengths and the resolution of y_{trk} - y_{tdc} in each counter were obtained. These values are summarized in Table *A*.1 in Appendix A.

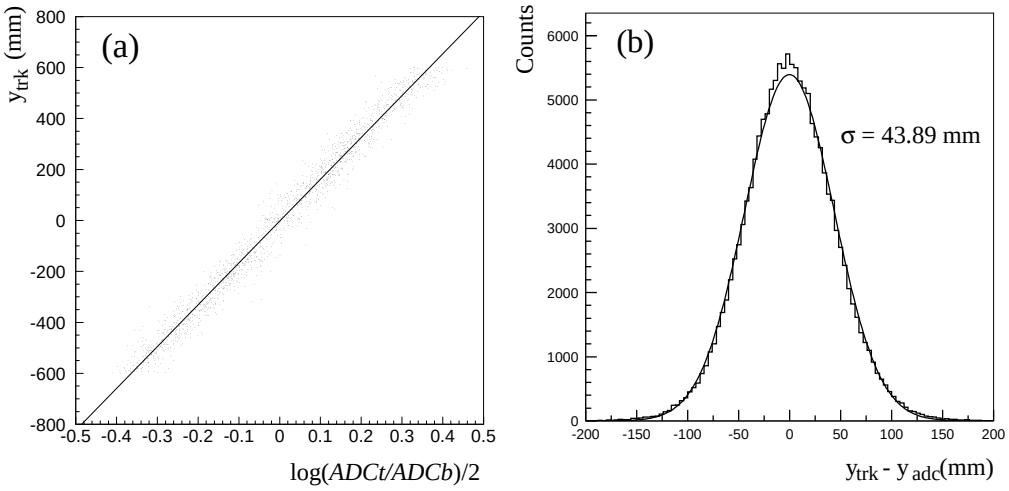

Figure 3.12: (a) Scatter plot of y_{trk} vs. $\frac{1}{2}log(\frac{ADC_t}{ADC_b})$. (b) Distribution of y_{trk} - y_{adc}.

3.4 Reconstruction of mass

The mass of a charged particle (M) is calculated with the momentum (p), the path length (L) and the time-of-flight (TOF) as

$$M^2 = p^2 \cdot (\frac{1}{\beta^2} - 1), \tag{3.31a}$$

$$\beta = \frac{L}{TOF \cdot c}, \tag{3.31b}$$

where c is the speed of light. The path length and the time-of-flight are from the target (the trigger counter) to the TOF wall when the RF signal (the trigger counter) is used to determine the start timing. Since the momentum and the path length are determined in the tracking analysis and the time-of-flight is determined in the TOF analysis, a correct combination between a track and a hit in the TOF wall should be found to reconstruct masses. The correct combinations are found by comparing the hit positions at the TOF wall obtained in the tracking analysis and in the TOF analysis. A trajectory is extrapolated from DC3 to the TOF wall with the Runge Kutta method. The hit position of the track in the TOF wall is predicted. The predicted y-position y_{trk} and the counter number id_{trk} are compared with the positions, y_{tof} and id_{tof}, obtained in the TOF analysis. The y-hit position y_{tof} is a position, y_{tdc}, determined by the TDC values in Eq. (3.28). The correct combinations between a track and a hit at the TOF wall are found under the following conditions in the LEPSana program.

$$\left|\mathrm{y}_{trk} - \mathrm{y}_{tof}\right| < 90\ (200)\ \mathrm{mm}, \tag{3.32a}$$

$$|\mathrm{id}_{trk} - \mathrm{id}_{tof}| \leq 2\ (3). \tag{3.32b}$$

( ): DC2-TOF tracking.

The critical value of 90 mm corresponds to 5σ of the resolution as shown in Fig. 3.11.

The mass is calculated for the correct combinations by using Eq.(3.31). In this experiment, the TOF resolution changed twice due to a problem of the electronics for the RF signals. The data sets are summarized in Table 3.1. The quantity of data in each data set, the average resolution of a time-of-flight and the counter to give the start time are described. We used the

Table 3.1: Summary of data sets.

Data set	Quantity of data	TOF resolution	Start time
I	26.3%	123 ps	RF
II	21.1%	175 ps	RF
III	52.6%	180 ps	TRG

RF signals to determine the start time in the data set I and II. The time resolution got worse between the data set I and II due to the problem of the RF signals. We used the TRG in the data set III because the electronics for the RF signals deteriorated and thus the time resolution of the TRG was better than that of the RF signals. We evaluated the particle identification (PID) in each period.

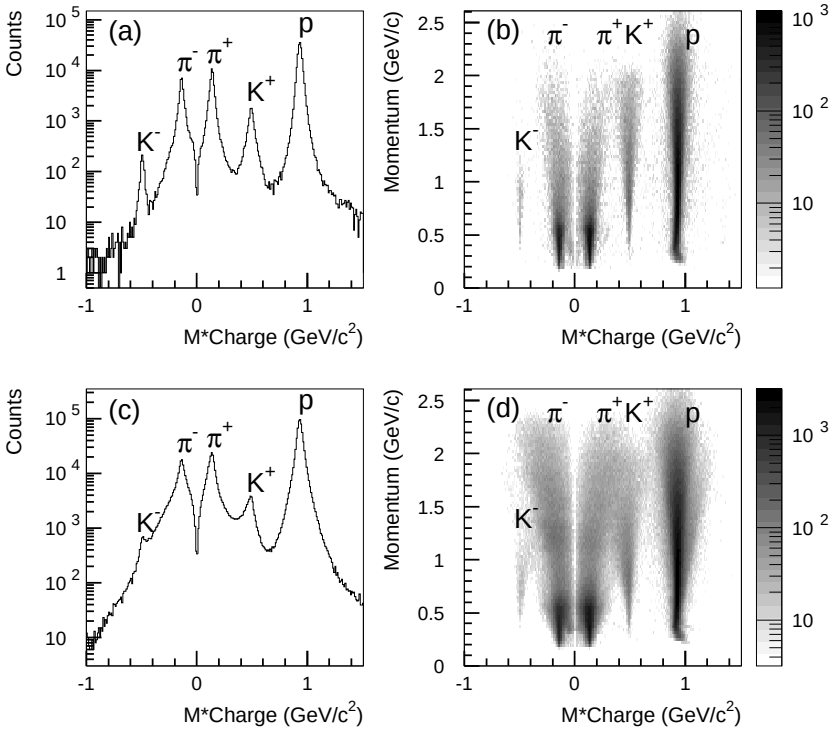

Figure 3.13: Mass plots with the liquid hydrogen target. (a) and (b): The mass spectrum and the scatter plot of momentum vs. mass in the data set I. (c) and (d): The mass spectrum and the scatter plot of momentum vs. mass obtained in the data set III.

Fig. 3.13 shows the mass spectra of photo-reactions obtained with the liquid hydrogen target. Fig. 3.13(a) and (b) show the mass spectrum and the scatter plot of momentum vs. mass obtained in the data set I. The peaks and loci corresponding to pions, kaons and protons are clearly identified. Fig. 3.13(c) and (d) show the mass plots obtained in the data set III. One can see that the mass resolution with the TRG is worse than that obtained with the RF signals. The bad mass resolution is not only due to the bad time resolution of the TRG comparing with the RF signals, but also a multi-hit in the TRG. When more than two particles hit the TRG, the time-walk correction can't be made because the relation between the energy deposit (ADC value) and the timing (TDC value) as Eq. (3.26) are not applicable. This multi-hit problem makes the mass resolution worse and causes that the mass peaks are not symmetric.

One can see the dark loci for the π^+ and π^- events below 0.6 GeV/c momentum in Fig. 3.13(b) and (d). The Čerenkov threshold of the aerogel counter (AC) is 0.57 GeV/c for pions. Pions with below 0.57 GeV/c momenta are not rejected but most of the π events with above 0.57 GeV/c momenta are rejected in the trigger level with the veto signal from the AC. A part of pions above the Čerenkov threshold still exits due to the insufficient efficiency of the AC for pions. The efficiency of the AC is low for pions compared with the e^+e^- events,

because both e^+ and e^- can pass through the AC while a single pion passes through the AC in the most cases. Moreover, the number of Čerenkov lights increases with increasing the velocity β. The value of the velocity of pions is smaller than that of the e^+e^- events.

The resolution of the reconstructed mass-squared (M^2) depends on the momentum as shown in Fig. 3.14. The data points in Fig. 3.14(a), (b) and (c) indicate the momentum dependences of the M^2 resolutions for protons, kaons and pions obtained in the data set I. The mass resolution

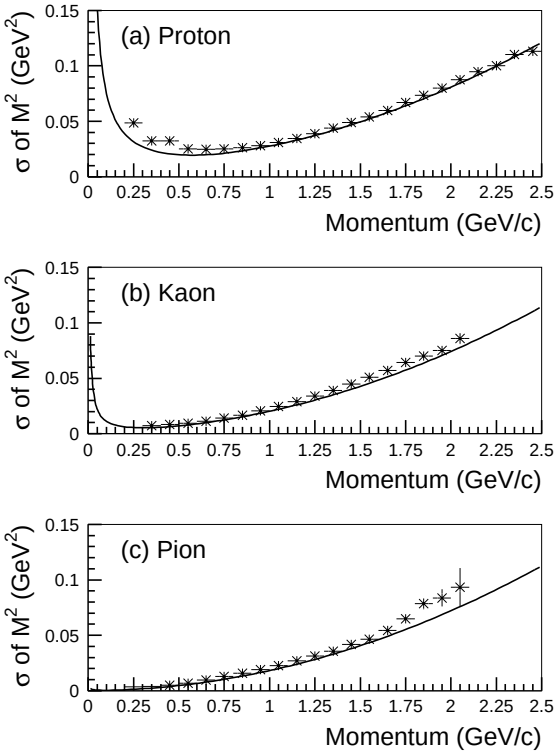

Figure 3.14: Momentum dependence of the M^2 resolution for pion (a), kaon (b) and proton (c) events in the data set I. The lines are the results of fitting using the function given by Eq. (3.33) with $a_3 = 0.123$ ns.

gets worse as the momentum increases except for the low momentum protons. We used the following parameterization for the mass resolution:

$$\sigma^2_{M^2} = 4M^4\left(1+\left(\frac{M}{p}\right)^2\right)a_1^2 + 4M^4p^2a_2^2 + 4p^2\left(p^2+M^2\right)\left(\frac{c}{L}a_3\right)^2, \qquad (3.33)$$

where a_1, a_2 and a_3 are parameters, M is the nominal value (the PDG value) of the pion, kaon and proton mass, and c is the speed of light. The path length (L) is set to 4100 mm which is the typical path length of charged particles in the LEPS spectrometer. The momentum resolution can be evaluated as

$$\left(\frac{\sigma_p}{p}\right)^2 = \frac{a_1^2}{\beta^2} + p^2a_2^2. \qquad (3.34)$$

These two terms correspond to the first and second terms in Eq. (3.33). The first term is the contribution from multiple scattering. The second term is the contribution from the resolution of the spectrometer. The last term in Eq. (3.33) is the contribution from the TOF resolution. The parameter a_3 is the TOF resolution in a unit of ns. The second and last terms increase as the momentum increases while the first term is proportional to $1/p^2$. The effects from the resolution of the detectors (the second and last terms in Eq. (3.33)) are larger than that of multiple scattering for the high momentum protons, kaons and pions. Therefore, the mass resolution increases as the momentum increases for these particles. On the other hand, the mass resolution of the low momentum protons ($p < 0.5$ GeV/c) and kaons ($p < 0.1$ GeV/c) increases as the decreasing of the momentum as shown in Fig. 3.14 because the effect of multiple scattering for the low momentum protons and kaons is larger than that of the spectrometer and the time-of-flight resolutions.

The parameters a_1 and a_2 are determined in a fitting procedure. The momentum dependence of the mass resolution was obtained by the MC simulation (called g3leps) by taking into account the effect of multiple scattering and the detector resolutions. The results of the MC simulation are fitted by the function given by Eq. (3.33). The parameters of the first and the second terms were determined as $a_1 = 0.00458$ and $a_2 = 0.00323$.

The lines in Fig. 3.14 are the functions given by Eq. (3.33) with $a_3 = 0.123$ which is the average value of the time resolution in the data set I. The measured mass resolution is reproduced by the parameterization function Eq. (3.33) as shown in Fig. 3.14. The mass resolution in the data set II is reproduced by using the function with $a_3 = 0.175$. The parameterization function was used to determine the cut positions for the PID.

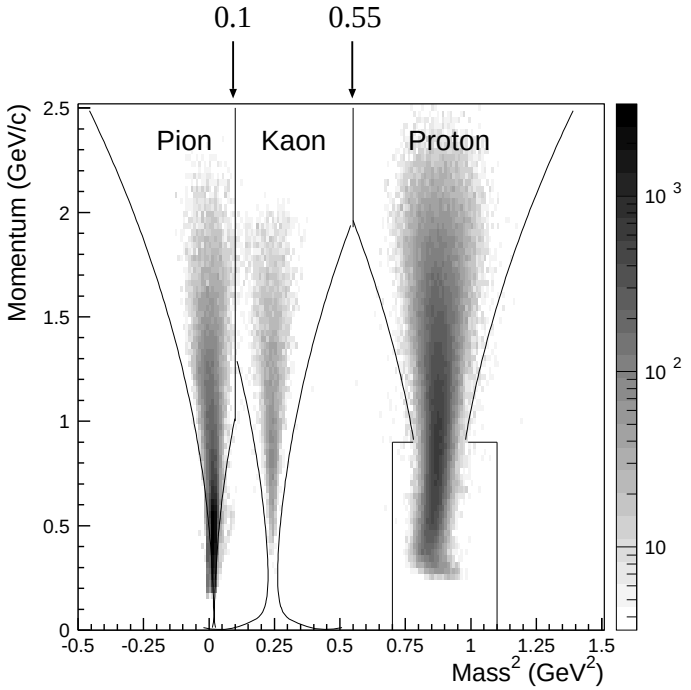

Figure 3.15: Cut positions of the PID selections of pions, kaons and protons in the scatter plot of momentum vs. mass-squared. The data points are for the data set I.

The momentum-dependent cut positions in the mass-squared distribution were used to select kaons. We used the same cut positions for each of the three data sets. Fig. 3.15 shows the cut positions for the PID in the scatter plot of the momentum vs. the mass-squared. The cut positions are used to select kaon events in the present analyses of the $p(\gamma,K^+)\Lambda$ and $p(\gamma,K^+)\Sigma^0$ reaction channels. The curved lines in Fig. 3.15 correspond to $M^2 \pm 3\sigma_{M^2}$ calculated by Eq. (3.33) with $a_3 = 0.175$ ns which is the average TOF resolution in the data set II. The lines are the cut positions (boundaries) for the PID which are used for the present experiment. The boundary between pions (protons) and kaons is set to 0.1 GeV^2 (0.55 GeV^2). The boundary of low momentum protons (p $<$ 0.9 GeV/c) is set to 0.7 GeV^2 $< M^2 <$ 1.1 GeV^2 because the mass resolution gets worse in the lower momentum side and there is few background events in the region.

3.5 Reconstruction of vertex points

Information on the reaction vertex point is important to select events produced at the target. The momentum vector and positions at the SVTX are obtained in the track fitting procedure. The vertices of particles are calculated by extrapolating the trajectory from the SVTX to the vertex point. Since the magnetic field of the dipole magnet is not negligible at the place between the target and the SVTX, the tracking is performed in the magnetic field by using the Runge-Kutta method.

Fig. 3.16 shows the distribution of the reaction vertex in the z direction. Fig. 3.16(a) is for single-track events and (b) is for double-track events. The vertex point of double-track events is determined as the cross point of two tracks, in which case no assumption on the hit position of the photon at the target is needed. However, the vertex point of single-track events is determined as the closest distance between the track and the z axis (the beam axis) because the photon beam has the size of $\sigma_x \sim 5$ mm and $\sigma_y \sim 3$ mm at the target position and we don't have information on the production point. Therefore, the vertices of double-track events are determined much more precisely than the ones of single-track events as shown in Fig. 3.16. The locations of the liquid hydrogen target (LH_2) and the trigger counter (TRG) can be recognized in both the figures. The liquid hydrogen target (LH_2) with a thickness of 56 mm was placed at z = -952 mm. The trigger counter (TRG) with a thickness of 5 mm was placed at z = -855 mm. The locations of the aerogel Čerenkov counter (AC) and the SVTX can also be recognized in Fig. 3.16(b).

The beam profile of the BCS photon is different for the horizontal polarization and vertical polarization. The cross section of the backward-Compton-scattering process with the polarized laser photons is defined as

$$\frac{d\sigma}{d\Omega} = \frac{d\sigma}{d\Omega}_{unpol}[1 + tS_{lin}Q_{lin}\cos(2\phi) + P_yS_{circ}Q_{circ}\cos(2\phi)], \tag{3.35}$$

where S_{lin} (S_{circ}) is the degree of the linear (circular) polarization ($S_{lin}^2 + S_{circ}^2 = 1$), Q_{lin} and Q_{circ} are kinematical factors, P_y is the transverse polarization of the incident electron beam, ϕ is the azimuthal angle of the BCS photon and t = -1 ($+1$) for the horizontal (vertical) polarization. Because of $S_{lin} = 1$ and $S_{circ} = 0$ in the present experiment, the function is

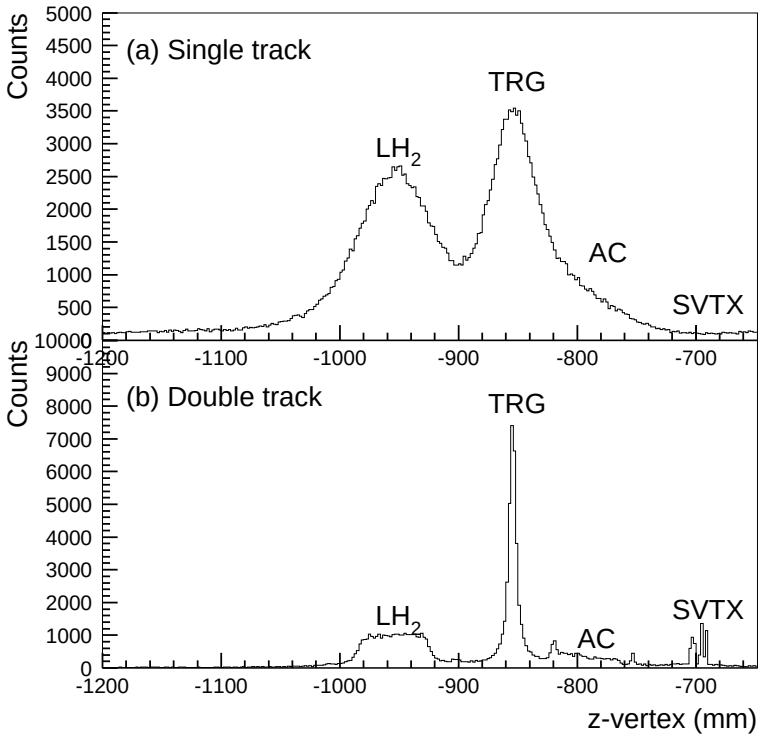

Figure 3.16: Distribution of the reaction vertex in the z direction for (a) z-vertex of single track events and (b) z-vertex of double track events.

rewritten as

$$\frac{d\sigma}{d\Omega} = \frac{d\sigma}{d\Omega}_{unpol}[1 + tQ_{lin}\cos(2\phi)]. \tag{3.36}$$

The second term causes the beam profile to be different for the horizontal polarization and vertical polarization.

Fig. 3.17 shows the distributions in the x and y-vertex for the horizontal polarization and vertical polarization. The solid line is the vertex distribution obtained from the real data. The dashed line is the result of the MC simulation program (g3leps) in which the beam simulator of Eq. (3.36) is included. The distributions are for double-track events in the energy range 1.5 GeV $< E_\gamma <$ 1.8 GeV. The difference can be seen more clearly at low energies. The difference is smeared out in $E_\gamma > 1.8$ GeV because the BCS photons are scattered in a narrower cone at high energies. The large effect of the second term in Eq. (3.36) is seen in the y-direction compared with that seen in the x-direction because the divergence/dispersion of the electron beam is stronger in the x-direction than in the y-direction. The small bump at x = -17 mm is seen in the real data. This bump is due to the events from the copper cell used for the target.

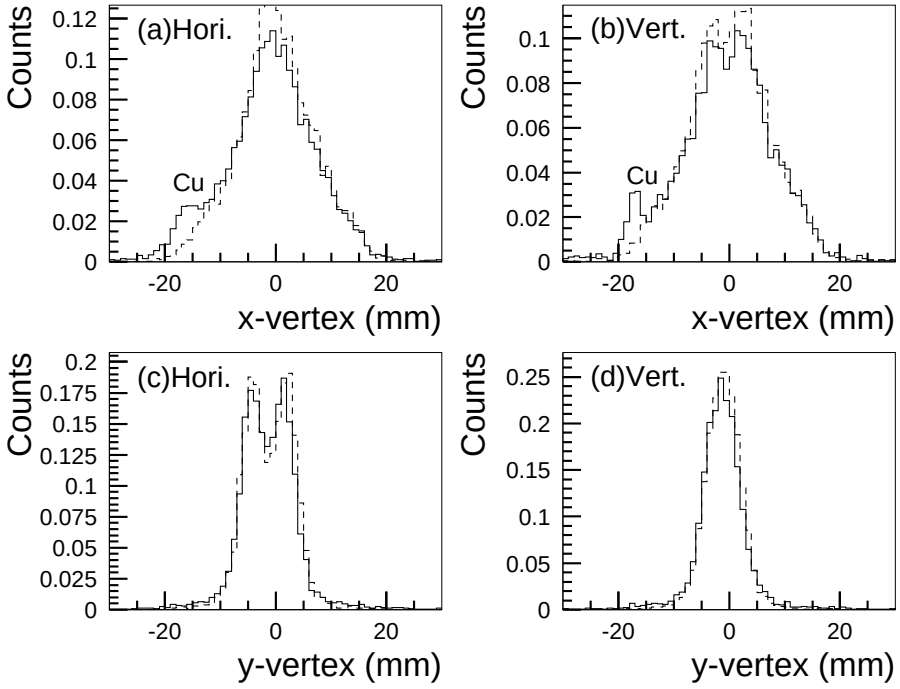

Figure 3.17: Vertex distributions for the horizontally and vertically polarized photons. The solid histograms are the vertex distribution obtained from the real data. The dashed histograms are the results obtained by the MC simulation (g3leps). (a) and (b): the distribution of the x-vertex for the horizontal polarization and vertical polarization. (c) and (d): the distribution of the y-vertex for the horizontal polarization and vertical polarization. Small peaks denoted as Cu are due to the background events from the frame of the target cell made by Cu.

The vertex point for single-track events is determined by using a weighted average of the intersections of the track and the beam axis in the horizontal and vertical directions instead of simply using the closest distance point between the track and the beam axis. The resolution of the vertex point for single-track events is improved by this method. After the vertex points v_x and v_y in the x-z plane and in the y-z plan are obtained, the vertex point is determined with the weights w_x and w_y in the x and y-direction as

$$v = \frac{w_x v_x + w_y v_y}{w_x + w_y}. \tag{3.37}$$

If the track goes in the y-z plane, the tracking information in the horizontal direction is no relevant to the determination of the track position and is thus ignored. Because the beam spot is wider in the x-direction than in the y-direction as shown in Fig. 3.17, the following weight

is applied in the tracking analysis to determine the vertex point:

$$w_y/w_x = 8tan^2\phi, \tag{3.38}$$

where ϕ is the azimuthal angle of the track and w_x is set to 1. The factor of 8 is the best empirical value determined in the MC simulation. The weight w_y was also used together with the vertex point to remove the background events from the copper cell.

3.6 GEANT simulation

The Monte Carlo simulation program called g3leps is based on the GEANT 3.21 package [36]. The program describes the structure of the LEPS detectors, generates a given reaction channel, and simulates the response of the apparatus for the production particles. The generated events in the GEANT code are analyzed by the LEPSana in the same way as the experimental data. In g3leps, the resolutions of the SVTX, the DC's, the photon energy and the time-of-flight are modeled with Gaussian distributions by assuming the realistic values. We use the g3leps program to check the validity of the LEPSana program, to compare the results by the g3leps with the experimental data on the detector response, and to obtain the reliable acceptance of the detectors.

3.7 Event selection for the $K^+\Lambda$ and $K^+\Sigma^0$ events

The $p(\gamma,K^+)\Lambda(1116)$ and $p(\gamma,K^+)\Sigma^0(1193)$ reaction event samples should be purified by rejecting background events such as events due to particle misidentification and events produced at contaminant materials. The selections which are used to identify the $p(\gamma,K^+)\Lambda$ and $p(\gamma,K^+)\Sigma^0$ reaction events are summarized in Table 3.2.

Table 3.2: Cuts for the selection of the $p(\gamma,K^+)\Lambda$ and $p(\gamma,K^+)\Sigma^0$ reaction events.

Cut name	Purpose
Vertex cut	To select events produced at the target
Mass cut	To select K^+ events in the mass distribution
MM cut	To select $\Lambda(1116)$ and $\Sigma^0(1193)$ events in the missing mass distribution
χ^2 cut	To reject bad tracks including decay-in-flight events
e^+e^- cut	To reject accidental e^+e^- events
Tag cut	To reject background events in the tagging system

Three cuts are used to select the $p(\gamma,K^+)\Lambda$ and $p(\gamma,K^+)\Sigma^0$ reaction events. The vertex points were used to select the events produced at the liquid hydrogen target. The K^+ events are selected in the mass distribution. The missing mass (MM) cut is used to select the $\Lambda(1116)$ and $\Sigma^0(1193)$ events in the missing mass distribution.

The other three cuts are used to remove background events. Background events including the decay-in-flight events are removed by using the χ^2 probability. The e^+e^- cut is used to remove the accidental events due to the e^+e^- pair creation. The last cut is used to reject background events in the tagging system.

3.7.1 Event selection with reaction vertices

To identify the $p(\gamma,K^+)\Lambda$ and $p(\gamma,K^+)\Sigma^0$ reactions, the events produced at the liquid hydrogen target are selected. The vertex-position cut is applied to select such events. For double-track events, the selection is easy since the resolution of vertices is a few mm as shown in Fig. 3.16. However, for single-track events the resolution is much worse and strongly dependent on the track angle.

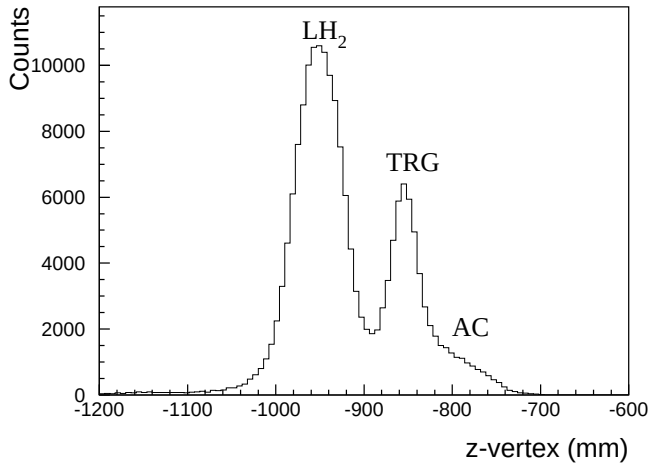

Figure 3.18: Distribution of the reaction vertex in the z direction for the $p(\gamma,K^+)\Lambda$ and $p(\gamma,K^+)\Sigma^0$ reaction events with all the cuts listed in Table 3.2 except for the vertex cut. The peaks correspond to the events produced at the liquid hydrogen target (LH_2) and the trigger counter (TRG). The shoulder part at ~ -800 mm corresponds to the events from the aerogel counter (AC).

Fig. 3.18 shows the vertex distribution in the z direction (vtz) for the $K^+\Lambda$ and $K^+\Sigma^0$ events. The peaks corresponding to the events produced at the liquid hydrogen target (LH_2) and the trigger counter (TRG) are seen in Fig. 3.18. The TRG events are reduced by applying the missing mass cut because the missing mass distribution of the TRG events is broad due to the Fermi-motion. The events produced at the target cannot be separated with the events produced at the TRG perfectly. The contamination events from the TRG would affect the results of the photon beam asymmetry of the $p(\gamma,K^+)\Lambda$ and $p(\gamma,K^+)\Sigma^0$ reactions if the photon beam asymmetry of the events in the TRG (CH) is different from that in the proton target. Therefore, we should determine the good cut-position to reduce the background events, and

estimate the background rates with the vertex cut. The cut position to select the events produced at the LH_2 target is determined as follows:

$$-1100 < \text{vtz} < -900. \tag{3.39}$$

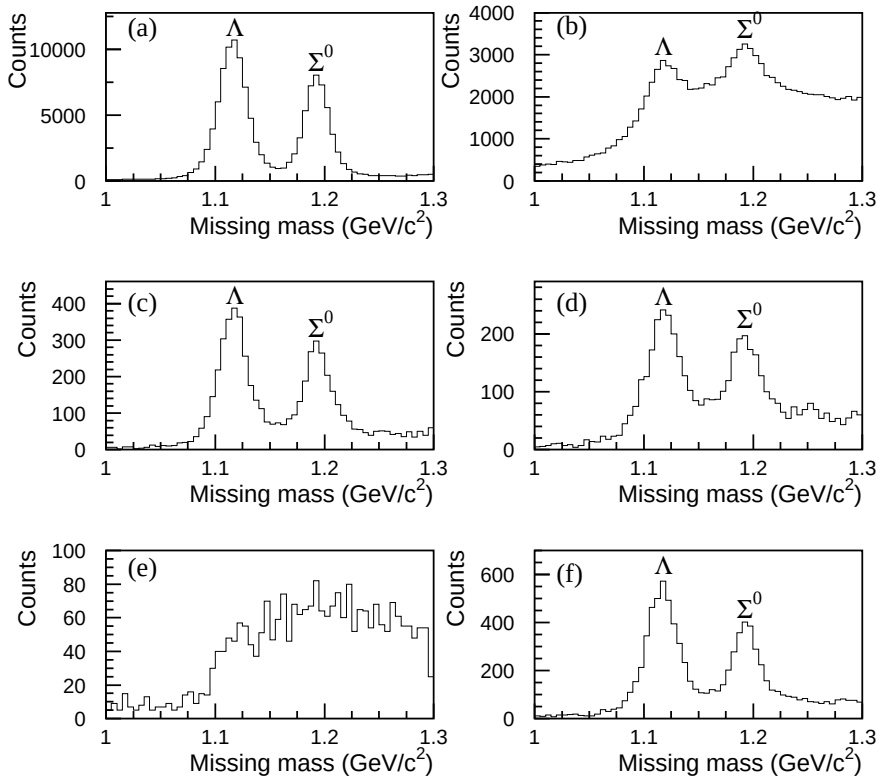

Figure 3.19: Missing mass spectra in different regions of the z-vertecies (vtz) for the events selected with all the cuts listed in Table 3.2 except for the missing mass cut and the vertex cut. (a): $-1000 <$vtz< -900, (b): $-900 <$vtz< -800, (c): $-910 <$vtz< -900, (d): $-900 <$vtz< -890, (e): $-1200 <$vtz< -1100 and (f): $-1100 <$vtz< -1000.

To see the quality of this cut position, the missing mass spectra in some different vertex regions are plotted as shown in Fig. 3.19. The events from protons in Carbon in the TRG cause the broad missing mass spectrum due to the Fermi-motion of protons inside the nucleus. Fig. 3.19(a) is the missing mass spectrum for the events by gating the LH_2 target region of $-1000 <$ vtz < -900 mm. The $\Lambda(1116)$ and $\Sigma^0(1193)$ peaks are clearly seen. Fig. 3.19(b) is the spectrum for the events in $-900 <$ vtz < -800 mm corresponding to the TRG region. The missing mass spectrum is much broader than that for the target region. The events smeared by the Fermi-motion are seen. Fig. 3.19(c) and (d) show the spectra in the regions between the target and the TRG. The resolution gets worse in the region, $-900 <$ vtz < -890. Therefore, we determine the cut position at the downstream side (the boundary to the TRG) to be vtz $= -900$.

Fig. 3.19(e) and (f) show the missing mass spectra in the upstream side of the target, $-1200 < \mathrm{vtz} < -1100$ and $-1100 < \mathrm{vtz} < -1000$. The peaks corresponding to the $\Lambda(1116)$ and $\Sigma^0(1193)$ events are clearly seen in the region $-1100 < \mathrm{vtz} < -1000$ as shown in Fig. 3.19(f). However, similar peaks are not seen in the region $-1200 <$vtz< -1100 as shown in Fig. 3.19(e). In the present experiment, the scintillation counter was placed at vtz $= -1150$ to use the charge veto counter together with the upstream-veto counter until the middle of the experiment. The photo-reaction events are also produced at this scintillation counter. Therefore the cut position at the upstream side is set to vtz $= -1100$.

Fig. 3.20(a) and (b) show the distribution of the x-vertex (vtx) and y-vertex (vty) for the single K^+ events. The vtx distribution is wider than the vty distribution because the beam size in the x-direction is larger than the size in the y-direction and the weights corresponding to the beam size are used to determine the vertex point. A bump is seen around vtx $= -17$ mm

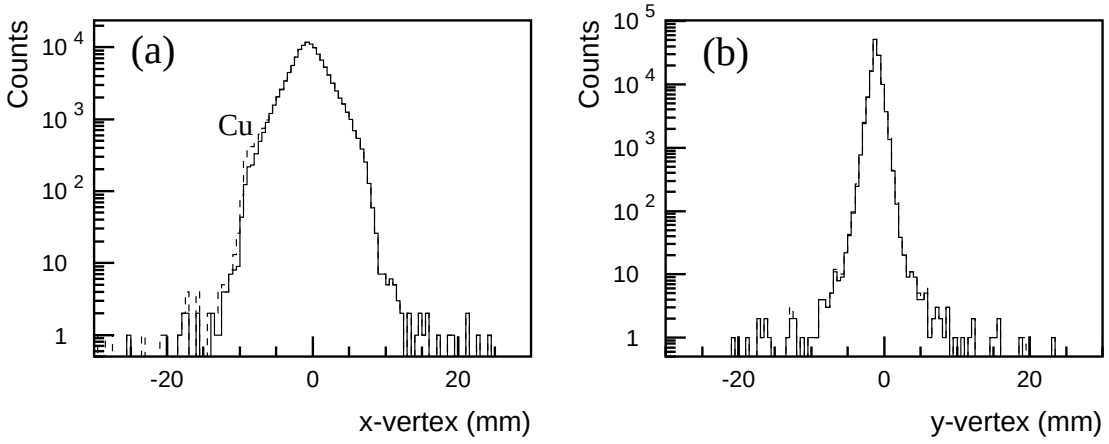

Figure 3.20: Distributions of the x and y-vertex for the $K^+\Lambda$ and $K^+\Sigma^0$ events with all cuts listed in Table 3.2. (a):x-vertex and (b):y-vertex. The dashed (solid) line shows the distributions before (after) applying the copper cut.

in the dashed line of Fig. 3.20(a). This is due to the events produced at the target cell. The target cell is made by copper and has the entrance with a diameter of 35 mm for the beam. The solid line shows the distribution after removing these copper events by using the z-vertex point and the weight w_y defined in Eq. (3.38). The cut condition to remove the copper events is empirically determined as

$$w_y > 3 \qquad \mathrm{vtz} < -950 \text{ .and. vtx (vtz=-981)} < -15 \tag{3.40a}$$

$$w_y < 3 \qquad \mathrm{vtz} < -980 \text{ .and. vtx (vtz=-981)} < -15. \tag{3.40b}$$

Most of these events are removed with this copper cut. The contamination rate of the copper events is 0.2% after applying the copper cut. The full condition of the vertex cut is Eq. (3.39) and Eq. (3.40).

The contamination rate of the events produced at the TRG with the vertex cut was estimated for the p(γ,K^+)Λ and p(γ,K^+)Σ^0 reaction events. The TRG contamination rate is obtained as a function of the K^+ scattering angle in the laboratory system because the vertex resolution depends on the scattering angle. Fig. 3.21(a) and (b) show the z-vertex distributions for the $K^+\Lambda$ and $K^+\Sigma^0$ events. The counts are normalized by the total number of events. The resolution of the z-vertex deteriorates at the large scattering angle as shown in Fig. 3.21.

The ratio of the TRG events to the LH_2 events in the $K^+\Sigma^0$ production (Fig. 3.21(b)) is about factor 2 larger than that in the $K^+\Lambda$ production (Fig. 3.21(a)). The $\Sigma^-(1197)$ events are produced at the TRG by the n(γ,K^+)Σ^- reaction. Not only the $\Sigma^0(1193)$ events but also the $\Sigma^-(1197)$ events are selected in the TRG by the missing mass cut for the selection of the Σ^0 events because the mass difference between $\Sigma^0(1193)$ and $\Sigma^-(1197)$ is small and they are not separated with the missing mass distribution. Therefore, the z-vertex distribution is different between the $K^+\Lambda$ and $K^+\Sigma^0$ production event samples. The contamination from the TRG is estimated for the $K^+\Lambda$ and $K^+\Sigma^0$ events separately because of the different distributions of the z-vertex.

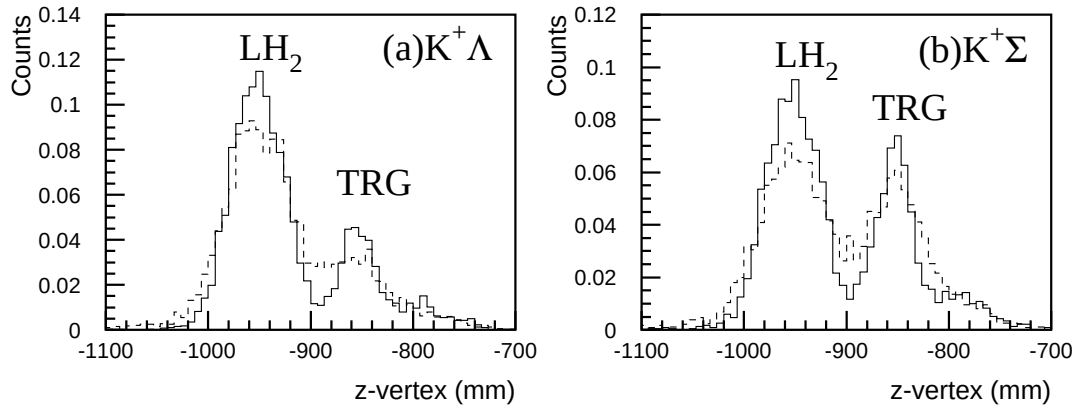

Figure 3.21: Distribution along the z-vertex for the (a) $K^+\Lambda$ and (b) $K^+\Sigma$ event samples after applying all the cuts listed in Table 3.2 except for the vertex cut. The events are for the vertically polarized photons. The solid lines are for the events with $0.96 < \cos\Theta^{K^+}_{lab} < 0.97$ ($\cos\Theta^{K^+}_{lab} \sim 15^\circ$). The dashed lines are for the events with $0.990 < \cos\Theta^{K^+}_{lab} < 0.995$ ($\cos\Theta^{K^+}_{lab} \sim 7^\circ$).

Furthermore, the z-vertex distribution is different for the horizontally polarized photons and for the vertically polarized photons because of the difference of the beam profile as shown in Fig. 3.17. The vertex resolution for the horizontal polarization is worse than that for the vertical polarization. Therefore, the contamination rate of the TRG events was estimated for the horizontally and vertically polarized photons separately.

The z-vertex distribution is not the Gaussian shape and not symmetric especially at the forward angles. The Monte Carlo simulation (g3leps) including information on the beam profile is used to estimate the contamination rate of the events produced at the TRG.

Fig. 3.22(a) and (b) show the TRG contamination rate as a function of $\cos\Theta_{lab}^{K^+}$ for the $K^+\Lambda$ and $K^+\Sigma^0$ events. The contamination rate for the horizontal polarization (solid circles) is larger than for the vertical polarization (open circles). The rate is less than 1% at $\cos\Theta_{lab}^{K^+} < 0.9975$ ($\Theta_{lab}^{K^+} > 4°$). However it is much larger at the very forward angles and is about 20% for the $K^+\Sigma^0$ reaction.

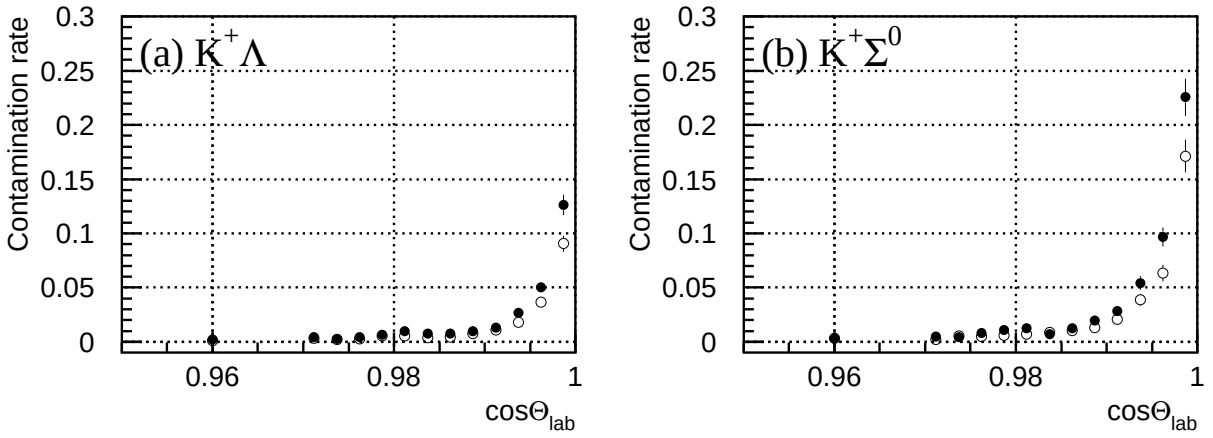

Figure 3.22: Contamination rate of the TRG events inside the target region with the vertex cut as a function of $\cos\Theta_{lab}^{K^+}$ for (a) $K^+\Lambda$ and (b) $K^+\Sigma^0$ events. The solid circles are for the horizontally polarized photon beam and the open circles are for the vertically polarized photon beam.

3.7.2 Event selection with the mass distribution

The K^+ events are selected with the charge and the mass obtained in the tracking analysis to identify the $p(\gamma,K^+)\Lambda$ and $p(\gamma,K^+)\Sigma^0$ reactions. The charge is required to be +1. The kaon events are selected by using the mass-squared distribution. The cut position for the kaon selection was determined in the mass-squared distribution as shown in Fig. 3.15.

The acceptance of the K^+ events, and the π^+ and proton contamination rates with the mass cut are estimated for the $p(\gamma,K^+)\Lambda(1116)$ and $p(\gamma,K^+)\Sigma^0(1193)$ reaction events separately because these values depend on the reaction modes. Since the mass distributions are different for the data set I, II and III in Table 3.1 due to the different mass resolutions, these values are obtained in each data set. The total acceptance and contaminations during all the runs are calculated with the photon-yield weights as described in Table 3.1.

Fig. 3.23(a) and (b) show the mass-squared spectrum and the scatter plot of the momentum vs. the mass-squared for the $K^+\Lambda$ and $K^+\Sigma^0$ events. The ratio of the π^+/proton events to

the K^+ events are different for the $K^+\Lambda$ (solid line) and $K^+\Sigma^0$ (dashed line) reaction events as shown in Fig. 3.23(a). The momentum range is limited to be from 0.8 GeV/c to 2.2 GeV/c by selecting the Λ and Σ^0 events with the missing mass (MM) cut as shown in Fig. 3.23(b). These events are used to obtain the K^+ acceptance and the π^+ and proton contamination rates.

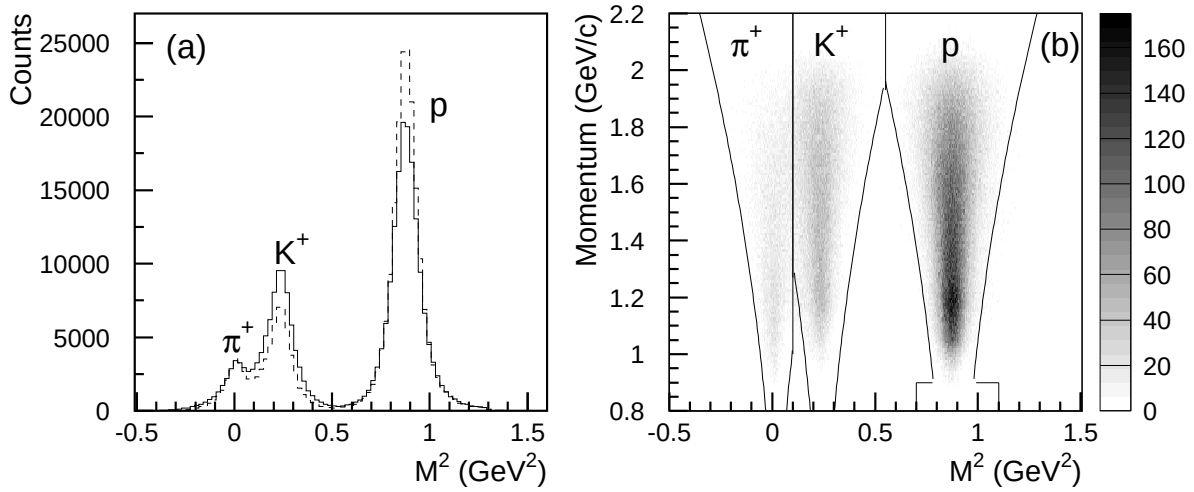

Figure 3.23: Mass plots for the events with all the cuts listed in Table 3.2 except for the mass cut. Both the $\Lambda(1116)$ and $\Sigma^0(1193)$ events are plotted for all the data sets I, II and III. (a): M^2 spectrum. The solid (dashed) line is for the $K^+\Lambda$ ($K^+\Sigma^0$) events. (b): Scatter plot of momentum vs. M^2 for both reactions. The solid lines are boundaries of the mass cut for pions, kaons and protons which are the same as Fig. 3.15.

Fig. 3.24(a) and (b) show the K^+ acceptance by the mass cut for the $p(\gamma,K^+)\Lambda$ and $p(\gamma,K^+)\Sigma^0$ reaction events. The K^+ acceptances are obtained as a function of the K^+ momentum because the mass resolution depends on the momentum. The acceptance decreases as the momentum is higher because the mass resolution is worse at the high momentum. The closed circles, squares and triangles are for the data set I, II and III, respectively. The K^+ acceptance values for the data set I and II are determined assuming that the mass distribution is the Gaussian shape in each momentum bin. Therefore, these values are the same for the $\Lambda(1116)$ and $\Sigma^0(1193)$ events. On the other hand, the acceptance depends on the reaction channels for the data set III as shown in Fig. 3.24 because the response of the trigger counter (TRG) is different for the different reaction modes due to the multi-hit problem in the TRG. The mass distribution is not symmetric and is not described by the Gaussian shape for the data set III. The acceptance and also the contamination rates are estimated by comparing the mass distributions obtained by the RF signals and the TRG by using the data set I. The total acceptances are calculated by combining all the data sets with the photon-yield weight as described in Table 3.1. The open circles in Fig. 3.24 show the total acceptance values. The

K^+ events are accepted by the mass cut with more than 75% efficiency.

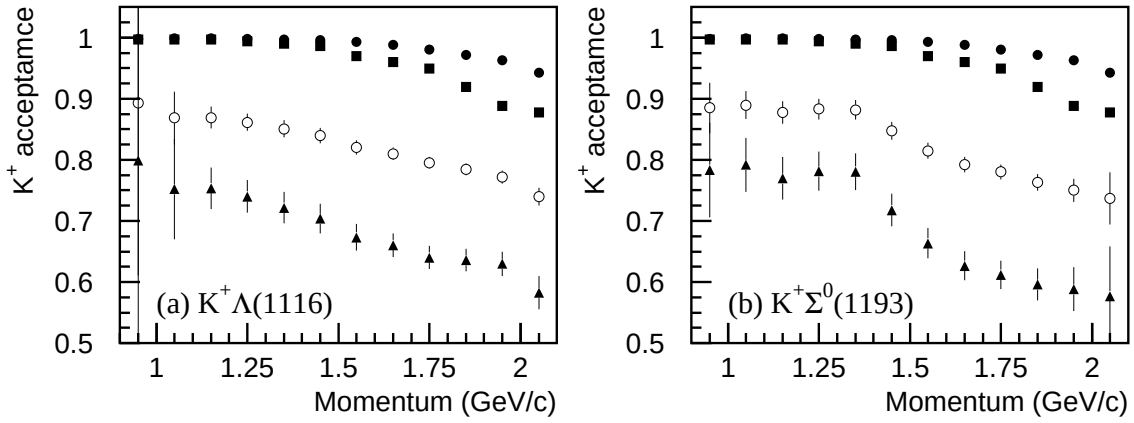

Figure 3.24: Acceptance of the K^+ events by the mass cut for (a) $\Lambda(1116)$ and (b) $\Sigma^0(1193)$ events. The closed circles, squares and triangles are the acceptance values obtained for the data set I, II and III, respectively. The open circles are the total acceptance values.

The π^+ and proton contamination rates in the K^+ event samples are also estimated in each of the $p(\gamma,K^+)\Lambda$ and $p(\gamma,K^+)\Sigma^0$ reaction channels. Fig. 3.25 shows the π^+ and proton contamination rates for the $p(\gamma,K^+)\Lambda$ and the $p(\gamma,K^+)\Sigma^0$ reaction events. The contamination rates are plotted as a function of the K^+ momentum. The values increase as the increase of the momentum. The π^+/proton contaminations for the $p(\gamma,K^+)\Sigma^0$ reaction events are larger than those for the $p(\gamma,K^+)\Lambda$ reaction events because the number of the π^+/proton events in the $K^+\Sigma^0$ events is larger than that for the $K^+\Lambda$ events as shown in Fig. 3.23(a). The π^+ contamination rates in the both reactions are less than 4% in the data set I and II when the RF signals are used to give the start time. The proton contamination rates are less than 2% for the data set I and II. The π^+/proton contaminations for the data set III are about two times larger than those for the data set I and II. The total contamination rates were calculated by using the photon-yield in each data set. The open circles are the total contamination rates of the π^+ and proton events. The contamination rates are less than 4 % except for the points at the 2.05 GeV/c momentum for the $p(\gamma,K^+)\Sigma^0$ reaction.

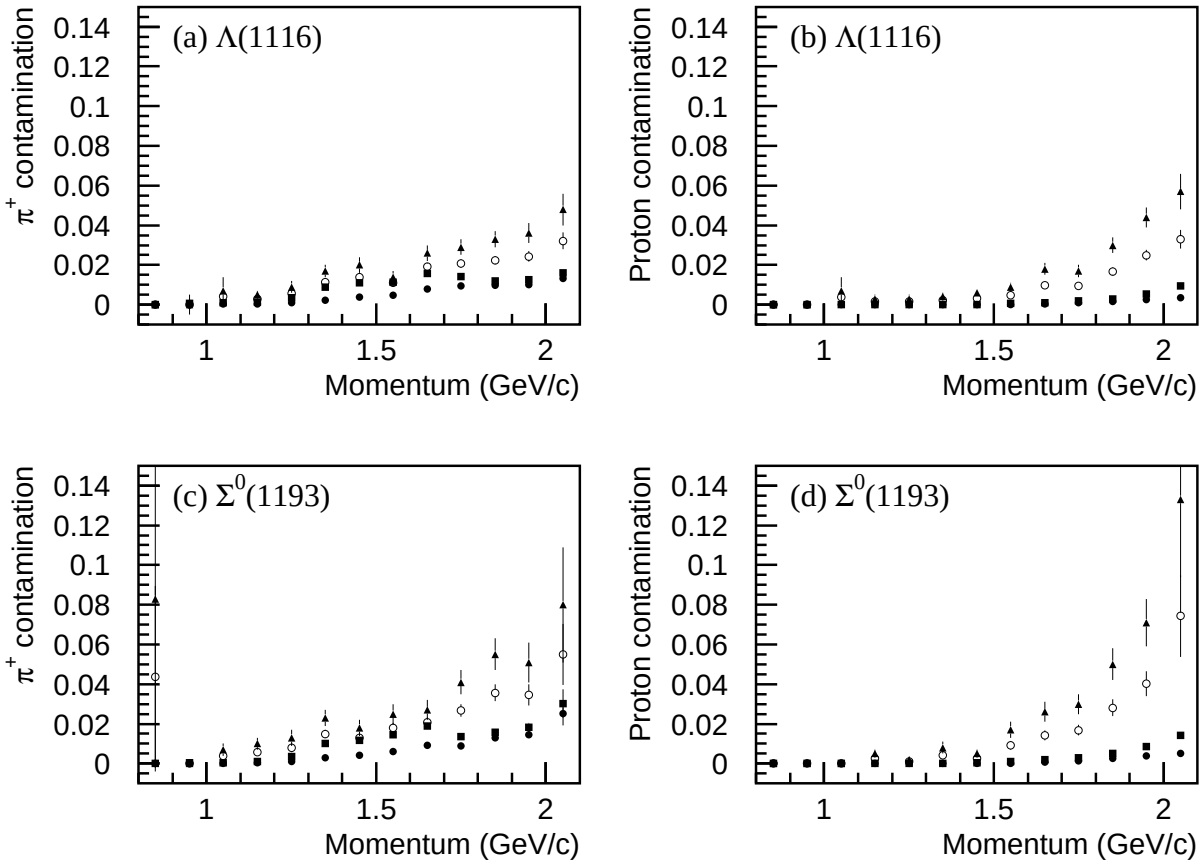

Figure 3.25: Contamination rates of the π^+ and proton events in the K^+ event samples with the mass cut. (a) and (b): the π^+ and proton contamination rate for the $p(\gamma,K^+)\Lambda$ reaction. (c) and (d): For the $p(\gamma,K^+)\Sigma^0$ reaction. The filled circles, squares and triangles are for the data set I, II and III, respectively. The open circles are the contamination rates in total for the all data sets.

3.7.3 Event selection with the missing mass distribution

The $p(\gamma,K^+)\Lambda$ and $p(\gamma,K^+)\Sigma^0$ reaction channels are identified by selecting the $\Lambda(1116)$ and $\Sigma^0(1193)$ events in the missing mass distribution of the $p(\gamma,K^+)X$ reaction. Fig. 3.26 shows the missing mass spectrum with the full statistics. One can distinguish the peaks corresponding to the $\Lambda(1116)$, $\Sigma^0(1193)$, $\Lambda(1405)/\Sigma(1385)$(not separated), and $\Lambda(1520)$ events clearly. The peak around 0.86 GeV/c^2 corresponds to the $p(\gamma,\pi^+)n$ reaction events. About 2% π^+ events contaminate the K^+ event samples described in the last section.

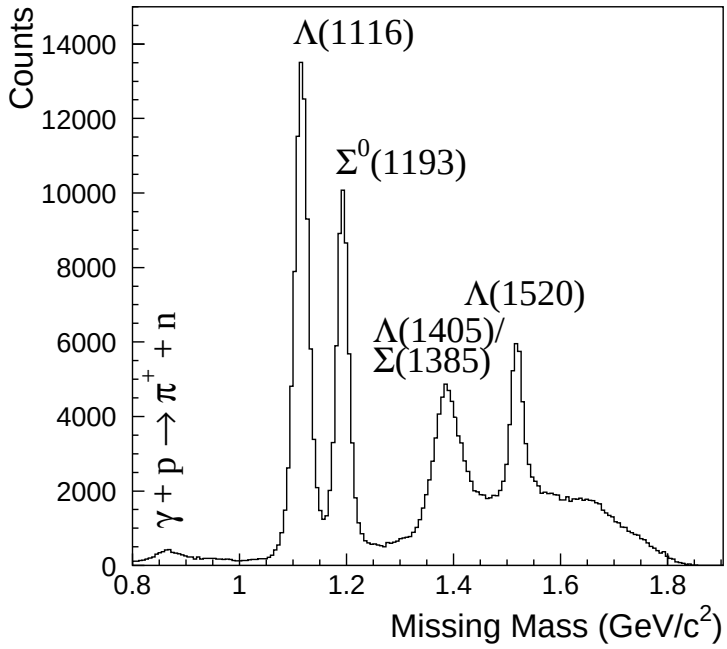

Figure 3.26: Missing mass spectrum of K^+ with the full statistics after applying all the cuts listed in Table 3.2 except for the missing mass cut. the peaks corresponding to the $\Lambda(1116)$, $\Sigma^0(1193)$ and hyperon resonances are seen. The peak around 0.86 GeV/c^2 is due to the π^+ contamination events.

Fig. 3.27(a) and (b) show the K^+ momentum dependences of the peak positions and resolutions (σ) of the missing mass (MM). The solid circles are for the $\Lambda(1116)$ events and the open circles are for the $\Sigma^0(1193)$ events. The peak positions of $\Lambda(1116)$ and $\Sigma^0(1193)$ agree well with the PDG (Particle Data Group) values within 5 MeV. These peaks are used to calibrate the photon beam energy and the momentum. The calibration is performed by making these peaks the PDG values and independent on the momentum and the photon energy. The resolution of the missing mass depends on the momentum. The resolution rises linearly as the momentum increases because the momentum resolution itself deteriorates with increasing momentum. Although the resolutions are independent on the photon beam energy, the E_γ dependence is observed because the photon beam energy is strongly correlated with the momentum for the fixed observed missing mass.

The momentum dependence cut is used to select the $\Lambda(1116)$ and $\Sigma^0(1193)$ events. The data points of the resolutions in Fig. 3.27(b) are fitted by a linear function for the $\Lambda(1116)$ and $\Sigma^0(1193)$ events. The results of the fitting are used to determine the cut positions. The resolution is denoted with the momentum p as

$$\sigma_\Lambda = 0.008295 \cdot p + 0.000627 \quad (3.41a)$$

$$\sigma_{\Sigma^0} = 0.007641 \cdot p + 0.001129. \quad (3.41b)$$

Fig. 3.28 shows a scatter plot of the K^+ momentum vs. the missing mass. The solid lines correspond to $M_\Lambda \pm 2\sigma_\Lambda$ and $M_{\Sigma^0} \pm 2\sigma_{\Sigma^0}$. The regions of the $\Lambda(1116)$ and $\Sigma^0(1193)$ events are

not overlapped. The dashed lines correspond to $M_\Lambda \pm 3\sigma_\Lambda$ and $M_{\Sigma^0} \pm 3\sigma_{\Sigma^0}$. The regions of the $\Lambda(1116)$ and $\Sigma^0(1193)$ events are overlapped above 1.5 GeV/c momentum in the case of the 3σ cut. We used the 2σ boundaries as the cut positions of the missing mass cut because the good separation between the Λ and Σ^0 events is more important than the improvement of the statistics for the present analysis. The statistics of these reaction events is good enough to obtain the photon beam asymmetry. The Λ (Σ^0) contamination rate in Σ^0 (Λ) event samples is less than 1% when the 2σ boundaries are used for the missing mass cut.

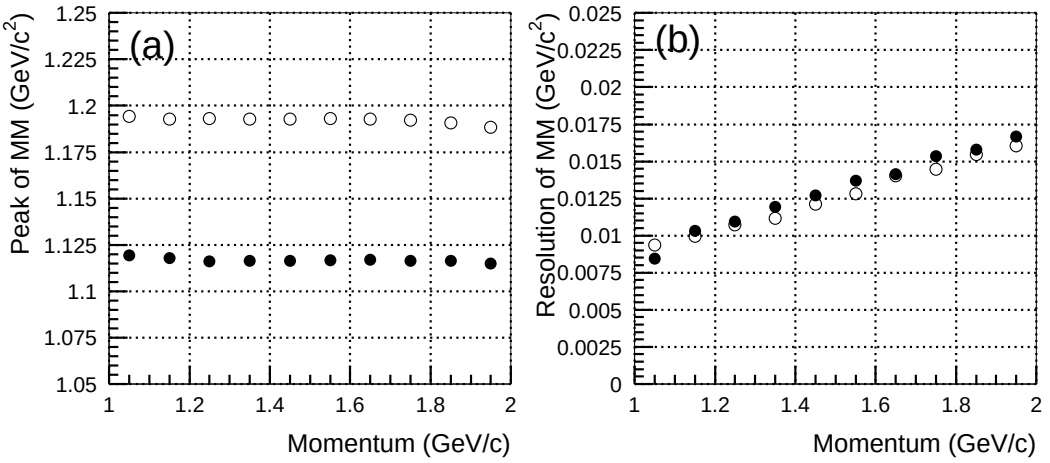

Figure 3.27: Momentum dependence of (a) the peak position and (b) the resolution (σ) of the missing mass of the K^+ events. The solid circles are for Λ and the open circles are for Σ^0.

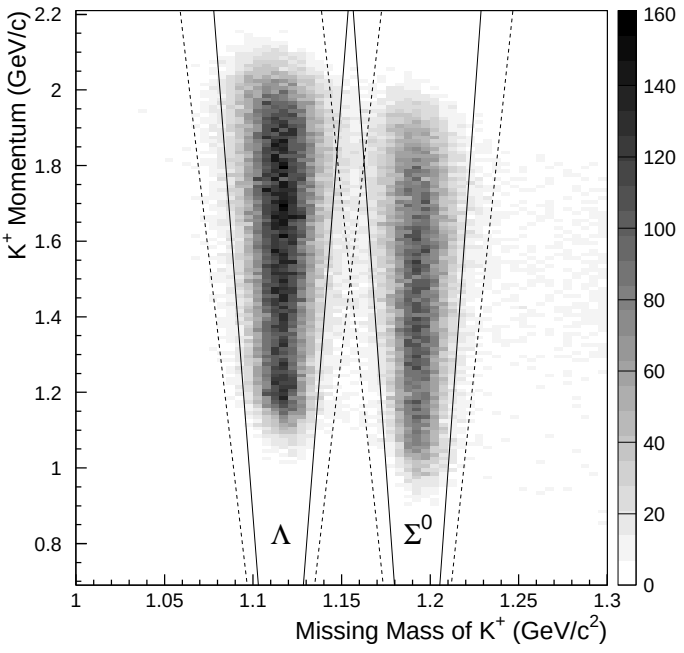

Figure 3.28: Scatter plot of Missing mass vs. momentum of K^+. The solid lines represent the boundaries for $M_\Lambda \pm 2\sigma$ and $M_{\Sigma^0} \pm 2\sigma$. The dashed lines are those for $M_\Lambda \pm 3\sigma$ and $M_{\Sigma^0} \pm 3\sigma$.

Data was taken with the empty target by vertically polarized photons in order to estimate the background events in 1 day. Fig. 3.29 shows the missing mass spectra. The solid line in Fig. 3.29(a) is for the LH_2 target and the dashed line is for the empty target. Data in the plot for the LH_2 target run was taken by the vertically polarized photons near the empty target run to reduce the systematic error. These plots are normalized by the number of photons. Fig. 3.29(b) shows the missing mass spectrum of the LH_2 target subtracted by the events of the empty target run. Most of the events taken with the empty target are produced at the TRG. The rest backgrounds are estimated to be due to the π^+ and proton particles. The peak around 0.86 GeV/c^2 corresponding to the p(γ,π^+)n reaction events is not removed by this subtraction.

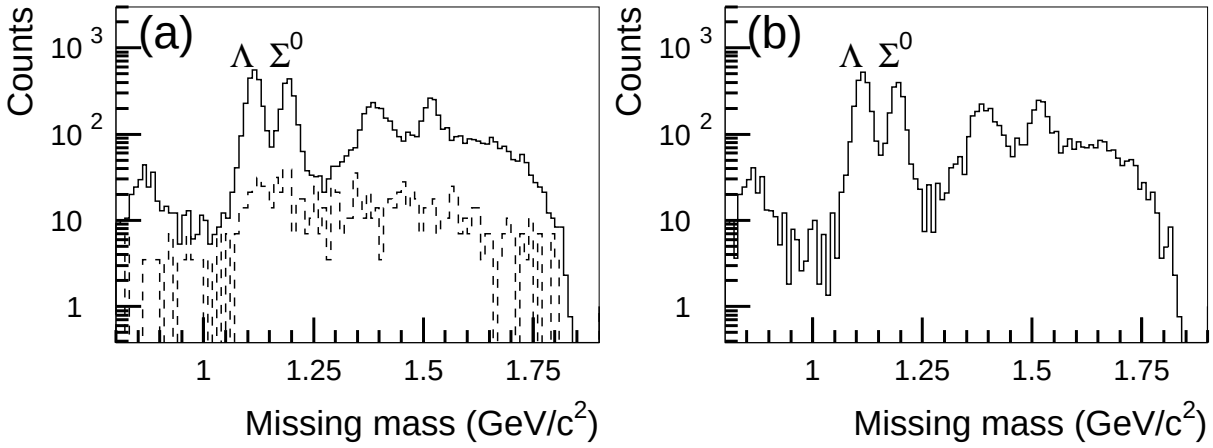

Figure 3.29: Missing mass spectra for (a) the LH_2 target (solid line) and the empty target (dashed line), and for (b) the LH_2 target subtracted by the events with the empty target.

3.7.4 Rejection of the accidental e^+e^- events

There is a possibility that the e^+e^- events are accepted accidentally even in the hadron trigger with the veto signal from the AC. Most of the accidental e^+e^- events are rejected by the mass cut for the PID. However, a part of the accidental e^+e^- events are misidentified as kaons in particular in the data set III due to the bad mass resolution. Although particles with below 1 GeV/c momenta emitted in the medium plane are blocked by the e^+e^- blocker placed in the dipole magnet, the e^+e^- events with above 1 GeV/c momenta escape through the gap between the two Pb blocks of the e^+e^- blocker (see Fig. 2.26). The thickness of the Pb blocks is 40 mm and the blocks are placed at y = -7 mm.

The y-position of a track at the e^+e^- blocker is used to remove these accidental events. To remove the accidental e^+e^- events, the following criterion is required.

$$\mathrm{y} < -30\,\mathrm{mm} \quad \text{or} \quad \mathrm{y} > 16\,\mathrm{mm}. \tag{3.42}$$

Fig. 3.30 shows the effect of the e^+e^- cut on the missing mass spectrum of the p(γ,K^+)X reaction. The dotted line shows the missing mass spectrum for the events selected without the e^+e^- cut. One can see a bump around 0.9 GeV/c^2. The dashed line shows the spectrum for the events rejected by the e^+e^- cut. The background events due to the accidental e^+e^- events make a bump around 0.9 GeV/c^2 in the missing mass spectrum. The solid line shows the missing mass spectrum with the e^+e^- cut. The background events due to the accidental e^+e^- events are removed with the e^+e^- cut.

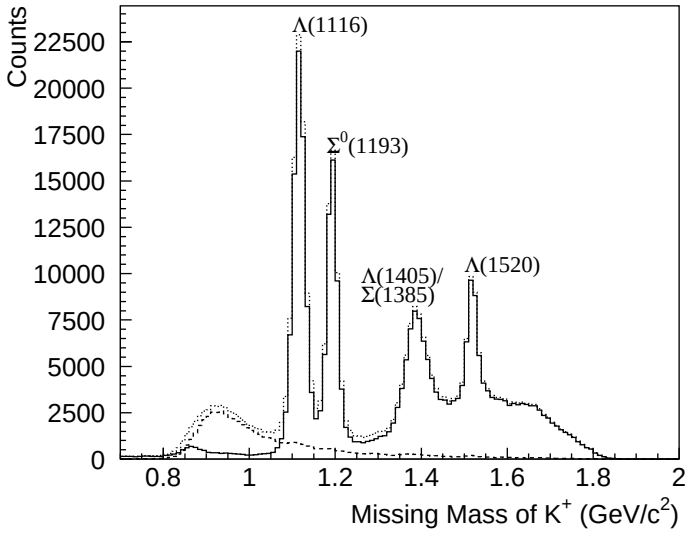

Figure 3.30: Missing mass spectrum of the p(γ,K^+)X reaction. The solid line shows the spectrum with all the cuts listed in Table 3.2. The dotted line shows the spectrum without the e^+e^- cut. The dashed line shows the spectrum for the events rejected by the e^+e^- cut.

3.7.5 Rejection of background events with the χ^2 probability

The χ^2 probability ($prob(\chi^2)$) is obtained in Eq. (3.9) in the tracking analysis with the Kalman filter method. The good tracks are selected with the cut,

$$prob(\chi^2) \;>\; 0.02. \tag{3.43}$$

The confidence level is 98%. The cut position of 0.02 is used as the critical cut value to remove outliers in the tracking analysis.

Fig. 3.31 shows the distribution of the χ^2 probability for the tracks reconstructed in the tracking analysis. There is a peak at $prob(\chi^2) < 0.02$ corresponding to the background tracks. Fig. 3.33(a) and (b) show the spectra of the mass-squared for the events with $prob(\chi^2) > 0.02$ and $prob(\chi^2) < 0.02$. The peak corresponding to kaons is clearly seen in Fig. 3.33(a). On the other hand, the peak of kaons is small and much wider in Fig. 3.33(b). The χ^2 probability

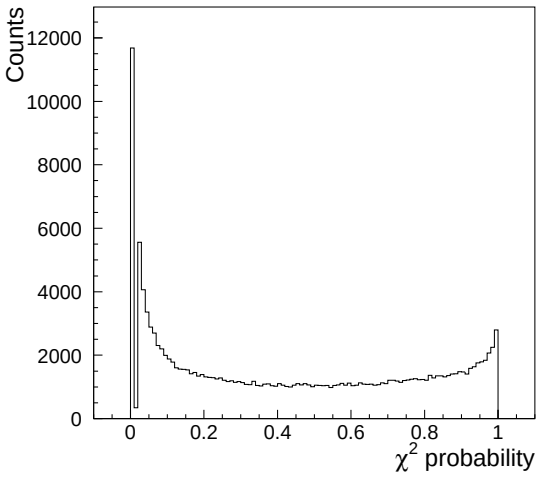

Figure 3.31: χ^2 probability for the events with the vertex cut and the e^+e^- cut.

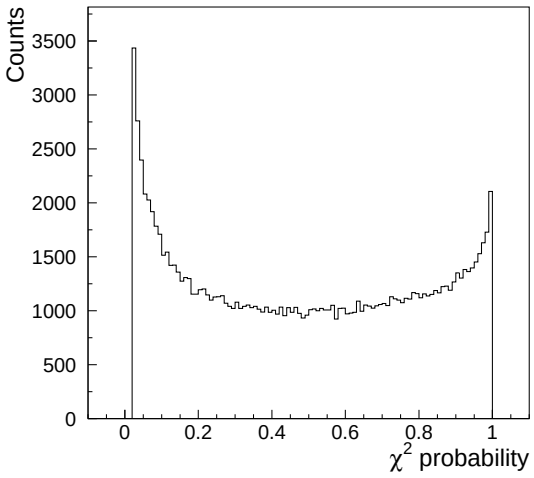

Figure 3.32: χ^2 probability for the K^+ events with all the cuts listed in Table 3.2.

cut rejects the decay-in-flight kaons between the SVTX and DC3. The rejection efficiency is estimated to be about 99.8% by the study with the Monte Carlo simulation (g3leps). The mass resolution is worse in Fig. 3.33(b) than in Fig. 3.33(a). Fig. 3.32 shows the distribution of the χ^2 probability for the p(γ,K^+)Λ(1116) and p(γ,K^+)Σ^0(1193) reaction events. The distribution slightly extends at the low $prob(\chi^2)$ and the high $prob(\chi^2)$. These events with the low $prob(\chi^2)$ have still outliers but the momentum is determined with the good accuracy. The distribution is limited by the accuracy of the measured resolutions and alignment of the tracking devices, the SVTX and DC's.

The decay-in-flight kaons between DC3 and the TOF wall are rejected with the following conditions:

$$\left|\mathrm{y}_{trk} - \mathrm{y}_{tof}\right| < 80 \text{ mm } (\sim 4\sigma), \tag{3.44a}$$

$$|\mathrm{id}_{trk} - \mathrm{id}_{tof}| \leq 1, \tag{3.44b}$$

$$\mathrm{noutl} \leq 6. \tag{3.44c}$$

The critical value of 80 mm corresponds to 4σ of the resolution as shown in Fig. 3.11. The number of outliers (noutl) are required to be less than 6. These conditions are tighter than those in Eq. (3.32) which are used to find the correct combinations between the track and the TOF hit in the LEPSana program. About 5% of the decay-in-flight events are estimated to pass the cuts given in Eq. (3.43) and (3.44) by the study of the MC simulation. Since these events decay in the front of the TOF wall, the time-of-flights and the momentum are determined correctly. Therefore, the masses of such events are mostly reconstructed. The cuts given in Eq. (3.43) and (3.44) are used to select the good tracks and reject the decay-in-flight events.

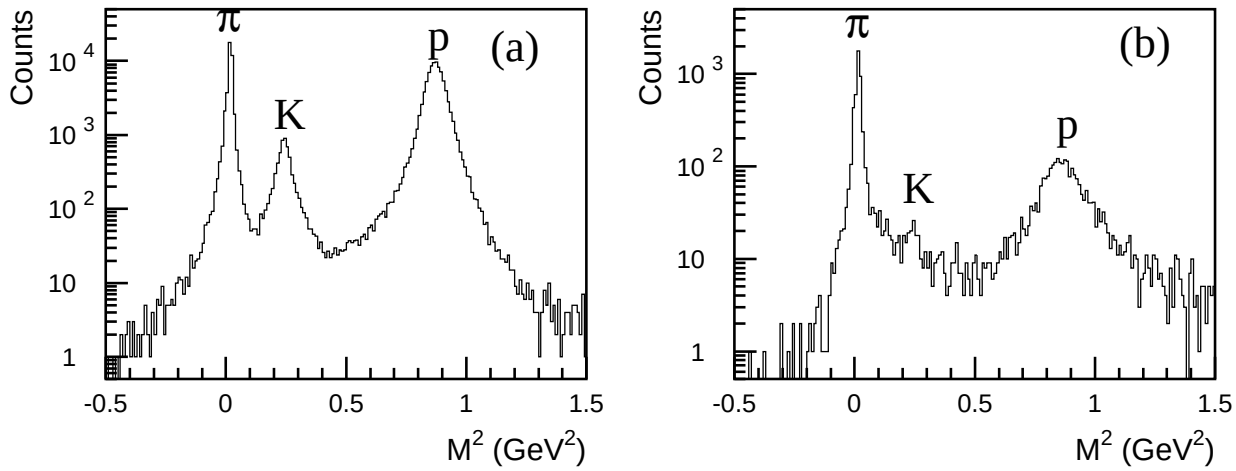

Figure 3.33: Mass-squared spectra for the events with the vertex cut and the e^+e^- cut. (a): prbchi2 > 0.02 and (b): prbchi2 < 0.02.

3.7.6 Rejection of background events with the tagging system

The photon beam energy is used to calculate the missing mass of the p(γ,K$^+$)X reactions. The tag cut is used to select the good track of the recoil electron by the backward-Compton scattering process in the tagging system. The number of tracks reconstructed (ntag) in the tagging system is required to be 1,

$$\text{ntag} = 1. \tag{3.45}$$

Shielding materials are placed at the high electron-energy side of the tagging system corresponding to the low photon-energy side as shown in Fig. 2.12. There remains a possibility that recoil electrons with the high energy outside the range of the tagging system scatter or produce a shower at the materials and the track is reconstructed in the tagging system. As a result, photons with $E_\gamma < 1.5$ GeV are reconstructed by these electrons. Since the reconstructed energies of such photons are not correct, these events are backgrounds. Although there is no good method to remove these events completely, a substantial amount of events are removed by using the following condition:

$$npl(1) = 0 \ \text{ or } \ npl(2) = 0 \tag{3.46}$$

where npl(1) and npl(2) are the number of hits, which are not associated with any recoil electron, in the plastic scintillator hodoscope 1 and 2, respectively. This condition selects events for which there is no other hit than the recoil electron, at least in one of the two hodoscopes. There are two narrow energy regions, up to 2.4 GeV, where this condition cannot

be used because of the presence of a few dead strips in the SSD layers. We allow that there is no hit in these dead strips to save tracks passed through these areas. A special treatment is made for these events in the tagging analysis. The above condition in Eq. (3.46) removes such tracks. Therefore, the two regions are excluded in the condition (3.46). The full condition of the tag cut to select a good recoil electron is

$$\text{ntag} = 1 \tag{3.47a}$$

and

$$(\text{npl}(1) = 0 \ \text{ or } \ \text{npl}(2) = 0) \text{ or } (1.91 < E_\gamma < 1.93 \ \text{ or } \ 2.27 < E_\gamma < 2.30). \tag{3.47b}$$

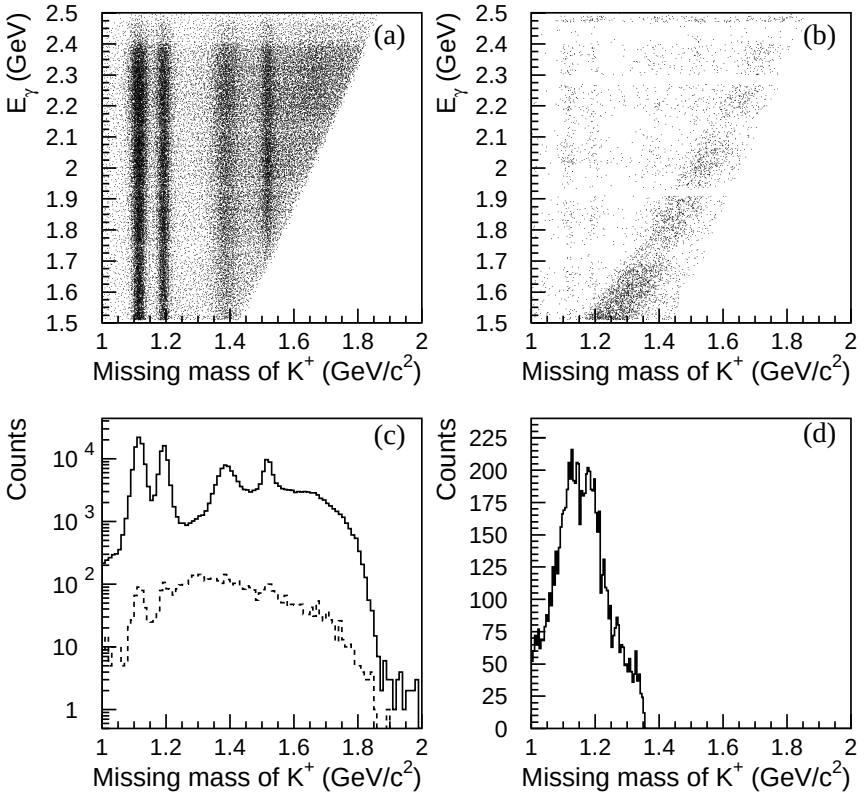

Figure 3.34: Effect of the tag cut. (a) and (b): Scatter plots of E_γ vs. the missing mass of the K^+ events for the events accepted and rejected with the tag cut. (c): Missing mass spectra. The solid line shows the accepted events with the tag cut. The dashed line is for the fail events. (d): Missing mass spectrum for the rejected events calculated by using 1.35 GeV as the photon energy E_γ.

Fig. 3.34(a) and (b) show the scatter plots of E_γ vs. the missing mass of the $p(\gamma,K^+)X$ reaction for the events accepted and rejected with the tag cut, respectively. The loci of the the

$\Lambda(1116)$, $\Sigma^0(1193)$ and hyperon resonances are seen in Fig. 3.34(a). The band in Fig. 3.34(b) corresponds to the events by photons with the wrong E_γ due to electrons scattered in the shielding material. The solid line and dashed line in Fig. 3.34(c) show the missing mass spectra corresponding to Fig. 3.34(a) and (b). Most of the events rejected by the tag cut are the background events with the wrong energy. These background events have the energy range centered around 1.35 GeV. Fig. 3.34(d) shows the missing mass spectrum for the rejected events calculated assuming 1.35 GeV for the photon energy E_γ. Although the resolution is bad, the peaks corresponding to $\Lambda(1116)$ and $\Sigma^0(1193)$ are seen. The total events are reduced to be about 98.4 % by the cut for the rejection of the background events with the wrong E_γ.

3.7.7 Distributions of the $K^+\Lambda$ and $K^+\Sigma^0$ events in the kinematical regions

All the cuts listed in Table 3.2 are applied to select the $p(\gamma,K^+)\Lambda(1116)$ and $p(\gamma,K^+)\Sigma^0(1193)$ reaction events. About 72,500 $K^+\Lambda$ and 48,900 $K^+\Sigma^0$ events are obtained. The $K^+\Lambda$ and $K^+\Sigma^0$ events are plotted in Fig. 3.35 as functions of various parameters. The loci corresponding to $\Lambda(1116)$, $\Sigma^0(1193)$, $\Lambda(1405)/\Sigma(1385)$ and $\Lambda(1520)$ are seen in Fig. 3.35(a) and (b). The K^+ momentum in the $p(\gamma,K^+)\Lambda(1116)$ and $p(\gamma,K^+)\Sigma^0(1193)$ reaction is ranged from 0.8 to 2.2 GeV/c. These reaction events are accepted in the full energy region covered by the tagging system, $1.5 \sim 2.4$ GeV. The $K^+\Lambda$ and $K^+\Sigma^0$ events are detected up to $\Theta_{cm}^{K^+} = 60^\circ$ by the LEPS spectrometer. Since the acceptance of the spectrometer in the y-direction is smaller than that in the x-direction, the region covering 2π in the azimuthal angles is up to $\Theta_{cm}^{K^+} = 30^\circ$ as shown in Fig. 3.35(c). The distributions of E_γ and $\Theta_{cm}^{K^+}$ are similar for the $K^+\Lambda$ and $K^+\Sigma^0$ events.

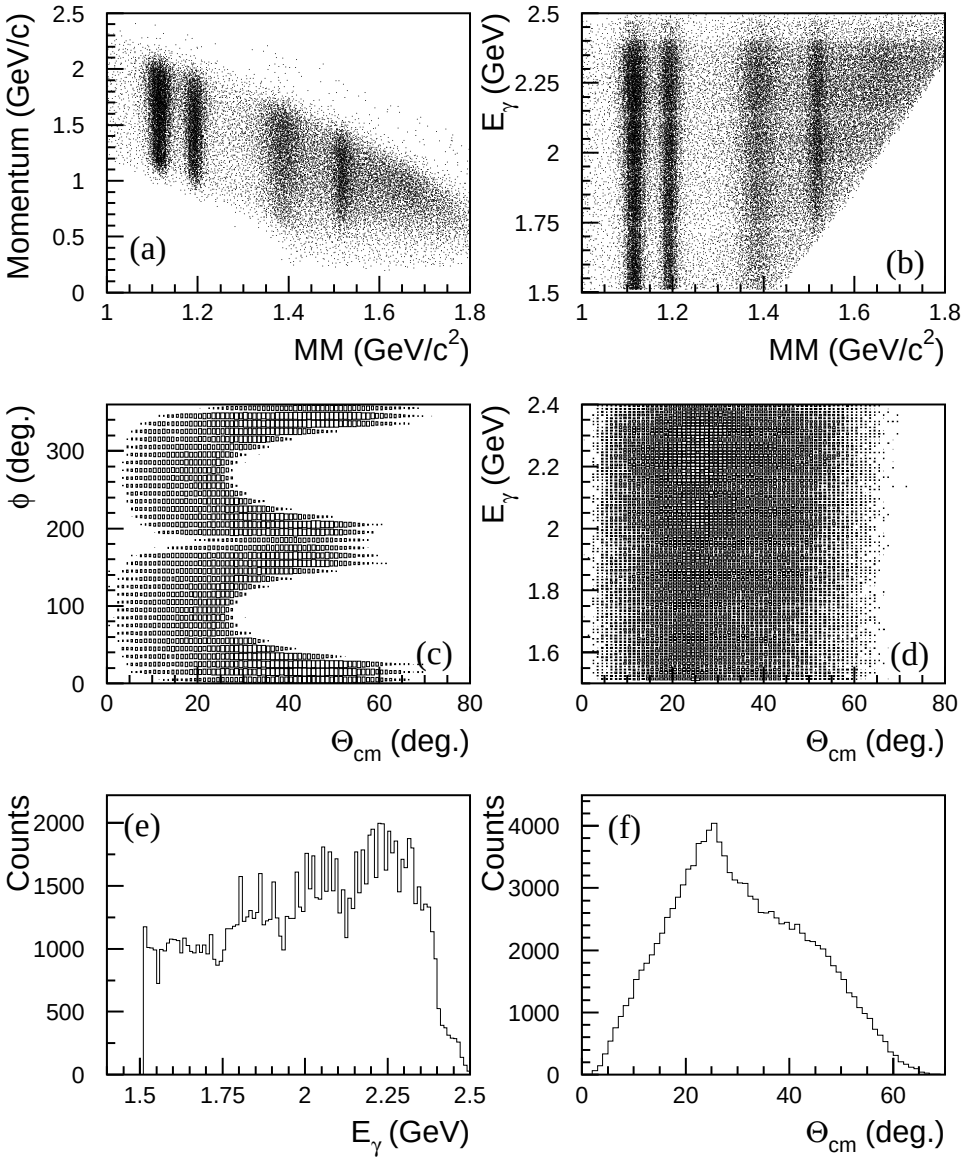

Figure 3.35: Plots of the K^+ photoproduction events as functions of various parameters. (a) Scatter plot of the K^+ momentum vs. the missing mass. (b) Scatter plot of E_γ vs. the missing mass. (a) and (b): for the events with all the cuts listed in Table 3.2 except for the MM cut. (c) Scatter plot of the K^+ azimuthal angle ϕ_{K^+} vs. the scattering angle $\Theta_{cm}^{K^+}$. (d) Scatter plot of E_γ vs. $\Theta_{cm}^{K^+}$. (e) E_γ distribution. (f) $\Theta_{cm}^{K^+}$ distribution. (c), (d), (e) and (f): for the $p(\gamma,K^+)\Lambda$ and $p(\gamma,K^+)\Sigma^0$ reaction events.

Chapter 4

Photon beam asymmetry

For a photon linearly polarized in the vertical and horizontal direction, the differential cross section for the kaon photoproduction is described as

$$\frac{d\sigma}{d\Omega}_{v} = \frac{d\sigma}{d\Omega}_{unpol}[1 + P\Sigma\cos(2\phi_{K^+})], \tag{4.1a}$$

$$\frac{d\sigma}{d\Omega}_{h} = \frac{d\sigma}{d\Omega}_{unpol}[1 - P\Sigma\cos(2\phi_{K^+})], \tag{4.1b}$$

where Σ is the photon beam asymmetry, P is the polarization of a photon and ϕ_{K^+} is the K^+ azimuthal production angle which is defined using the reaction plane and the horizontal plane [41]. By using vertically and horizontally polarized photons, two sets of data were collected to obtain the photon beam asymmetry. The relation between the production yields in the two data sets and the photon beam asymmetry is given as follows:

$$\frac{n \cdot N_v - N_h}{n \cdot N_v + N_h} = P\Sigma\cos(2\phi_{K^+}), \tag{4.2}$$

where $N_v(N_h)$ is the K^+ photoproduction yield with vertically (horizontally) polarized photons and n is the normalization factor for N_v. It is possible to correct for anisotropies in the azimuthal response of the detectors by combining the two data set.

The normalization factor n was determined by using the numbers of horizontally polarized photons and vertically polarized photons (n_h and n_v) at the target as

$$n = n_h/n_v. \tag{4.3}$$

The number of photons produced by the backward-Compton scattering process is estimated by using the tagging counter (the hodoscopes of the tagging system, TAG-PL) after taking into account the accidental rate at the tagging counter. The transmission of the photons from the reaction point to the target is about 58%. The transmission value is assumed to be the same for both the polarizations. The photon yield at the target was obtained after the dead time of the DAQ system and the accidental veto rate of the upstream counter were estimated in each run. The photon yield at the target for the data used in the present analysis was 1.098×10^{12} (1.013×10^{12}) for the vertically (horizontally) polarized photons. The normalization factor was determined by these photon yields,

$$n = 0.923. \tag{4.4}$$

Fig. 4.1 shows the ratios of $(n \cdot N_v - N_h)/(n \cdot N_v + N_h)$ as a function of the K^+ azimuthal angle (ϕ_{K^+}). These ratios are obtained by integrating over all the events in the energy range 1.5 GeV $\leq E_\gamma \leq$ 2.4 GeV and the K^+ angular range $0.6 \leq \cos\Theta_{cm} \leq 1$. The data points are

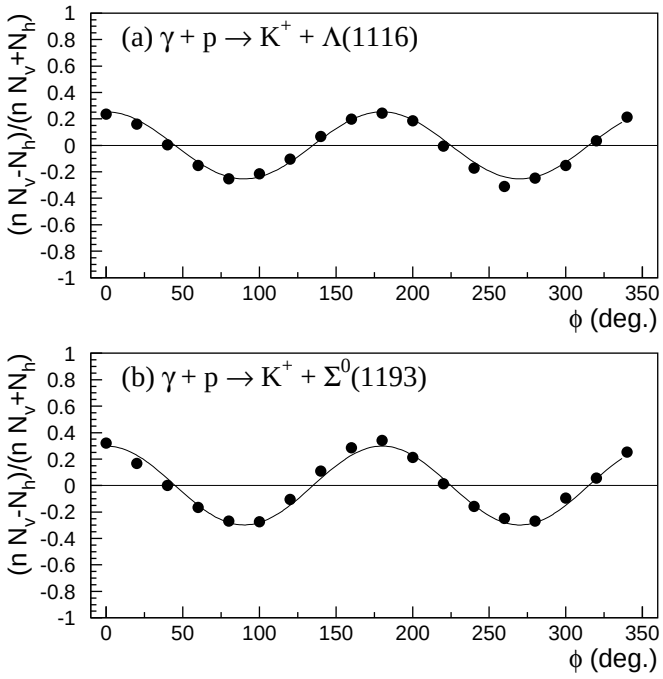

Figure 4.1: Azimuthal angle ϕ_{K^+} dependence of the ratio $(n \cdot N_v - N_h)/(n \cdot N_v + N_h)$ in Eq. (4.2) for (a) the p(γ,K^+)Λ reaction and (b) the p(γ,K^+)Σ^0 reaction integrating over all the events in 1.5 GeV $\leq E_\gamma \leq$ 2.4 GeV and $0.6 \leq \cos\Theta_{cm} \leq 1$. The solid lines are the results of a fitting using a function of $\cos(2\phi_{K^+})$.

fitted with a function of $\cos(2\phi_{K^+})$ (solid line). The amplitude $P\Sigma$ is obtained by this fitting.

$$P\Sigma_\Lambda = 0.253 \pm 0.0053, \tag{4.5a}$$

$$P\Sigma_{\Sigma^0} = 0.298 \pm 0.0064. \tag{4.5b}$$

The polarization of photons produced by the backward-Compton scattering process follows Eq. (2.5). The polarization P is calculated with Eq. (2.5) by using the photon energy E_γ. Because the multi-line mode of the Ar laser was used during the present experiment (see Fig. 2.10), the weight mean of the wavelengths from 33.6 nm to 363.8 nm is used to obtain the polarization P_γ. The weight mean is 352.3 nm. The polarization of laser photons P_{laser} was measured in every one run of about 3 hours. The photon polarization P_γ is calculated event by event by using Eq. (2.5). The average polarizations $\bar{P}_\gamma^h$ and $\bar{P}_\gamma^v$ are obtained for horizontally and vertically polarized photons in the data set. We used the average polarization $\bar{P}_\gamma$ in Eq. (4.2) determined as

$$\bar{P}_\gamma = \frac{\bar{P}_\gamma^h + \bar{P}_\gamma^v}{2}. \tag{4.6}$$

The photon beam asymmetry is obtained by using the fitting results and the polarization $P(= \bar{P}_\gamma)$. The results of the photon beam asymmetry and the polarizations for the events integrating over all events are

$$\Sigma_\Lambda = 0.315 \pm 0.0066, \; P = 0.805, \tag{4.7a}$$

$$\Sigma_{\Sigma^0} = 0.371 \pm 0.0080, \; P = 0.803. \tag{4.7b}$$

The photon beam asymmetries for the $p(\gamma,K^+)\Lambda$ and $p(\gamma,K^+)\Sigma^0$ reactions were plotted as a function of E_γ and the K^+ scattering angle $\cos\Theta_{cm}$ in Fig. 4.2. Only statistical errors are

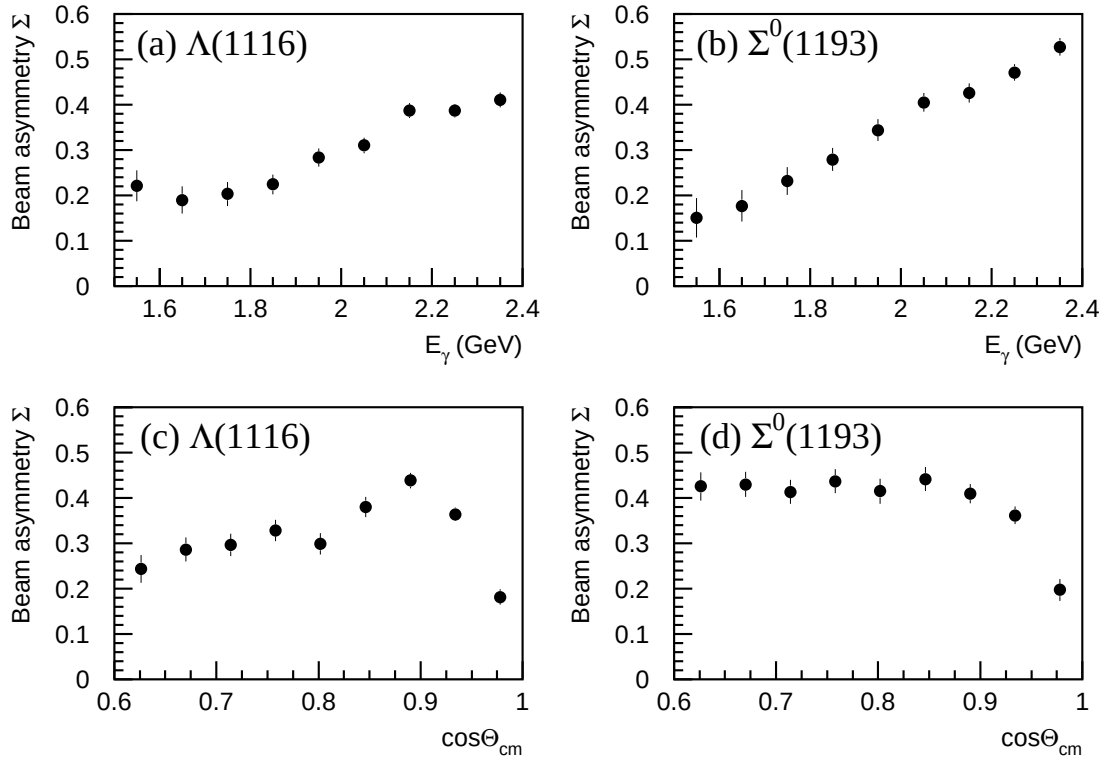

Figure 4.2: Photon beam asymmetries Σ as a function of E_γ and $\cos\Theta_{cm}$. (a) and (b): Energy dependences for the $p(\gamma,K^+)\Lambda$ and $p(\gamma,K^+)\Sigma^0$ reactions integrating over all the angles $0.6 < \cos\Theta_{cm} < 1$. (c) and (d): Angular dependences for the $p(\gamma,K^+)\Lambda$ and the $p(\gamma,K^+)\Sigma^0$ reactions integrating for $E_\gamma = 1.5 \sim 2.4$ GeV.

included in the error bars. The photon beam asymmetry for the $p(\gamma,K^+)\Lambda$ reaction increases above $E_\gamma = 1.6$ GeV as the photon energy increases as shown in Fig. 4.2(a). The energy distribution becomes flat above $E_\gamma = 2.1$ GeV. The photon asymmetry increases at $E_\gamma = 1.55$ GeV. On the other hand, the photon beam asymmetry for the $p(\gamma,K^+)\Sigma^0$ reaction increases linearly as the increase of the photon energy over all energy range.

The photon beam asymmetries for both reactions go to zero at the forward angles, $\cos\Theta_{cm} = 1$, as shown in Fig. 4.2(c) and (d). The photon beam asymmetries are zero at $\cos\Theta_{cm} = 1$

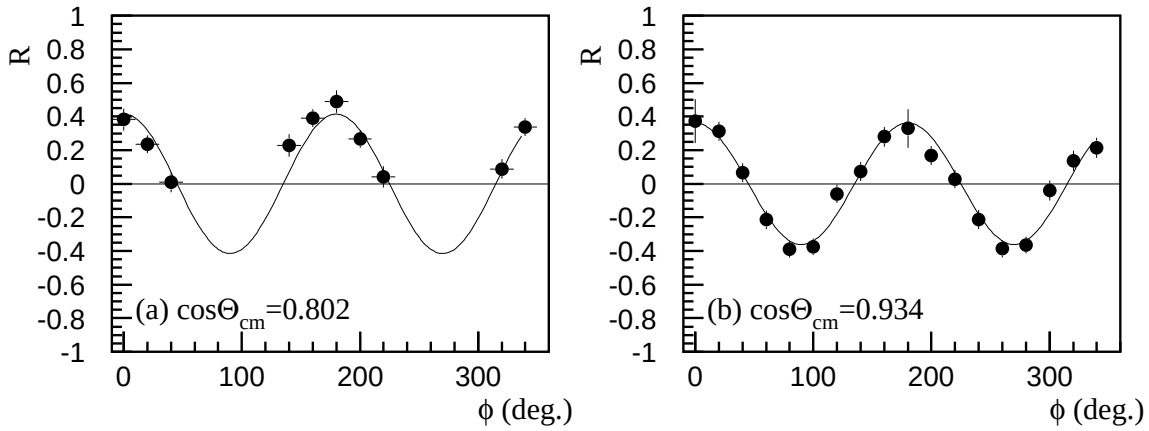

Figure 4.3: Azimuthal angle ϕ_{K^+} dependence of the ratio R for the p(γ,K$^+$)Σ^0 reaction integrating over all E$_\gamma$ at (a) cos$\Theta_{cm} = 0.802$ and (b) cos$\Theta_{cm} = 0.934$.

because a kaon emits in the same direction as one of the photon beam and it is not affected by the polarization of the photon beam. The photon beam asymmetry for the p(γ,K$^+$)Λ reaction drops at cos$\Theta_{cm} < 0.88$ in Fig. 4.2(c) while the beam asymmetry for the p(γ,K$^+$)Σ^0 reaction shows the flat angular distribution over all angles as shown in Fig. 4.2(d). The region covering 2π in the azimuthal angles is up to $\Theta^{K^+}_{cm} \sim 28^\circ$ as shown in Fig. 3.35(c). Only the data points ranged in $\phi \sim 0^\circ$ or $\phi \sim 180^\circ$ are used to determine the photon beam asymmetry in cos$\Theta_{cm} < 0.82$ as shown in Fig. 4.3(a). Fig. 4.3 shows the ϕ_{K^+} dependence of the ratio $R = (n \cdot N_v - N_h)/(n \cdot N_v + N_h)$ at (a) cos$\Theta_{cm} = 0.802$ and (b) cos$\Theta_{cm} = 0.934$. The data points covering the 2π region are used for a fitting in the angular range cos$\Theta_{cm} > 0.82$ as shown in Fig. 4.3(b).

The results of the E$_\gamma$ and angular dependence of the photon beam asymmetries, the statistical errors, χ^2 of the fitting and the average polarizations are summarized in Table $B.1$ and $B.2$ in Appendix B. The ϕ distributions of the ratio $(n \cdot N_v - N_h)/(n \cdot N_v + N_h)$ are shown in Appendix B.

We obtain the angular distributions of the photon beam asymmetry in some different energy regions for the p(γ,K$^+$)Λ(1116) and the p(γ,K$^+$)Σ^0(1193) reaction. The data are divided into three energy bins with 100 MeV width from 1.5 to 1.8 GeV and the other three energy bins with 200 MeV width from 1.8 to 2.4 GeV. The events are further divided into 5 angular bins in the range $0.6 <$ cos$\Theta_{cm} < 1.0$. Main backgrounds are π^+ and proton contaminations due to the misidentification in the mass distribution, and contamination events produced at the TRG. There is a few background events produced at the target cell. The effects of these background events on the photon beam asymmetries are investigated.

4.1 Correction for the π^+ and proton contaminations

The contamination rates of the π^+ and proton events in the p(γ,K$^+$)Λ and the p(γ,K$^+$)Σ^0 reaction data samples were estimated as shown in Fig. 3.25. The photon beam asymmetries

for these reaction data samples are the measured photon beam asymmetries including the π^+ and proton contamination events. Therefore the correction for these contamination events is performed. By using the π^+ and proton contamination rates (C_{π^+} and C_p), and the photon beam asymmetries of the K^+, π^+ and proton events, (Σ_{K^+}, Σ_{π^+} and Σ_p), the measured photon beam asymmetry $\Sigma_{K^+}^{meas}$ is written as

$$\Sigma_{K^+}^{meas} = (1 - C_{\pi^+} - C_p)\Sigma_{K^+} + C_{\pi^+}\Sigma_{\pi^+} + C_p\Sigma_p. \tag{4.8}$$

Fig. 4.4(a) and (b) show the angular distributions of the photon beam asymmetries. The

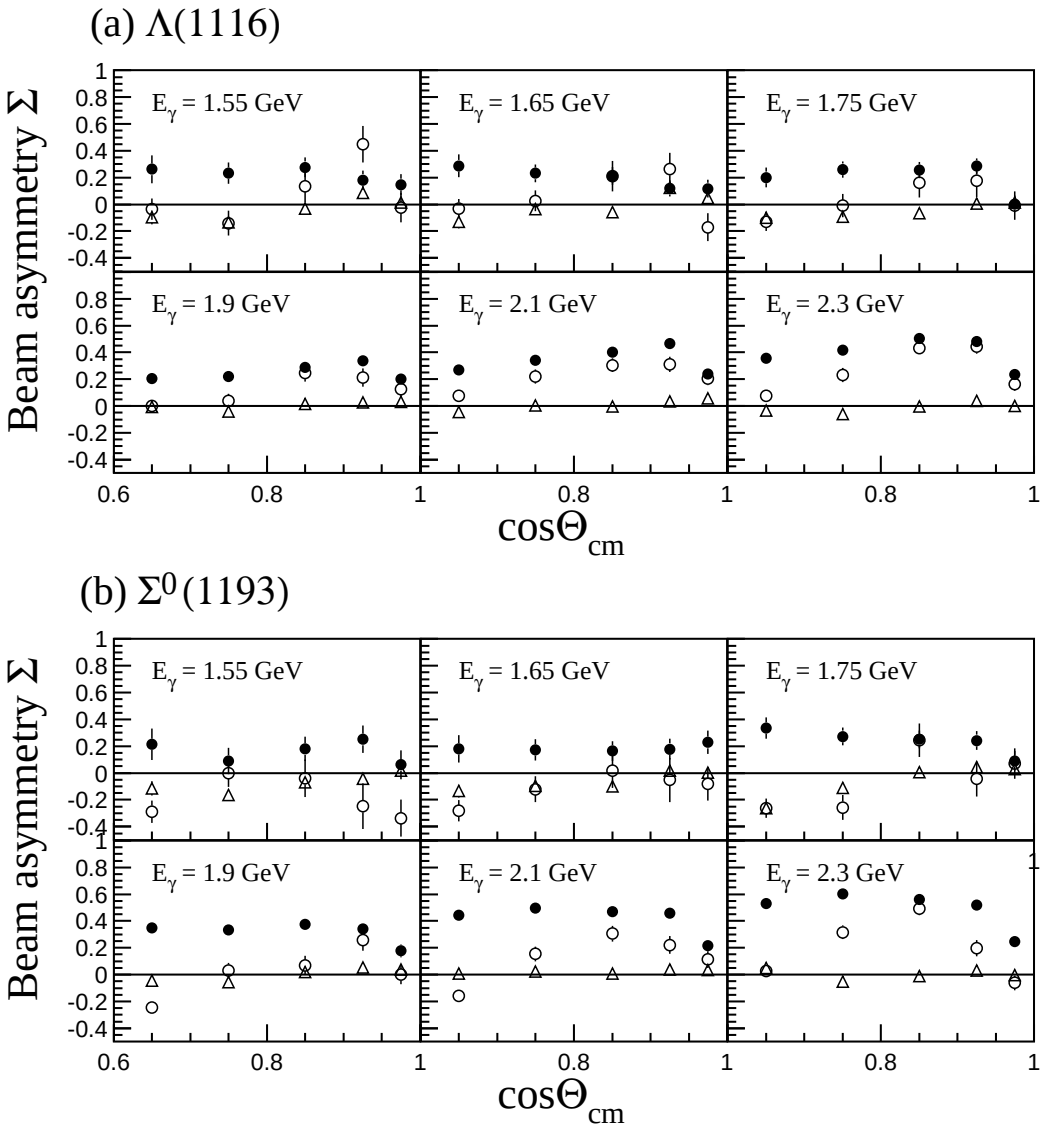

Figure 4.4: Photon beam asymmetries for (a) the p(γ,X)Λ and (b) the p(γ,X)Σ^0 reaction. The filled circles are the measured photon beam asymmetries $\Sigma_{K^+}^{meas}$. The open circles (triangles) are the photon beam asymmetries for the π^+ (proton) events, Σ_{π^+} and Σ_p. The statistical errors are included into the error bars.

filled circles are the measured photon beam asymmetries $\Sigma_{K^+}^{meas}$ for the p(γ,K$^+$)Λ and the p(γ,K$^+$)Σ^0 reaction event samples which are selected by the cuts listed in Table 3.2. The open circles are for the π^+ events. The open triangles are for the proton events. The π^+ and proton events are selected with the mass-square distribution as shown in Fig. 3.23(b) after applying the same cuts as the selection of the p(γ,K$^+$)Λ and the p(γ,K$^+$)Σ^0 reaction events listed in Table 3.2 except for the kaon mass cut.

The measured beam asymmetries indicates the positive signs as shown in Fig. 4.4. The values are larger than those for the π^+ and proton events except for two data points in the p(γ,K$^+$)Λ reaction. The photon beam asymmetries of the proton events in the both reactions are close to zero in the energy range $E_\gamma > 1.8$ GeV. There is a small angle dependence below $E_\gamma = 1.8$ GeV. The photon beam asymmetries slightly drop and have the negative sign at the large angles. The proton events make the photon beam asymmetry of the K$^+$ events small. The π^+ events also make the photon beam asymmetry of the K$^+$ events small except for the two data points in the p(γ,K$^+$)Λ reaction. The difference between $\Sigma_{K^+}^{meas}$ and Σ_{π^+} is small at the forward angles.

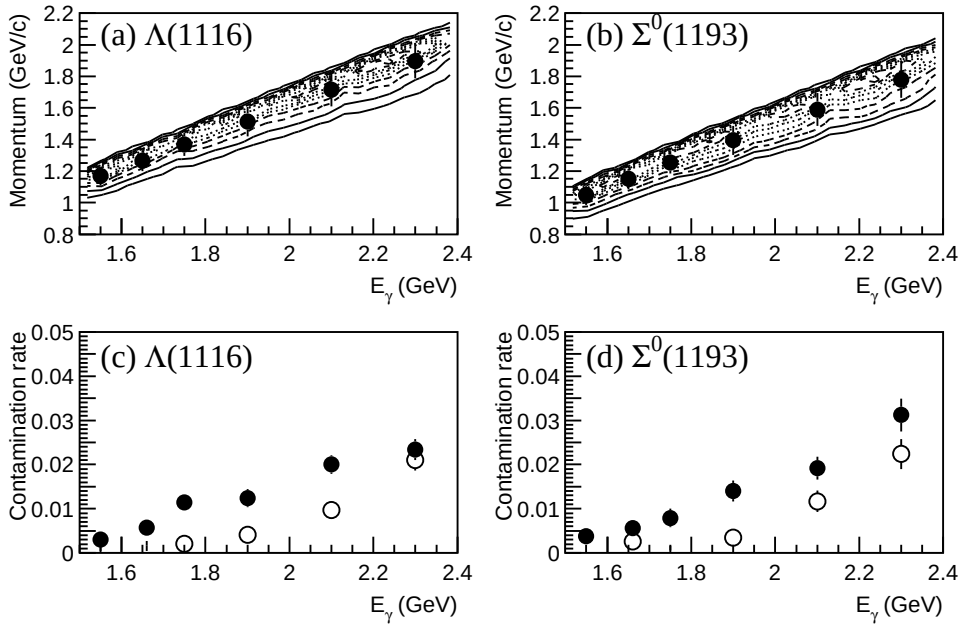

Figure 4.5: Relation between the K$^+$ momentum and E_γ for (a) the p(γ,K$^+$)Λ and (b) the p(γ,K$^+$)Σ^0 reactions. Contamination rate of π^+ (filled circles) and proton (open circles) events as a function of E_γ for (c) the p(γ,K$^+$)Λ and (d) the p(γ,K$^+$)Σ^0 reactions.

The π^+ and proton contamination rates were obtained as a function of the K$^+$ momentum as shown in Fig. 3.25 because the mass resolution depends on the momentum. The contamination rates in each photon energy bin are estimated by using the relation between the K$^+$ momentum and E_γ. The photon energy E_γ is strongly correlated with the K$^+$ momentum for the fixed missing masses. Fig. 4.5(a) and (b) show the relation between the K$^+$ momentum and E_γ for

the p(γ,K$^+$)Λ and the p(γ,K$^+$)Σ^0 reaction. The data points of the mean values of the K$^+$ momentum and E$_\gamma$ distributions in each bin are shown with the scatter plots in Fig. 4.5(a) and (b). The error bars in the data points indicate the RMS values of the momentum distributions in each of the energy bins. The π^+ and proton contamination rates at the mean values of the K$^+$ momentum in each E$_\gamma$ bin are obtained from the plots of the open circles in Fig. 3.25. These contamination rates are plotted as a function of E$_\gamma$ in Fig. 4.5(c) and (d). The filled circles are the π^+ contamination rate C_{π^+}. The open circles are the proton contamination rate C_p. The π^+ contamination rate is larger than the proton contamination rate. These contamination rates are less than 3.5% for the both reactions.

The photon beam asymmetry Σ_{K^+} of the K$^+$ events is calculated by using Eq. 4.8. The correction of the π^+ and proton contamination is made. Fig. 4.6 shows the difference between the beam asymmetries before the correction $\Sigma_{K^+}^{meas}$ and after the correction Σ_{K^+} for the p(γ,K$^+$)Λ and p(γ,K$^+$)Σ^0 reaction events. The error bars are the statistical errors. After the correction of the π^+ and proton contamination events, the photon beam asymmetries increase except for th two data points in the p(γ,K$^+$)Λ reaction where the photon asymmetry of the π^+ events is larger than one of the K^+ events. The effect of the correction is small at the low energy side. the differences are zero at E$_\gamma < 1.7$ GeV. The differences becomes larger at the higher energy due to the large contamination rates of the π^+ and proton events at the high momentum (E$_\gamma$) regions as shown in Fig. 4.5. The effect of the proton contamination is larger than that of the π^+ events because the difference between the beam asymmetries of the K$^+$ events and the proton events is larger that for the π^+ events and the π^+ and proton contamination rates are similar at the high energy. The difference is maximum at the data point of E$_\gamma = 2.3$ GeV and cos$\Theta_{cm} = 0.65$ for the p(γ,K$^+$)Σ^0 reaction. The maximum value is 0.026.

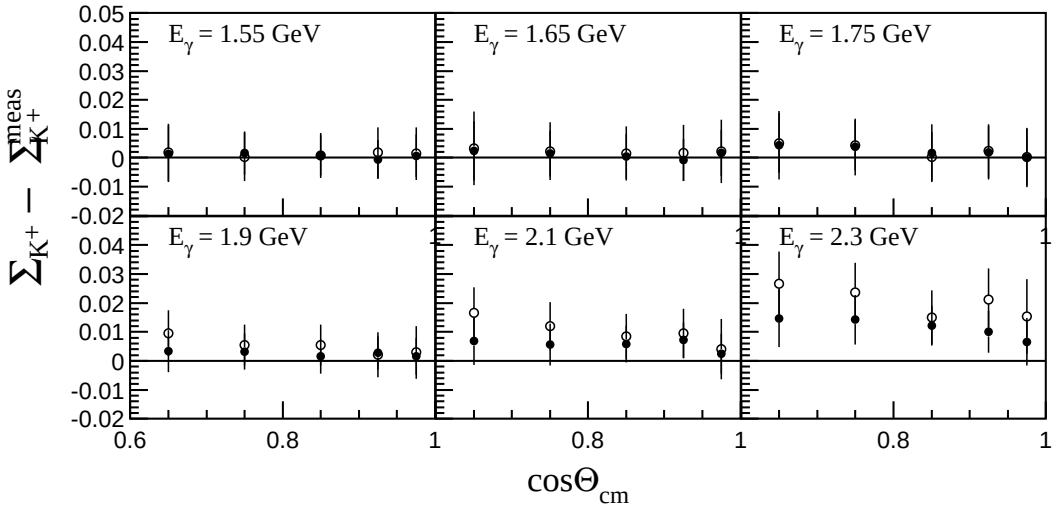

Figure 4.6: Difference Σ_{K^+} - $\Sigma_{K^+}^{meas}$ by the correction of the π^+ and proton contamination events. The filled circles are for the p(γ,K$^+$)Λ reaction and the open circles are for the p(γ,K$^+$)Σ^0 reaction. The statistical errors are shown in the figures.

4.2 Correction for contaminations from the TRG

The correction of the photon beam asymmetry for the TRG contamination events is performed as well as the correction for the π^+ and proton contamination. By using the contamination rate (C_{TRG}) and the photon beam asymmetry of the TRG events (Σ_{TRG}), the correction is made with the function of

$$\Sigma^{meas}_{K^+}(=\Sigma_{K^+}) = (1 - C_{TRG})\Sigma'_{K^+} + C_{TRG}\Sigma_{TRG}, \tag{4.9}$$

where Σ'_{K^+} is the photon beam asymmetry after the correction.

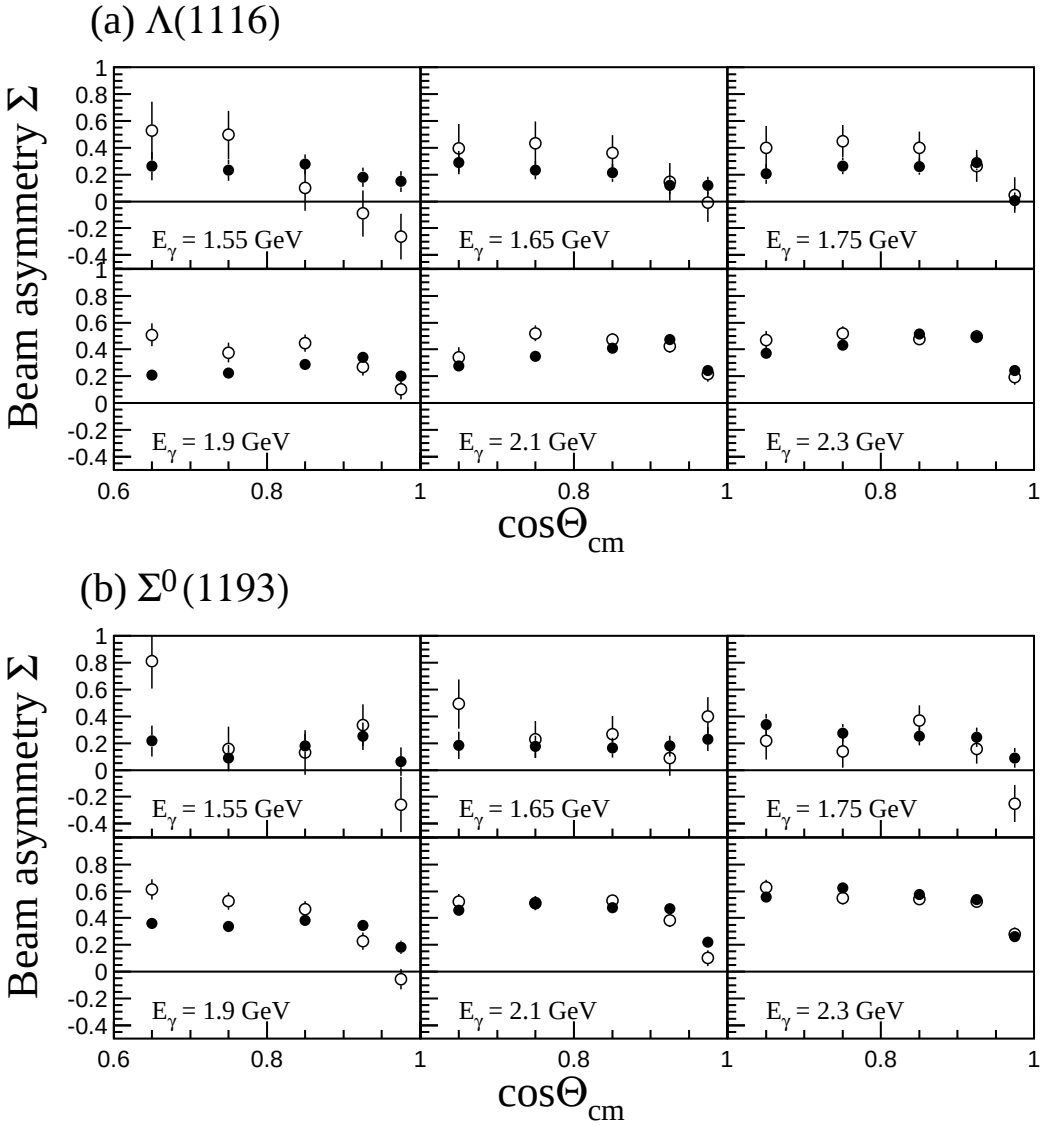

Figure 4.7: Photon beam asymmetries for (a) the K^+ Λ channel and (b) the K^+ Σ^0 channel. The The filled circles are for the events produced at the target and the open circles are for the TRG events.

The correction for the TRG events is performed to the beam asymmetry Σ_{K^+} in Eq. (4.8) obtained after the correction of the the π^+ and proton contamination. We assume that the TRG contamination rate is not different between for the K^+ event samples and for the π^+/proton event samples.

The photon beam asymmetries of the TRG events are obtained by using the events produced at the TRG which are selected by the z-vertex cut of $-880 <$ vtz < -830 after applying the cuts listed in Table 3.2 except for the vertex cut. Fig. 4.7(a) and (b) show the photon beam asymmetries for the K^+ Λ and K^+ Σ^0 production events. The filled circles are the beam asymmetries for the events produced at the target which are the same as the beam asymmetries Σ_{K^+} in Eq. (4.8) after the correction of the π^+ and proton contamination. The open circles are the beam asymmetries for the TRG events. The difference between the target events and the TRG events is small within the statistical error at most data points.

The contamination rate of the TRG events is plotted as a function of $\cos\Theta_{lab}$ in Fig. 3.22. The contamination rate at each $\cos\Theta_{cm}$ bin are obtained as the average of the contamination rate in the associated $\cos\Theta_{lab}$ range from the Fig. 3.22. Fig. 4.8(a) and (b) show the TRG contamination rate as a function of $\cos\Theta_{cm}$ for the K^+ Λ and K^+ Σ^0 production events. The

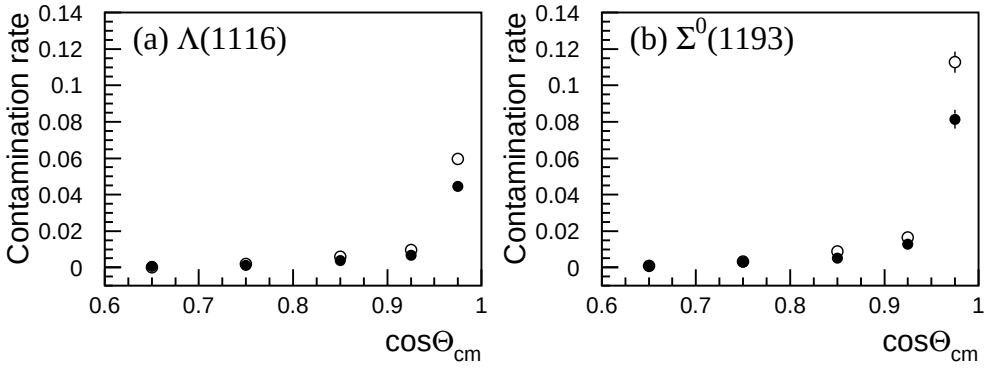

Figure 4.8: Contamination rate of the TRG events for (a) the $p(\gamma,K^+)\Lambda$ reaction and (b) the $p(\gamma,K^+)\Sigma^0$ reaction. The filled (open) circles are for the vertically (horizontally) polarized photon beam.

filled circles are for the vertically polarized photon beam and the open circles are for the horizontally polarized photon beam. These contamination rates are for the events integrating all over the photon energy. The average contamination rate of the vertically and horizontally polarized photon beams is used as C_{TRG}. The contamination rate is less than 2% in $\cos\Theta_{cm}$ < 0.95. It is much larger at the forward angle, $\cos\Theta_{cm} = 0.975$ and is 5% (10%) for the K^+ Λ (K^+ Σ^0) channel.

The photon beam asymmetry Σ_{K^+} is corrected for the TRG contamination by using Eq. 4.9. Fig. 4.9 shows the difference $\Sigma'_{K^+} - \Sigma_{K^+}$ for the $p(\gamma,K^+)\Lambda$ and $p(\gamma,K^+)\Sigma^0$ reaction. The error bars indicate the statistical errors. The difference is zero in $\cos\Theta_{cm} < 0.95$ due to the small contamination rate of the TRG events. At $\cos\Theta_{cm} = 0.975$, the difference is large due

to the large contamination rate. The difference is maximum at $E_\gamma = 1.75$ GeV and $\cos\Theta_{cm} = 0.975$ in the $p(\gamma,K^+)\Sigma^0$ reaction.

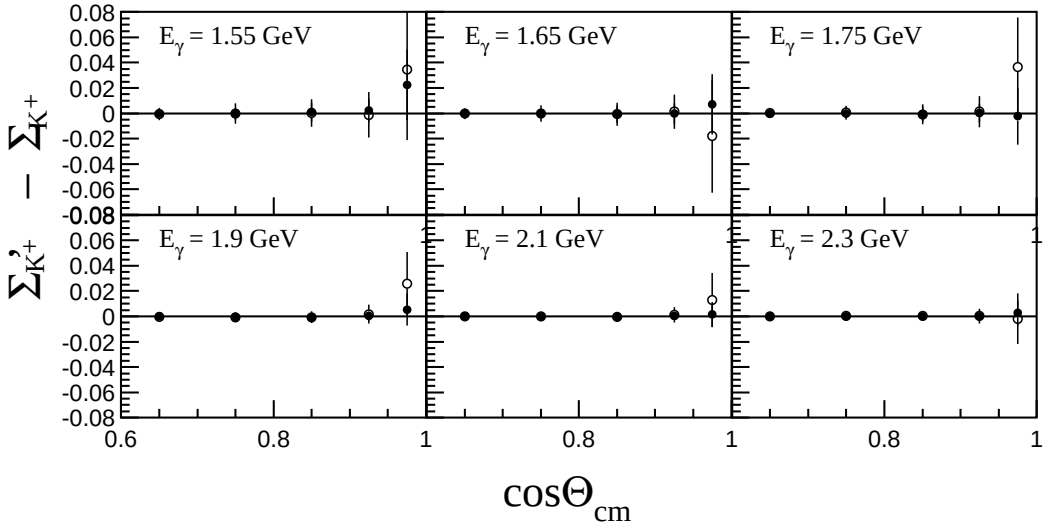

Figure 4.9: Difference $\Sigma'_{K^+} - \Sigma_{K^+}$ (after and before the correction) by the correction for the TRG contamination events. The filled and open circles are for the $p(\gamma,K^+)\Lambda$ and $p(\gamma,K^+)\Sigma^0$ reaction.

4.3 Contamination from the copper cell

A part of the photon beam hit the copper cell of the liquid hydrogen target and events are produced at the cell. Most of events produced at the copper cell are removed with the vertex positions (see Fig. 3.20). However there still remains a few of the events. The contamination rate of the events (C_{Cu}) is estimated to be $0.2 \pm 0.1\%$ from the x- and y-vertex distributions. The photon beam asymmetry of the events produced at the copper cell is obtained for the K^+ Λ and K^+ Σ^0 production events integrating over all the photon energy and angles. The results are

$$\Sigma_{Cu}^{\Lambda} = 0.353 \pm 0.086 \quad (4.10a)$$

$$\Sigma_{Cu}^{\Sigma^0} = 0.240 \pm 0.072. \quad (4.10b)$$

Although the photon beam asymmetry of the events produced at the copper cell would depend on the photon energy and scattering angle, we estimate the effect of the background events on the photon beam asymmetry by using these values assuming that there is no energy and angular dependences. By using the photon beam asymmetries of the copper events in Eq. (4.10) and the contamination rate 0.2%, the measured photon asymmetry Σ_{meas} is written as,

$$\Sigma_{meas} = (1 - C_{Cu})\Sigma_{K^+} + C_{Cu}\Sigma_{Cu}. \quad (4.11)$$

The difference $\Sigma_{meas} - \Sigma_{K^+}$ is within ± 0.001. Event if the beam asymmetry of the copper events is -1 or $+1$, the difference $\Sigma_{meas} - \Sigma_{K^+}$ is less than 0.003 at all the data points. Therefore, the effect of the copper events on the photon beam asymmetry is estimated to be ± 0.003 and is negligible.

4.4 Polarization degree and angle

The polarization degree and angle are measured by the monitor system per one run of about 3 hours. The average polarizations of laser photons were 98.7% and 95.0% for the vertical polarization and horizontal polarization during the present experiment. The polarization degree of laser photons was determined by measuring the intensity distribution with the photodiode in the monitor system. The intensity distribution (ADC spectrum) is fitted by a function of sinϕ as shown in Fig. 2.11. The systematic error for the measured polarization degree is estimated to be $\pm 1.5\%$.

The polarization angle defined as the angle ϕ from the horizontal plane (in the y direction) is also determined by the fitting with the intensity distribution. The angle of the polarization direction is shifted from 0° or 90° when the laser beam is optimized to have the maximum polarization. The average angle for the horizontal (vertical) polarization was 1.8° (88.2°) during the present experiment. The photon beam asymmetry is obtained assuming that the polarization angle is 0° (90°) in the case of the horizontal (vertical) polarization. When the polarization angle ϕ_h (ϕ_v) is shifted from 0° (90°), the amplitude $P\Sigma$ in Eq. (4.2) obtained by the fitting with a function of cos(2ϕ) is smaller than the real values. Therefore, the effect by this shift on the photon beam asymmetry is estimated.

If the photon beam asymmetry is 1, the yields N_v and N_h are written as

$$N_v(\phi) = 1 + \cos 2(\phi - \Delta\phi_v), \tag{4.12a}$$
$$N_h(\phi) = 1 - \cos 2(\phi - \Delta\phi_h), \tag{4.12b}$$

where $\Delta\phi_h$ ($\Delta\phi_v$) is the shift of the angle from the horizontal (vertical) direction. When the shifts were $\Delta\phi_v = 3°$ and $\Delta\phi_h = -4°$, the difference $\Delta\phi_v$ - $\Delta\phi_h$ was largest in the present experiment. The effect is estimated in this case. The plots in Fig. 4.10 show the ϕ distribution of the ratio as follows:

$$R = \frac{N_v(\phi) - N_h(\phi)}{N_v(\phi) + N_h(\phi)} = \frac{\cos 2(\phi - \Delta\phi_v) + \cos 2(\phi - \Delta\phi_h)}{2 + \cos 2(\phi - \Delta\phi_v) - \cos 2(\phi - \Delta\phi_h)} \tag{4.13}$$

where $\Delta\phi_v = 3°$ and $\Delta\phi_h = -4°$.

The solid line is the result of a fitting with a function of cos2ϕ. The result of the fitting is 0.996 for the amplitude 1. Therefore, the effect by the shift of the polarization angle is estimated to be less than 0.4%.

The systematic error for th polarization degree and angle is less than 2% in total.

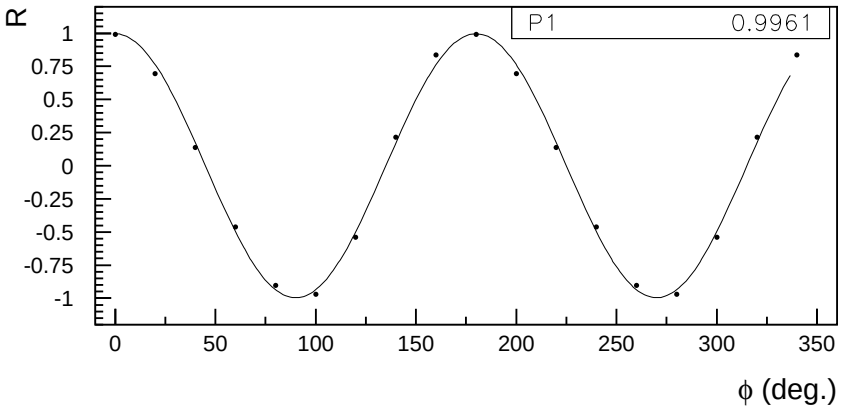

Figure 4.10: Ratio R of $(N_v(\phi) - N_h(\phi))/(N_v(\phi) + N_h(\phi))$ as a function of ϕ with $\Delta\phi_v$ = -4° and $\Delta\phi_h = 3°$. The solid line shows the result of a fitting by a function of cos2ϕ.

4.5 Normalization of the photon yield

The normalization factor Eq. (4.4) for the yields of the vertically and horizontally polarized photons is used to obtain the photon beam asymmetries. The normalization factor is important to apply a fitting with a function of

$$f(\phi) = p1 \cdot cos(2\phi) \tag{4.14}$$

where $p1$ is a fitting parameter for the amplitude. Especially the proper factor is essential to determine the photon asymmetry at cos$\Theta_{cm} < 0.82$ because the data points are limited in $\phi \sim 0°$ or $\phi \sim 180°$ as shown in Fig. 4.3(a).

The factor is determined by using the photon yield. However, the effect of the efficiency of the detectors is not taken into account. Although data was taken changing the photon polarization per a couple of hours to make the systematic error small, there may still remain the systematic error due to the efficiency of the detectors. The z-vertex distribution is different between the vertically and horizontally polarized photons, because the beam profile at the target is different for the vertical polarization and for the horizontal polarization. Therefore there is a possibility that the photon yields for the two polarizations are different by applying the z-vertex cut.

To investigate the accuracy of the normalization factor, a fitting with a function with an additional constant parameter ($p2$) is performed to the data points at cos$\Theta_{cm} > 0.82$ where the detectors cover 2π in the azimuthal angle. The fitting function is

$$f(\phi) = p1 \cdot cos(2\phi) + p2. \tag{4.15}$$

If the normalization factor is correctly determined, the result of the fitting for the parameter $p2$ would be zero. Fig. 4.11 shows the fitting results of the parameter $p2$ at some data points.

The constant parameter $p2$ is slightly lower than zero. The average value of the parameter $p2$ for these data points is -0.034 ± 0.394. When the normalization factor is determined again to make the average values of the parameter $p2$ for these data points zero, the factor $n' = 0.97$. The photon beam asymmetries are obtained by using this factor $n' = 0.97$ instead of $n = 0.923$ in Eq. (4.2). Fig. 4.12 shows the differences of the photon beam asymmetries determined by $n' = 0.97$ and by $n = 0.923$. The photon beam asymmetries increase at $\cos\Theta_{cm} < 0.9$ by using the larger values for the normalization factor while the asymmetries decreases at the forward angles. The differences are included in the systematic errors.

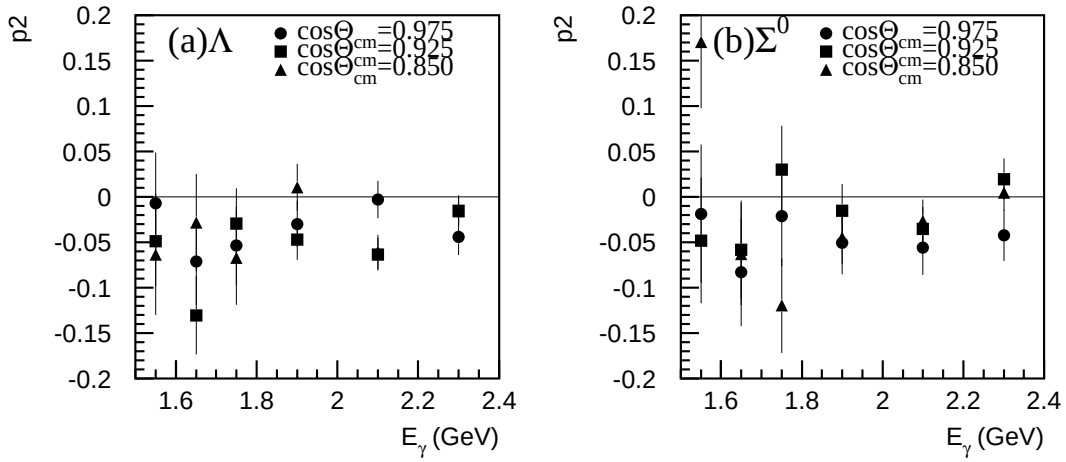

Figure 4.11: Results of a fitting for the constant parameter $p2$ for (a) the Λ and (b) the Σ^0 production.

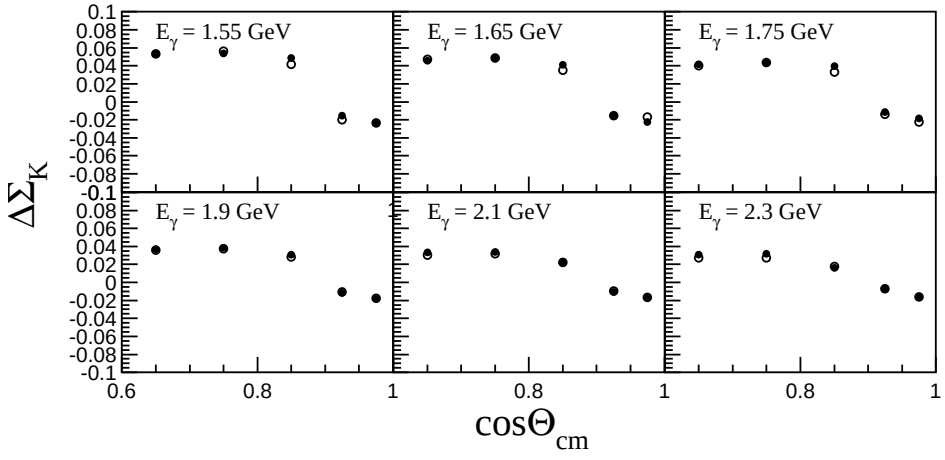

Figure 4.12: Difference Σ'_{K^+}(with $n' = 0.97$) - Σ_{K^+} (with $n = 0.923$). The filled circles are for the p(γ,K$^+$)Λ reaction and the open circles are for the p(γ,K$^+$)Σ^0 reaction.

4.6 Experimental results

Fig. 4.13(a) and (b) show the final results of the photon beam asymmetries. The plots are the present data. Only the statistical error is included in the error bars. The systematic error

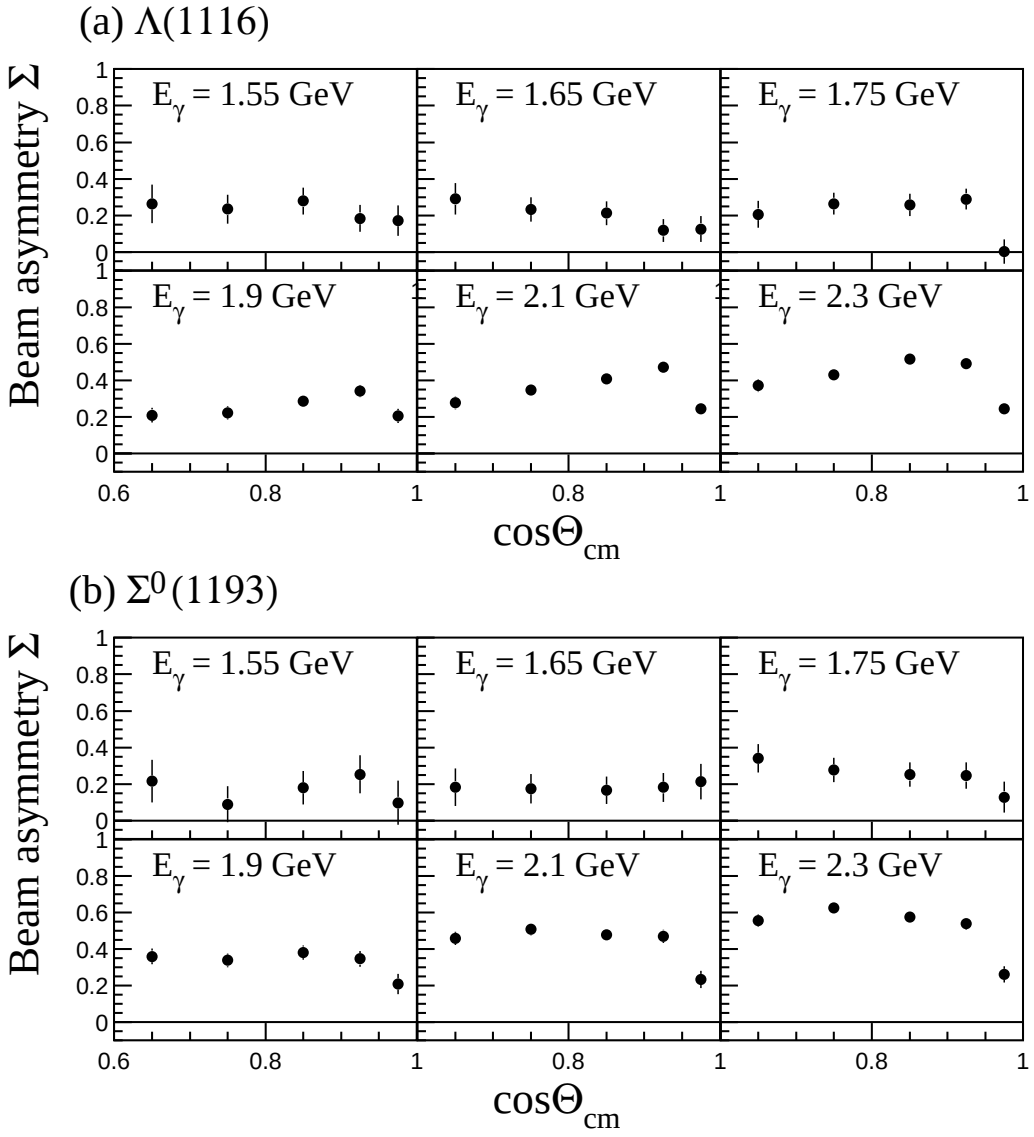

Figure 4.13: Photon beam asymmetries for (a) the p($\vec{\gamma}$,K$^+$)Λ and (b) the p($\vec{\gamma}$,K$^+$)Σ^0 reaction. The filled circles are the final results.

for the polarization degree and angle of the photons is less than 2%. The systematic error for the normalization factor is $\Delta\Sigma$ = -0.02 $\sim$ 0.06. The final results are summarized in Table 4.1. The ϕ distributions in Eq. (4.2) and the fitting results are shown in Fig. C.1 and Fig. C.2 in Appendix C. The detail results of the correction of the π^+/proton and the TRG contamination

events, and the values of the photon beam asymmetry of the K^+ event samples are summarized in Appendix C. The results of the photon beam asymmetries are also obtained by the same studies when the data are divided into nine energy bins with 100 MeV width from 1.5 to 2.4 GeV. The results are shown in Appendix D.

Table 4.1: The final results of the photon beam asymmetry for the $p(\gamma,K^+)\Lambda$ and $p(\vec{\gamma},K^+)\Sigma^0$ reaction. The systematic error for the normalization factor is shown. The other 2% systematic error exists.

E_γ (GeV)	$\cos\Theta_{cm}$	$\Sigma^{\Lambda}_{K^+}$ $\pm$ statistical error	Systematic error	$\Sigma^{\Sigma^0}_{K^+}$ $\pm$ statistical error	Systematic error
1.55	0.650	0.263 $\pm$0.1045	0.0529	0.216 $\pm$0.1167	0.0531
1.55	0.750	0.234 $\pm$0.0786	0.0535	0.089 $\pm$0.0990	0.0563
1.55	0.850	0.278 $\pm$0.0742	0.0487	0.180 $\pm$0.0915	0.0418
1.55	0.925	0.183 $\pm$0.0725	-0.0156	0.252 $\pm$0.1037	-0.0200
1.55	0.975	0.171 $\pm$0.0828	-0.0231	0.097 $\pm$0.1205	-0.0234
1.65	0.650	0.291 $\pm$0.0866	0.0456	0.184 $\pm$0.1027	0.0475
1.65	0.750	0.233 $\pm$0.0676	0.0483	0.175 $\pm$0.0801	0.0490
1.65	0.850	0.213 $\pm$0.0661	0.0416	0.166 $\pm$0.0754	0.0351
1.65	0.925	0.118 $\pm$0.0622	-0.0154	0.182 $\pm$0.0789	-0.0155
1.65	0.975	0.126 $\pm$0.0715	-0.0225	0.214 $\pm$0.0986	-0.0171
1.75	0.650	0.205 $\pm$0.0737	0.0417	0.341 $\pm$0.0789	0.0404
1.75	0.750	0.264 $\pm$0.0606	0.0431	0.277 $\pm$0.0662	0.0435
1.75	0.850	0.257 $\pm$0.0607	0.0397	0.251 $\pm$0.0668	0.0329
1.75	0.925	0.288 $\pm$0.0573	-0.0112	0.245 $\pm$0.0718	-0.0136
1.75	0.975	0.002 $\pm$0.0670	-0.0183	0.128 $\pm$0.0849	-0.0223
1.90	0.650	0.209 $\pm$0.0407	0.0369	0.359 $\pm$0.0427	0.0357
1.90	0.750	0.222 $\pm$0.0351	0.0383	0.338 $\pm$0.0383	0.0375
1.90	0.850	0.287 $\pm$0.0331	0.0309	0.380 $\pm$0.0382	0.0284
1.90	0.925	0.341 $\pm$0.0321	-0.0119	0.346 $\pm$0.0429	-0.0105
1.90	0.975	0.206 $\pm$0.0378	-0.0179	0.208 $\pm$0.0557	-0.0177
2.10	0.650	0.276 $\pm$0.0347	0.0332	0.458 $\pm$0.0356	0.0304
2.10	0.750	0.346 $\pm$0.0302	0.0335	0.508 $\pm$0.0337	0.0314
2.10	0.850	0.407 $\pm$0.0264	0.0224	0.476 $\pm$0.0318	0.0223
2.10	0.925	0.472 $\pm$0.0256	-0.0105	0.469 $\pm$0.0354	-0.0093
2.10	0.975	0.244 $\pm$0.0301	-0.0168	0.233 $\pm$0.0474	-0.0165
2.30	0.650	0.371 $\pm$0.0344	0.0307	0.556 $\pm$0.0342	0.0272
2.30	0.750	0.431 $\pm$0.0295	0.0315	0.624 $\pm$0.0315	0.0273
2.30	0.850	0.515 $\pm$0.0236	0.0162	0.575 $\pm$0.0293	0.0177
2.30	0.925	0.490 $\pm$0.0248	-0.0076	0.539 $\pm$0.0339	-0.0072
2.30	0.975	0.245 $\pm$0.0299	-0.0158	0.261 $\pm$0.0449	-0.0162

4.7 Discussion

1. The signs of the experimental results for the photon beam asymmetries are positive for both reactions in the measured kinematical region as shown in Fig. 4.13(a) and (b). The magnitude of the photon beam asymmetries for the $p(\vec{\gamma},K^+)\Lambda$ reaction is not so different from that for the $p(\vec{\gamma},K^+)\Sigma^0$ reaction.

   The photon beam asymmetry for the $p(\vec{\gamma},K^+)\Lambda$ reaction increases as the photon energy increases. The photon beam asymmetry above $E_\gamma = 1.7$ GeV slightly drops at larger angles while it shows the flat angular distribution below $E_\gamma = 1.7$ GeV. The shape of the angular distribution does not depend on the photon energy above $E_\gamma = 1.7$ GeV although the values increase as the increase of the photon energy.

   The photon beam asymmetry for the $p(\vec{\gamma},K^+)\Sigma^0$ reaction also increases as the photon energy increases. The angular distributions are flat over all the photon energy range.

2. Recently the photon beam asymmetries for the $p(\vec{\gamma},K^+)\Lambda$ reaction were measured by the GRAAL collaboration up to 1.4 GeV in the photon energy [42]. Fig. 4.14 shows the preliminary GRAAL data. The photon beam asymmetries were measured in the photon energy from 1.05 GeV to 1.4 GeV in the 4π angular range. Our data for the $p(\vec{\gamma},K^+)\Lambda$ reaction is compared with the GRAAL data around $E_\gamma = 1.5$ GeV. The experimental result obtained by the GRAAL collaboration shows the flat angular distribution at $E_\gamma = 1.4$ GeV. The values of the photon asymmetries are about 0.25 at $E_\gamma = 1.4$ GeV. Our results also show the flat angular distribution and the values are about 0.25 at $E_\gamma = 1.55$ GeV. Our results indicate a good connection to the GRAAL data.

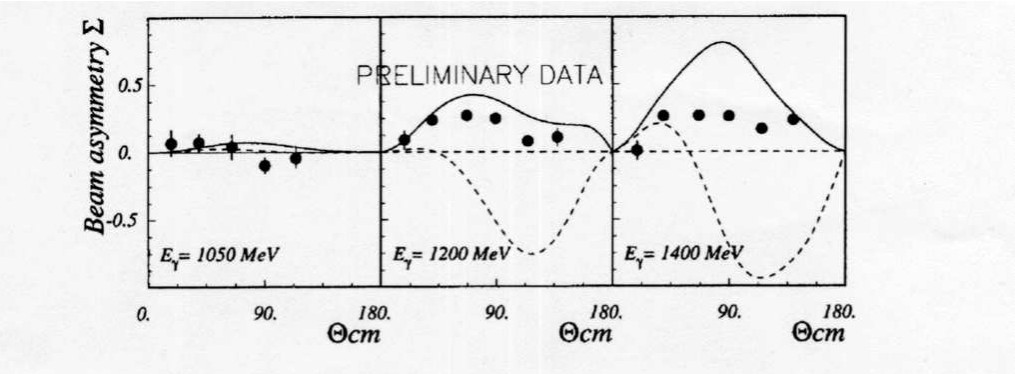

Figure 4.14: Photon beam asymmetries for the $p(\vec{\gamma},K^+)\Lambda$ reaction measured by the GRAAL collaboration [42]. The solid (dashed) lines show the results of the theoretical calculations with (without) the missing resonance D_{13} by Mart and Bennhold [6].

3. Our experimental results are compared with the theoretical predictions in Fig. 4.15 and Fig. 4.16. The plots are our data. The lines indicate the theoretical predictions which are the same as those in Fig. 1.3, Fig. 1.4 and Fig. 1.5. The solid and dashed lines in Fig. 4.15 show the results predicted by the theoretical models with and without the

missing resonance $D_{13}(1960)$, respectively, in the s-channel by Mart and Bennhold [6]. Both models result in the positive sign which is the same as our data. The solid line reproduces our data better than the dashed line at $E_\gamma = 1.75$ GeV.

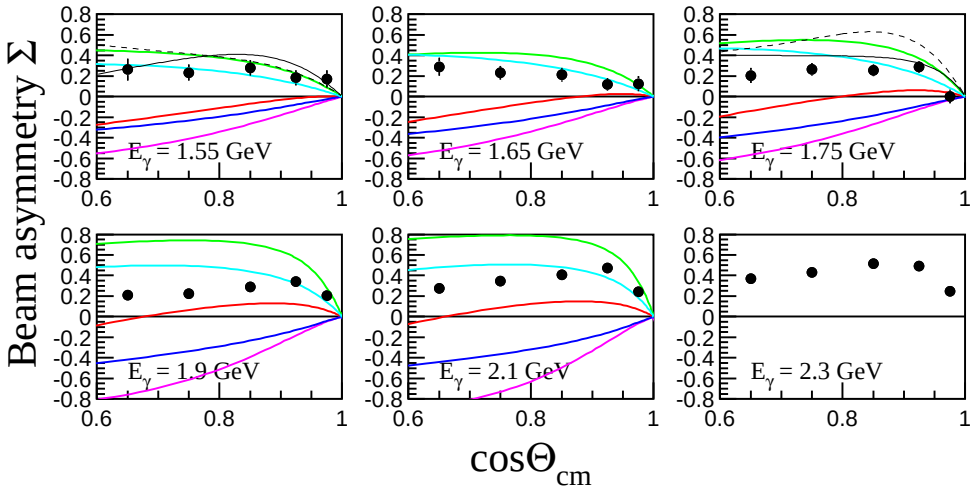

Figure 4.15: Photon beam asymmetries for the $p(\vec{\gamma},K^+)\Lambda$ reaction. The data plots are the present data. The lines are theoretical predictions [6, 7, 14].

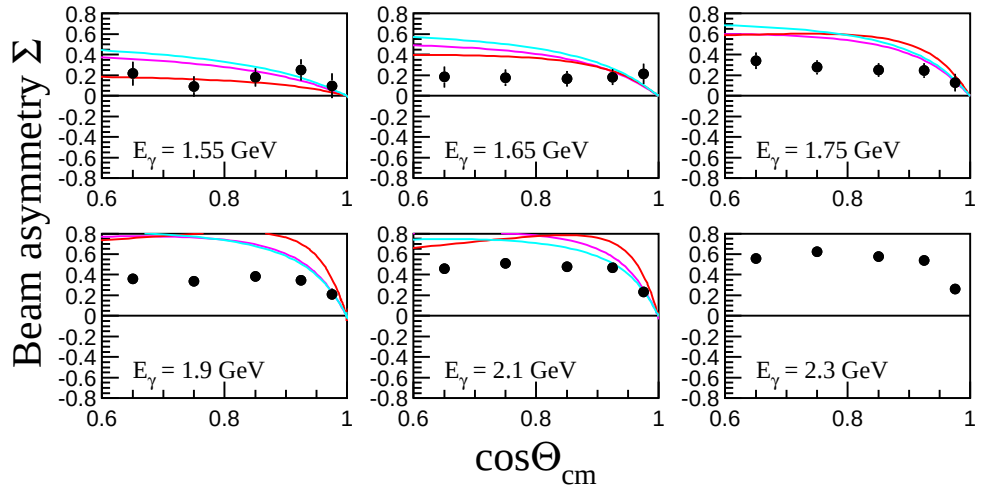

Figure 4.16: Photon beam asymmetries for the $p(\vec{\gamma},K^+)\Sigma^0$ reaction. The data plots are the present data. The lines are theoretical predictions [7, 14].

The color lines in Fig. 4.15 and Fig. 4.16 are the results of the theoretical calculations by Janssen *et al.* [7, 14]. These lines are the same as the statements of Fig. 1.4 and Fig. 1.5. For the $p(\vec{\gamma},K^+)\Lambda$ reaction, the blue and pink lines show the negative signs in all the energy region and the red line also indicates the negative sign in $E_\gamma < 1.7$ GeV while the sign of the present experimental results is positive over all the ranges. The green lines

show much larger values than the present data at the high energy region $E_\gamma > 1.7$ GeV. The light blue, which is the model C without the restriction of the SU(3) symmetry and using hadronic form factors F_{DW} suggested by Davidson and Workman [13], reproduces the present data better than the other models. However, this model (light blue) dose not show the angular distribution as seen in the experimental results in the energy region $E_\gamma > 1.7$ GeV.

For the $p(\gamma,K^+)\Sigma^0$ reaction, the results of the theoretical models have all positive signs as shown in Fig. 1.5 and Fig. 4.16. The values are not different for the various models. Although the photon asymmetries calculated by the theoretical models are similar to the present data at $E_\gamma = 1.55$ GeV, they are much larger than the data at the higher energy.

4. The present theoretical models cannot reproduce our data perfectly over all energy region, especially at the high energy side. Our experimental data shows the energy dependence clearly for both the reactions. The photon beam asymmetry of our data increases as the increase of the photon energy. On the other hand, the theoretical models do not show the energy dependence at the high energy. The contribution of the t-channel may cause this energy dependence. Further theoretical studies on the t-channel contribution are required in the high energy region.

5. Currently there are ambiguities in the theoretical models and it is difficult to conclude the existence of missing resonances because of the lack of the experimental data. Our experimental results should be included into the theoretical studies. Even if the models can reproduce the cross section data measured by the SAPHIR, the theoretical models should be examined by using the photon asymmetry data.

6. Recently, the differential cross sections and the recoil polarizations of the $p(\gamma,K^+)\Lambda$ and $p(\gamma,K^+)\Sigma^0$ reactions were measured by the JLAB/CLAS collaboration [44, 45] with much more statistics than the SAPHIR data. Since the spectrometer in CLAS covers almost 4π, they determine the differential cross sections with the large acceptance. Their data indicates the two structures at different angular ranges in the differential cross sections for the $p(\gamma,K^+)\Lambda$ reaction. They suggest a possibility that there are two missing resonances in this reaction channel around $E_\gamma = 1.5$ GeV. Although the current theoretical models including only one missing resonance $D_{13}(1960)$ cannot reproduce our data perfectly, models may explain our data by including these resonances.

7. It is more difficult to analyze the channels involving Σ because not only N^* but also Δ^* can contribute to this reaction. There are difficulties associated with broad or overlapping resonances. We obtained the photon beam asymmetries for the $p(\gamma,K^+)\Sigma^0$ reaction as well as the $p(\gamma,K^+)\Lambda$ reaction. We want more theoretical studies in the $p(\gamma,K^+)\Sigma^0$ reaction, because missing resonances may be found in this reaction.

Chapter 5

Summary

Experimental information on the baryon resonances, N^* and Δ^*, has been mainly accumulated by the studies of the πN and N(γ,π) reactions. However, considerably large number of nucleon resonances predicted by quark models have not been observed in the pionic reactions [1, 2]. Therefore, the K^+ photoproduction is a promising field to obtain information on the existence of new excited states of the nucleon. We measured the photon beam asymmetries of the K^+ photoproduction.

In order to study the meson and baryon photoproduction experimentally, we constructed the LEPS beam line at SPring-8 in 2000. The LEPS facility provides linear-polarized photons with the high energy, the high polarization and the high intensity by using the backward-Compton scattering (BCS) process of laser photons from 8-GeV electrons in the storage ring. The Ar laser with the wavelength of 351 nm is used. Since the polarization of laser photons is achieved to be about 98%, the polarization of the BCS photons is also high and is about 92% at the maximum photon energy. The energy of the BCS photons ranged from 1.5 GeV to 2.4 GeV is measured by the tagging system with the energy resolution of 15 MeV (RMS). The intensity of the tagged photon is about 5×10^5 photons/sec.

We constructed a new magnetic spectrometer in the experimental hutch. The magnetic spectrometer is optimized to study the ϕ-meson photoproduction at forward angles. The charged particles are identified by the time-of-flight and momentum measurement. The time-of-flight is measured by using the RF signals from the 8-GeV storage ring, and the TOF wall. The time resolution of 110 ps is achieved by using the RF signals with a width of 12 ps. The momentum measurement is performed by using the silicon strip detectors and the drift chambers. The Kalman filter method is employed to determine the momentum in the track fitting. The effect of multiple scattering is treated correctly in the Kalman filter code. The background events including the decay-in-flight events are removed by the χ^2 probability. The momentum resolution is roughly 5 MeV/c.

The first experiment in the SPring-8/LEPS facility has been carried out from December 2000 to June 2001. The hadron photoproduction was measured by using the BCS photons and the liquid hydrogen target. Two data sets were collected by vertically and horizontally polarized photons. From this experimental data, we study the ϕ, ω, $2\pi^0$ and K^+ photoproduction and baryon resonance Z^+ with $S = +1$ [46, 47, 48, 49, 50, 51].

In the present analysis, the photon beam asymmetries for the $p(\vec{\gamma},K^+)\Lambda(1116)$ and $p(\vec{\gamma},K^+)\Sigma^0$ (1193) reactions were obtained in the energy range 1.5 GeV $\leq E_\gamma \leq$ 2.4 GeV and the K^+ angular range $0.6 \leq \cos\Theta_{cm} \leq 1$. The photon beam asymmetries for these reactions were measured for the first time in this photon energy range. About 72,500 $K^+\Lambda$ and 48,900 $K^+\Sigma^0$ reaction events were detected and used for this analysis. The $p(\vec{\gamma},K^+)\Lambda$ and $p(\vec{\gamma},K^+)\Sigma^0$ reaction events were identified by using the reaction vertex, the mass distribution and the missing mass distribution. The separation between the K^+ events and the π^+/proton events in the mass distribution was good. The contamination rates from the π^+ events and proton events were about 4% at the highest momentum $\sim$ 2 GeV/c. Background events, which were mostly due to the decay-in-flight events, were rejected by the χ^2 values of the track reconstruction. The separation between the $\Lambda(1116)$ and Σ^0 (1193) events in the missing mass distribution was also good. Each reaction event was identified with a 2σ cut with the contamination rate of $< 1\%$.

We obtained the angular distributions of the photon beam asymmetry in some energy bins. The experimental results of the photon beam asymmetries are the positive sign for both the reactions in the measured kinematical regions. The difference between the $p(\vec{\gamma},K^+)\Lambda$ and $p(\vec{\gamma},K^+)\Sigma^0$ reactions is seen in the angular distributions in the high energy region. The values of the photon beam asymmetry for the $p(\vec{\gamma},K^+)\Lambda$ reaction drops in the larger angles while the results for the $p(\vec{\gamma},K^+)\Sigma^0$ reaction show the flat angular distributions. The values of the photon beam asymmetries for both reactions increase as the photon energy increases. This energy dependence may be caused by the contribution of the t-channel meson exchange.

The present models cannot reproduce our data of the photon asymmetries perfectly since theoretical models of the K^+ photoproduction are not fixed due to the lack of data. Theoretical models will be examined and improved by including our data. Current data will extend our knowledge of the K^+ photoproduction mechanism including the effect of nucleon resonances.

Acknowledgments

I would like to thank many people for their supports, encouragement and advice to complete the present work.

I would like to express my sincere gratitude to my supervisors, Prof. Atsushi Sakaguchi, Prof. Takashi Nakano, Prof. Mamoru Fujiwara and Prof. Tadafumi Kishimoto. I had the great opportunity to work on the experiment at the SPring-8/LEPS facility under the guidance of all of them. And I completed this thesis under the guidance of Prof. Atsushi Sakaguchi.

I would like to express my sincere appreciation to Ms. E. Matsumoto, Ms. M. Aratake and Ms. I. Nakano for many works to support me.

I would like to acknowledge Advanced Science Research Center of JAERI for the financial support to stay at the SPring-8 site. Thanks to the support, I devoted myself to the present study.

I would like to thank Dr. R.G.T. Zegers for the discussions with him and his supports, encouragement and advice, especially for the present analyses of the K^+ photoproduction.

I really appreciate Prof. J-K. Ahn, Dr. T. Hotta, Dr. Y. Sugaya, Dr. T. Yorita, Dr. W.C. Chang, Dr. H. Kohri, Dr. N. Muramatsu, Mr. T. Ishikawa, Mr. T. Matsumura, Mr. T. Mibe, Mr. T. Ooba and Mr. Y. Shiino. I am deeply grateful for their helpful suggestions and supports to work on the experiment and the data analyses.

I would like to thank Prof. M. Nomachi, Prof. H. Shimizu, Dr. N. Matsuoka, Dr. M. Yosoi, Prof. H. Akimune, Dr. K. Yonehara Prof. T. Iwata and Dr. A. Wakai for many works and supports to perform the experiment with the detection systems, the laser operation system, etc.

I would like to thank Dr. Y. Ohashi, Dr. S. Date, Dr. Y. Asano, Dr. H. Toyokawa, Dr. N. Kumagai, Dr. H. Ookuma and other staffs of SPring-8. The LEPS beam line (BL33LEP) would not be established successfully without their helpful and great supports.

I would like to thank my collaborators, Prof. H.Hicks, Prof. C.Rangacharyulu, Dr. P. Shagin, Prof. H. Ejiri, Dr. H. Fujimura, Mr. M. Morita, Ms. D.S. Ahn, Prof. K. Imai, Mr. T. Sasaki, Mr. M. Miyabe, Mr. M. Niiyama, Mr. T. Miwa Mr. Z.Y. Kim, Dr. D.S. Oshuev, Prof. C.W. Wang, Dr. S.C. Wang, Dr. K. Kino, Mr. Y.Toi, Prof. H. Kawai and Prof. S.Makino for their supports. I believe the experiment was not successfully finished without their supports.

Appendix A

Performance of TOF counters

The time resolution, y-position resolution, attenuation length and effective velocity in each TOF counter which were used during the present experiment are plotted in Fig.A.1 and are summarized in Table A.1. The counter #1 was placed at the right side and the counter #40 was placed at the left side in the TOF wall in the beam (+z) direction. The attenuation lengths (effective velocities) deteriorated within 10% (0.5%) during the experiment. In Table A.1, the average values during the experiment are listed. The errors are statistical errors.

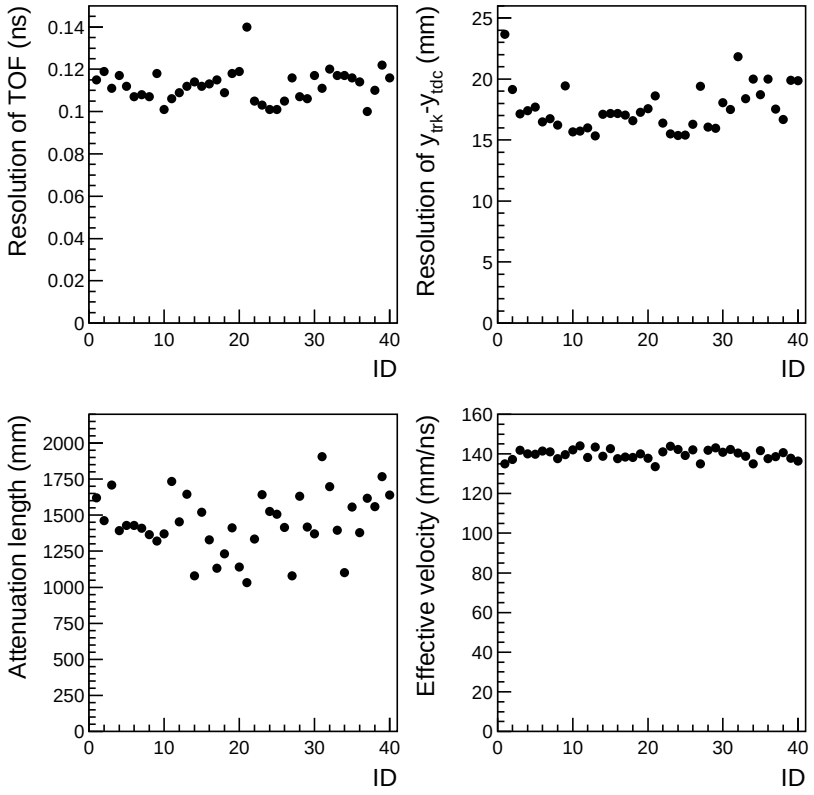

Figure A.1: (a):Resolutions of time-of-flights (ns), (b):Resolutions of Δ(y_{trk} - y_{tdc}) (mm), (c):Attenuation lengths (mm) and (d):Effective velocity. The x-axis is the counter number of the TOF wall.

counter #	Time resolution (nsec)	Position resolution $\Delta(y_{trk} - y_{tdc})$ (mm)	Attenuation length (mm)	Effective velocity (mm/nsec)
1	.115	23.65	1620.4 ± .190	134.93 ± .016
2	.119	19.15	1463.0 ± .135	137.16 ± .013
3	.111	17.15	1707.8 ± .160	141.78 ± .013
4	.117	17.42	1393.6 ± .123	139.95 ± .012
5	.112	17.69	1428.5 ± .132	139.92 ± .013
6	.107	16.50	1430.1 ± .120	141.41 ± .012
7	.108	16.75	1408.3 ± .120	140.98 ± .012
8	.107	16.23	1364.7 ± .108	137.53 ± .011
9	.118	19.44	1322.1 ± .115	139.55 ± .012
10	.101	15.66	1371.7 ± .118	141.96 ± .012
11	.106	15.74	1733.6 ± .136	144.15 ± .011
12	.109	16.00	1453.3 ± .108	138.16 ± .010
13	.112	15.35	1643.9 ± .121	143.41 ± .010
14	.114	17.12	1078.6 ± .086	138.74 ± .011
15	.112	17.18	1519.5 ± .108	142.71 ± .010
16	.113	17.17	1328.4 ± .105	137.70 ± .011
17	.115	17.03	1131.0 ± .085	138.44 ± .010
18	.109	16.57	1232.4 ± .091	138.30 ± .010
19	.118	17.26	1411.9 ± .097	140.01 ± .009
20	.119	17.56	1140.1 ± .087	137.89 ± .010
21	.140	18.63	1033.4 ± .075	133.52 ± .010
22	.105	16.38	1333.3 ± .101	141.13 ± .011
23	.103	15.50	1641.4 ± .119	143.84 ± .010
24	.101	15.36	1524.8 ± .114	142.32 ± .011
25	.101	15.42	1505.2 ± .116	139.19 ± .011
26	.105	16.28	1415.0 ± .113	142.12 ± .011
27	.116	19.42	1080.7 ± .097	135.00 ± .012
28	.107	16.05	1632.7 ± .145	141.74 ± .013
29	.106	15.95	1419.1 ± .135	143.12 ± .014
30	.117	18.06	1369.4 ± .138	140.81 ± .014
31	.111	17.52	1906.1 ± .212	142.30 ± .016
32	.120	21.83	1699.1 ± .205	140.33 ± .017
33	.117	18.40	1396.7 ± .171	138.90 ± .017
34	.117	20.01	1102.7 ± .138	134.89 ± .017
35	.116	18.72	1557.3 ± .207	141.61 ± .019
36	.114	19.98	1380.2 ± .206	137.62 ± .020
37	.100	17.54	1618.0 ± .228	138.65 ± .019
38	.110	16.69	1558.1 ± .245	140.72 ± .022
39	.122	19.89	1768.3 ± .264	137.72 ± .020
40	.116	19.88	1638.5 ± .291	136.35 ± .024

Table A.1: Parameters of TOF counters.

Appendix B

Tables of the asymmetries - E_γ and $\cos\Theta_{cm}$ dependences

The E_γ dependence and angular dependence of the photon beam asymmetry for the $p(\gamma,K^+)\Lambda$ and $p(\gamma,K^+)\Sigma^0$ reactions are obtained by integrating over all the angles and over all the photon energy.

The photon beam asymmetries Σ_Λ and Σ_{Σ^0}, the statistical errors, χ^2 of the fitting and the average polarizations $\bar{P}_\gamma$ are listed in Table $B.1$ and $B.2$.

Fig. B.1 and Fig. B.2 show the ϕ distributions of the ratios R of $(n \cdot N_v - N_h)/(n \cdot N_v + N_h)$ in Eq.(4.2) to obtain the E_γ dependence. The photon energy and the fitting results are displayed in the figures. Fig. B.3 and Fig. B.4 also show the ϕ distributions of the ratios R of $(n \cdot N_v - N_h)/(n \cdot N_v + N_h)$ in Eq.(4.2) to obtain the $\cos\Theta_{cm}$ dependence. The K^+ scattering angle $\cos\Theta_{cm}$ and the fitting results are displayed in the figures. The solid lines are the results of the fitting using a function of $\cos(2\phi)$.

Table B.1: Energy dependence of the photon beam asymmetry in the $p(\gamma,K^+)\Lambda$ and the $p(\gamma,K^+)\Sigma^0$ reaction integrating over all the angles.

E_γ (GeV)	$\Sigma_\Lambda \pm$error	χ^2	P_γ	$\Sigma_{\Sigma^0} \pm$error	χ^2	P_γ
1.55	0.221 ±0.0341	0.91	0.571	0.150 ±0.0430	0.50	0.571
1.65	0.190 ±0.0296	0.69	0.641	0.177 ±0.0350	1.16	0.642
1.75	0.203 ±0.0266	1.10	0.712	0.232 ±0.0302	1.41	0.711
1.85	0.224 ±0.0216	1.00	0.768	0.279 ±0.0250	0.98	0.768
1.95	0.282 ±0.0201	1.89	0.817	0.342 ±0.0242	0.80	0.817
2.05	0.309 ±0.0170	1.18	0.854	0.404 ±0.0203	1.40	0.854
2.15	0.386 ±0.0167	1.61	0.881	0.425 ±0.0207	1.06	0.881
2.25	0.386 ±0.0151	1.68	0.897	0.470 ±0.0182	1.74	0.897
2.35	0.409 ±0.0170	1.98	0.905	0.526 ±0.0193	1.69	0.905

Table B.2: Angular dependence of the photon beam asymmetry in the $p(\gamma,K^+)\Lambda$ and the $p(\gamma,K^+)\Sigma^0$ reaction integrating over all the photon energy.

$\cos\Theta_{cm}$	$\Sigma_\Lambda \pm$error	χ^2	$\bar{P}_\gamma$	$\Sigma_{\Sigma^0} \pm$error	χ^2	$\bar{P}_\gamma$
0.626	0.243 ±0.0306	1.18	0.817	0.424 ±0.0311	2.09	0.819
0.670	0.286 ±0.0266	1.03	0.808	0.429 ±0.0276	2.96	0.812
0.714	0.296 ±0.0246	1.80	0.798	0.412 ±0.0267	2.43	0.806
0.758	0.327 ±0.0238	1.51	0.801	0.436 ±0.0265	3.03	0.803
0.802	0.298 ±0.0236	2.98	0.806	0.414 ±0.0274	1.56	0.801
0.846	0.379 ±0.0220	1.53	0.810	0.440 ±0.0266	1.72	0.808
0.890	0.438 ±0.0171	2.57	0.812	0.408 ±0.0212	1.93	0.807
0.934	0.363 ±0.0146	2.19	0.803	0.361 ±0.0197	1.23	0.800
0.978	0.181 ±0.0167	1.89	0.804	0.197 ±0.0235	0.88	0.797

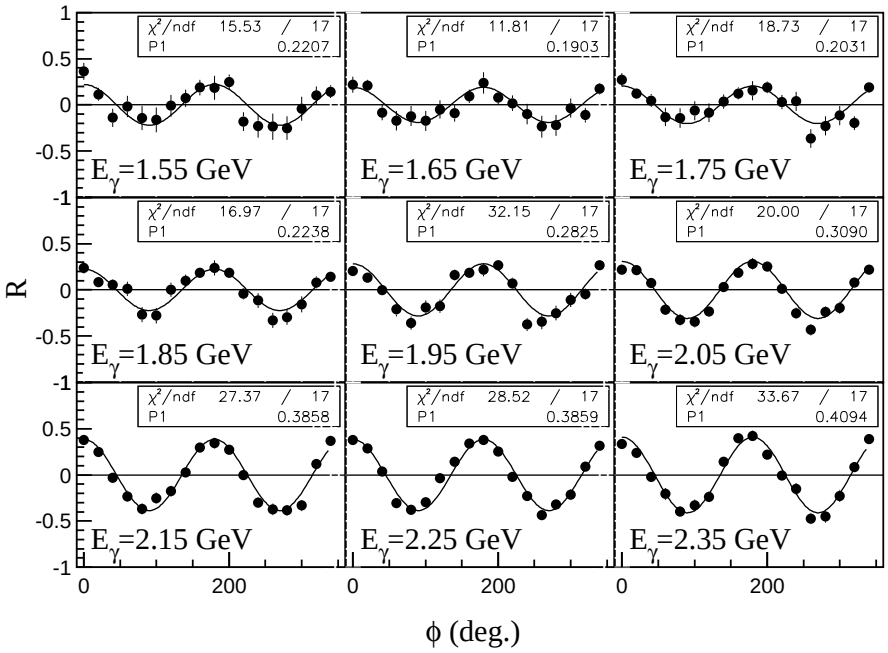

Figure B.1: ϕ distribution of the ratio R for the p(γ,K$^+$)Λ reaction. The E_γ dependence integrating over all angles.

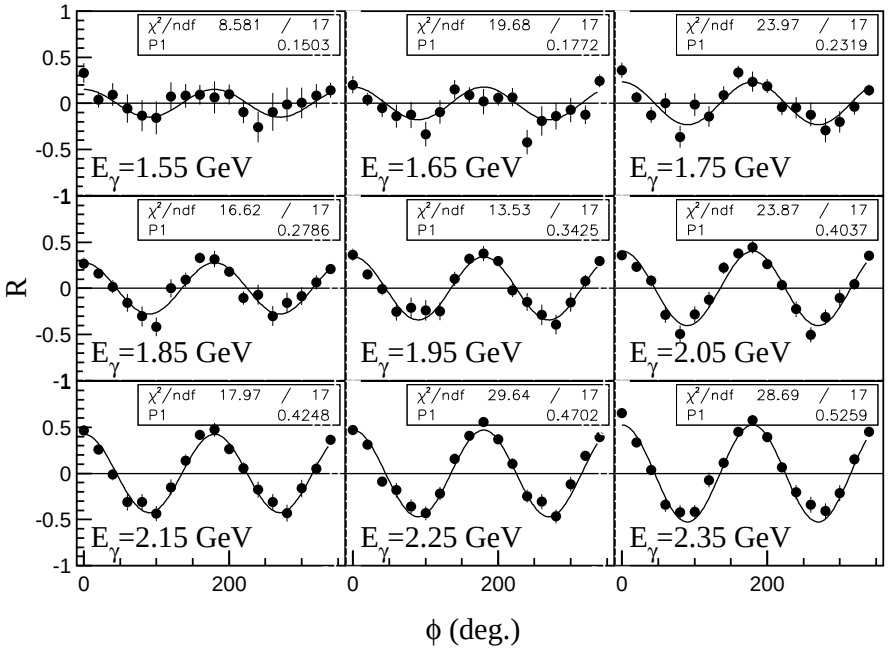

Figure B.2: ϕ distribution of the ratio R for the p(γ,K$^+$)Σ^0 reaction. The E_γ dependence integrating over all angles.

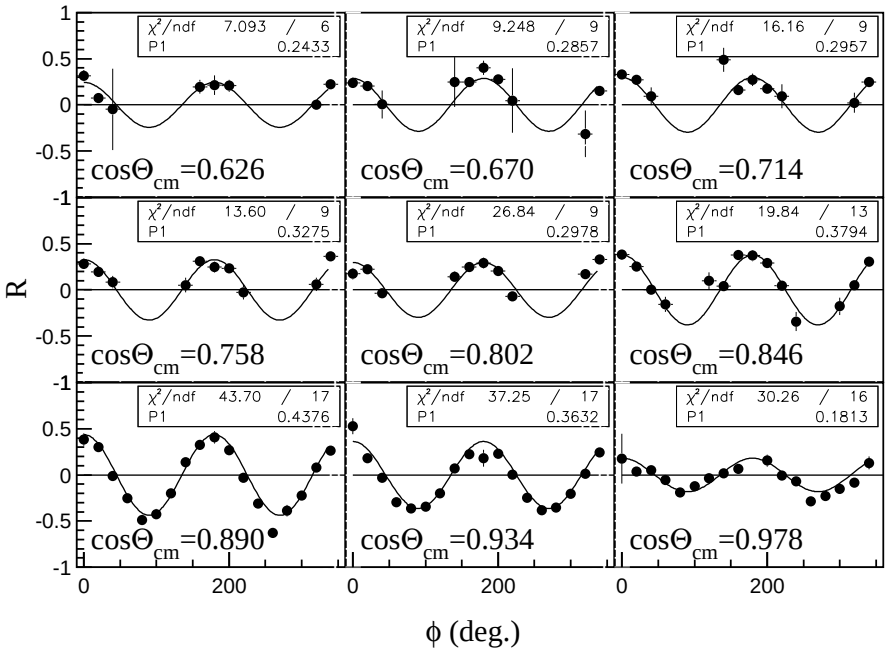

Figure B.3: ϕ distribution of the ratio R for the p(γ,K$^+$)Λ reaction. The Θ_{cm} dependence integrating all over the photon energy.

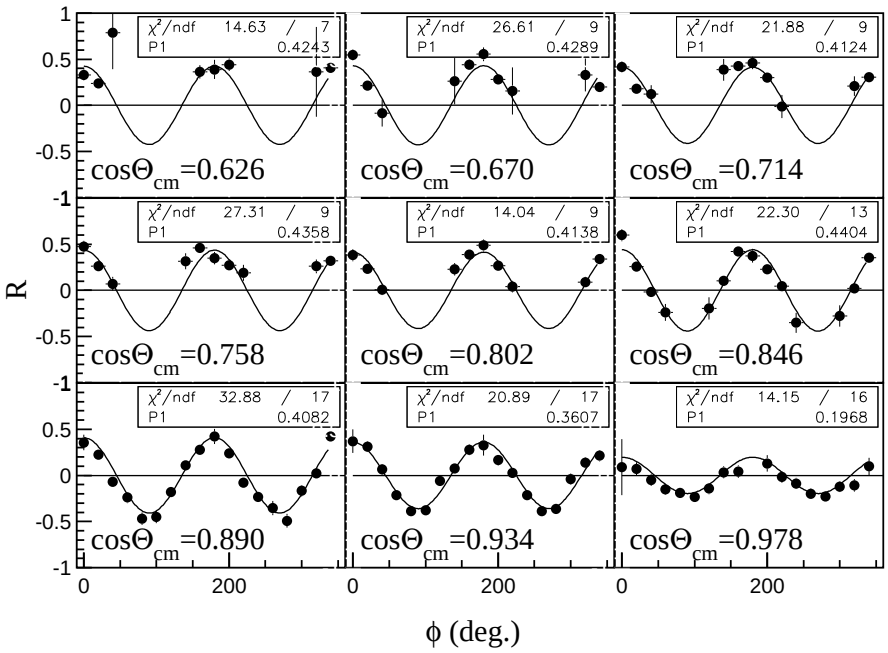

Figure B.4: ϕ distribution of the ratio R for the p(γ,K$^+$)Σ^0 reaction. The Θ_{cm} dependence integrating all over the photon energy.

Appendix C

Tables of the asymmetries - the six energy bins

The angular distributions of the photon beam asymmetries in the six energy bins are summarized for the p(γ,K$^+$)Λ and p(γ,K$^+$)Σ^0 reactions.

The results of the photon beam asymmetries for the K$^+$ event samples are summarized in Table C.1 and Table C.2. The photon beam asymmetries $\Sigma_{K^+}^{meas}$, the statistical errors, χ^2 of the fitting and the average polarizations $\bar{P}_\gamma$ are listed. The photon beam asymmetries $\Sigma_{K^+}^{meas}$ are before the correction of the background contamination (the π^+/proton and the TRG events). Fig. C.1 and Fig. C.2 show the ϕ distributions of the ratios R of $(n \cdot N_v - N_h)/(n \cdot N_v + N_h)$ in Eq.(4.2) for the p(γ,K$^+$)Λ and p(γ,K$^+$)Σ^0 reactions. The photon energy E$_\gamma$, the scattering angle cosΘ_{cm} and the fitting results are displayed in the figures. The solid lines are the results of the fitting using a function of cos(2ϕ).

The photon beam asymmetries $\Sigma_{K^+}^{meas}$, Σ_p and Σ_π for the K$^+$ event samples, the proton events and the π^+ events are listed with the statistical errors in Table C.3 and Table C.4.

The correction of the π^+/proton contamination is done for the photon beam asymmetries $\Sigma_{K^+}^{meas}$. The results are summarized in Table C.5 and Table C.6. The values in the forth column are the photon asymmetries after the correction for the π^+/proton contamination events. The values in the fifth column are the differences of the photon asymmetries between before and after the correction. In the last column, the errors from the statistical errors of the photon asymmetries of the π^+/proton events are shown. The error $\delta_{\pi p}$ is defined as

$$\delta_{\pi p} = \frac{C_{\pi^+}\Delta\Sigma_{\pi^+} + C_p\Delta\Sigma_p}{1 - C_{\pi^+} - C_p}, \tag{C.1}$$

where $\Delta\Sigma_{\pi^+}$ and $\Delta\Sigma_p$ are the statistical errors for the photon asymmetries of the π^+ and proton events.

After the correction for the π^+/proton contamination, the correction for the TRG contamination is done for the photon beam asymmetries Σ_{K^+}. The results are summarized in Table C.7 and Table C.8. The values in the forth column are the photon asymmetries after the correction for the TRG contamination events. The values in the fifth column are the differences of the photon asymmetries between before and after the correction. In the last column, the errors from the statistical errors of the photon asymmetries of the TRG events are shown. The error

δ_{TRG} is defined as

$$\delta_{TRG} = \frac{C_{TRG}\Delta\Sigma_{TRG}}{1 - C_{TRG}}, \tag{C.2}$$

where $\Delta\Sigma_{TRG}$ is the statistical errors for the photon asymmetries of the TRG events.

Table C.1: Photon beam asymmetry of the K^+ event samples for the $p(\gamma,K^+)\Lambda$.

E_γ (GeV)	$\cos\Theta_{cm}$	$\Sigma^{meas}_{K^+}\pm$error	χ^2	P_γ
1.55	0.650	0.261 ±0.1040	1.33	0.572
1.55	0.750	0.232 ±0.0781	0.73	0.571
1.55	0.850	0.276 ±0.0734	0.79	0.571
1.55	0.925	0.181 ±0.0715	0.38	0.571
1.55	0.975	0.147 ±0.0776	0.48	0.571
1.65	0.650	0.288 ±0.0859	0.49	0.641
1.65	0.750	0.232 ±0.0670	1.30	0.639
1.65	0.850	0.213 ±0.0653	0.69	0.640
1.65	0.925	0.119 ±0.0612	1.17	0.642
1.65	0.975	0.117 ±0.0669	0.64	0.641
1.75	0.650	0.201 ±0.0727	1.10	0.713
1.75	0.750	0.261 ±0.0597	1.02	0.709
1.75	0.850	0.256 ±0.0596	0.65	0.712
1.75	0.925	0.286 ±0.0560	0.77	0.712
1.75	0.975	0.004 ±0.0623	1.36	0.712
1.90	0.650	0.206 ±0.0400	2.17	0.794
1.90	0.750	0.219 ±0.0344	0.82	0.792
1.90	0.850	0.286 ±0.0324	0.53	0.792
1.90	0.925	0.338 ±0.0313	1.91	0.793
1.90	0.975	0.199 ±0.0350	0.77	0.793
2.10	0.650	0.269 ±0.0336	1.20	0.868
2.10	0.750	0.341 ±0.0293	0.89	0.867
2.10	0.850	0.401 ±0.0255	2.05	0.867
2.10	0.925	0.464 ±0.0246	1.89	0.867
2.10	0.975	0.240 ±0.0275	0.67	0.867
2.30	0.650	0.356 ±0.0329	1.83	0.901
2.30	0.750	0.416 ±0.0282	1.71	0.899
2.30	0.850	0.502 ±0.0224	1.98	0.901
2.30	0.925	0.480 ±0.0235	1.72	0.901
2.30	0.975	0.235 ±0.0269	1.62	0.899

Table C.2: Photon beam asymmetry of the K^+ event samples for the $p(\gamma,K^+)\Sigma^0$.

E_γ (GeV)	$\cos\Theta_{cm}$	$\Sigma_{K^+}^{meas}\pm$error	χ^2	P_γ
1.55	0.650	0.214 ±0.1161	1.28	0.573
1.55	0.750	0.089 ±0.0983	1.51	0.569
1.55	0.850	0.178 ±0.0904	1.35	0.572
1.55	0.925	0.251 ±0.1017	0.67	0.571
1.55	0.975	0.061 ±0.1065	0.75	0.571
1.65	0.650	0.181 ±0.1017	0.93	0.647
1.65	0.750	0.173 ±0.0791	1.15	0.640
1.65	0.850	0.165 ±0.0742	1.31	0.642
1.65	0.925	0.178 ±0.0770	0.80	0.642
1.65	0.975	0.229 ±0.0871	1.07	0.642
1.75	0.650	0.336 ±0.0781	0.64	0.710
1.75	0.750	0.272 ±0.0654	2.26	0.712
1.75	0.850	0.251 ±0.0657	1.07	0.713
1.75	0.925	0.242 ±0.0701	0.72	0.711
1.75	0.975	0.091 ±0.0747	1.02	0.709
1.90	0.650	0.349 ±0.0419	0.98	0.793
1.90	0.750	0.332 ±0.0375	3.00	0.793
1.90	0.850	0.375 ±0.0372	0.95	0.792
1.90	0.925	0.342 ±0.0415	1.35	0.791
1.90	0.975	0.179 ±0.0488	1.20	0.790
2.10	0.650	0.441 ±0.0344	0.29	0.868
2.10	0.750	0.496 ±0.0325	2.30	0.867
2.10	0.850	0.468 ±0.0306	1.79	0.866
2.10	0.925	0.458 ±0.0338	0.74	0.867
2.10	0.975	0.216 ±0.0411	0.84	0.868
2.30	0.650	0.529 ±0.0323	1.21	0.903
2.30	0.750	0.600 ±0.0297	1.34	0.899
2.30	0.850	0.559 ±0.0275	2.41	0.901
2.30	0.925	0.517 ±0.0315	0.90	0.901
2.30	0.975	0.247 ±0.0380	0.68	0.899

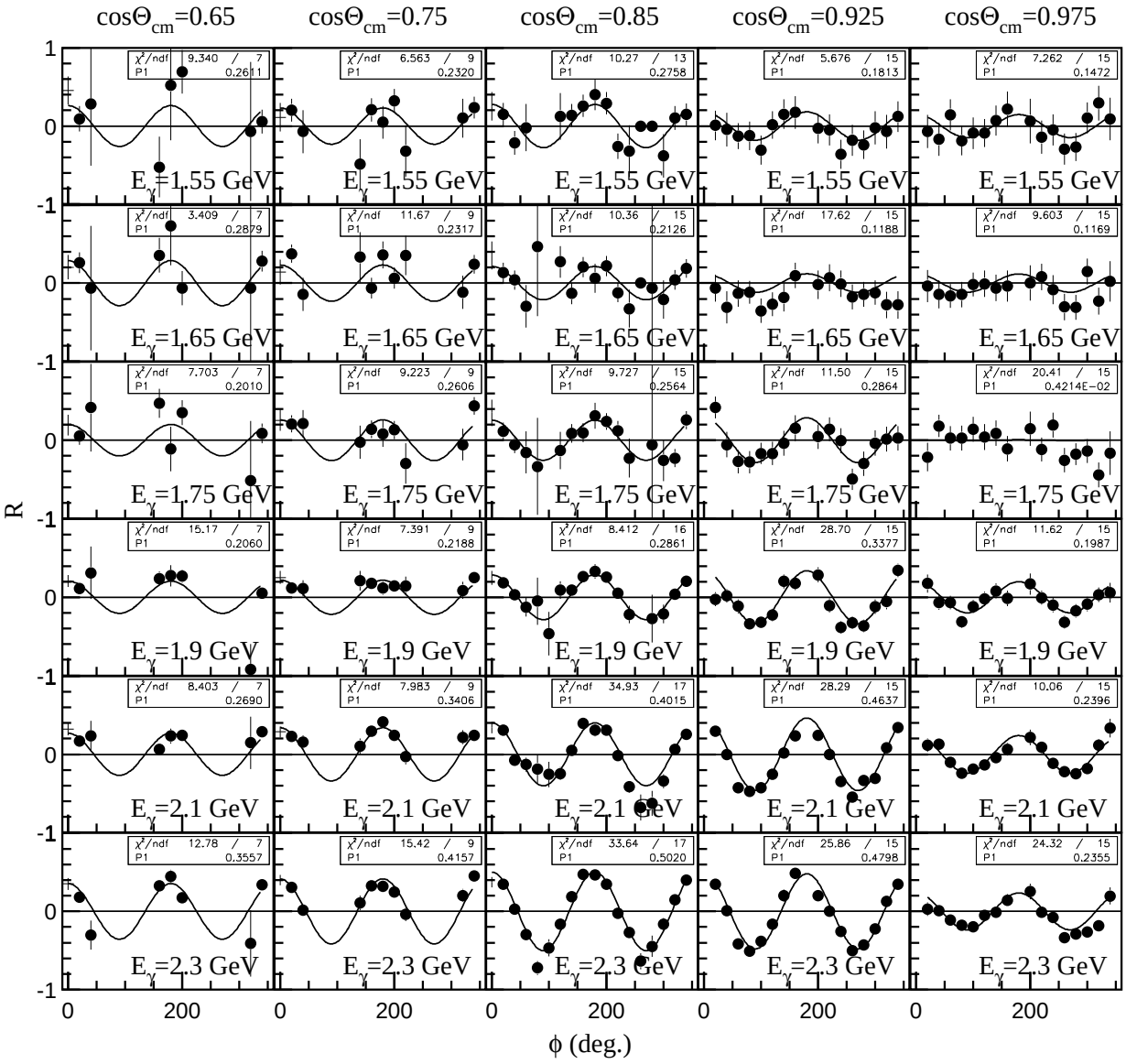

Figure C.1: ϕ distribution of the ratio R for the p(γ,K$^+$)Λ reaction event samples after the correction of the polarization degree. The fitting results are the photon beam asymmetries $\Sigma_{K^+}^{meas}$.

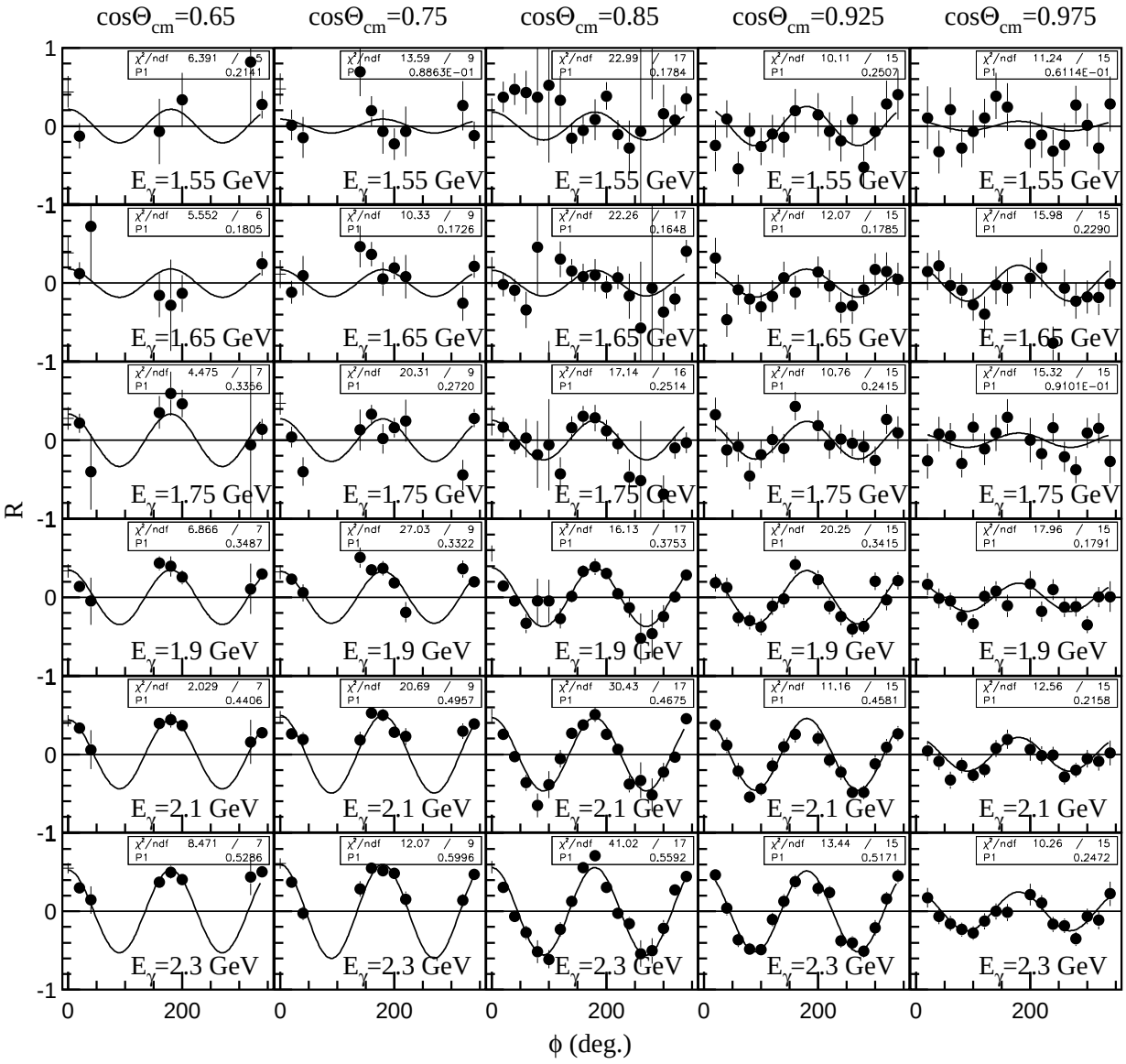

Figure C.2: ϕ distribution of the ratio R for the p(γ,K$^+$)Σ^0 reaction event samples after the correction of the polarization degree. The fitting results are the photon beam asymmetries $\Sigma_{K^+}^{meas}$.

Table C.3: Photon beam asymmetry of the K^+ event samples, π^+, proton and the TRG events in the Λ production channel. The statistical errors are listed.

E_γ (GeV)	$\cos\Theta_{cm}$	Σ_K^{meas}	Σ_p	Σ_π	Σ_{TRG}
1.55	0.650	0.261 ±0.1040	-0.096 ±0.0511	-0.035 ±0.0807	0.530 ±0.2130
1.55	0.750	0.232 ±0.0781	-0.134 ±0.0417	-0.141 ±0.0929	0.497 ±0.1798
1.55	0.850	0.276 ±0.0734	-0.032 ±0.0405	0.134 ±0.1203	0.101 ±0.1717
1.55	0.925	0.181 ±0.0715	0.086 ±0.0416	0.449 ±0.1355	-0.089 ±0.1719
1.55	0.975	0.147 ±0.0776	0.014 ±0.0425	-0.025 ±0.1111	-0.263 ±0.1714
1.65	0.650	0.288 ±0.0859	-0.132 ±0.0470	-0.031 ±0.0708	0.397 ±0.1806
1.65	0.750	0.232 ±0.0670	-0.036 ±0.0390	0.026 ±0.0789	0.435 ±0.1627
1.65	0.850	0.213 ±0.0653	-0.058 ±0.0370	0.211 ±0.1139	0.360 ±0.1343
1.65	0.925	0.119 ±0.0612	0.124 ±0.0379	0.262 ±0.1210	0.145 ±0.1402
1.65	0.975	0.117 ±0.0669	0.046 ±0.0391	-0.171 ±0.1042	-0.010 ±0.1445
1.75	0.650	0.201 ±0.0727	-0.101 ±0.0465	-0.129 ±0.0681	0.401 ±0.1608
1.75	0.750	0.261 ±0.0597	-0.091 ±0.0390	-0.010 ±0.0864	0.449 ±0.1225
1.75	0.850	0.256 ±0.0596	-0.064 ±0.0370	0.161 ±0.1076	0.399 ±0.1236
1.75	0.925	0.286 ±0.0560	0.006 ±0.0370	0.178 ±0.1239	0.264 ±0.1197
1.75	0.975	0.004 ±0.0623	0.014 ±0.0370	-0.008 ±0.1057	0.047 ±0.1322
1.90	0.650	0.206 ±0.0400	-0.009 ±0.0282	-0.001 ±0.0440	0.508 ±0.0849
1.90	0.750	0.219 ±0.0344	-0.042 ±0.0249	0.038 ±0.0531	0.376 ±0.0736
1.90	0.850	0.286 ±0.0324	0.017 ±0.0225	0.245 ±0.0637	0.447 ±0.0648
1.90	0.925	0.338 ±0.0313	0.027 ±0.0223	0.212 ±0.0695	0.271 ±0.0654
1.90	0.975	0.199 ±0.0350	0.030 ±0.0225	0.126 ±0.0601	0.104 ±0.0759
2.10	0.650	0.269 ±0.0336	-0.045 ±0.0256	0.075 ±0.0423	0.341 ±0.0747
2.10	0.750	0.341 ±0.0293	0.004 ±0.0233	0.220 ±0.0522	0.521 ±0.0597
2.10	0.850	0.401 ±0.0255	-0.003 ±0.0195	0.304 ±0.0509	0.475 ±0.0481
2.10	0.925	0.464 ±0.0246	0.035 ±0.0193	0.311 ±0.0572	0.426 ±0.0523
2.10	0.975	0.240 ±0.0275	0.055 ±0.0200	0.204 ±0.0503	0.216 ±0.0577
2.30	0.650	0.356 ±0.0329	-0.034 ±0.0254	0.076 ±0.0423	0.471 ±0.0666
2.30	0.750	0.416 ±0.0282	-0.059 ±0.0235	0.230 ±0.0523	0.519 ±0.0535
2.30	0.850	0.502 ±0.0224	-0.004 ±0.0187	0.431 ±0.0445	0.479 ±0.0433
2.30	0.925	0.480 ±0.0235	0.039 ±0.0190	0.442 ±0.0508	0.496 ±0.0478
2.30	0.975	0.235 ±0.0269	0.001 ±0.0198	0.164 ±0.0485	0.194 ±0.0561

Table C.4: Photon beam asymmetry of the K^+ event samples, π^+, proton and the TRG events in the Σ^0 production channel. The statistical errors are listed.

E_γ (GeV)	$\cos\Theta_{cm}$	Σ_K^{meas}	Σ_p	Σ_π	Σ_{TRG}
1.55	0.650	0.214 ±0.1161	-0.115 ±0.0540	-0.288 ±0.0832	0.810 ±0.2021
1.55	0.750	0.089 ±0.0983	-0.163 ±0.0421	-0.001 ±0.1036	0.159 ±0.1635
1.55	0.850	0.178 ±0.0904	-0.070 ±0.0391	-0.040 ±0.1412	0.133 ±0.1664
1.55	0.925	0.251 ±0.1017	-0.043 ±0.0413	-0.248 ±0.1695	0.336 ±0.1559
1.55	0.975	0.061 ±0.1065	0.017 ±0.0413	-0.337 ±0.1369	-0.257 ±0.2055
1.65	0.650	0.181 ±0.1017	-0.134 ±0.0475	-0.282 ±0.0786	0.493 ±0.1838
1.65	0.750	0.173 ±0.0791	-0.097 ±0.0376	-0.121 ±0.0962	0.228 ±0.1370
1.65	0.850	0.165 ±0.0742	-0.100 ±0.0349	0.017 ±0.1291	0.266 ±0.1387
1.65	0.925	0.178 ±0.0770	0.016 ±0.0361	-0.052 ±0.1639	0.090 ±0.1322
1.65	0.975	0.229 ±0.0871	0.004 ±0.0356	-0.081 ±0.1232	0.399 ±0.1466
1.75	0.650	0.336 ±0.0781	-0.264 ±0.0449	-0.261 ±0.0716	0.219 ±0.1408
1.75	0.750	0.272 ±0.0654	-0.112 ±0.0385	-0.257 ±0.0931	0.139 ±0.1197
1.75	0.850	0.251 ±0.0657	0.005 ±0.0337	0.244 ±0.1238	0.370 ±0.1142
1.75	0.925	0.242 ±0.0701	0.045 ±0.0337	-0.044 ±0.1301	0.159 ±0.1127
1.75	0.975	0.091 ±0.0747	0.030 ±0.0348	0.072 ±0.1141	-0.250 ±0.1388
1.90	0.650	0.349 ±0.0419	-0.045 ±0.0266	-0.247 ±0.0437	0.613 ±0.0749
1.90	0.750	0.332 ±0.0375	-0.058 ±0.0223	0.032 ±0.0549	0.525 ±0.0643
1.90	0.850	0.375 ±0.0372	0.018 ±0.0197	0.068 ±0.0711	0.467 ±0.0578
1.90	0.925	0.342 ±0.0415	0.052 ±0.0203	0.259 ±0.0802	0.227 ±0.0635
1.90	0.975	0.179 ±0.0488	0.038 ±0.0214	0.000 ±0.0714	-0.057 ±0.0765
2.10	0.650	0.441 ±0.0344	0.009 ±0.0226	-0.158 ±0.0419	0.522 ±0.0592
2.10	0.750	0.496 ±0.0325	0.023 ±0.0202	0.154 ±0.0535	0.511 ±0.0527
2.10	0.850	0.468 ±0.0306	0.008 ±0.0177	0.305 ±0.0569	0.529 ±0.0430
2.10	0.925	0.458 ±0.0338	0.036 ±0.0186	0.221 ±0.0666	0.384 ±0.0499
2.10	0.975	0.216 ±0.0411	0.036 ±0.0195	0.113 ±0.0619	0.101 ±0.0603
2.30	0.650	0.529 ±0.0323	0.051 ±0.0221	0.028 ±0.0432	0.629 ±0.0549
2.30	0.750	0.600 ±0.0297	-0.052 ±0.0208	0.316 ±0.0522	0.548 ±0.0482
2.30	0.850	0.559 ±0.0275	-0.009 ±0.0178	0.492 ±0.0483	0.541 ±0.0385
2.30	0.925	0.517 ±0.0315	0.031 ±0.0193	0.197 ±0.0591	0.521 ±0.0415
2.30	0.975	0.247 ±0.0380	-0.002 ±0.0203	-0.061 ±0.0548	0.280 ±0.0511

Table C.5: Correction of the photon beam asymmetry for the π/proton contamination in the $p(\gamma,K^+)\Lambda$ reaction.

E_γ (GeV)	$\cos\Theta_{cm}$	$\Sigma_{K^+}^{meas}$	$\Sigma_{K^+}\pm$error	Σ_{K^+}-$\Sigma_{K^+}^{meas}\pm$error	$\delta_{\pi p}$
1.55	0.650	0.2611	0.2627 ±0.1045	0.0016 ±0.0105	±0.0003
1.55	0.750	0.2320	0.2339 ±0.0785	0.0019 ±0.0079	±0.0004
1.55	0.850	0.2758	0.2768 ±0.0738	0.0010 ±0.0074	±0.0004
1.55	0.925	0.1813	0.1807 ±0.0719	-0.0006 ±0.0072	±0.0005
1.55	0.975	0.1472	0.1480 ±0.0780	0.0008 ±0.0078	±0.0004
1.65	0.650	0.2879	0.2907 ±0.0866	0.0028 ±0.0110	±0.0005
1.65	0.750	0.2317	0.2335 ±0.0675	0.0018 ±0.0085	±0.0006
1.65	0.850	0.2126	0.2132 ±0.0658	0.0006 ±0.0083	±0.0008
1.65	0.925	0.1188	0.1179 ±0.0617	-0.0009 ±0.0078	±0.0008
1.65	0.975	0.1169	0.1188 ±0.0674	0.0019 ±0.0086	±0.0007
1.75	0.650	0.2010	0.2053 ±0.0737	0.0043 ±0.0119	±0.0009
1.75	0.750	0.2606	0.2643 ±0.0605	0.0037 ±0.0098	±0.0010
1.75	0.850	0.2564	0.2581 ±0.0604	0.0017 ±0.0098	±0.0013
1.75	0.925	0.2864	0.2882 ±0.0568	0.0018 ±0.0092	±0.0015
1.75	0.975	0.0042	0.0043 ±0.0631	0.0001 ±0.0102	±0.0013
1.90	0.650	0.2060	0.2094 ±0.0407	0.0034 ±0.0073	±0.0007
1.90	0.750	0.2188	0.2221 ±0.0350	0.0033 ±0.0063	±0.0007
1.90	0.850	0.2861	0.2877 ±0.0329	0.0016 ±0.0059	±0.0009
1.90	0.925	0.3377	0.3405 ±0.0318	0.0028 ±0.0057	±0.0009
1.90	0.975	0.1987	0.2003 ±0.0356	0.0016 ±0.0064	±0.0008
2.10	0.650	0.2690	0.2762 ±0.0347	0.0072 ±0.0085	±0.0011
2.10	0.750	0.3406	0.3466 ±0.0302	0.0060 ±0.0074	±0.0013
2.10	0.850	0.4015	0.4077 ±0.0263	0.0062 ±0.0065	±0.0013
2.10	0.925	0.4637	0.4713 ±0.0254	0.0076 ±0.0063	±0.0014
2.10	0.975	0.2396	0.2422 ±0.0284	0.0026 ±0.0070	±0.0012
2.30	0.650	0.3557	0.3710 ±0.0344	0.0153 ±0.0102	±0.0016
2.30	0.750	0.4157	0.4306 ±0.0295	0.0149 ±0.0088	±0.0018
2.30	0.850	0.5020	0.5148 ±0.0235	0.0128 ±0.0070	±0.0015
2.30	0.925	0.4798	0.4904 ±0.0246	0.0106 ±0.0073	±0.0016
2.30	0.975	0.2355	0.2424 ±0.0282	0.0069 ±0.0084	±0.0016

Table C.6: Correction of the photon beam asymmetry for the π/proton contamination in the $p(\gamma,K^+)\Sigma^0$ reaction.

E_γ (GeV)	$\cos\Theta_{cm}$	$\Sigma_{K^+}^{meas}$	$\Sigma_{K^+}\pm$error	Σ_{K^+}-$\Sigma_{K^+}^{meas}\pm$error	$\delta_{\pi p}$
1.55	0.650	0.2141	0.2161 ±0.1166	0.0020 ±0.0105	±0.0003
1.55	0.750	0.0886	0.0890 ±0.0987	0.0004 ±0.0088	±0.0004
1.55	0.850	0.1784	0.1793 ±0.0908	0.0009 ±0.0081	±0.0006
1.55	0.925	0.2507	0.2527 ±0.1021	0.0020 ±0.0092	±0.0007
1.55	0.975	0.0611	0.0627 ±0.1069	0.0016 ±0.0096	±0.0005
1.65	0.650	0.1805	0.1843 ±0.1026	0.0038 ±0.0138	±0.0006
1.65	0.750	0.1726	0.1752 ±0.0798	0.0026 ±0.0107	±0.0007
1.65	0.850	0.1648	0.1665 ±0.0749	0.0017 ±0.0101	±0.0009
1.65	0.925	0.1785	0.1804 ±0.0777	0.0019 ±0.0105	±0.0011
1.65	0.975	0.2290	0.2316 ±0.0879	0.0026 ±0.0118	±0.0009
1.75	0.650	0.3356	0.3410 ±0.0788	0.0054 ±0.0106	±0.0006
1.75	0.750	0.2720	0.2767 ±0.0660	0.0047 ±0.0089	±0.0008
1.75	0.850	0.2514	0.2517 ±0.0663	0.0003 ±0.0089	±0.0010
1.75	0.925	0.2415	0.2440 ±0.0707	0.0025 ±0.0095	±0.0011
1.75	0.975	0.0910	0.0912 ±0.0754	0.0002 ±0.0101	±0.0010
1.90	0.650	0.3487	0.3588 ±0.0427	0.0101 ±0.0082	±0.0007
1.90	0.750	0.3322	0.3381 ±0.0382	0.0059 ±0.0073	±0.0009
1.90	0.850	0.3753	0.3811 ±0.0379	0.0058 ±0.0073	±0.0011
1.90	0.925	0.3415	0.3439 ±0.0423	0.0024 ±0.0081	±0.0012
1.90	0.975	0.1791	0.1822 ±0.0497	0.0031 ±0.0095	±0.0011
2.10	0.650	0.4406	0.4577 ±0.0356	0.0171 ±0.0090	±0.0011
2.10	0.750	0.4957	0.5082 ±0.0336	0.0125 ±0.0084	±0.0013
2.10	0.850	0.4675	0.4764 ±0.0316	0.0089 ±0.0079	±0.0013
2.10	0.925	0.4581	0.4680 ±0.0349	0.0099 ±0.0088	±0.0015
2.10	0.975	0.2158	0.2200 ±0.0424	0.0042 ±0.0106	±0.0015
2.30	0.650	0.5286	0.5561 ±0.0342	0.0275 ±0.0113	±0.0019
2.30	0.750	0.5996	0.6240 ±0.0314	0.0244 ±0.0103	±0.0022
2.30	0.850	0.5592	0.5746 ±0.0291	0.0154 ±0.0095	±0.0020
2.30	0.925	0.5171	0.5389 ±0.0334	0.0218 ±0.0110	±0.0024
2.30	0.975	0.2472	0.2631 ±0.0402	0.0159 ±0.0131	±0.0023

Table C.7: Correction of the photon beam asymmetry for the TRG contamination in the $p(\gamma,K^+)\Lambda$ reaction.

E_γ (GeV)	$\cos\Theta_{cm}$	Σ_{K^+}	$\Sigma'_{K^+}\pm$error	Σ'_{K^+}-$\Sigma_{K^+}\pm$error	δ_{TRG}
1.55	0.650	0.2627	0.2626 ±0.1045	-0.0001 ±0.0030	±0.0001
1.55	0.750	0.2339	0.2335 ±0.0786	-0.0004 ±0.0045	±0.0003
1.55	0.850	0.2768	0.2777 ±0.0742	0.0009 ±0.0074	±0.0009
1.55	0.925	0.1807	0.1829 ±0.0725	0.0022 ±0.0093	±0.0014
1.55	0.975	0.1480	0.1706 ±0.0828	0.0226 ±0.0279	±0.0094
1.65	0.650	0.2907	0.2907 ±0.0866	0.0000 ±0.0025	±0.0001
1.65	0.750	0.2335	0.2332 ±0.0676	-0.0003 ±0.0038	±0.0003
1.65	0.850	0.2132	0.2125 ±0.0661	-0.0007 ±0.0066	±0.0007
1.65	0.925	0.1179	0.1177 ±0.0622	-0.0002 ±0.0080	±0.0012
1.65	0.975	0.1188	0.1259 ±0.0715	0.0071 ±0.0240	±0.0079
1.75	0.650	0.2053	0.2052 ±0.0737	-0.0001 ±0.0021	±0.0001
1.75	0.750	0.2643	0.2640 ±0.0606	-0.0003 ±0.0034	±0.0002
1.75	0.850	0.2581	0.2574 ±0.0607	-0.0007 ±0.0061	±0.0006
1.75	0.925	0.2882	0.2884 ±0.0573	0.0002 ±0.0074	±0.0010
1.75	0.975	0.0043	0.0020 ±0.0670	-0.0023 ±0.0224	±0.0073
1.90	0.650	0.2094	0.2093 ±0.0407	-0.0001 ±0.0012	±0.0000
1.90	0.750	0.2221	0.2219 ±0.0351	-0.0002 ±0.0020	±0.0001
1.90	0.850	0.2877	0.2869 ±0.0331	-0.0008 ±0.0033	±0.0003
1.90	0.925	0.3405	0.3411 ±0.0321	0.0006 ±0.0041	±0.0005
1.90	0.975	0.2003	0.2056 ±0.0378	0.0053 ±0.0127	±0.0042
2.10	0.650	0.2762	0.2762 ±0.0347	0.0000 ±0.0010	±0.0000
2.10	0.750	0.3466	0.3463 ±0.0302	-0.0003 ±0.0017	±0.0001
2.10	0.850	0.4077	0.4074 ±0.0264	-0.0003 ±0.0026	±0.0002
2.10	0.925	0.4713	0.4717 ±0.0256	0.0004 ±0.0033	±0.0004
2.10	0.975	0.2422	0.2436 ±0.0301	0.0014 ±0.0101	±0.0032
2.30	0.650	0.3710	0.3710 ±0.0344	0.0000 ±0.0010	±0.0000
2.30	0.750	0.4306	0.4305 ±0.0295	-0.0001 ±0.0017	±0.0001
2.30	0.850	0.5148	0.5150 ±0.0236	0.0002 ±0.0024	±0.0002
2.30	0.925	0.4904	0.4904 ±0.0248	0.0000 ±0.0032	±0.0004
2.30	0.975	0.2424	0.2450 ±0.0299	0.0026 ±0.0100	±0.0031

Table C.8: Correction of the photon beam asymmetry for the TRG contamination in the $p(\gamma,K^+)\Sigma^0$ reaction.

E_γ (GeV)	$\cos\Theta_{cm}$	Σ_{K^+}	$\Sigma'_{K^+}\pm$error	Σ'_{K^+}-$\Sigma_{K^+}\pm$error	δ_{TRG}
1.55	0.650	0.2161	0.2156 ±0.1167	-0.0005 ±0.0048	±0.0002
1.55	0.750	0.0890	0.0888 ±0.0990	-0.0002 ±0.0080	±0.0005
1.55	0.850	0.1793	0.1796 ±0.0915	0.0003 ±0.0109	±0.0012
1.55	0.925	0.2527	0.2515 ±0.1037	-0.0012 ±0.0179	±0.0023
1.55	0.975	0.0627	0.0972 ±0.1205	0.0345 ±0.0555	±0.0221
1.65	0.650	0.1843	0.1840 ±0.1027	-0.0003 ±0.0042	±0.0002
1.65	0.750	0.1752	0.1750 ±0.0801	-0.0002 ±0.0065	±0.0004
1.65	0.850	0.1665	0.1658 ±0.0754	-0.0007 ±0.0090	±0.0010
1.65	0.925	0.1804	0.1818 ±0.0789	0.0014 ±0.0136	±0.0020
1.65	0.975	0.2316	0.2136 ±0.0986	-0.0180 ±0.0447	±0.0158
1.75	0.650	0.3410	0.3411 ±0.0789	0.0001 ±0.0033	±0.0001
1.75	0.750	0.2767	0.2771 ±0.0662	0.0004 ±0.0053	±0.0004
1.75	0.850	0.2517	0.2509 ±0.0668	-0.0008 ±0.0080	±0.0008
1.75	0.925	0.2440	0.2453 ±0.0718	0.0013 ±0.0124	±0.0017
1.75	0.975	0.0912	0.1279 ±0.0849	0.0367 ±0.0390	±0.0149
1.90	0.650	0.3588	0.3586 ±0.0427	-0.0002 ±0.0018	±0.0001
1.90	0.750	0.3381	0.3375 ±0.0383	-0.0006 ±0.0031	±0.0002
1.90	0.850	0.3811	0.3805 ±0.0382	-0.0006 ±0.0045	±0.0004
1.90	0.925	0.3439	0.3457 ±0.0429	0.0018 ±0.0074	±0.0010
1.90	0.975	0.1822	0.2080 ±0.0557	0.0258 ±0.0251	±0.0082
2.10	0.650	0.4577	0.4576 ±0.0356	-0.0001 ±0.0015	±0.0001
2.10	0.750	0.5082	0.5082 ±0.0337	0.0000 ±0.0027	±0.0002
2.10	0.850	0.4764	0.4760 ±0.0318	-0.0004 ±0.0038	±0.0003
2.10	0.925	0.4680	0.4693 ±0.0354	0.0013 ±0.0061	±0.0007
2.10	0.975	0.2200	0.2328 ±0.0474	0.0128 ±0.0212	±0.0065
2.30	0.650	0.5561	0.5560 ±0.0342	-0.0001 ±0.0014	±0.0000
2.30	0.750	0.6240	0.6242 ±0.0315	0.0002 ±0.0025	±0.0002
2.30	0.850	0.5746	0.5748 ±0.0293	0.0002 ±0.0035	±0.0003
2.30	0.925	0.5389	0.5392 ±0.0339	0.0003 ±0.0058	±0.0006
2.30	0.975	0.2631	0.2613 ±0.0449	-0.0018 ±0.0199	±0.0055

Appendix D

Tables of the asymmetries - the nine energy bins

The angular distributions of the photon beam asymmetries in the nine energy bins are summarized for the p(γ,K^+)Λ and p(γ,K^+)Σ^0 reactions. The results at E_γ = 1.55, 1.65 and 1.75 GeV are the same as ones using the six energy bins.

The results of the photon beam asymmetries for the K^+ event samples are summarized in Table D.1 and Table D.2. The photon beam asymmetries $\Sigma_{K^+}^{meas}$, the statistical errors, χ^2 of the fitting and the average polarizations $\bar{P}_\gamma$ are listed. The photon beam asymmetries $\Sigma_{K^+}^{meas}$ are before the correction of the background contamination (the π^+/proton and the TRG events). Fig. D.1 and Fig. D.2 show the ϕ distributions of the ratios R of $(n \cdot N_v - N_h)/(n \cdot N_v + N_h)$ in Eq.(4.2) for the p(γ,K^+)Λ and p(γ,K^+)Σ^0 reactions. The photon energy E_γ, the scattering angle cosΘ_{cm} and the fitting results are displayed in the figures. The solid lines are the results of the fitting using a function of cos(2ϕ).

Fig. D.3(a) and (b) show the final results of the photon beam asymmetries. The plots are the present data. Only the statistical error is included in the error bars. The systematic error for the polarization degree and angle of the photons is less than 2%. The systematic error for the normalization factor is -0.02 to 0.06. The final results are summarized in Table D.3.

Table D.1: Photon beam asymmetry of the K^+ event samples for the $p(\gamma,K^+)\Lambda$.

E_γ (GeV)	$\cos\Theta_{cm}$	$\Sigma^{meas}_{K^+}\pm$error	χ^2	P_γ
1.85	0.650	0.159 ±0.0598	1.39	0.769
1.85	0.750	0.159 ±0.0496	0.76	0.768
1.85	0.850	0.312 ±0.0472	0.97	0.766
1.85	0.925	0.249 ±0.0463	1.36	0.768
1.85	0.975	0.212 ±0.0511	0.41	0.768
1.95	0.650	0.250 ±0.0535	1.47	0.817
1.95	0.750	0.281 ±0.0476	0.84	0.817
1.95	0.850	0.271 ±0.0444	0.73	0.818
1.95	0.925	0.423 ±0.0422	1.58	0.817
1.95	0.975	0.187 ±0.0477	0.78	0.818
2.05	0.650	0.213 ±0.0475	1.50	0.856
2.05	0.750	0.337 ±0.0408	1.45	0.854
2.05	0.850	0.310 ±0.0368	1.01	0.855
2.05	0.925	0.438 ±0.0350	0.88	0.854
2.05	0.975	0.254 ±0.0392	0.80	0.853
2.15	0.650	0.330 ±0.0473	0.60	0.882
2.15	0.750	0.347 ±0.0421	0.14	0.881
2.15	0.850	0.497 ±0.0351	1.51	0.881
2.15	0.925	0.494 ±0.0344	1.75	0.881
2.15	0.975	0.228 ±0.0384	0.67	0.881
2.25	0.650	0.315 ±0.0440	1.59	0.898
2.25	0.750	0.434 ±0.0376	1.27	0.895
2.25	0.850	0.516 ±0.0305	1.58	0.898
2.25	0.925	0.456 ±0.0314	1.66	0.897
2.25	0.975	0.237 ±0.0346	1.34	0.895
2.35	0.650	0.420 ±0.0491	1.59	0.905
2.35	0.750	0.401 ±0.0422	1.79	0.905
2.35	0.850	0.499 ±0.0327	1.77	0.905
2.35	0.925	0.517 ±0.0352	0.81	0.906
2.35	0.975	0.234 ±0.0427	0.67	0.905

Table D.2: Photon beam asymmetry of the K^+ event samples for the $p(\gamma,K^+)\Sigma^0$.

E_γ (GeV)	$\cos\Theta_{cm}$	$\Sigma^{meas}_{K^+}\pm$error	χ^2	P_γ
1.85	0.650	0.301 ±0.0611	0.88	0.768
1.85	0.750	0.252 ±0.0549	1.69	0.768
1.85	0.850	0.359 ±0.0539	0.60	0.767
1.85	0.925	0.312 ±0.0583	0.95	0.768
1.85	0.975	0.219 ±0.0676	1.67	0.767
1.95	0.650	0.402 ±0.0571	1.18	0.818
1.95	0.750	0.411 ±0.0510	1.61	0.818
1.95	0.850	0.406 ±0.0509	1.25	0.817
1.95	0.925	0.376 ±0.0590	0.79	0.817
1.95	0.975	0.152 ±0.0689	0.96	0.817
2.05	0.650	0.431 ±0.0479	0.82	0.856
2.05	0.750	0.501 ±0.0448	1.56	0.855
2.05	0.850	0.479 ±0.0425	1.70	0.854
2.05	0.925	0.442 ±0.0467	1.51	0.854
2.05	0.975	0.241 ±0.0594	0.90	0.854
2.15	0.650	0.460 ±0.0490	0.44	0.882
2.15	0.750	0.495 ±0.0471	1.71	0.882
2.15	0.850	0.476 ±0.0436	0.86	0.880
2.15	0.925	0.489 ±0.0485	0.38	0.881
2.15	0.975	0.209 ±0.0559	1.84	0.882
2.25	0.650	0.516 ±0.0441	0.43	0.899
2.25	0.750	0.564 ±0.0402	1.26	0.896
2.25	0.850	0.540 ±0.0388	1.47	0.897
2.25	0.925	0.525 ±0.0432	0.94	0.898
2.25	0.975	0.214 ±0.0514	0.78	0.895
2.35	0.650	0.555 ±0.0468	1.58	0.908
2.35	0.750	0.655 ±0.0434	0.84	0.904
2.35	0.850	0.596 ±0.0385	1.76	0.906
2.35	0.925	0.521 ±0.0456	1.27	0.905
2.35	0.975	0.288 ±0.0561	0.99	0.904

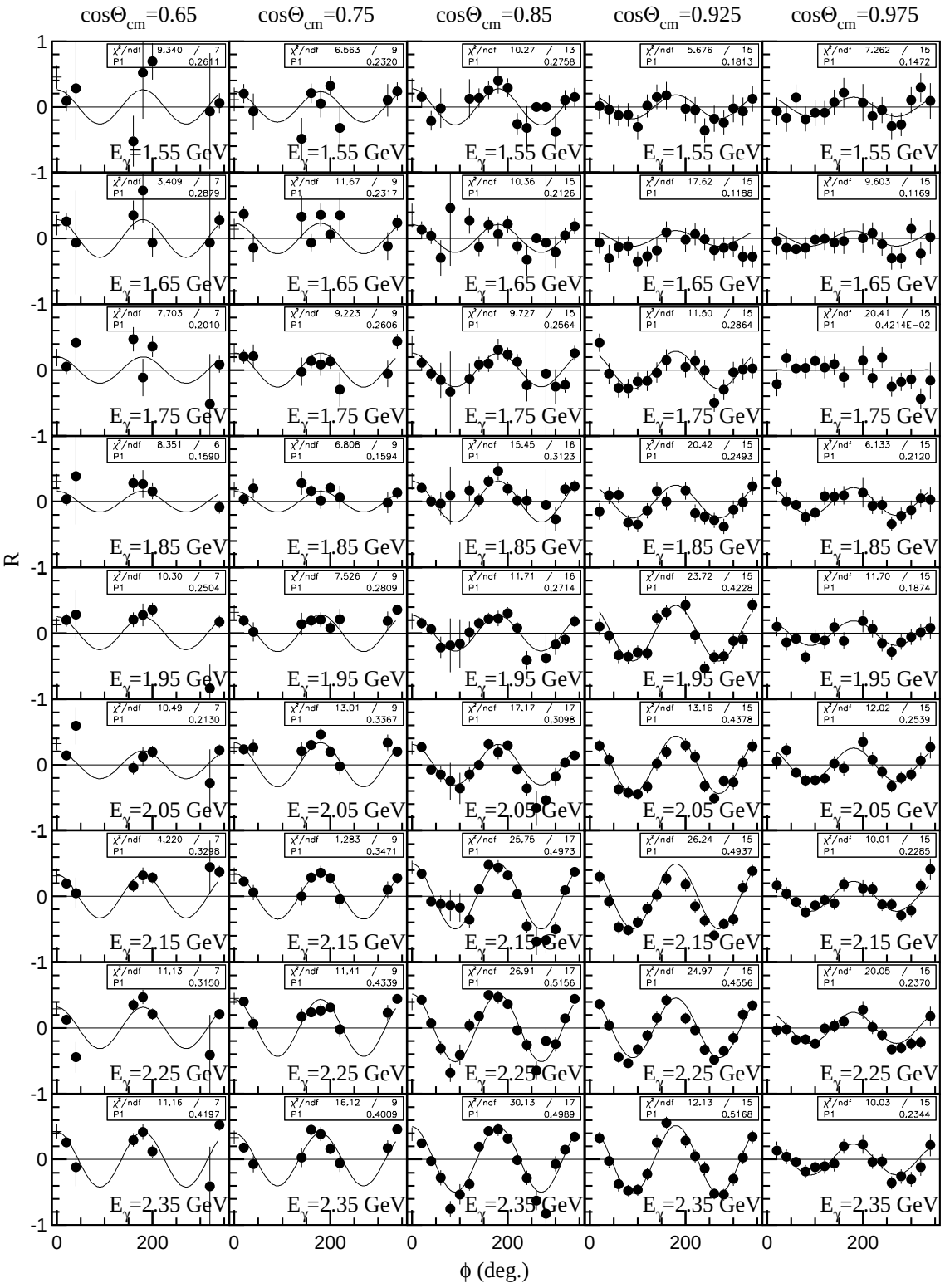

Figure D.1: ϕ distribution of the ratio R for the p(γ,K^+)Λ reaction event samples after the correction of the polarization degree. The fitting results are the photon beam asymmetries $\Sigma_{K^+}^{meas}$.

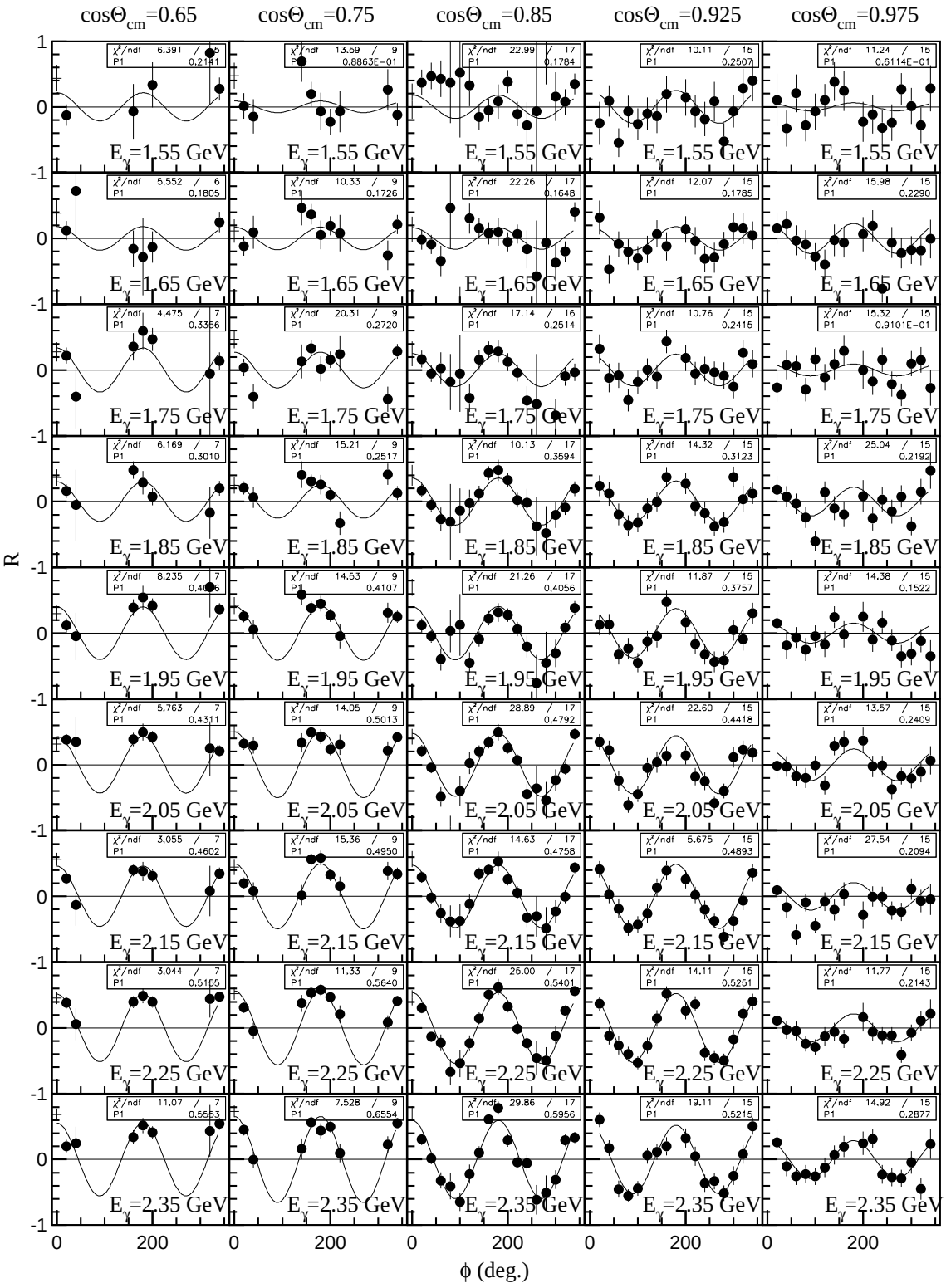

Figure D.2: ϕ distribution of the ratio R for the p(γ,K$^+$)Σ^0 reaction event samples after the correction of the polarization degree. The fitting results are the photon beam asymmetries $\Sigma_{K^+}^{meas}$.

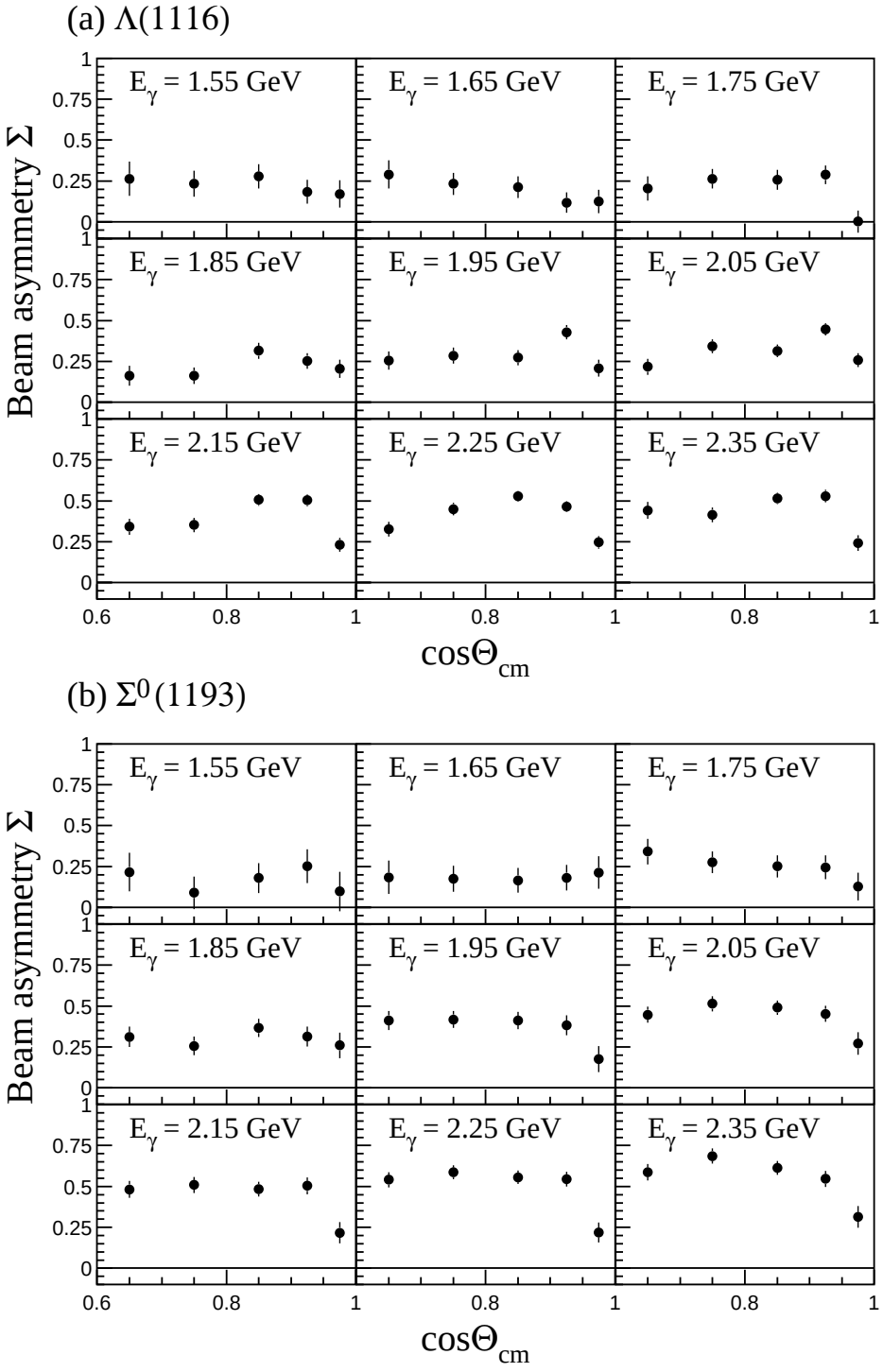

Figure D.3: Photon beam asymmetries for (a) the $p(\vec{\gamma},K^+)\Lambda$ and (b) the $p(\vec{\gamma},K^+)\Sigma^0$ reaction. The filled circles are the final results. The statistical errors are plotted.

Table D.3: The final results of the photon beam asymmetry for the p(γ,K$^+$)Λ and p($\vec{\gamma}$,K$^+$)Σ^0 reaction. The systematic error for the normalization factor is shown. The other 2% systematic error exists.

E_γ (GeV)	$\cos\Theta_{cm}$	$\Sigma^{\Lambda}_{K^+}$ $\pm$ statistical error	Systematic error	$\Sigma^{\Sigma^0}_{K^+}$ $\pm$ statistical error	Systematic error
1.85	0.650	0.162 $\pm$0.0608	0.0390	0.311 $\pm$0.0624	0.0376
1.85	0.750	0.163 $\pm$0.0506	0.0400	0.256 $\pm$0.0562	0.0396
1.85	0.850	0.315 $\pm$0.0482	0.0315	0.365 $\pm$0.0554	0.0305
1.85	0.925	0.253 $\pm$0.0475	-0.0130	0.313 $\pm$0.0604	-0.0107
1.85	0.975	0.205 $\pm$0.0552	-0.0197	0.259 $\pm$0.0773	-0.0209
1.95	0.650	0.254 $\pm$0.0544	0.0355	0.411 $\pm$0.0581	0.0342
1.95	0.750	0.284 $\pm$0.0485	0.0366	0.416 $\pm$0.0520	0.0351
1.95	0.850	0.271 $\pm$0.0453	0.0295	0.410 $\pm$0.0521	0.0264
1.95	0.925	0.426 $\pm$0.0433	-0.0107	0.381 $\pm$0.0609	-0.0106
1.95	0.975	0.207 $\pm$0.0515	-0.0161	0.176 $\pm$0.0783	-0.0150
2.05	0.650	0.216 $\pm$0.0489	0.0344	0.446 $\pm$0.0493	0.0314
2.05	0.750	0.342 $\pm$0.0421	0.0340	0.513 $\pm$0.0463	0.0319
2.05	0.850	0.314 $\pm$0.0381	0.0246	0.489 $\pm$0.0440	0.0201
2.05	0.925	0.445 $\pm$0.0364	-0.0103	0.451 $\pm$0.0487	-0.0110
2.05	0.975	0.257 $\pm$0.0429	-0.0179	0.270 $\pm$0.0683	-0.0155
2.15	0.650	0.341 $\pm$0.0488	0.0319	0.481 $\pm$0.0508	0.0297
2.15	0.750	0.353 $\pm$0.0436	0.0331	0.509 $\pm$0.0490	0.0312
2.15	0.850	0.505 $\pm$0.0365	0.0200	0.483 $\pm$0.0455	0.0225
2.15	0.925	0.502 $\pm$0.0358	-0.0106	0.503 $\pm$0.0511	-0.0081
2.15	0.975	0.232 $\pm$0.0421	-0.0157	0.217 $\pm$0.0649	-0.0180
2.25	0.650	0.327 $\pm$0.0459	0.0315	0.540 $\pm$0.0462	0.0276
2.25	0.750	0.449 $\pm$0.0393	0.0317	0.586 $\pm$0.0422	0.0282
2.25	0.850	0.528 $\pm$0.0320	0.0173	0.555 $\pm$0.0409	0.0187
2.25	0.925	0.465 $\pm$0.0331	-0.0083	0.544 $\pm$0.0460	-0.0059
2.25	0.975	0.246 $\pm$0.0383	-0.0165	0.218 $\pm$0.0601	-0.0170
2.35	0.650	0.440 $\pm$0.0517	0.0299	0.586 $\pm$0.0501	0.0267
2.35	0.750	0.414 $\pm$0.0445	0.0319	0.684 $\pm$0.0467	0.0259
2.35	0.850	0.513 $\pm$0.0346	0.0136	0.612 $\pm$0.0415	0.0169
2.35	0.925	0.529 $\pm$0.0374	-0.0070	0.545 $\pm$0.0495	-0.0079
2.35	0.975	0.242 $\pm$0.0476	-0.0150	0.313 $\pm$0.0670	-0.0146

Bibliography

[1] S. Capstick and W. Roberts, Phys. Rev. **D49** (1994) 4570.

[2] S. Capstick and W. Roberts, Phys. Rev. **D58** (1998) 074011.

[3] M.Q. Tran, *et al.*, Phys. Lett. **B445** (1998) 20.

[4] S. Goers, *et al.*, Phys. Lett. **B464** (1999) 331.

[5] R. Erbe, H. G. Hilpert, E. Schœ.AœN—ttler, and W. Struczinski (Aachen-Berlin-Bonn-Hamburg-Heidelberg-MœN—nchen Collaboration), Phys. Rev. **188**, (1969) 2060.

[6] T. Mart and C. Bennhold, Phys. Rev. **C61** (1999) 012201.

[7] S. Janssen, J. Ryckebusch, D. Debruyne, and T.V. Cauteren, Phys. Rev. **C65** (2002) 015201.

[8] B. Saghai, nucl-th/0105001, 2001, 'International Symposium on Hadrons and Nuclei' Seoul 2001.

[9] R. A. Adelseck and L. E. Wright, Phys. Rev. **C38** (1988)

[10] S. S. Hsiao, D. H. Lu, and Shin Nan Yang, Phys. Rev. **C61** (2000) 068201.

[11] H. Haberzettl, Phys. Rev. **C56** (1997) 2041.

[12] H. Haberzettl, C. Bennhold, T. Mart, and T. Feuster, Phys. Rev. **C58** (1998) R40.

[13] R. M. Davidson and Ron Workman, Phys. Rev. **C63** (2001) 025210.

[14] S. Janssen, Doctor thesis of University of Gent.

[15] A.M. Boyarski, F. Bulos, W. Busza, R. Diebold, S.D. Ecklund, G.E. Fischer, Y. Murata, J.R. Rees, B. Richter, and W.S. C. Williams, Phys. Rev. Lett. **22** (1969) 1131.

[16] D.J. Quinn, J.P. Rutherford, M.A. Shupe, D.J. Sherden, R.H. Siemann, and C.K. Sinclair, Phys. Rev. **D20** (1979) 1553.

[17] M. Guidal, M. Laget and M. Vanderhaeghen, Nucl. Phys. **A627** (1997) 645.

[18] P. Stichel, Z. Phys. **180** (1964) 170.

[19] J.P. Ader, M. Capdeville, G. C. Tannoudji and Ph. Salin Nuovo Cimento **LVIA, N.4** (1968) 953.

[20] http://www.spring8.or.jp.

[21] A. D'Angelo, O. Bartalini, V. Bellini, P. Levi Sandri, D. Moricciani, L. Nicoletti and A. Zucchiatti, Nucl. Instr. Meth. **A455** (2000) 1.

[22] M. Fujiwara, *et al.*, Jornal of the Japanese Society for Synchrotron Radiation Research, **10** (1997) 23.

[23] M. Fujiwara, *et al.*, Acta. Phys. Pol. **29** (1998) 141.

[24] T. Nakano, *et al.*, Nucl. Phys. **A629** (1998) 559C.

[25] T. Nakano, *et al.*, Nucl. Phys. **A670** (2000) 332.

[26] T. Nakano, *et al.*, Nucl. Phys. **A684** (2001) 71.

[27] T. Matsumura, Master thesis of University of Osaka (2000)

[28] SPring-8 annual report (1998) 132

[29] T. Mibe, Master thesis of University of Osaka (2000).

[30] H. Kohri et al, RCNP Annual report 2001.

[31] R. Suda, M. Watanabe, R. Enomoto, T. Iijima, I. Adachi, H. Hattori, T. Kuniya, T. Ooba, T. Sumiyoshi and Y. Yoshida, Nucl. Instr. Meth. **A406** (1998) 213.

[32] O.Toker, S. Masciocchi, E. Nygard, A. Rudge and P. Weilhammer, Nucl. Instr. Meth. **A340** (1994) 572.

[33] T. Sasaki, Master thesis of University of Kyoto (2000).

[34] Y. Sugaya and M.Nomachi, Nucl. Instr. Meth. **A437** (1999) 68

[35] Y. Sugaya *et al.*, IEEE transactions on nuclear science **48** No.4 (2001) 1282

[36] CERN Program library

[37] R. Frühwirth, M. Regler, R.K. Bock, H. Grote, "Data Analysis Techniques for High-Energy Physics", Cambridge Univ. Press.

[38] R. Frühwirth, Nucl. Instr. Meth. **A262** (1987) 444.

[39] J. Myrheim and L. Bugge, Nucl. Instr. Meth. **160** (1979) 43.

[40] E.J. Wolin and L.L. Ho, Nucl. Instr. Meth. **A329** (1993) 493.

[41] J. Ajaka, *et al.*, Phys. Rev. Lett. **81** (1998) 1797.

[42] J.P. Bocquet, M. Anghinolfi, O. Bartalini, V. Bellini, M. Castoldi, P. Corvisiero, A. D'Angelo, J.-P. Didelez, R. Di Salvo, G. Gervino, *et al.*, Nucl. Phys. **A691** (2001) 466c.

[43] L. Nicoletti, Doctor thesis of University of Joseph Fourier.

[44] R.A. Schumacher, Nucl. Phys. **A663&664** (2000) 440.

[45] R.A. Schumacher, to be published in 'proceedings of PANIC02'.

[46] W.C. Chang and T. Mibe for the LEPS collaboration, to be published in 'proceedings of PANIC02'.

[47] T. Hotta for the LEPS collaboration, to be published in 'proceedings of PANIC02'.

[48] T. Matsumura, *et al.*, to be published in 'proceedings of PANIC02'.

[49] J.K. Ahn for the LEPS collaboration, to be published in 'proceedings of PANIC02'.

[50] M. Sumihama for the LEPS collaboration, to be published in 'proceedings of PANIC02', hep-ex/0212065

[51] T. Nakano, *et al.*, hep-ex/0301020, 2003.